JOINT INVERSION OF TIME-LAPSE SEISMIC DATA

Final Report – Deliverable D6

(for the period of January 19, 2018, through December 31, 2019)

Prepared for:

AAD Document Control

National Energy Technology Laboratory
U.S. Department of Energy
626 Cochrans Mill Road
PO Box 10940, MS 921-107
Pittsburgh, PA 15236-0940

Cooperative Agreement No.: DE-FE0031540
DOE Technical Monitor: Mary Underwood
Project Reporting Period: January 19, 2018 – January 18, 2020
DUNS No. 102280781

Prepared by:

César Barajas-Olalde
Donald C. Adams
Lu Jin
Jun He
Nicholas S. Kalenze
John A. Hamling
Charles D. Gorecki

Energy & Environmental Research Center
University of North Dakota
15 North 23rd Street, Stop 9018
Grand Forks, ND 58202-9018

2019-EERC-12-10 December 2019

EERC DISCLAIMER

LEGAL NOTICE This research report was prepared by the Energy & Environmental Research Center (EERC), an agency of the University of North Dakota (UND), as an account of work sponsored by the U.S. Department of Energy National Energy Technology Laboratory. Because of the research nature of the work performed, neither the EERC nor any of its employees makes any warranty, express or implied, or assumes any legal liability or responsibility for the accuracy, completeness, or usefulness of any information, apparatus, product, or process disclosed or represented that its use would not infringe privately owned rights. Reference herein to any specific commercial product, process, or service by trade name, trademark, manufacturer, or otherwise does not necessarily constitute or imply its endorsement or recommendation by the EERC.

ACKNOWLEDGMENTS

The authors would like to thank project partners Peter Haffinger, Dries Gisolf, Mengmeng Zhang, Anna Droujinina, Panos Doulgeris (Delft Inversion); Alan Mur and Dan Tostado (Ikon Science); Sofiane Djezzar (EERC); former UND EERC student Seyedalireza Khatibi; and former EERC colleague Dr. Olarinre Salako for their contributions to this report.

DOE DISCLAIMER

TABLE OF CONTENTS

Continued . . .

TABLE OF CONTENTS (continued)

LIST OF FIGURES

Continued . . .

LIST OF FIGURES (continued)

Continued . . .

LIST OF FIGURES (continued)

Continued . . .

LIST OF FIGURES (continued)

Continued . . .

LIST OF FIGURES (continued)

LIST OF TABLES

JOINT INVERSION OF TIME-LAPSE SEISMIC DATA

EXECUTIVE SUMMARY

The Energy & Environmental Research Center (EERC) conducted the Joint Inversion of Time-Lapse Seismic Data project in which two joint inversion modeling and monitoring workflows were developed to address and resolve shortcomings of existing inversion technology and time-lapse amplitude difference interpretation.

The first workflow is based on the seismic wave-equation based (WEB) amplitude variation with offset (AVO) inversion which was performed in collaboration with project partner Delft Inversion. The nonlinear WEB-AVO inversion solves the full elastic wave-equation for the properties as well as the total wave-field in the object domain. The Joint Impedance and Facies Inversion (Ji-Fi) developed by project partner Ikon Science is the other technique applied in this project. This technique is based on Bayesian principles, geologic facies as priors, and powerful image-processing techniques to invert seismic data iteratively for impedances given facies and inverting the impedances for facies.

Both techniques were successfully applied to an existing time-lapse seismic data set. The WEB-AVO workflow is based on a new feature of the technology specifically developed for this project: the simultaneous joint inversion of the monitor and baseline. One of its main advantages is the robustness against the noise associated with the “no repeatability” of seismic surveys. This development of the WEB-AVO inversion is part of the process to upgrade the technique from a technology readiness level (TRL) 3 to TRL4. The estimated time-lapse changes of WEB-AVO compressibility and shear compliance were assessed, and it was concluded that shear compliance is a good indicator of the pressure effect due to the CO_2 enhanced oil recovery (EOR) activities in the study area. This ability to separate the effect of pressure from CO_2 saturation can be used to better assess the location of CO_2 within the target reservoir.

As part of the Ji-Fi workflow, the facies and their probability distributions corresponding to the highly heterogeneous target reservoir and its fluid conditions due to the CO_2 EOR activities were successfully separated in the seismic elastic space. This separation provided favorable conditions for the application of the Ji-Fi method. Reliable acoustic impedances and, most probably, litho-fluid facies of the target reservoir were obtained from the application of the Ji-Fi method separately to the baseline and monitor surveys. Information about the probability of the presence of litho-fluid facies is paramount to reducing uncertainty in forecasting CO_2 saturation changes within the target reservoir.

WEB-AVO compressibility data were integrated into the reservoir simulation model by employing two widely accepted compressibility–porosity correlations for sandstones. Flow mechanism analysis and engineering calculations showed that pore and fluid compressibility can affect the pressure response in the reservoir. A closed-loop workflow has been developed in this study to integrate the seismic inversion data into an existing reservoir simulation model and update the model with different pore compressibility distribution scenarios. The comparison of simulation results and field observations confirms the estimated time-lapse seismic response for compressibility distribution and saturation in the Bell Creek Field.

JOINT INVERSION OF TIME-LAPSE SEISMIC DATA

INTRODUCTION

The Energy & Environmental Research Center (EERC) conducted the Joint Inversion of Time-Lapse Seismic Data project in which two joint inversion modeling and monitoring workflows were developed to address and resolve shortcomings of existing inversion technology and time-lapse amplitude difference interpretation. The two inversion techniques were applied to an existing time-lapse seismic data set. One of the techniques is intended to separate the effect of pressure from CO_2 saturation to better assess the location of CO_2 within the target reservoir. The other technique evaluates the probability of the presence of a particular geologic facies at each location in order to guide the subsequent estimation of rock property distributions, ultimately reducing uncertainty in forecasting CO_2 saturation changes within the target reservoir through improved geologic/geophysical models.

The seismic wave-equation based (WEB) amplitude variation with offset (AVO) inversion was performed in collaboration with project partner Delft Inversion. The WEB-AVO technique is a nonlinear inversion that solves the full elastic wave equation, for the properties as well as the total wave-field in the object domain, from a set of observations. The relationship between the data and the property set to invert is essentially nonlinear. A way of visualizing this nonlinearity is by noting that all internal multiple scattering and mode conversions, as well as travel time differences between the real medium and the background medium, are accounted for by the wave-equation.

The second inversion technique considered in this project, joint impedance and facies inversion (Ji-Fi), was conducted in collaboration with project partner Ikon Science. Ji-Fi estimates a three-dimensional facies classification scheme based on Bayesian principles, geologic facies as priors, and powerful image-processing techniques. The most probable facies labels are used to query a set of trends or elastic facies models that supply a more limited and realistic distribution of absolute impedance values to be used for impedance model optimization.

Each technique provides solutions to one or more current challenges associated with the interpretation of surface seismic monitoring of injected CO_2 in geologic formations, whether it be for enhanced oil recovery (EOR) or geologic storage. Successful application of these inversion techniques will result in the extraction of more information from existing data; improve methods for detecting, assessing, and forecasting CO_2 saturation changes over time; inform cost-effective operational and monitoring decisions; and improve the ability to delineate the extent and location of CO_2 to verify conformance, stability, and containment. This project is part of the U.S. Department of Energy (DOE) Carbon Storage Program to develop and validate technologies to ensure 99% storage permanence and develop technologies to improve reservoir storage efficiency while ensuring containment effectiveness.

PURPOSE OF REPORT

This report describes the results of the two joint inversion workflows developed in this project to overcome fundamental shortcomings of existing inversion technologies in the monitoring of injected CO_2, either for EOR or geologic storage. The activities to integrate the inversion results into the reservoir simulation workflow to improve the static and dynamic model are also included in the report.

The WEB-AVO section describes the workflow to invert two seismic data sets simultaneously. This type of joint inversion is a natural extension of the technology in which the baseline reservoir properties and the associated time-lapse differences are estimated simultaneously. This scheme is different from the conventional time-lapse algorithms based on independent inversions of baseline and monitor data sets and then the differencing of the estimated properties. The performance of the time-lapse joint WEB-AVO inversion workflow is assessed on real data and synthetic data driven by rock physics simulations. This assessment is part of the research related to extending the original algorithm from independent inversions of baseline and monitor surveys to the time-lapse joint inversion. The results of the workflow show that WEB-AVO shear compliance is a good indicator of the pressure effect due to the CO_2 injected to the reservoir.

The section dedicated to the Ji-Fi workflow describes the steps to integrate geologic facies into the initial Ji-Fi depth trend analysis (DTA) (the equivalent low-frequency model in other inversion algorithms) to estimate seismic acoustic impedances and facies that reflect the characteristics of individual geologic facies and fluid conditions of a reservoir subject to CO_2 injection. The workflow is applied separately to the baseline and monitor surveys. The probabilities estimated by Ji-Fi for the reservoir's litho-fluid facies can be used as a tool for forecasting CO_2 saturation and pressure changes within the target reservoir.

A closed-loop workflow developed in this study to integrate the seismic data into an existing reservoir simulation model and update the model is presented in the last section of this report. The comparison of simulation results and field observations complements this section and illustrates that the time-lapse seismic response estimated by the inversion algorithms represents spatial distribution of fluid and pressure conditions in the reservoir after CO_2 injection in the Bell Creek Field.

BACKGROUND

The study area is in the Bell Creek oil field operated by Denbury Onshore LLC. This field is in southeastern Montana near the northeastern corner of the Powder River Basin in the United States. The Bell Creek Field is a complex stratigraphic trap formed by a combination of lateral facies change and erosional truncation by the 98.5-Ma sequence boundary (Molnar and Porter, 1990). The oil field is located structurally on a shallow monocline with a 1°–2° dip to the northwest and with an axis trending southwest to northeast for approximately 32 km. The 6–9-m thickness oil-bearing reservoir is part of the Lower Cretaceous Muddy Formation at a depth of approximately 1372 m. This formation is dominated by high-porosity (15%–35%), high-permeability (150–1175-mD) sandstones. Sand with fluvial channels, back barrier, lagoonal deposits, permeability barriers, baffles, and communication pathways between various compartmentalized geobodies are some of the characteristics of the heterogeneous Bell Creek reservoir (e.g., Bosshart and others, 2015; Burnison and others, 2016).

Since the discovery of oil and gas in the 1960s, the Bell Creek Field has undergone primary and secondary recovery that resulted in a gradual production decline leading to the implementation of tertiary oil recovery using CO_2 flooding. CO_2 EOR is progressing through nine development phases (regions within the Bell Creek Field). Development Phases 1 and 2 were pressurized sequentially using water injection in preparation for CO_2 EOR. Water injection for pressure support was also done in Development Phase 8. CO_2 injection began in Development Phase 1 in May 2013 and Development Phase 2 in December 2013.

The 3-D seismic data sets to monitor the time-lapse changes within the reservoir as a result of the CO_2 EOR operations correspond to the September 2012 baseline survey acquired pre-CO_2 injection activities and the October 2014 monitor survey acquired after CO_2 injection had initiated. The 2014 monitor survey overlaps the 2012 baseline survey at Development Phase 1 and part of Development Phase 2. The thin Bell Creek Sand reservoir (approximately 6–9 m) is not resolvable seismically. Nonetheless, the thicker Muddy Formation (approximately 21 m) enclosing the reservoir is seismically resolvable at the top by the Springen Ranch horizon and at the bottom by the Skull Creek horizon. Figure 1 shows a detailed view of the CO_2 distribution in the reservoir on a time-lapse seismic amplitude difference map estimated from the 2014 monitor and 2012 baseline data sets (Burnison and others, 2016; Salako and others, 2017).

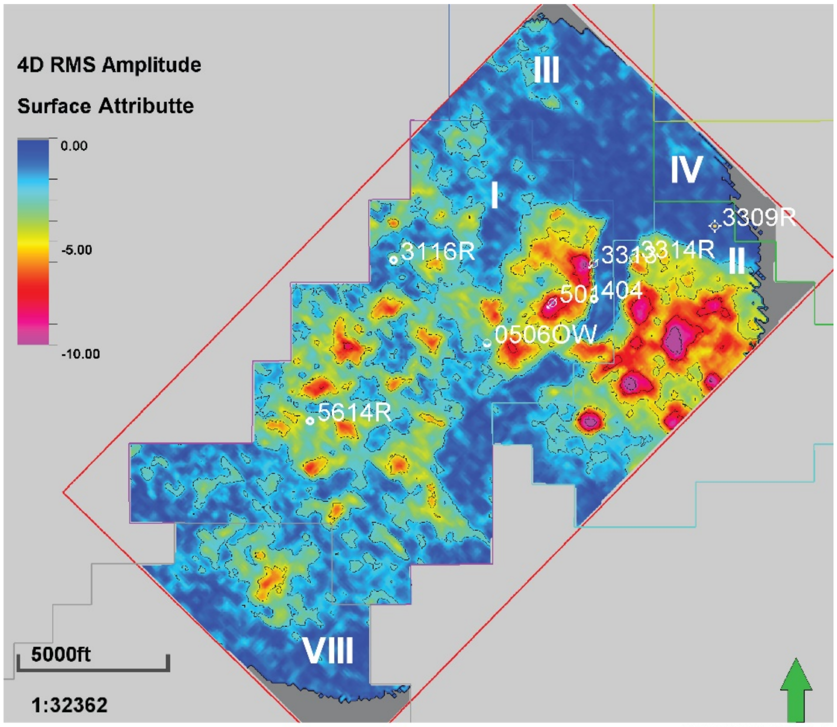

EERC CBO57160.AI

Figure 1. Time-lapse amplitude difference between the monitor and baseline. The root mean square (RMS) amplitude values that are interpreted to correspond to the CO_2 distribution in the reservoir are calculated from the Springen Ranch to Skull Creek horizons using a grid size of 82.5 × 82.5 ft.

Extensive work has been conducted at the EERC to build a geologic model incorporating 3-D seismic data, well logs, and core data (Jin and others, 2016). The model includes depositional facies that can be used to constrain petrophysical property distributions, enabling a better history match and more accurate predictive simulations of pressure response, injected/produced volumes, and saturation changes. Figure 2 shows the four facies interpreted in Development Phases 1 and 2.

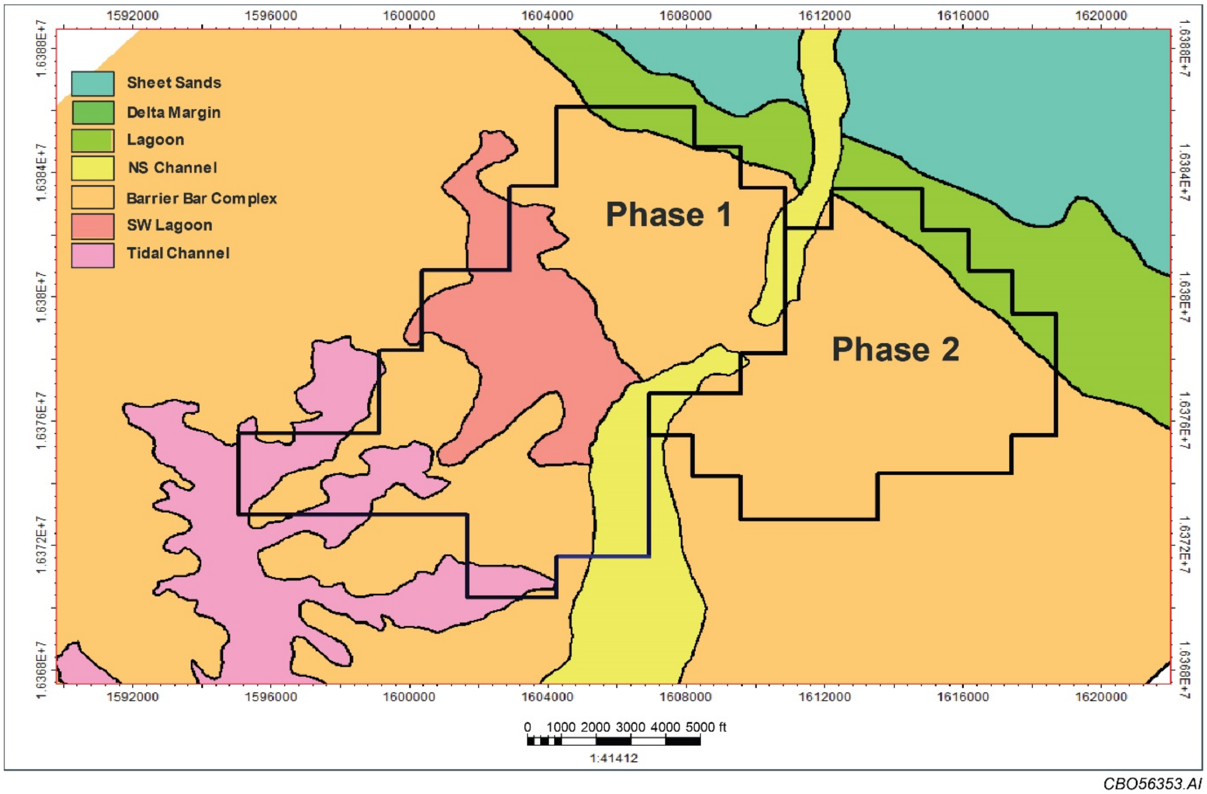

Figure 2. Facies interpreted in the study area: Lagoon, Barrier Bar Complex, NS Channel, and Tidal Channel. The polygons represent the study area (Development Phases 1 and 2).

WEB-AVO

The WEB-AVO inversion method is a target-oriented, full-waveform elastic inversion of seismic data. Target-oriented refers to the application of the inversion algorithm to an interval between a reservoir sequence and a top and bottom seal (Gisolf and others, 2017).

The full elastic wave-equation is solved iteratively; therefore, multiple scattering and mode conversions over the target interval are considered. Moreover, the inherent detuning of the seismic amplitudes in the inversion gives a reservoir model with a spatial bandwidth wider than what could be expected from the temporal bandwidth of the seismic data. A first estimate of the reservoir model is obtained starting with an incident field in a smooth background model, under the assumption of a linear relationship between elastic subsurface properties and seismic amplitudes.

In the next step, the wave-equation is deployed to include second-order scattering based on the first estimate of the reservoir properties.

The complete scheme consists of an iterative procedure of AVO inversions, using the best estimate of the wave-field in the reservoir, followed by updating the wave-field based on the latest reservoir model. The procedure is repeated until neither the reservoir model nor the wave-field changes anymore (see Figure 3). Another unique feature of the method is that it solves directly for compressibility (inverse of bulk modulus) and shear compliance (inverse of shear modulus) instead of impedances as obtained by conventional linear AVO techniques.

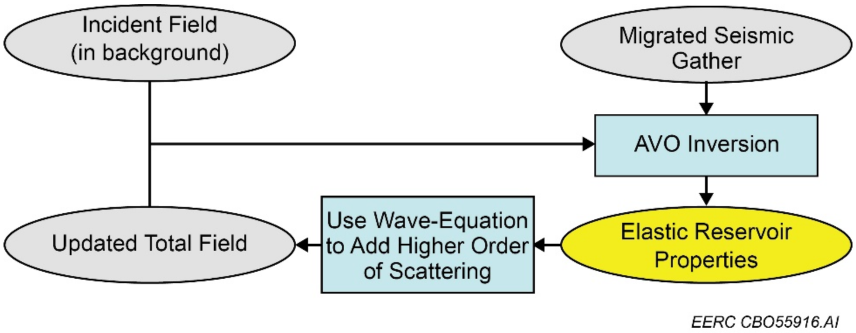

Figure 3. A simplified description of the WEB-AVO inversion scheme (modified after Gisolf and others, 2017).

Whereas adding value at several stages of seismic interpretation, the computational costs of solving the wave equation grow strongly with the number of grid cells of the inversion domain. The scheme is applied in a target-oriented mode covering a depth interval of approximately 500 m to keep the process feasible. The exact depth interval is dependent on the vertical depth sampling, which in turn depends on the maximum frequency in the seismic data and the lowest velocity over the target.

Being target-oriented implies that the methodology properly predicts only multiple scattering and mode conversions that are generated over the target interval. At the same time, overburden- and surface-related multiples should be removed from the input data by standard processing or, preferably, by full wave-field processing. While linear AVO techniques inevitably misinterpret these types of events, WEB-AVO tends to reject this noise as it does not obey the target-oriented wave-equation. This feature makes the technology very robust even in setups with low signal-to-noise or where older seismic data are available only, which initially was not acquired for the primary purpose of quantitative interpretation studies.

WEB-AVO Workflow

Input Data

Seismic Data

Two data sets were considered for this study. The first one, the baseline survey, was acquired in September 2012 prior to the start of CO_2 injection. The data set representing the monitor survey was acquired in October 2014 after the commercial CO_2 EOR operations had progressed over several portions of the field. Examples of a baseline and monitor prestack time-migrated (PSTM) seismic offset gathers are shown in Figure 4. The interpreted Springen Ranch and Skull Creek interpreted formation tops are depicted on the gathers to facilitate the identification of the reservoir.

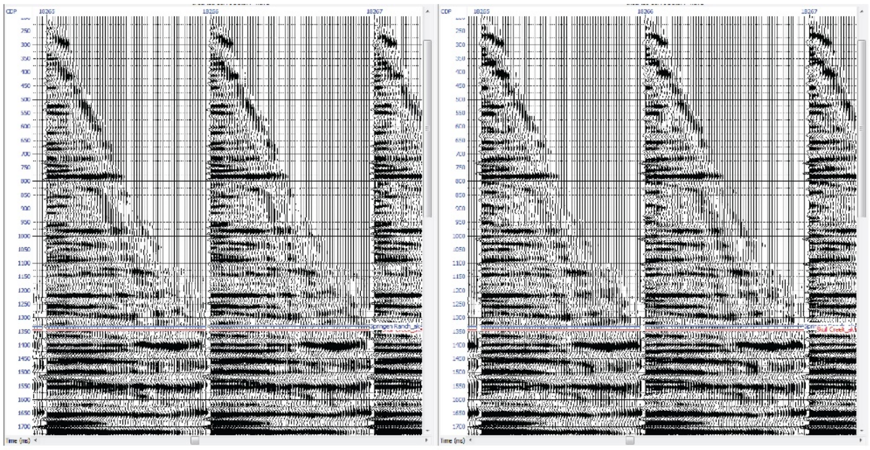
EERC CBO55922.AI

Figure 4. Example of PSTM offset gathers used in this project. Left: baseline survey acquired in 2012, right: monitor survey acquired in 2014. The Springen Ranch and Skull Creek interpreted formation tops representing the top and bottom of the reservoir are shown for reference.

Interpreted Horizons of the Study Area

Four horizons were interpreted in the time and depth domains on a seismic cube created by the stacked PSTM gathers of the baseline survey: Springen Ranch and Skull Creek representing the top and the bottom of reservoir interval, respectively; Horizon 1 and low-branch Bell Creek (LBBC) horizons corresponding to strong reflectivity events above and below the reservoir, respectively. Figure 5 shows the Springen Ranch horizon in time. The colors represent the time variations in milliseconds. Notice the trend northwest-southeast representing the dip of the reservoir.

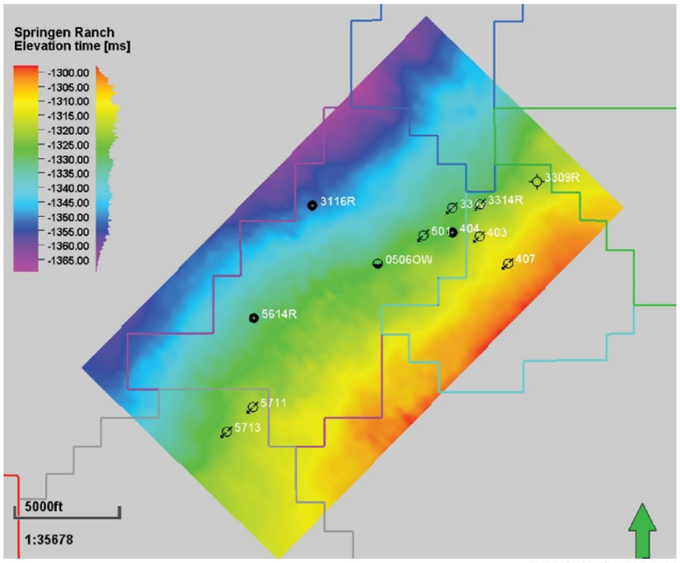

EERC CBO55924.AI

Figure 5. Example of an input horizon in time for the WEB-AVO inversion. This horizon called Springen Ranch represents the top of the reservoir.

Velocity Model Estimated in the PSTM Process

The velocity field was estimated to flatten the PSTM gathers during the data processing optimally. It is a smoothed 3-D RMS field in time (see Figure 6). The quality of this velocity model is fundamental not only for the optimum performance of the migration algorithm but also for the conversion of the offset data into the required domain for the seismic inversion.

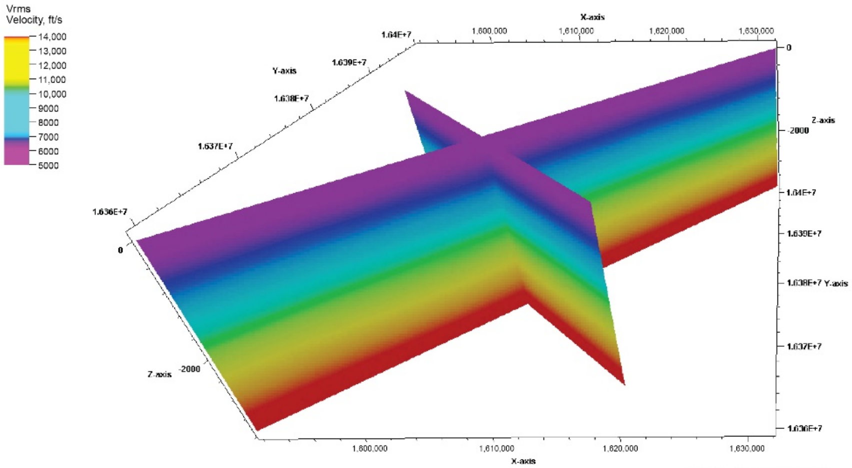

EERC CBO55925.AI

Figure 6. Three-dimensional RMS velocity field estimated in the PSTM process and used as input for the WEB-AVO inversion.

Well Logs

Wells 05-06 OW, 33-14R, and 56-14R with complete sonic, shear sonic, and density information were included in this study (Figure 7). In addition to the type of log information available at those wells, the criterion to select these wells was based on the different amplitude responses observed at seismic traces nearby the wells. Other wells that were analyzed because of their location near or at the time-lapse anomalies shown in Figure 1 are depicted on the next figures, including maps of seismic information as a reference for comparing the maps.

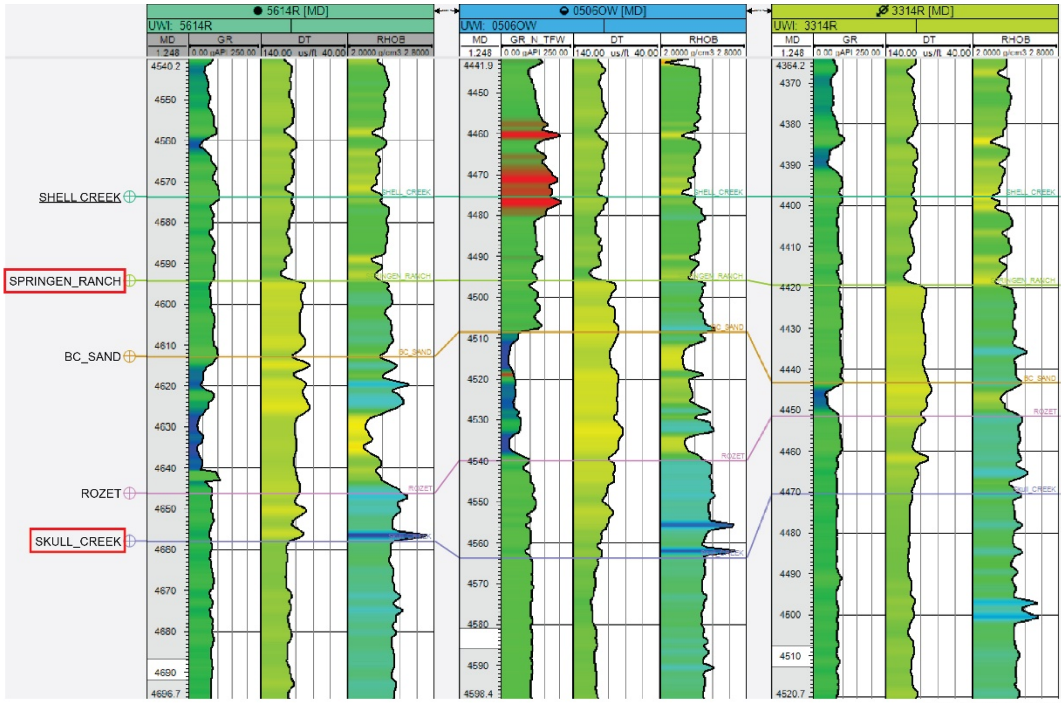

EERC CBO55923.AI

Figure 7. Well Logs 56-14R, 05-06 OW, and 33-14R (left to right) were included in the workflow. Only a section of the logs is shown to emphasize the differences in the reservoir (Springen Ranch – Skull Creek interpreted Formation tops are illustrated for reference). Gamma ray, sonic, and density logs of each well are depicted (from left to right).

Seismic Data Preconditioning

A multidimensional dip filter and amplitude balancing along the offset were applied to both baseline and monitor data sets to reduce residual migration noise and enhance the quality of the data. The improvements at the level of the reservoir can be observed at approximately 0.21 to 0.26 seconds, which correspond to the reservoir in the example gathers shown in Figure 8.

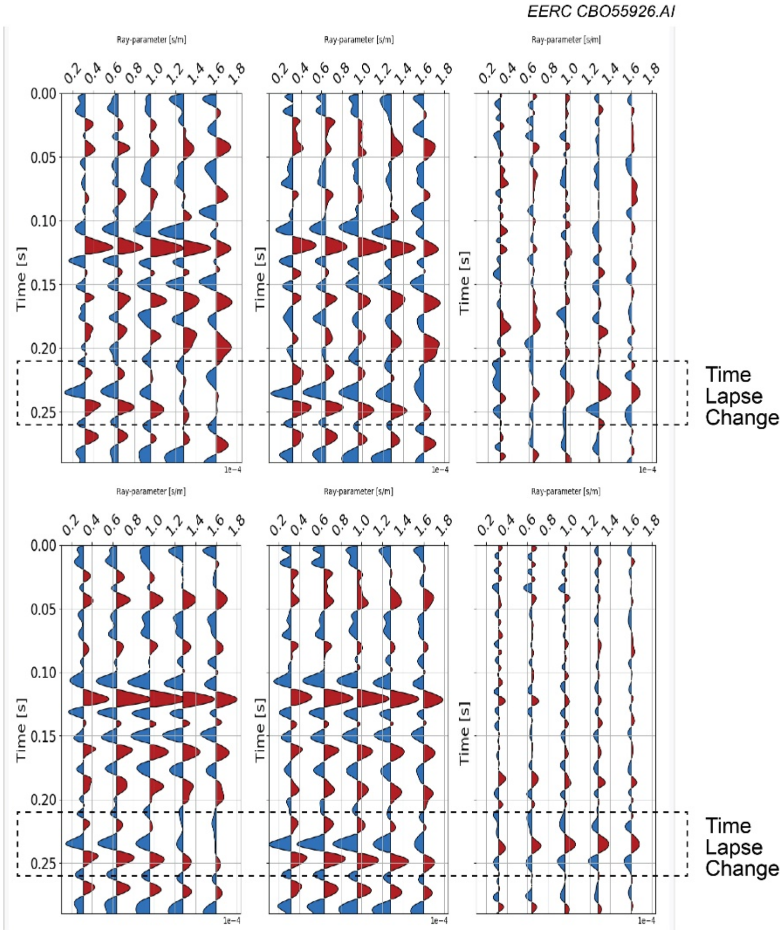

Figure 8. Example of seismic data preconditioning for WEB-AVO inversion. Top: before conditioning; bottom: after conditioning. Panels from left to right are baseline, monitor, and difference (monitor minus baseline). Gathers are shown in the slowness domain to simplify the analysis on the same domain as the WEB-AVO inversion. The inversion time window interval is shown.

Conversion of Seismic Data from Offset to Slowness Domain

Since the WEB-AVO inversion is applied in the plane-wave (tau/p) domain, the input offset seismic migrated gathers are converted to the slowness domain. This step is like the conversion from the offset to the angle domain required by other AVO inversion algorithms. The conversion is based on the velocity model estimated during the PSTM. In the case of the WEB-AVO, a stratified overburden with a velocity profile corresponding to the velocity trace vertically above the output location was assumed (Gisolf and others, 2017). Figure 9 shows an example of the conversion of offset gathers to the slowness domain at Well Location 05-06 OW. The green lines on the offset gather indicate the time-dependent offset corresponding to the output slowness value. This example shows an equivalent 6°–28° at a velocity of 2900 m/s for conventional angle gathers.

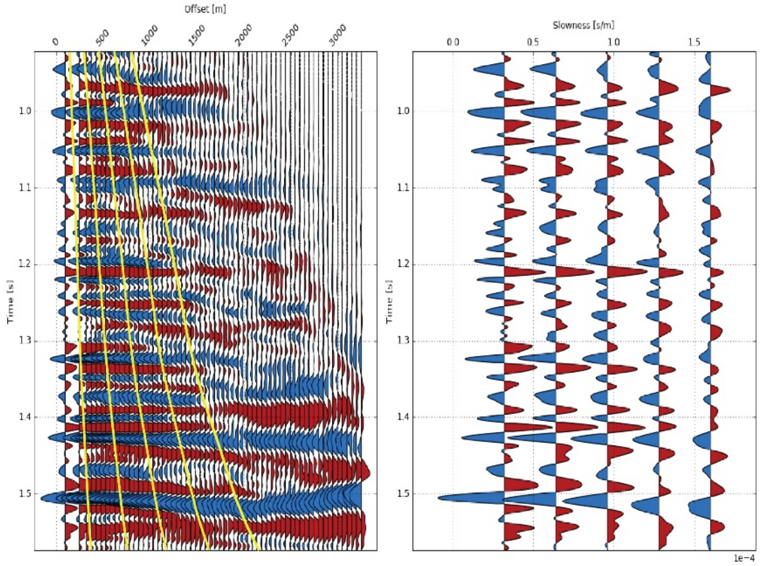

EERC CBO55927.AI

Figure 9. Example of converting seismic migrated data from the offset (left) to slowness (right) at Well 05-06 OW. The green lines indicate the time-dependent offset corresponding to the output slowness values.

Extraction of Slowness-Dependent Wavelets by Tying Wells to Seismic Data

The required wavelets for the inversion are obtained from the well-to-seismic ties. In this process, well synthetic data (broadband) are matched with seismic data at well locations in a least-squares sense. The match is achieved with a modeling tool able to generate multiples, mode conversions, and transmission effects so that the synthetic data are consistent with the WEB-AVO. The Kennett modeling method (Kennett, 1984) was used to satisfy the wave-field requirements. Synthetic data were created with a broadband wavelet (0-2-120-125 Hz). However, the bandwidth and phase of the final wavelets are estimated in the synthetic-to-seismic matching procedure. An example of this procedure at Well 05-06 OW is shown in Figure 10. Notice the matched synthetic gather and the corresponding residuals (third and fourth panel from the left on the top figure). Consistent wavelets were estimated at the three well locations. The seismic-to-well ties corresponding to Wells 56-14R and 33-14R are depicted in Appendix A.

Building a Low-Frequency Background (LFB) Model

This step was performed in two iterations:

- In the first step, the well logs are filtered to preserve only the low frequencies (4-Hz high-cut filter) not available in the seismic data. The horizons are used as constraints. An example of the Vp, Vs, and density background models generated in this step are depicted in Figure 11.

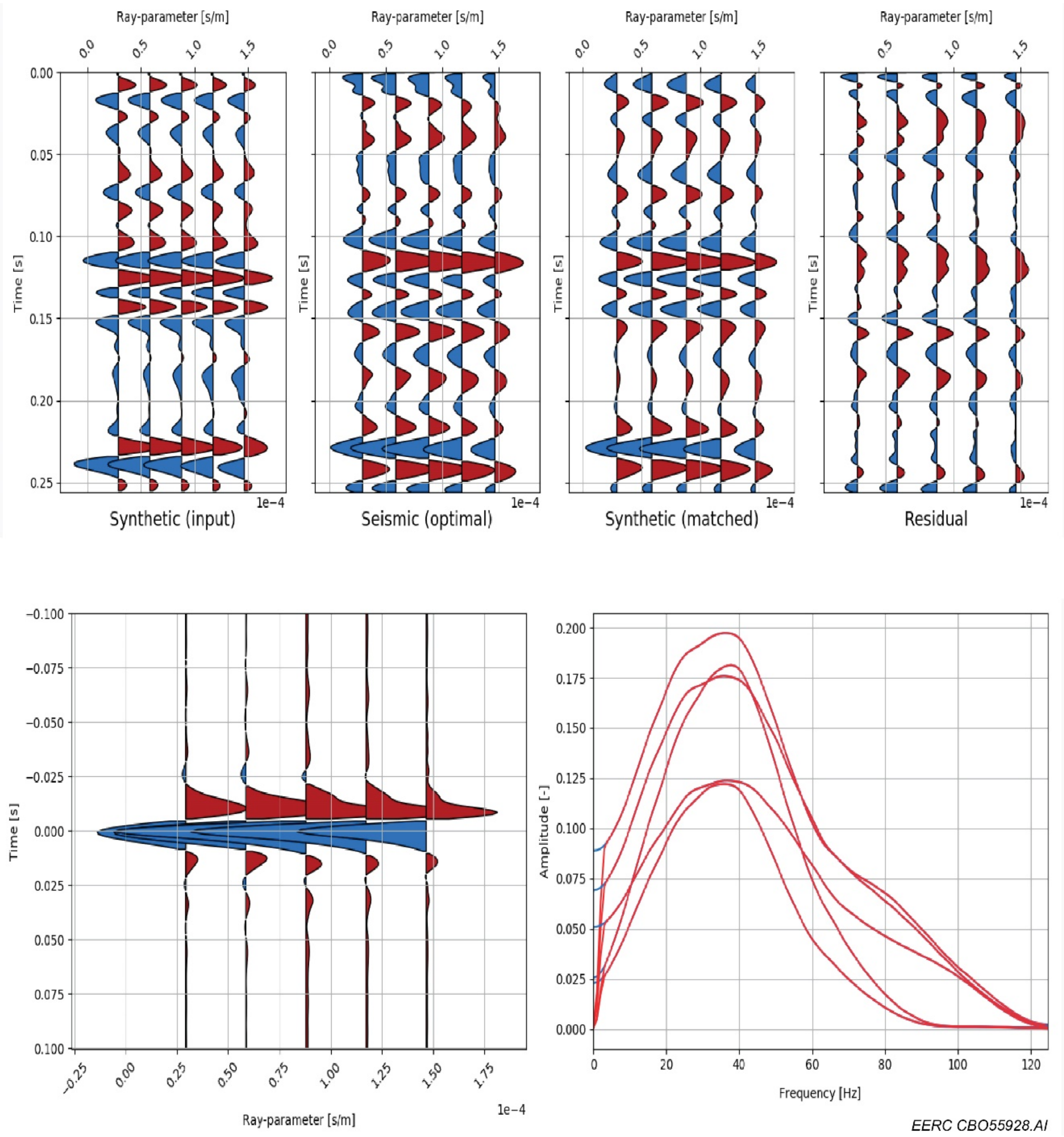

Figure 10. Example of well-to-seismic tie at Well 05-06 OW using the Kennett modeling method to generate synthetic data. Top (left to right): initial synthetic data, seismic data, matched synthetic data, and residuals. Bottom (left to right): estimated wavelets in the time and frequency domains.

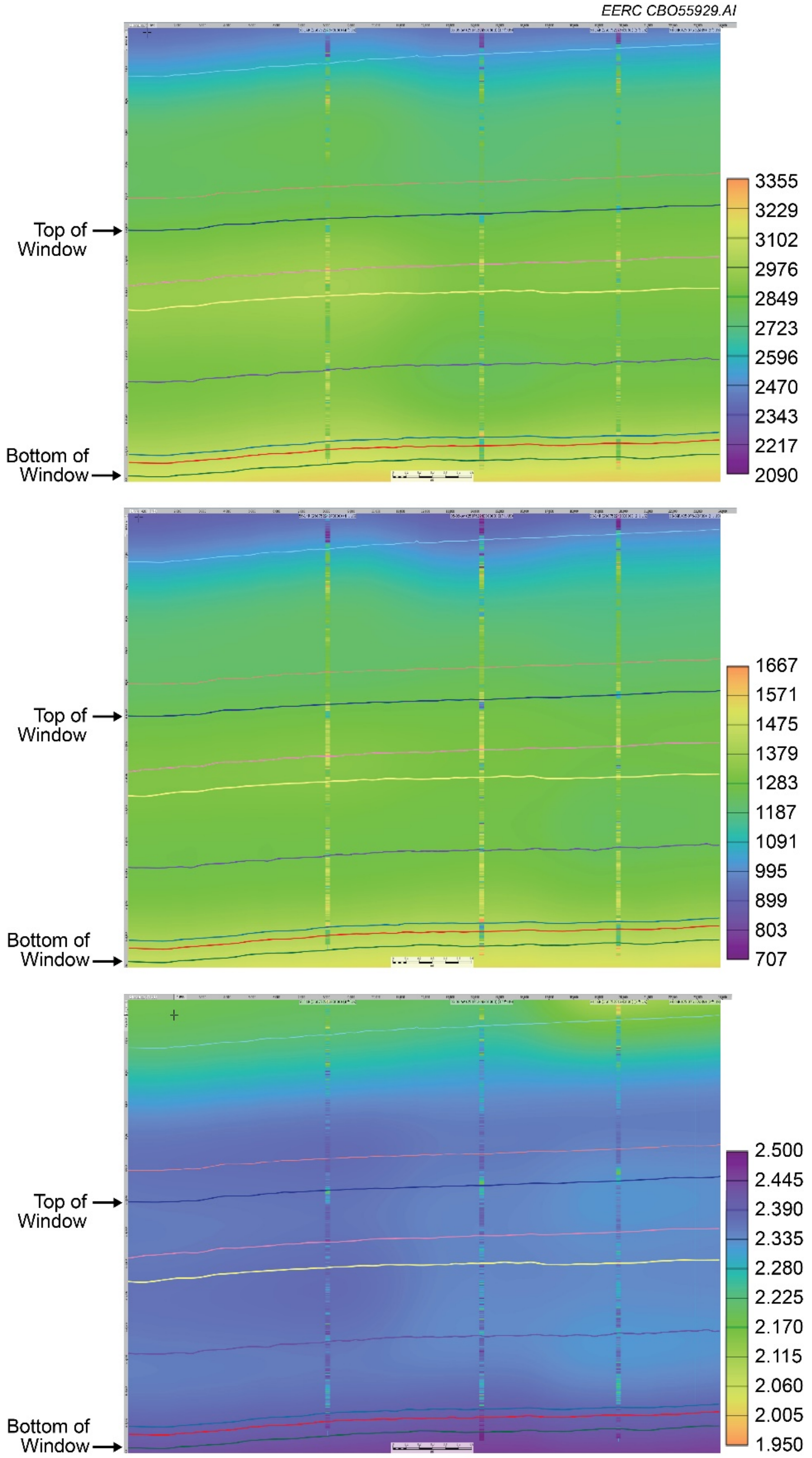

Figure 11. Sections of background model Vp (top), Vs (middle), and density (bottom). A 4-Hz high-cut filter was applied. The three wells used in the project are shown as vertical lines.

- In the next step, the LFBs are updated to consider the available bandwidth, angle range, geology, and the type of inversion algorithm. The procedure is as follows:
  - A synthetic model is created based on well logs, estimated seismic wavelets, and the slowness (angle) range estimated for the inversion.
  - WEB-AVO inversion is performed using the LFBs.
  - The background is updated based on the mismatch between inverted and logged properties.
  - The bandwidth of the backgrounds can be different for each estimated elastic property (compressibility, shear compliance, and density).
- An example of the original 4-Hz LFBs and the updated LFBs at Well 05-06 OW are shown in Figures 12 and 13, respectively. The logs have been matched to compensate for the needed locally different bandwidth.
- In the final step, the estimated LFBs at the wells are interpolated over the entire 3-D area.

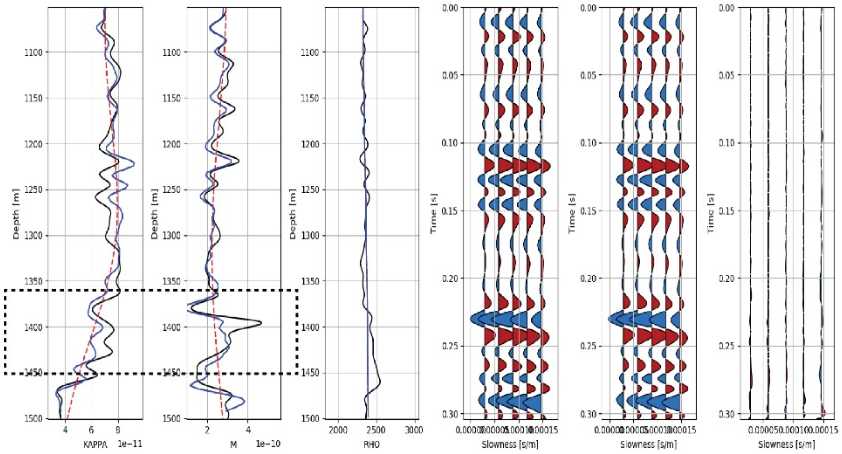

EERC CBO55930.AI

Figure 12. Example of inverted data using the initial background models at Well 05-06 OW. First three panels from left to right: compressibility (kappa), shear compliance (M), and density (rho); red line: background, black line: smoothed well log, blue line: inverted log. Last three panels: seismic data at the well, synthetic data, and residuals.

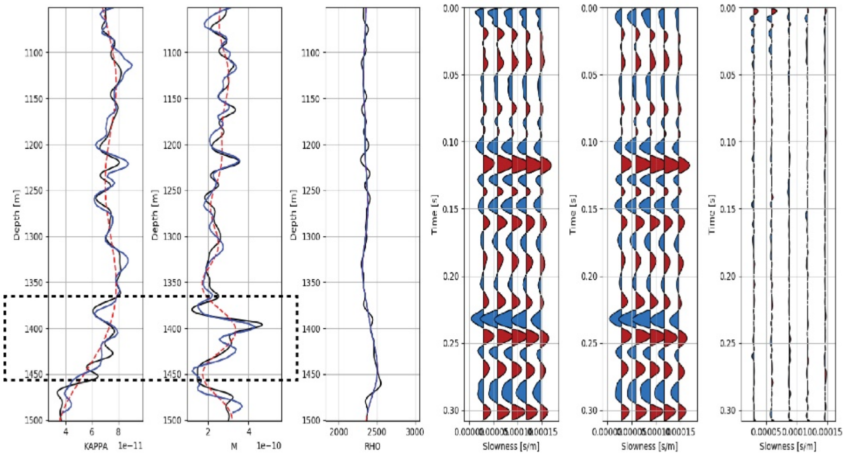

EERC CBO55931.AI

Figure 13. Example of inverted data with the updated background models at Well 05-06 OW. First three panels from left to right: compressibility (kappa), shear compliance (M), and density (rho); red line: background, black line: smoothed well log, blue line: inverted log. Last three panels: seismic data at the well, synthetic data, and residuals. The logs have been matched to compensate the needed locally different bandwidth.

WEB-AVO Inversion Application to Baseline and Monitor Surveys

Assessment of Internal Multiples in Seismic Data Sets and WEB-AVO Parameterization

The WEB internal multiples investigation (IMI) was applied to assess the impact of internal multiples on the seismic data and to define the optimum window size for the WEB-AVO inversion. WEB-IMI is a forward modeling tool that calculates elastic wave-fields to simulate multiples, mode conversions, and transmission effects. The input to the WEB-IMI is well log data (sonic, shear sonic, and density), a seismic wavelet (potentially slowness dependent), and the available slowness range from the seismic data used in the simulation. The synthetic gathers are modeled based on an integral representation of the wave-equation (Doulgeris and others, 2018). Understanding the seismic wave-field in a zone including above the reservoir, at the reservoir, and below the reservoir is crucial not only to defining the window size for the inversion so that the WEB-AVO technique can properly consider the wave-field contributing to the final solution but also to optimizing the run time to solve the full wave-equation. The WEB-IMI simulation was conducted at Well 05-06 OW. A window of 620 m and a smaller window of 400 m were analyzed using an angle/slowness of 30 degrees. Figure 14 shows the location of the windows with regard to the reservoir. The results of the simulation demonstrate that the 400-m window was the optimum window size for running the WEB-AVO inversion.

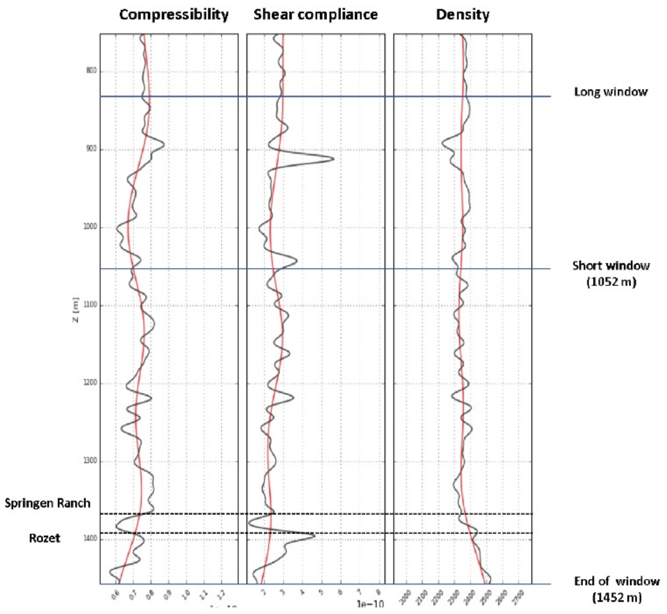

EERC CBO55932.AI

Figure 14. Windows tested for the WEB-AVO inversion using the WEB-IMI tool. Red line: background model, black line: WEB-AVO parameters.

Simultaneous Inversion of Baseline and Monitor Surveys

The standard procedure to conduct time-lapse inversions is running an independent inversion on the baseline and the monitor surveys. After that, subtraction of the individual estimated inversion parameters is performed. A more robust and consistent approach is a simultaneous inversion of the monitor and baseline surveys, which includes the calculation of the time-lapse changes of the estimated properties. Some theoretical conditions should be met to build such a simultaneous inversion scheme. Since WEB-AVO can properly model nonlinear effects not only because of multiples, mode conversion, and transmission but also because of travel time differences as a result of time-lapse changes of the rock properties, the implementation of a simultaneous time-lapse WEB-AVO is a natural extension of the method. The development of the WEB-AVO technology to a simultaneous scheme is a research objective of this project.

Since only very local time-lapse changes are expected in seismic monitoring, a sparseness constraint on the time-lapse property differences can be used to stabilize the inversion procedure. This constraint is due to the fact of having the same amount of seismic data with a significantly reduced number of unknown reservoir properties. Furthermore, the inversion becomes robust against the repeatability challenge of seismic surveys and associated noise.

An arbitrary line was selected to run efficient WEB-AVO tests. The line intersects different zones of Phase 1 and 2, and well locations where time-lapse seismic anomalies estimated in previous studies are observed (not shown here, but already presented at DOE’s Mastering the Subsurface Through Technology Innovation, Partnerships, and Collaboration review meeting, August 13–16, 2018). A product of these tests is an optimum starting point for the parameterization of the 3-D WEB-AVO.

The results of the 3-D simultaneous time-lapse WEB-AVO are shown in Figures 15 and 16 and Appendix B. Similar to as the time-lapse maps, the WEB-AVO maps were calculated using the RMS values of the estimated parameters from the Springen Ranch to Skull Creek horizons and a grid size of 82.5 × 82.5 ft. The estimated time-lapse compressibility (Figure 15) and shear compliance (Figure 16) provide a more detailed spatial description of the complex interaction between the reservoir's sedimentary conditions and the physical/chemical processes associated to changes in water saturation, CO_2 saturation, and pressure than the amplitude maps. Notice the exact match of the compressibility's spatial distribution with the time-lapse amplitude anomalies (Figure 1). Because the shear compliance is sensitive to pressure and not to saturation, the map in Figure 16 can be used to discriminate the effect of pressure and saturation qualitatively. The origin of the low shear compliance values is still a topic being investigated by Delft Inversion and EERC researchers. As part of this investigation, WEB-AVO compressibility is being tested in reservoir simulation models to estimate pressure changes that can be associated with shear compliance distribution.

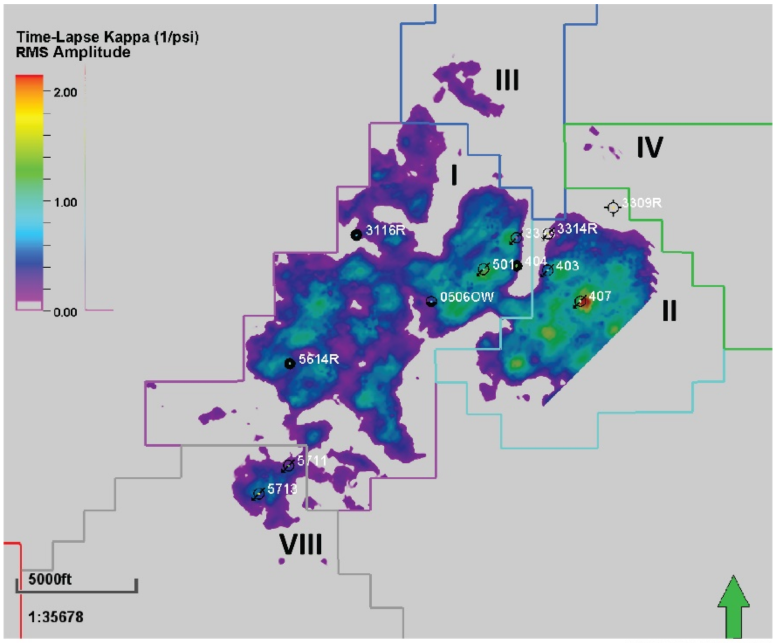

EERC CBO55933.AI

Figure 15. The time-lapse difference in compressibility (kappa). The RMS values of kappa are calculated from the Springen Ranch to Skull Creek horizons using a grid size of 82.5 × 82.5 ft.

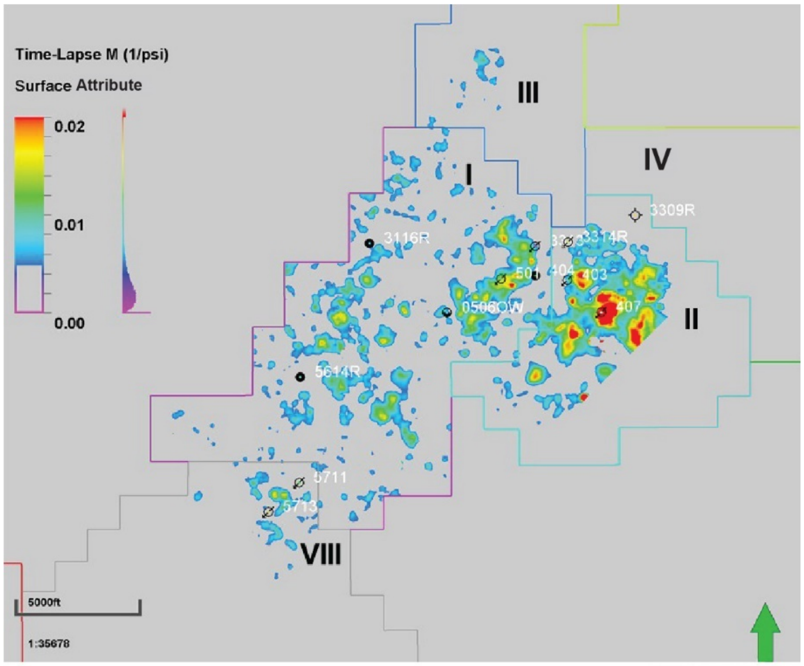

EERC CBO57163.AI

Figure 16. The time-lapse difference in shear compliance (M). The RMS values of M are calculated from the Springen Ranch to Skull Creek horizons using a grid size of 82.5 × 82.5 ft.

Rock Physics Analysis of Expected Time-Lapse Effects in the Well Log and Seismic Domains (WEB-AVO to reservoir properties)

Although the parameters derived by the WEB-AVO are more directly related to reservoir parameters such as saturation, porosity, and lithology than other conventional inversion algorithms, rock physics can be used to associate WEB-AVO compressibility and shear compliance to pressure and saturation, two of the target parameters in this effort.

Rock physics and seismic simulations were conducted to link the WEB-AVO parameters to saturation and pressure scenarios associated with the Bell Creek reservoir. Well 05-06 OW was the only well with all the necessary information to conduct the simulations. The following scenarios were tested:

- Scenario 1: Time-lapse changes due to saturation and pressure as measured in the well due to common CO_2 EOR activities using baseline (January 4, 2013) and monitor (August 7, 2014) surveys. Saturation information for the simulation is obtained from the available RST (reservoir saturation tool) logs. In this case, only saturation due to oil and water but not to CO_2 at the baseline is considered. This scenario is a real time-lapse example.

- Scenario 2: Time-lapse changes due only to saturation: monitor with only saturation changes minus baseline. This example represents a theoretical case to assess a general time-lapse saturation effect.

- Scenario 3: Time-lapse changes due only to pressure: monitor with only pressure changes of 712 psi regarding the baseline. The objective of this theoretical example is to evaluate only the time-lapse pressure changes between the two seismic surveys.

- Scenario 4: Time-lapse changes due only to exaggerated pressure: monitor with an exaggerated pressure change of 1700 psi with regard to the baseline. This theoretical example allows comparison with Scenario 3.

- Scenario 5: Time-lapse changes due only to the substitution of all the oil by CO_2 (assuming constant pressure). This scenario is equivalent to a perfect EOR process with CCI (continuous CO_2 injection) in the oil leg.

- Scenario 6: Time-lapse changes due only to the substitution of all the water by CO_2 (assuming constant pressure). This case corresponds to a perfect CO_2 displacement in the water leg.

The results of the six scenarios derived from the rock physics simulation based on MacBeth (2004) and Gassmann (1951) are summarized in Figures 17–19. The calculated logs are normalized by their respective baseline logs to facilitate the comparison of scenarios. Whereas Figure 17 shows the estimated logs for Vp, Vs, density (rho), compressibility (kappa), shear compliance (M), and their respective differences (Delta_Vp, Delta_Vs, Delta_Rho, Delta_Kappa, and Delta_M), Figure 18 shows the smoothed version of those logs. The smoothing is based on a

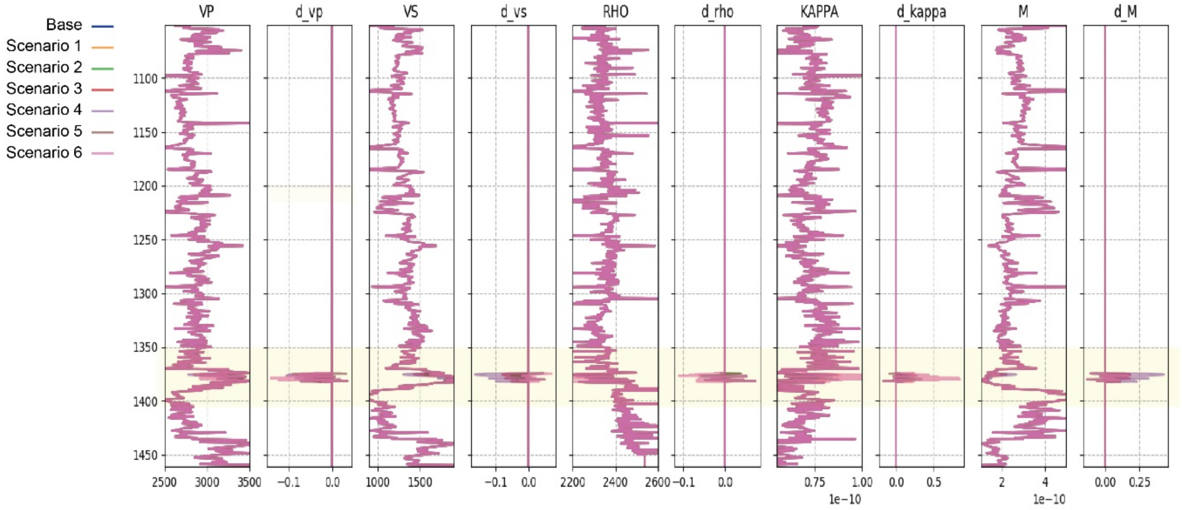

EERC CBO55936.AI

Figure 17. Simulated logs from the six rock physics scenarios at the Bell Creek study area. Time-lapse differences were normalized with the respective baseline logs (base).

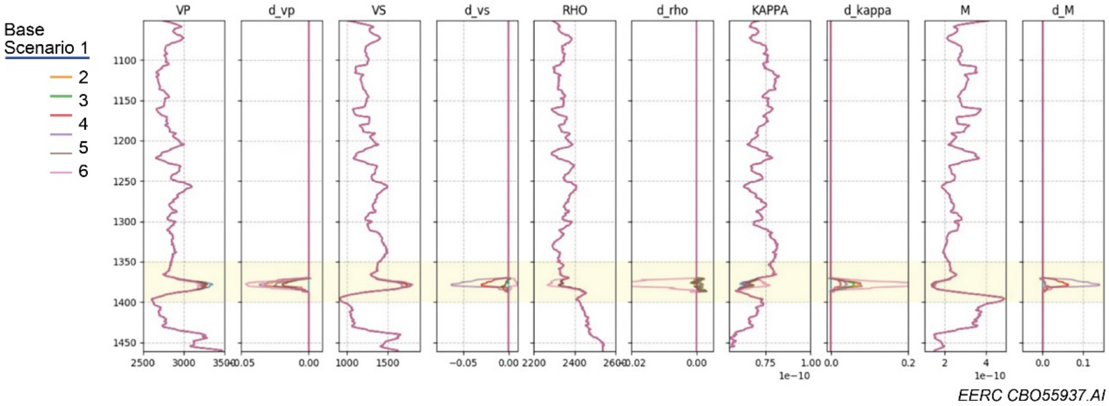

Figure 18. Simulated logs from rock physics scenarios. The logs are smoothed over the target interval. A 10-m Backus averaging was used to upscale logs to effective properties on the seismic scale.

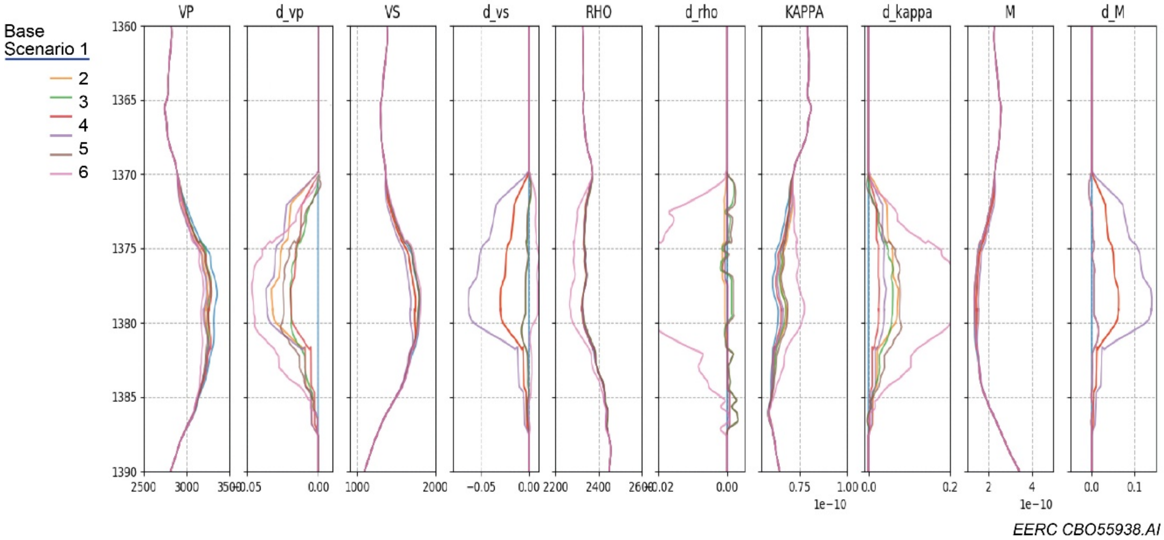

Figure 19. Simulated logs from rock physics scenarios. Smoothed logs (zoom in to the interval of 1360–1390 m). With upscaling to seismic scale, the absolute value of 4-D impact is reduced, while the thickness of the impacted interval is increased.

10-m Backus averaging to upscale the logs to effective properties on the seismic scale. A more detailed view (including the reservoir) of the simulated logs and their difference is shown in Figure 19. Besides the different magnitude responses of Vp and compressibility to saturation and fluid substitution, notice the high sensitivity of Vs and shear compliance to pressure effects (last panel from left to right in Figures 18 and 19). These effective properties can serve as a first reference for the interpretation of the compressibility and shear compliance estimated by the simultaneous WEB-AVO (Figures 15 and 16).

Numerical seismic simulation is required to have a comprehensive assessment of the scenarios generated by the rock physics task. The seismic simulation was performed with the Kennett modeling method using the estimated wavelets (Figure C-3) considering the baseline logs (Figure C-4) and slowness range equivalent to angles of 5° to 28° at reservoir level (*p* = 3.2e-5, 6.4e-5, 9.6e-5, 1.28e-4, 1.6e-4). The discretization in depth of the inversion domain was 7 m. The WEB-AVO inversion was run in five iterations to estimate compressibility and shear compliance. Density was kept equal to its background values.

The results of the seismic simulation for Scenarios 1, 2, 3, and 4 around Well 05-06 OW are depicted in Figures 20–23, respectively. All the scenarios show a small but observable time-lapse signature and a small AVO effect. However, Scenarios 3 and 4 show a clearer AVO Class I. The estimated magnitude of the time-lapse signature is concordant with the real time-lapse signal around Well 05-06 OW in Figure 1. The other two simulated scenarios available in Appendix C also show similar characteristics as described here.

The comparison of the seismic and rock physics simulations can be simplified using the WEB-AVO inversion to estimate the logs generated in the six scenarios as shown in Figures 24 and 25. Notice the similarities with the estimated logs by the rock physics simulation in Figure 19.

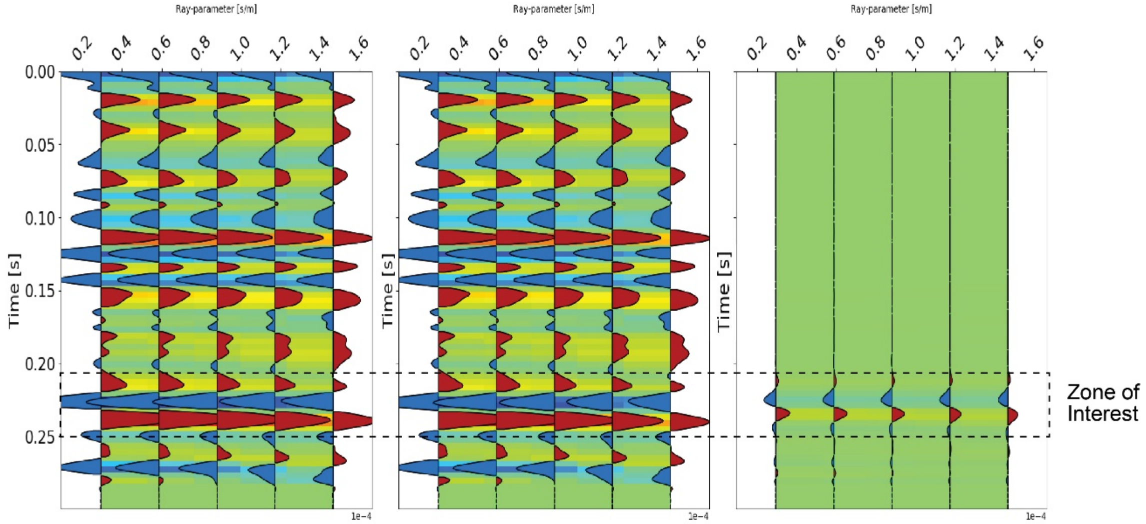

EERC CBO55939.AI

Figure 20. Simulated synthetic seismic data at Well 05-06 OW. Scenario 1: baseline vs. monitor (pressure + saturation). Left to right panels: baseline, monitor, difference.

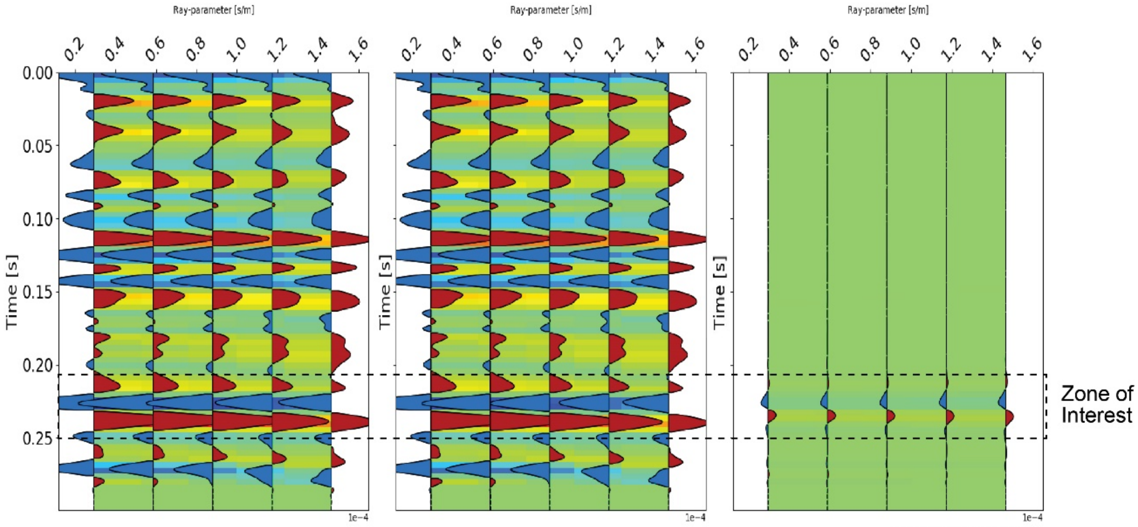

EERC CBO55940.AI

Figure 21. Simulated synthetic seismic data at Well 05-06 OW. Scenario 2: Time-lapse changes due only to saturation. Left to right panels: baseline, monitor, difference. A very small time-lapse signal and AVO effect due to saturation are observed.

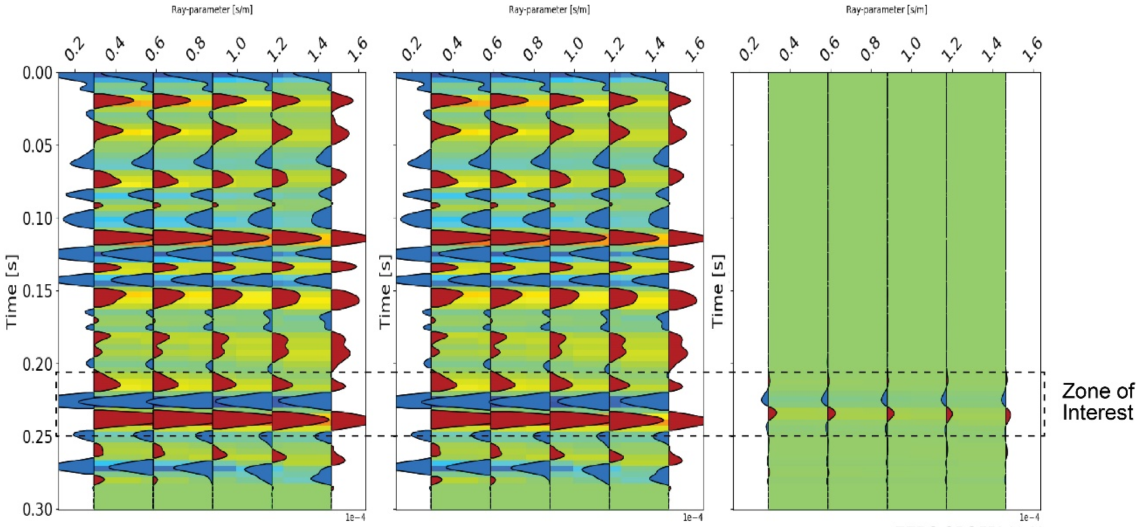

EERC CBO55941.AI

Figure 22. Simulated synthetic seismic data at Well 05-06 OW. Scenario 3: monitor with only pressure (712 psi) minus baseline (imaginary case). Left to right panels: baseline, monitor, difference. A small time-lapse signal and an AVO effect (Class I) due only to pressure are observed.

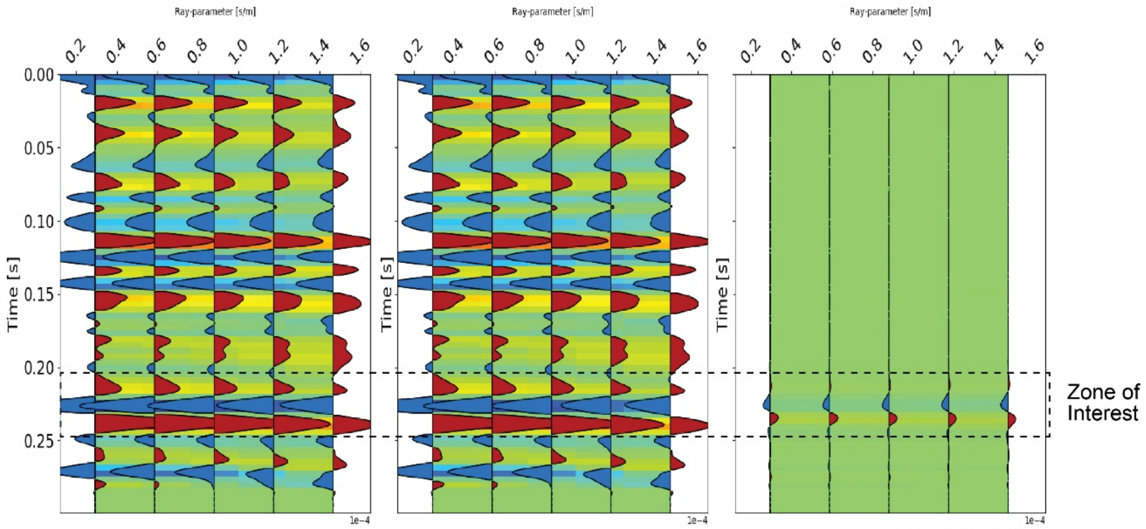

EERC CBO55942.AI

Figure 23. Simulated synthetic seismic data at Well 05-06 OW. Scenario 4: monitor with only exaggerated pressure (1700 psi) minus baseline (imaginary case). Left to right panels: baseline, monitor, difference. A small but well-defined time-lapse signal and a clear AVO effect (Class I) due only to pressure are observed.

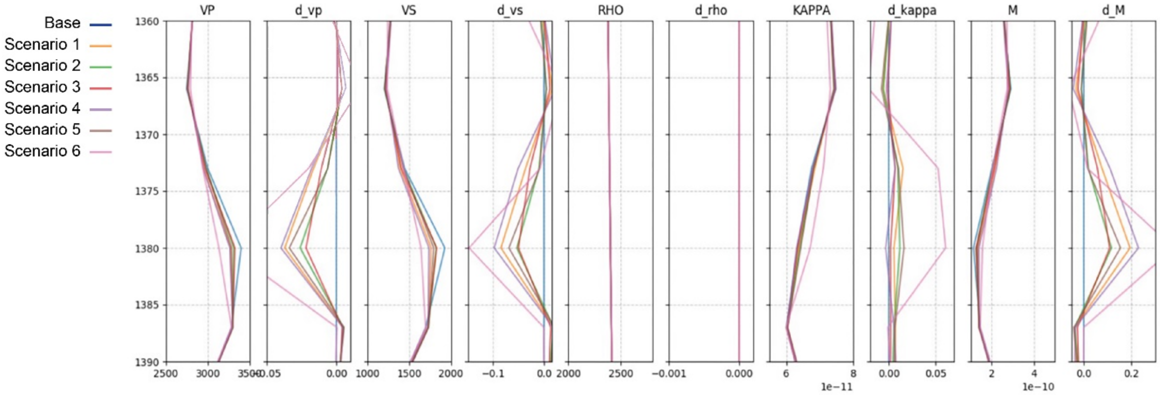

EERC CBO55943.AI

Figure 24. WEB-AVO inversion of synthetic scenarios. Summary of inversion results for well logs in the interval 1360–1390 m.

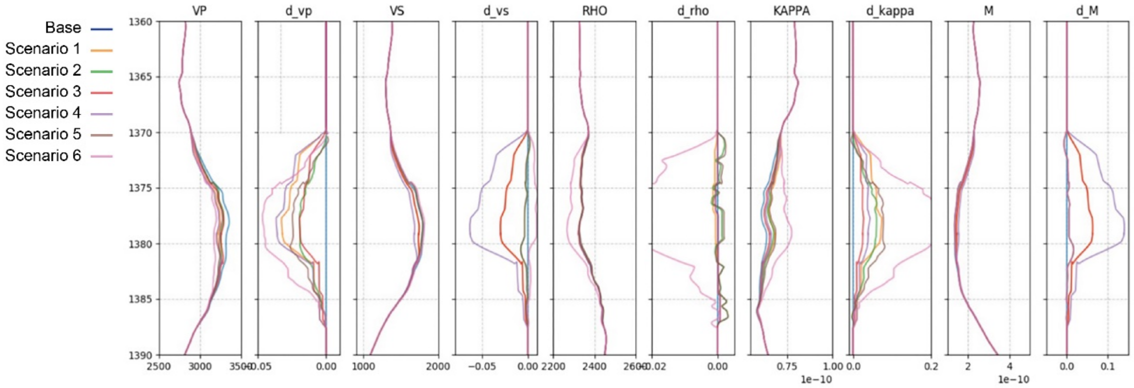

EERC CBO55944.AI

Figure 25. WEB-AVO inversion of synthetic scenarios. Summary of inversion results for well logs in the interval 1360–1390 m. A 10-m Backus averaging was used to upscale the logs to effective properties on the seismic scale.

JOINT IMPEDANCE AND FACIES INVERSION

Rock physics and simultaneous seismic inversion are fundamental tools of quantitative reservoir characterization. In this process, the impedance and elastic parameters estimated by the simultaneous inversion of seismic data can be related to rock properties using rock physics models. Ji-Fi seamlessly integrates rock physics and simultaneous inversion using seismic facies (Kemper and Gunning, 2014). Contrary to standard inversion algorithms, Ji-Fi builds a background model per facies, and the rock physics relationships are done per facies. This scheme ensures consistency of results; since Ji-Fi is formulated as a Bayesian approach, the inversion workflow can easily be updated with new information during the life of the project.

Figure 26a shows a simplified workflow of a standard model-based inversion. It starts with an LFM (low-frequency model), which is iteratively updated by minimizing the misfit between synthetic seismic generated from the model and the observed seismic traces. Once the misfit has reached a satisfactory level, the final updated impedance model is output. In the basic Bayesian Ji-Fi workflow (Figure 26b), depth-dependent trends (the equivalent to LFMs) are established for each of the expected facies (reservoir and nonreservoir). These prior facies-based trends, a set of estimated prior facies proportions, the seismic data (partial angle stacks, e.g., near, mid-, and far angle stacks), and wavelets (with an estimate of each wavelet's RMS error) are used in the inversion to solve for both the most likely facies model and its corresponding set of impedances (Waters and others, 2016).

The depth trends of Vp, Vs, density, and impedances can be obtained from logs, 1-D basin models, or analog fields. They are referenced to a single datum, which reduces the need for detailed seismic interpretation. The crossploted depth trends (Vp vs. density, Vp vs. Vs, AI (acoustic impedance) vs. shear impedance (SI), AI vs. Vp/Vs), and an assessment of their uncertainty are used for quality control. An essential feature of the Ji-Fi approach is that the LFM trends are not interpolated between wells. Therefore, the depth trends are not compromised by bias in the interpretation of seismic horizons or interpolation artifacts. Since the facies represented in the depth trends depend on rock physics models, more plausible elastic properties and density estimates can be obtained.

The Ji-Fi algorithm iteratively inverts for impedances given a facies and then inverts for facies given an impedance model until convergence is reached. This scheme implies that better impedances lead to a better facies estimate and vice versa at each iteration of the workflow shown in Figure 26b. The inversion can be constrained to promote facies continuity (lateral or vertical) and to honoring realistic geologic and hydrodynamic, facies conditions (Kemper and others, 2017). The outputs of the Ji-Fi workflow are AI, SI, density (with their standard deviations), and the most probable facies.

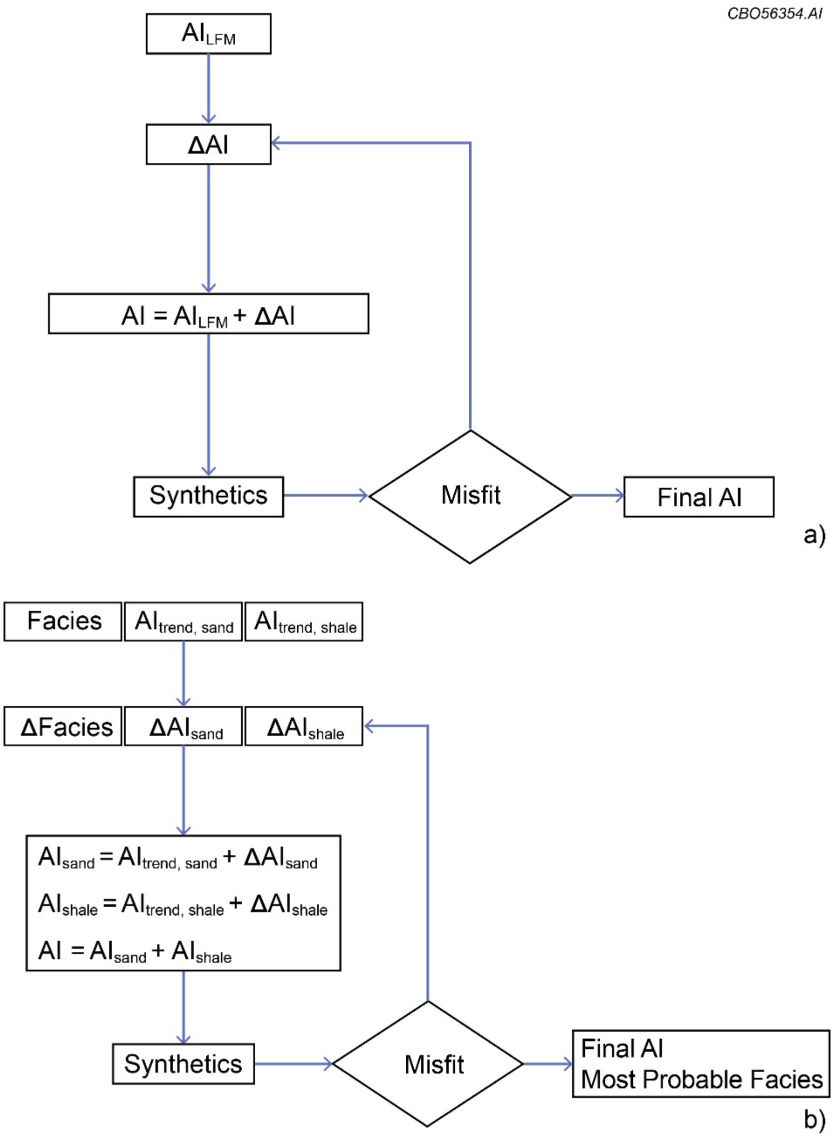

Figure 26. Comparison of simplified simultaneous model inversion vs. Ji-Fi workflow: a) standard model-based inversion and b) Ji-Fi (modified after Waters and others, 2016).

Ji-Fi Workflow

Input Data

Seismic Data

Two data sets were considered for this study. The first one, the baseline survey, was acquired in September 2012 before the start of CO_2 injection. The data set representing the monitor survey was acquired in October 2014 after the commercial CO_2 EOR operations had progressed over several portions of the field (see Figure 4).

Interpreted Horizons of the Study Area

A seismic cube obtained from the stacking of the PSTM offset gathers was used for the interpretation of time and depth horizons. These horizons were used to build the model for the seismic inversion and one of them as a datum for the DTA in Ji-Fi. The interpreted horizons are the following:

- Horizon 1: a strong event above the reservoir. This horizon was used as a datum for the DTA.
- Springen Ranch: the top of the reservoir (Figure 5)
- Skull Creek: bottom of the reservoir.
- LBBC: a strong event below the reservoir.

Velocity Model Estimated in the PSTM Process

The velocity field was estimated to flatten the PSTM gathers during the data processing optimally. It is a smoothed 3-D RMS field in time (see Figure 6). The quality of this velocity model is fundamental not only for the optimum performance of the migration algorithm but also for the conversion of the offset data into the required domain for the seismic inversion.

Well Logs

The following thirteen wells were initially considered to be used in the Ji-Fi workflow: 05-06 OW, 31-16R, 33-14R, 56-16R, 04-03, 04-04, 05-01, 33-13, 04-06, 04-07, 04-11, 04-13, 33-09R. The well logs were analyzed to assess their quality and potential impact on the inversion workflow. Table 1 summarizes the first available logs and the well classification according to the available logs and the type of well. Markers of the main geologic formations in the logs were defined to facilitate the log assessment and simplify the application of the Ji-Fi algorithm. These markers are used to define a zone of interest (or "working intervals" as they are called in the RokDoc® software) in a well. The markers considered for the work presented in this report and their approximated two-way time (TWT), measured depth (MD), and true vertical depth subsea (TVDss) at 05-06 OW are shown in Table 2. While the Horizon 1 and TD Horizon represent the application limits of the Ji-Fi algorithm, the Springen Ranch and Skull Creek constitute boundaries of the Bell Creek reservoir where the changes on facies due to fluid changes are studied.

Table 1. Summary of Wells Analyzed for the Ji-Fi Workflow

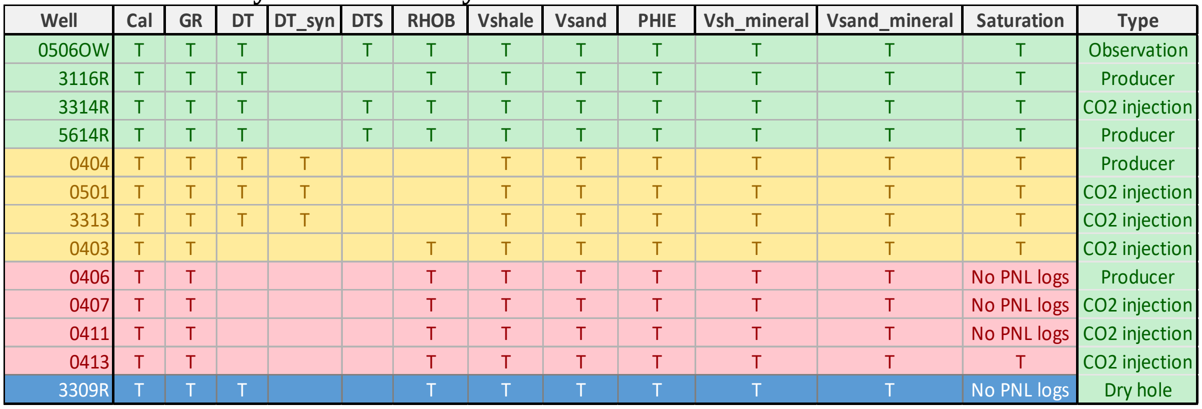

Well	Cal	GR	DT	DT_syn	DTS	RHOB	Vshale	Vsand	PHIE	Vsh_mineral	Vsand_mineral	Saturation	Type
0506OW	T	T	T		T	T	T	T	T	T	T	T	Observation
3116R	T	T	T			T	T	T	T	T	T	T	Producer
3314R	T	T	T		T	T	T	T	T	T	T	T	CO2 injection
5614R	T	T	T		T	T	T	T	T	T	T	T	Producer
0404	T	T	T	T			T	T	T	T	T	T	Producer
0501	T	T	T	T			T	T	T	T	T	T	CO2 injection
3313	T	T	T	T			T	T	T	T	T	T	CO2 injection
0403	T	T				T	T	T	T	T	T	T	CO2 injection
0406	T	T				T	T	T	T	T	T	No PNL logs	Producer
0407	T	T				T	T	T	T	T	T	No PNL logs	CO2 injection
0411	T	T				T	T	T	T	T	T	No PNL logs	CO2 injection
0413	T	T				T	T	T	T	T	T	T	CO2 injection
3309R	T	T	T			T	T	T	T	T	T	No PNL logs	Dry hole

Note: Columns represent number of well (Well); type of log: caliper (Cal), gamma ray (GR), sonic log (compressional) (DT), sonic log (synthetic) (DT_syn), sonic log (shear) (DTS), (bulk) density (RHOB), shale volume fraction (Vshale), sand volume fraction (Vsand), effective porosity (PHIE); volume of shale mineral (Vsh_mineral), volume of sand mineral (Vsand_mineral), saturation, and type of well (Type). The colors represent the availability of log information: green: most of the logs are available, yellow: less information, red: minimum of information available. The blue color represents a dry hole. PNL stands for pulsed-neutron logs.

Table 2. Time and Depth Markers Used to Divide the Sections of the Wells into Working Intervals. Example of TWT, MD, and TVDss for 05-06 OW Well

Name	TWT, ms	MD, ft	TVDss, ft
Horizon 1	1219	3989.79	186.78
Mowry	1283	4290.88	487.88
Shell Creek	1323	4473.72	670.72
Springen Ranch	1328	4494.59	691.59
BC Sand	1330	4506.52	703.52
Rozet	1336	4540.3	737.3
Skull Creek	1341	4564.15	761.15
TD Horizon	1372	4709.24	906.24

Core Data

The core data can provide ground truth information on lithology, density, and porosity. This information can be used to relate geology to well log data. Porosity, petrology, and x-ray diffractometry (XRD) information from core plugs was available for the 05-06 OW, 56-14R, and 33-14R wells. The wells were whole, and sidewall cored in through the reservoir interval.

The analysis of thin sections and scanning electron microscopy (SEM) mineral maps as reported by Eylands and others (2013) indicates that most of the sidewall cores from the 05-06 OW well are grain supported with variable amounts of clay and cement. The clays can be pore filling, pore lining, grain coating, and dispersed and as grain replacement or structural clays. The samples are dominantly clay cemented with minor amounts of quartz overgrowths and cement as noted in the available thin section descriptions. Braunberger and others (2013) studied legacy core from the Bell Creek reservoir and reported that carbonate may be a locally important cement. The significant differences in the porosity and permeability of the Muddy Formation sand intervals of the Bell Creek reservoir can be attributed to clay concentration and distribution within the samples (acting as a contact cement). Decreased porosity and permeability can be attributed to higher concentrations of clay, especially kaolinite, filling the pore spaces between sample grains (Eylands and others, 2013).

Seismic Data Conditioning

As the original data sets were available in the form of PSTM offset gathers, they were converted to partial-angle stacks required for the Ji-Fi prestack inversion. Four data sets were created: near (0–10 degrees), mid (10–20 degrees), far (20–30 degrees), and ultrafar (30–40 degrees) partial-angle stacks. These data sets were extensively used in the Ji-Fi workflow, initially using scalers to compensate for the residual differences between data sets attributed to the effect of near-surface and noise conditions not completely attenuated in the data processing. Although this time-lapse conditioning scheme was satisfactory, additional data conditioning options were tested.

The most relevant results were obtained with the removal of the ultrafar partial-angle stacks from the inversion data set and applying data conditioning only to the near, mid, and far angles. First, a 2-4-65-80 finite impulse bandpass filter was applied to each partial-angle stack to remove high-frequency noise. Then a robust time-shift estimation between near, mid, and far angles of the baseline and monitor data sets was applied. This second step was intended to remove normal moveout correction (NMO) residual time shifts related to PSTM velocity corrections not included in the data processing. The parameters for time-shift estimation were 175-ms correlation window with time shift averaging over a three-trace radius followed by a 90-ms time-shift smoothing window. Figure 27 (left) shows time slices at 1332 ms of the baseline (top) and monitor (bottom) of the stacked near, mid, and far partial stacks, before (left) and after (right) data conditioning.

Well Log Conditioning

To assess any issues in the data acquisition and processing of the logs that can affect the inversion results, quality control of the available well logs was conducted. Any spikes and noise bursts were replaced, and gaps were filled using either spline functions away from the zone of interest or more robust Ikon Science methods within the zone of interest. Histograms were used to assess the log distribution between the three wells 05-06 OW, 56-14R, and 33-14R with the complete sets of elastic logs (p-wave sonic, s-wave sonic, and density) in the Bell Creek interval. Consistent results were obtained between wells, except for the density in the 56-14R well (see Appendix D). A wider density distribution than expected was observed for this well. However, the values are still in the range for sandstone reservoirs based on Appendix A1 of Mavko and others (2009). This well appears to have both the cleanest sands and the highest clay volume of the three wells. A review of density correction logs from all three wells shows that all the density logs are within tolerance < ±0.25 g/cm^3.

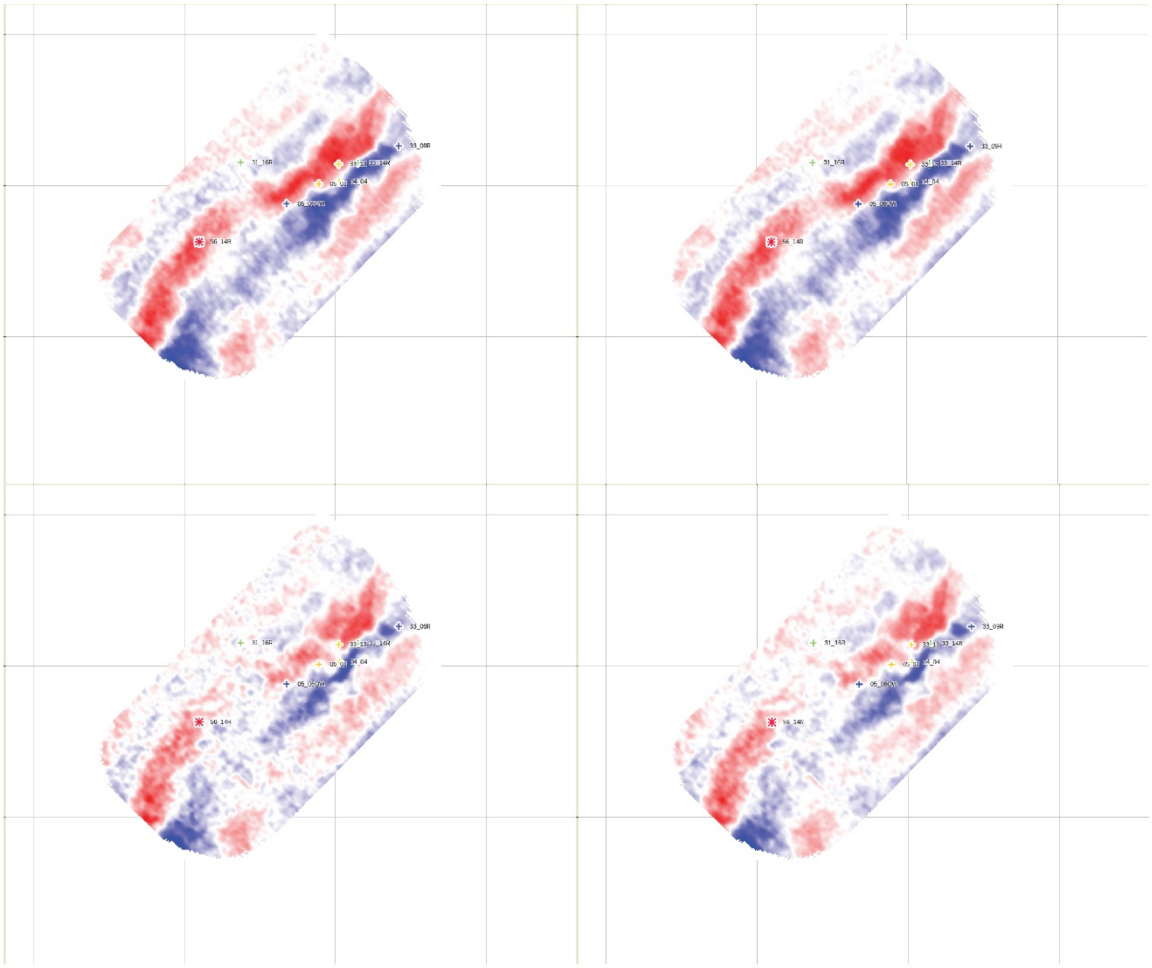

EERC CBO57161.AI

Figure 27. Example of a seismic time slice of stacked near, mid, and far (5-15-25) degrees partial-stack angles at the reservoir level (1332 ms) (top: baseline, bottom: monitor, left: before data conditioning, right: after conditioning).

Since the other available wells do not include fundamental logs with elastic properties for the application of Ji-Fi, a combination of rock physics methods with empirical relationships were used to estimate shear-wave velocity (Vs) for 31-16R, 04-04, 05-01, 33-13 wells and density for 04-04, 05-01, 33-13 wells. A hybrid method was used to estimate Vs for the defined working intervals: a modified Gassmann approach (Mavko and others, 2009) for the interval representing the reservoir. The Gassmann approach was optimized with porosities, in situ fluids, and P-wave velocity (Vp) to predict water-saturated Vp-Vs-density and then substituted to in situ fluids. Empirically calibrated Vp-Vs relationships were used for the prediction for the overburden (from Horizon 1 to Shell Creek markers) and the underburden (from Rozet to Skull Creek markers) working intervals. In the case of density prediction, while linear Vp-density relationships calibrated per working interval were used for working intervals other than the Bell Creek interval, a mix of two methods scaled by porosity were used for the Bell Creek interval. The first method uses mineral volumes, calibrated mineral densities, porosity, fluid logs, and fluid densities to predict log densities directly. In the second method, shale density is locally calibrated between the

Springen Ranch and Skull Creek markers for fluid substitution (density of shale = 2.338) from a fluid subshale average set previously calculated. An example of data log conditioning is shown in Appendix D. Attempts were made to predict Vp for some wells. However, it was not possible to define a method to predict all the working intervals for all the wells correctly. After data conditioning, eight wells were considered for the final application of Ji-Fi: 05-06 OW, 31-16R, 33-14R, 56-16R, 04-04, 05-01, 33-13, and 33-09R wells. The location of the eight wells in the rectangular area representing the boundaries of the seismic surveys is shown in Figure 28.

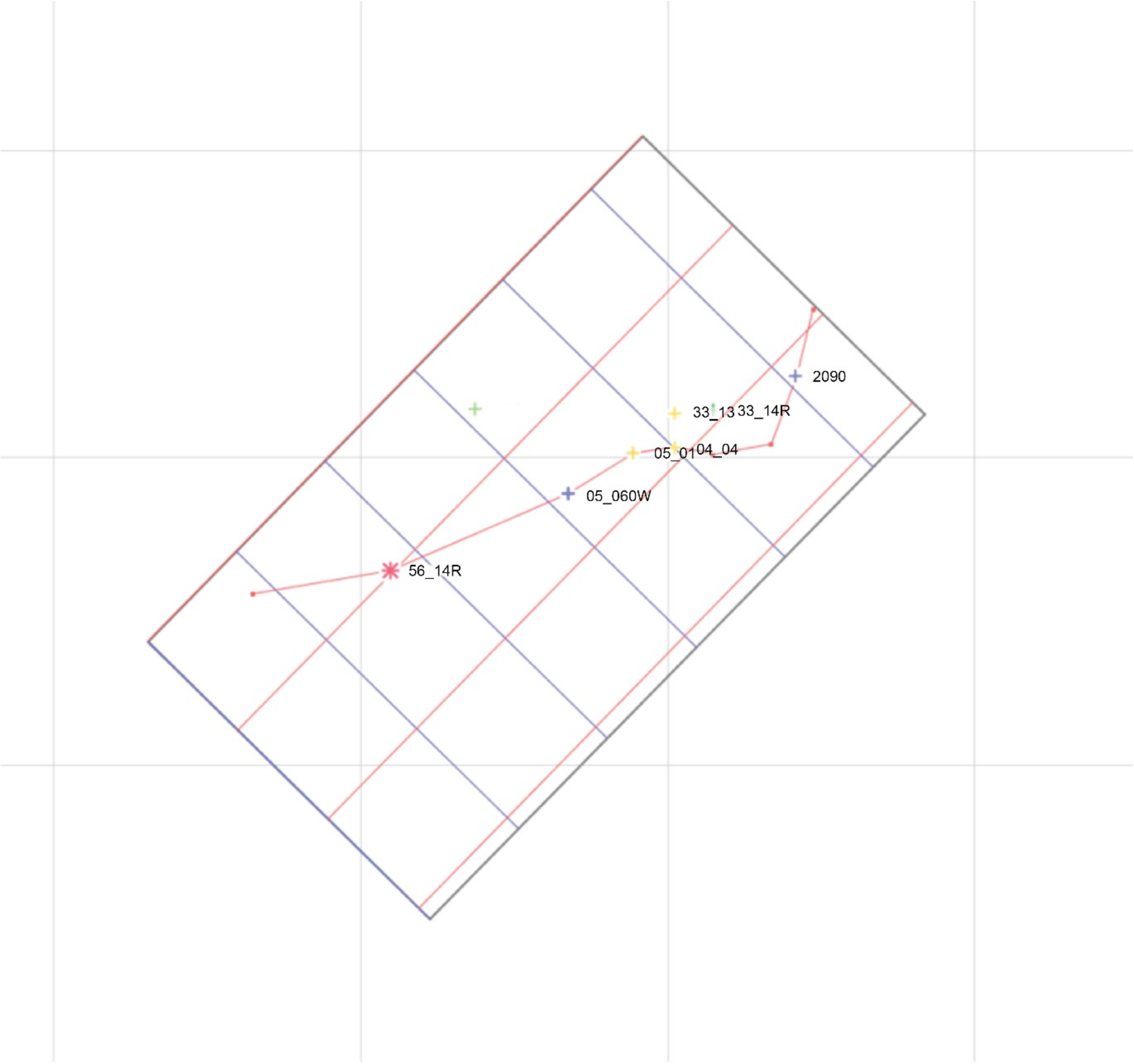

Figure 28. Location of the eight wells (05-06 OW, 31-16R, 33-14R, 56-16R, 04-04, 05-01, 33-13, and 33-09R) used in the Ji-Fi workflow. The rectangle represents the seismic survey area. An arbitrary line, a red line joining the 56-14R, 05-06 OW, 05-01, 04-04, and 33-09R wells, is used to show some of the Ji-Fi results in this report. The blue and red lines exemplify the directions of the Inlines and the Xlines, respectively.

Using Core Data to Relate Well Logs with Geology

Sidewall cores in the 05-06 OW, 56-14R, and 33-14R wells were used to link wireline data information with the geology of the study area. A close agreement of bulk density, porosity, and lithology volumes with corresponding values from wireline logs was expected after allowing for differences due to depth uncertainty, resolution and sampling bias. In general, a ±2-ft depth uncertainty for sidewall cores in the three wells was observed. The following comparisons were conducted:

- Bulk densities derived from core grain density and porosity vs. density logs. Good agreement between both types of density measurement was observed.

- Measured core porosities vs. various porosity logs (Schlumberger RST Advisor, neutron, sonic, density). The best agreement was found with density porosity (dphi) on a sandstone matrix. This finding is consistent with the results reported by Sutherland (2011) and Pasternack (2009). A density of 2.65 g/cm^3 was used to calculate the sandstone density porosity curve. This value is close to the values of 2.60–2.63 g/cm^3 for the Bell Creek clay grain density reported by Pasternack (2009). Density porosity is used as total porosity in the rock physics models considered in this report.

- Mineral types and volumes estimated from XRD analysis of sidewall core samples vs. results from Schlumberger's RST SpectroLith estimates WCAR (carbonate), WQFM (quartz, feldspar, mica), and WCLA (clay) derived from wireline logs. The log data are consistent with the XRD data. The comparison suggests that the WCLA log provides a reasonable estimate of the weight fraction of clay. It can also be inferred from the XRD results that kaolinite is the dominant clay in the Bell Creek interval, and illite and chlorite are also present.

Figure 29 summarizes the comparison of core data with well logs. Because of the quality of the well logs mentioned above, they were considered as the initial reference for rock physics analysis and inversion tests.

Rock Physics as a Diagnostic Tool for Estimating Rock Characteristics and Fluids

Rock physics analysis can be used to estimate changes in the reservoir elastic properties due to changes in stress, fluid type, pore pressure, saturation, and variations of mineralogy.

Analysis of the Members of the Muddy Formation

The Muddy Formation comprises three members: Springen Ranch, Bell Creek, and Rozet. Near Bell Creek Field, the Bell Creek is the reservoir comprising sandy facies associated with the barrier bar system. The Springen Ranch and Rozet are dominated by siltstone and shale facies. The Rozet is below the Bell Creek, and Springen Ranch forms the seal for the Bell Creek reservoir. The trap is primarily stratigraphically controlled by updip pinch-out of the Bell Creek.

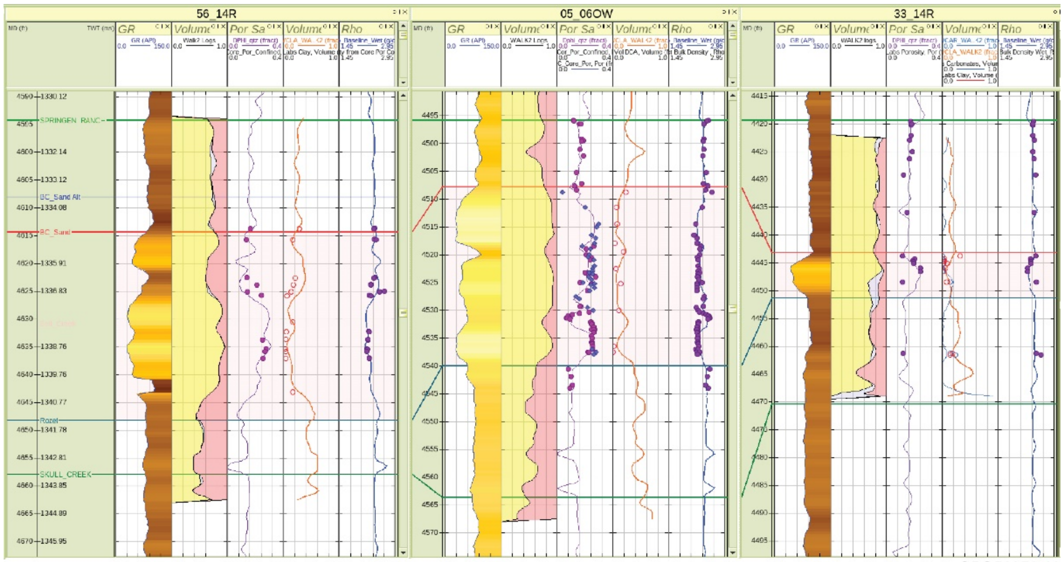

CBO56356.AI

Figure 29. Comparison of core measurements of porosity, volume clay, volume carbonate, and bulk density with log data from the 56-14R, 05-06 OW, and 33-14R wells. The tracks from left to right in each well are GR, volume (yellow sand, pink clay), density porosity (phid) with core porosity, volume clay (orange), or carbonate (blue) with core volume from XRD, wet density with core bulk density. Core bulk density was calculated from grain density and porosity, assuming the fluid density of 1.0 g/cm^3.

All three members are seismically thin and well below tuning. In combination, they reach a thickness close to tuning. Seismic reflections are associated with the approximate top and base of the Muddy Formation. Hence, the elastic properties of all the members contribute to the apparent impedance contrast sensed by the reflections. Figure 30 shows that the properties of all three units overlap to some extent. The Bell Creek at any porosity has, in general, a faster Vp and Vs than Rozet. It can be inferred from the wide range of velocities relative to porosity that Bell Creek is an elastically complicated reservoir. The Rozet has a smaller range of porosities and is generally slower than the Bell Creek. The samples associated with the Springen Ranch are contained entirely within the data cloud formed by the Bell Creek and Rozet. Springen Ranch plots near the transition between Bell Creek and Rozet.

A relationship between density porosity and clay volume from the Bell Creek member is depicted in Figure 31. A wide variation in porosity at low dry clay volumes is observed, which suggests that grain sorting plays an important role in determining porosity. This observation is consistent with the type of the reservoir's depositional environment.

The elastic rock physics crossplots in Figure 32 illustrate a complex relationship between density and velocity in the Bell Creek reservoir. In general, Vp increases and Vs decreases as clay volume increases. High clay volume samples have high density and lower velocities. The increase of bulk modulus and decrease in shear modulus with an increase in volume of clay (Vclay < 0.3) is much less apparent than it is with velocity. Therefore, it can be assumed that the change in velocity is mostly density-driven.

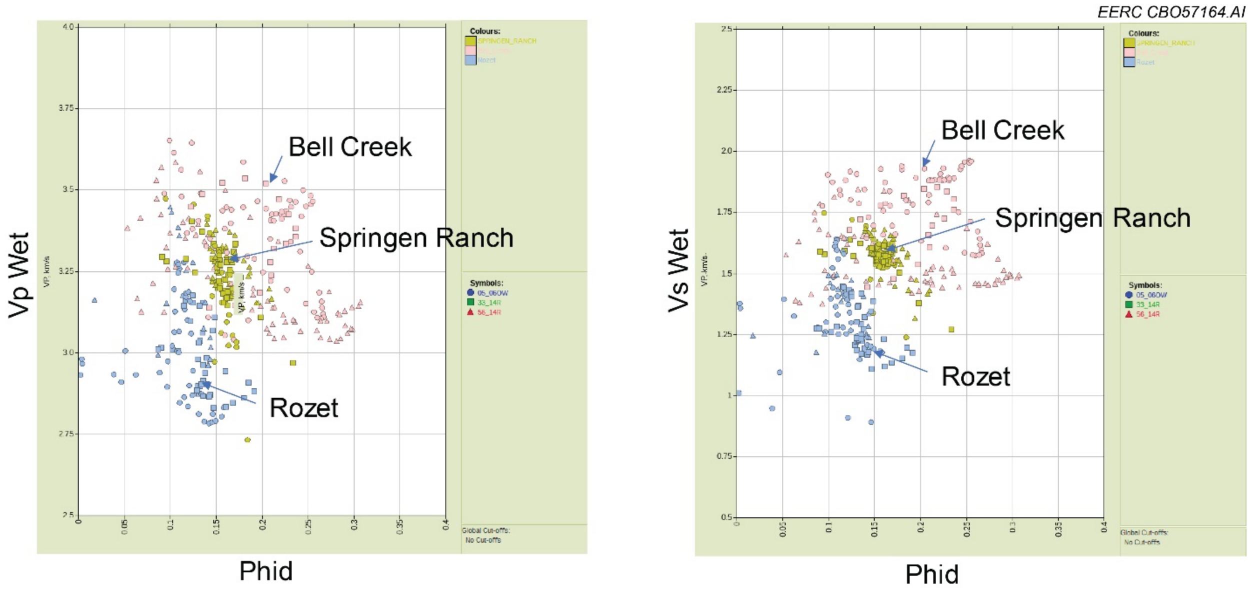

Figure 30. Muddy Formation. Springen Ranch plots within the Bell Creek. Rozet has different properties that cause it to be slower and lower porosity than the rest of the Muddy.

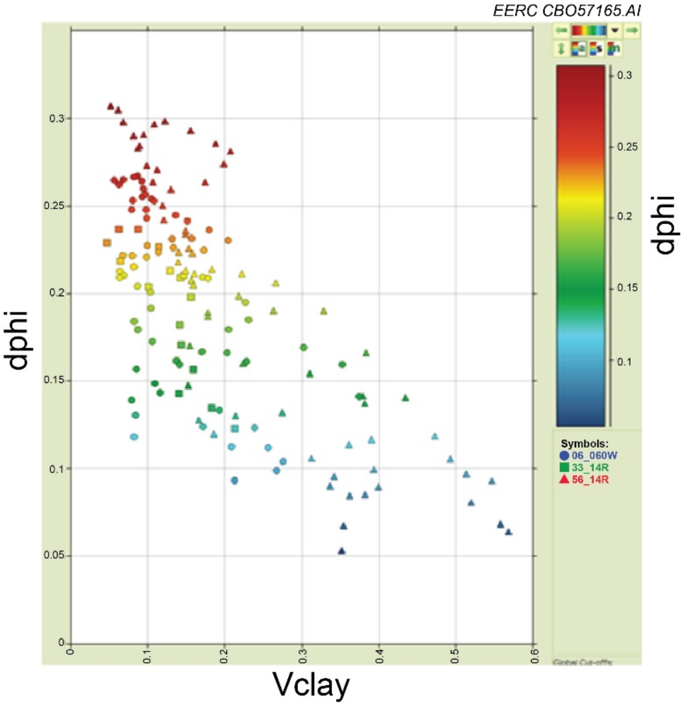

Figure 31. Bell Creek crossplot of density porosity (dphi) vs. volume of dry clay. There is a wide variation of porosity at small volumes of clay which suggests the strong role of sorting in determining porosity.

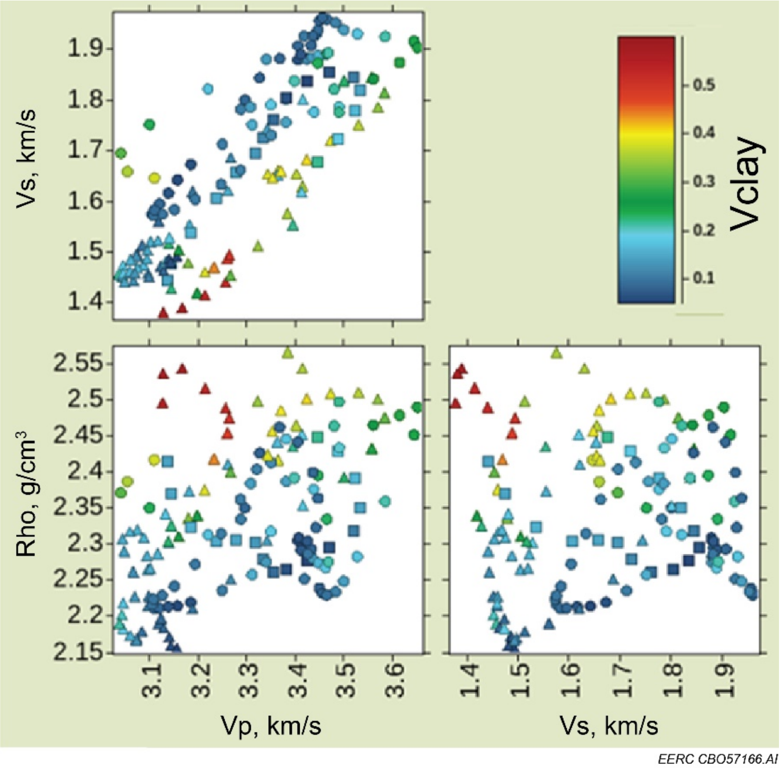

Figure 32. Seismic rock physics crossplots colored by dry clay volume.

Log data from 05-06 OW well were used to determine Springen Ranch, Bell Creek, and Rozet shale properties. Springen Ranch and Rozet properties were selected at the point of maximum separation of the neutron and density porosity curves. In Springen Ranch, this separation occurs at 4502-ft MD and at 4549 ft MD in the Rozet. Bell Creek properties were selected based on samples close to the maximum volume of clay in Figure 33. The results are listed in Table 3. The Bell Creek has slightly higher Vp and density and intermediate Vs relative to the Springen Ranch and Rozet.

Rock Physics Analysis and Diagnostics

Diagnostic models are the rock physics tools to relate seismic and elastic properties of the reservoir and the surrounding formations to geologic observations. They can facilitate predictions of seismic properties away from the wells and for stratigraphic conditions and fluid saturations that have not been encountered by drilling or in outcrop. A well-calibrated model may be used to predict geologic properties, away from well control, based on observed seismic or derived elastic properties.

When rock physics diagnostic models are fit to Vp and porosity, they often predict Vs, bulk, and shear moduli poorly. Granular rocks often have lower shear modulus than expected from the models, possibly as a result of slip at grain contacts under shear and no-slip at the same contacts under compression. Since Vp involves both moduli, fitting a model to Vp alone often results in an underprediction of bulk modulus and an overprediction of shear modulus. The overprediction of

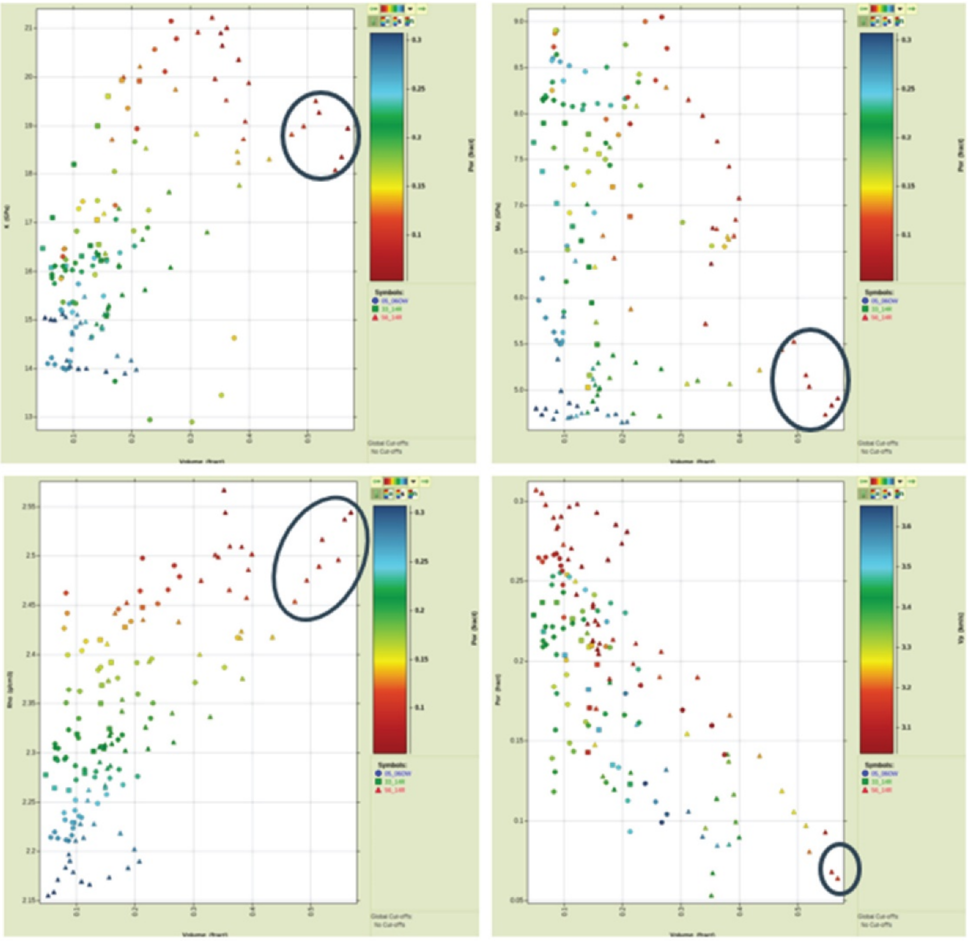

EERC CBO57167.AI

Figure 33. Estimate of Bell Creek shale properties using averages of the selected high shale volume samples. The crossplots are clockwise from upper left: wet bulk modulus vs. dry clay volume, wet shear modulus vs. dry clay volume, density porosity vs. dry clay volume, and bulk density vs. dry clay volume.

Table 3. Shale Properties in the 05-06 OW Well for Springen Ranch, Bell Creek, and Rozet Based on Log Data

	Vp, km/s	Vs, km/s	Density, g/cm^3	K, GPa	Mu, GPa	Phid
Bell Creek	3.18	1.39	2.52	18.9	4.9	0.06
Springen Ranch	3.07	1.53	2.40	15.2	5.59	0.155
Rozet	2.93	1.27	2.51	16.1	4.07	0.09

shear modulus causes an overprediction of Vs. An ad hoc shear reduction factor was used in this study to represent grain slip and to improve the model fitting. One of the problems with the shear reduction factor is that it changes the shear components of the entire model, including the parts with well-defined values like the mineral points. The models used in this study were fitted in the moduli space to constrain the shear reduction factor better and obtain an improved estimate of bulk modulus. Following this approach, it was possible to fit bulk modulus and then adjust the shear reduction factor to fit the shear modulus. Then, fitting Vp and Vs only required adjusting the density model. Additionally, the model fitting was tested in Vp/Vs vs. AI space.

Several rock physics models were considered in the rock physics diagnostic analysis of the Bell Creek reservoir conducted in this study. The following is a short description of the models; more detail can be found in Avseth and others (2005):

- Friable sand: models elastic properties of an uncemented sand as sorting changes and porosity is lost given an effective pressure and critical porosity.

- Friable shale: same as friable sand except that it is used to model changes in elastic properties of a constant mixture of sand and clay as porosity is lost.

- Contact cement: models the effect of initial cementation at grain contacts of a high-porosity grain pack. The model is only valid at high porosity and for small volumes of cement.

- Increasing cement: models the effect of increasing volumes of cement above those modeled by the contact cement model. It is valid for intermediate cement volumes. The porosity limits are interpretive.

- Constant cement: like the friable sand model except here the grains are cemented with a constant volume of cement. Notice that under the conditions of no cement, 100% sand, and equal critical porosity, the friable sand, friable shale, and constant cement models are the same.

- Dvorkin–Gutierrez shaley sand model: models the elastic properties of a grain-supported grain pack as the pores are filled with dispersed porous clay. When the pores are filled to the critical clay volume, the model changes to modeling a matrix-supported sandy shale as sand grains are replaced with clay.

Although the rock physics analysis refers to models for real rocks, plotting thin-section images relative to their log properties can provide a useful reference for the analysis and connect wireline data and petrophysics models with the geology of the study area. In general, independent porosity and Vp measurements for the sidewall cores are preferred; however, the available cores from Bell Creek have only porosity. The Vp measurements, as mentioned in a previous section, were based on finding a good agreement between core sample depth, lithology and porosity, and the associated wireline data, allowing for depth uncertainty. Figure 34 shows the thin sections on a Vp vs. density porosity (dphi) plot of the 05-06 OW (circles), 33-14R (squares), and 56-14R

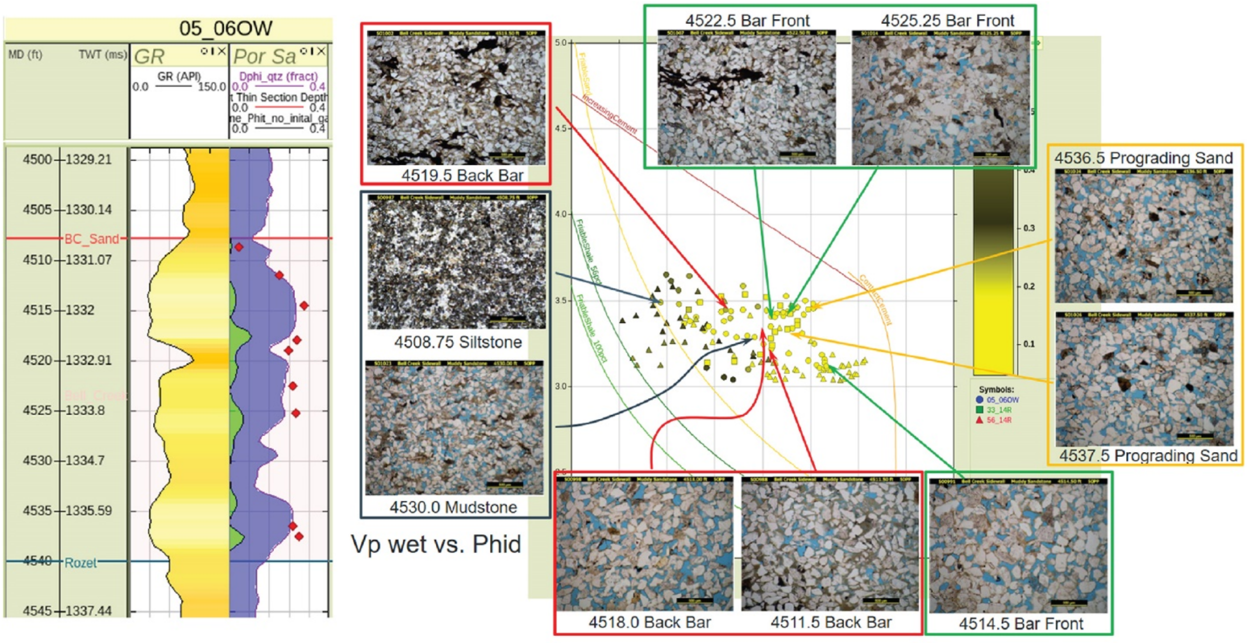

EERC CBO57168.AI

Figure 34. Core data from Bell Creek reservoir at the 05-06 OW well are placed on a Vp (wet) vs. density porosity (phid) plot colored by clay volume with data from 05-06 OW (circles), 33-14R (squares), and 56-14R (triangles) wells. The curves represent the effective medium models: contact cement (dark orange), friable sand (bright orange), increasing cement (red), friable shale 56% (clay) (dark green), and friable shale 100% (clay) (bright green). The depth (ft) and the interpreted facies labels of the core plug are located below and at the side of the thin section.

wells from the reservoir section colored by clay volume. The curves of the contact cement, increasing cement, friable sand, and friable shale (0.56 and 100% shale) models are shown as a reference for the interpretation. Notice how well the models describe the distribution of shales and sands in the reservoir. Furthermore, the bar front and prograding sand facies have the highest porosities for their Vp followed by the back bar facies and then nonreservoir facies. The loss of porosity is consistent with decaying sorting where the bar front and prograding sand facies are best sorted followed by the back bar facies. As expected, Vp increases as porosity decreases, which may be related to changes in sorting and cement volume. The same rock physics models for bulk modulus, shear modulus, Vp, Vs, and elastic model show similar satisfactory results.

A composite framework model resulting from the combination of the friable sand, friable shale, contact cement, and increasing cement models was used to assess the volume of cement and shale properties of the Bell Creek reservoir. This analysis was complemented with the investigation of the behavior of a grain pack, with a constant absolute volume of cement, as sorting decays and porosity decreases using constant cement models. The constant cement model appears to explain the trends of the cleanest sands as sands with a constant volume of cement and decaying sorting. These trends are consistent with the trends of the barrier bar and back bar samples plotted in Figure 34. However, the ability to predict cement volume is limited by the inconsistent fit of the shear modulus component of the model.

The Bell Creek reservoir is a mixture of shaley sand and sandy shale deposited in a barrier bar–strand plain sedimentary environment. The reservoir facies are relatively thin and complicated by the vertical and lateral variability of the depositional environment. This combination of factors creates inconsistency in porosity, sorting, and clay content all of which influence elastic properties of the rocks.

Marion and others (1992) developed a model to explain changes of elastic properties of unconsolidated mixtures of sand and dispersed clay as the mixtures are varied (Figure 35). The model was extended to consolidated mixtures measured with wireline logs by Dvorkin and Gutierrez (2002). This model starts from a clean sand and adds clay to the pore space until filled without disturbing the grain contacts. This point is called the critical clay volume. If more clay is added, then sand must be removed, and the grains begin to separate. More clay is added, and sand removed until the sample is 100% clay. The critical clay volume marks the transition from grain-supported shaley sand to matrix-supported sandy shale.

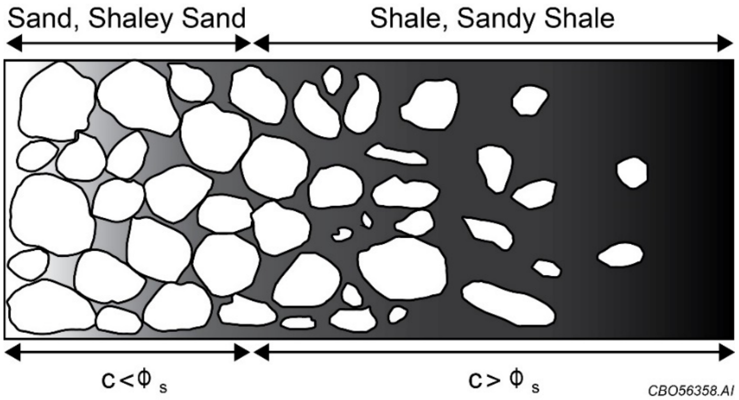

Figure 35. Model for the transition from grain-supported sand to shaley sand to sandy shale to shale (modified after Marion and others, 1992).

From Marion and others (1992) and Dvorkin and Gutierrez (2002) models, it can be inferred that Vp increases and porosity decreases as clay fills the pore space replacing fluid until critical clay volume reached. When clay volumes are greater than critical clay volume porosity increases and Vp decreases. The porosity increase is due to nonporous quartz being replaced with porous clay. Vp decreases at clay volumes greater than the clay full point because of the replacement of high-velocity quartz with lower-velocity clay.

The Dvorkin and Gutierrez (2002) model was applied to the Bell Creek and Springen Ranch to find the critical clay volume (Figure 36). Maximum Vp (3.652 km/s) occurs at a volume of 0.267 dry clay. This is in the expected range for critical clay volume (the critical clay volume is normally between 0.2 and 0.4 volume clay). Density porosity from Figure 36 is 0.1 at the critical

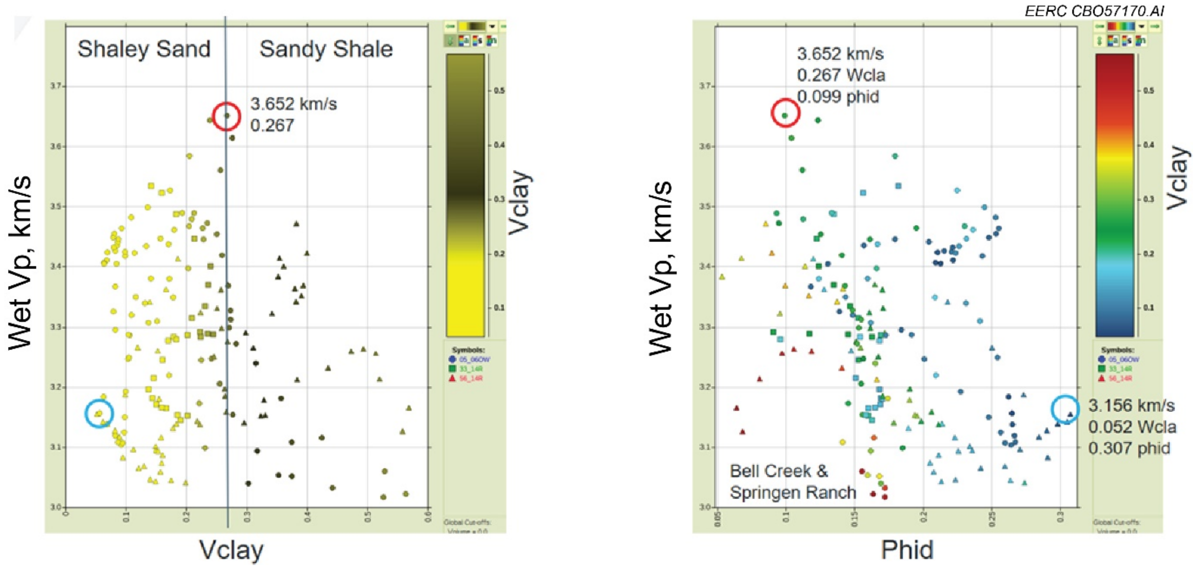
EERC CBO57170.AI

Figure 36. Identification of shaley sand to sand shale transition using Marion and others (1992) model. The left plot is Vp wet vs. volume of dry clay. Maximum Vp occurs at 3.652 km/s and 0.267 volume clay. The right plot is Vp vs. density porosity colored by volume fraction dry clay. The critical clay volume is in red and the highest porosity sand in blue. The high-porosity sand still contains 0.05 weight fraction clay. Samples are from Bell Creek and Springen Ranch, with Vcar > 0.0 excluded.

clay volume. When converted to a total volume, the critical clay volume with porosity is 0.34. This is close to the maximum density porosity in the Bell Creek which is 0.31 in the 56-14R well with 0.05 volume clay. When converted to total volume and the clay removed, a clean sand porosity of 0.34 is observed, which agrees with the critical clay volume. The critical porosity for clean sand is likely to be close to 0.34 which supports the hypothetical clean sand critical porosity used in the rock physics models. The data, in general, show a lot of variability in Vp for any given volume of clay. This could be explained by a changing depositional environment causing changes in sorting and in the contribution of clay to the elastic properties. It is likely that some of the clays are laminated and others may be in the contacts between grains. In both cases, they will tend to lower Vp relative to a grain pack with dispersed clay. Variation in the volume of contact cement may also contribute to the variability. Changes in clay physical characteristics between Rozet and Springen Ranch could also add to the variability.

The following parameters were used to produce the Dvorkin–Gutierrez models shown in Figure 37:

- Dvorkin–Gutierrez shaley sand, sand endpoints
- DG-A – intersects contact cement model at 0.001 volume cement
- DG-B – intersects contact cement model at 0.011 volume cement
- DG-C – intersects increasing cement model at 0.035 volume cement
- DG-D – intersects increasing cement model at 0.075 volume cement
- DG-E – intersects increasing cement model at 0.092 volume cement

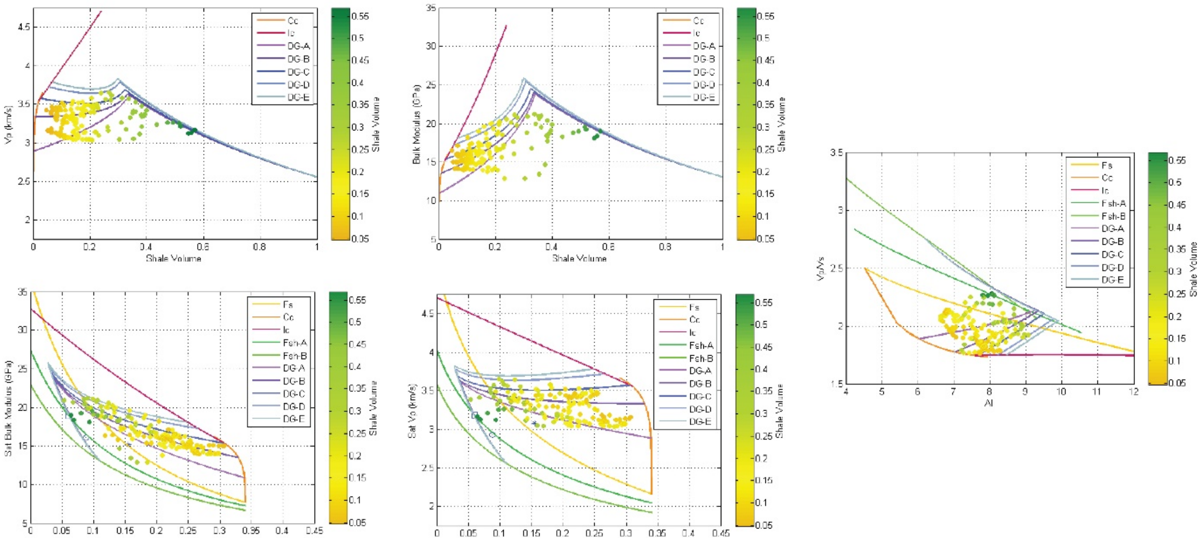

EERC CBO57171.AI

Figure 37. Rock physics diagnostic Dvorkin–Gutierrez and framework models, where the models are Fs – friable sand, Cc – contact cement, Ic – increasing cement, Fsh-A – friable shale with 0.56 clay and 0.44 quartz, Fsh-B – friable shale with 1.0 clay, Dvorkin–Gutierrez shaley sand models DG-A – cement volume 0.001, DG-B – cement volume 0.011, DG-C – cement volume 0.035, DG-D – cement volume 0.075, DG-E – cement volume 0.092. Estimated shale properties from Table 3: blue square – Bell Creek, blue circle – Rozet, and blue asterisk – Springen Ranch.

Although common practice is to parameterize the model based on the cleanest sand and shaliest shale, poor results were obtained with this parameterization. Therefore, the contact, cement or increasing cement model for properties of the sand and the friable shale model at 100% clay for the shale properties were used for the model parameterization and iterated to find the shale porosity that fit the data. The models derived with these properties in Figure 37 are consistent with the observations. The overall shape of the models in Vp vs. porosity or volume clay is consistent with the data. The sandy shale model produces a trend that passes close to markers for the average properties of the Bell Creek and Rozet shales. Although individual models in Figure 37 are difficult to identify in the observations, the upper limit of the models appears to conform to the upper limit of the data when plotted on bulk modulus and Vp vs. clay volume plots. The sandy shale portion of the model fits best when clay porosity is 0.11.

The depositional complexity reflected in the wide variation of sand porosity may create variation in the elastic properties, leading to some uncertainty in the critical clay volume. Variation in clay grain properties and porosity may also contribute. The possibility exists that there may be more than one critical clay volume. Additionally, the depositional environment changes from nearshore – barrier bar – lagoon – onshore; in some cases, the style of deposition (e.g., laminated deposits) is inconsistent with the assumptions of the model. Finally, a potential second shale trend is observed in bulk modulus vs. clay volume plot in Figure 37 but not in the Vp vs. clay volume; thus the existence of a second, higher-porosity shale trend is indicated which, based on Table 3, may possibly be related to the Springen Ranch.

Pressure Sensitivity and Fluid Substitution Modeling

Time-lapse seismic measurements are primarily affected by changes in reservoir pore pressure and saturation. Rock physics modeling was conducted to estimate the pressure and saturation scenarios of the Bell Creek reservoir. Reservoir and fluid properties obtained from petrophysics, geology, and reservoir simulation were used for the pressure and fluid substitution modeling (see Table E-1 in Appendix E).

The considered average pressure in the study area for the baseline (September 2012) and monitor (October 2014) surveys were 1718 and 2539 psia, respectively. Reed and others (2018) reported an observable time-lapse pressure response due to CO_2 injection in the Bell Creek reservoir.

Pressure Sensitivity

Since neither laboratory measurements of Vp and Vs on dry rocks of the Bell Creek nor an analogous set of measurements from an area with similar geology and structural history were available, the MacBeth (2004) empirical model was used to predict the pressure sensitivity for the Bell Creek reservoir. Pressure response data are typically limited to the permeable parts of the reservoir; therefore, the application of the model was limited to the sandy facies of the Bell Creek.

The stress sensitivity relations from the MacBeth model are based on laboratory measurements on rocks over a wide range of conditions. This model requires knowledge of the average porosity, initial and final pore pressures, and overburden pressure. Average porosity is the only parameter required to determine model coefficients from MacBeth (2004) pressure sensitivity crossplots. The Bell Creek average porosity was derived from histograms of density porosity from the sandy facies of the reservoir at the 05-06 OW, 56-14R, and 33-14R wells. The estimated average porosity of 23% was used to derive the MacBeth model's sensitivity parameters shown in Table 4.

Table 4. MacBeth Model Parameters Estimated from Porosity

phi, %	S_κ	P_κ, MPa	κ_∞, MPa	S_μ	P_μ, MPa	μ_∞, GPa
23	0.59	6	12.4	0.59	7	10.9

Note: phi: porosity, S_κ: total stress sensitivity for bulk modulus, P_κ: pressure constant for bulk modulus, κ_∞: highest-pressure asymptote for bulk modulus, S_μ: total stress sensitivity for shear modulus, P_μ: pressure constant for shear modulus, and μ_∞: highest-pressure asymptote for shear modulus.

Overburden pressure was calculated by the integration of a density log from the 05-06 OW well between the surface and reservoir, assuming a density of 2.07 g/cm^3 between the top of the log and the surface. The overburden pressure at the reservoir in the 05-06 OW well is in the range between 4380 and 4413 psi. A value of 4400 psi was adopted for the overburden pressure of the Bell Creek reservoir.

The estimation of pore pressure is more complicated because pressure values are required at the time when the well was drilled and when each seismic survey was acquired. Pore pressure can be derived from wireline formation testers, drillstem tests, production data, or reservoir modeling. As pore pressure data for individual wells at Bell Creek were not available, average values from the reservoir simulation were used (see Table E-1 in Appendix E). The available data are discussed below:

- The 05-06 OW well was logged in December 2012 when the average reservoir pressure was 2262 psi. The baseline seismic was acquired in September 2012 when the average reservoir pressure was 1718 psi. The monitor seismic was acquired in October 2014 when the average reservoir pressure was 2539 psi. Whereas the pore pressure changed −544 psi from logging to baseline seismic survey, it changed +277 psi between logging and monitor seismic survey.

- The 33-14R and 56-14R wells were logged in March 2013 when the average reservoir pressure was 2269 psi. While the pore pressure changed −551 psi from logging to baseline seismic survey, it changed + 270 psi between logging and monitor seismic survey.

Pressure substitution using MacBeth's relationships is a built-in function in RokDoc® software. It involves a combination of fluid substitution to remove fluid effects and pressure substitution applied to the dry matrix and resubstitution of the fluids modeled at the new pore pressure back into the rock. Following this scheme, the rocks in the model were fluid substituted to wet before pressure substitution. In general, increasing pore pressure should cause Vp and Vs to decrease (decreasing pore pressure has the opposite effect). The application of the model to Bell Creek reservoir produces the results shown in Figure 38. Vp and Vs are sensitive to the pore pressure changes at the three wells. Whereas the pore pressure at the time of the baseline seismic survey was lower (green curves) and Vp and Vs were higher than when the wells were drilled in late 2012 and early 2013, the pore pressure at the time of the monitor seismic survey was higher (pink curves), and velocities were lower.

Fluid Substitution

Diagnostic analysis of rock properties and the effects of changes in fluid saturation require that the reservoir in all the wells have the same initial fluid saturation. Gassmann's equation (1951) was used for fluid substitution from in situ to brine-filled conditions. The equation requires information on initial fluid saturation, fluid elastic properties, rock elastic properties, and total porosity.

Fluid substitution requires in situ and final fluid and reservoir properties inputs which are obtained from petrophysics and engineering sources. Initial fluid saturation was obtained from the Schlumberger RST Advisor analysis of the wireline and baseline PNL logs. According to production data, the baseline reservoir gas/oil ratio (GOR) is very low (< 2 l/l); therefore, it is assumed that the gas saturations reported by Schlumberger RST Advisor for baseline data are noise and were set to zero. Fluid properties for in situ oil and brine were obtained from measurements on produced fluids (see Table E-1 in Appendix E). Rock composition was obtained from

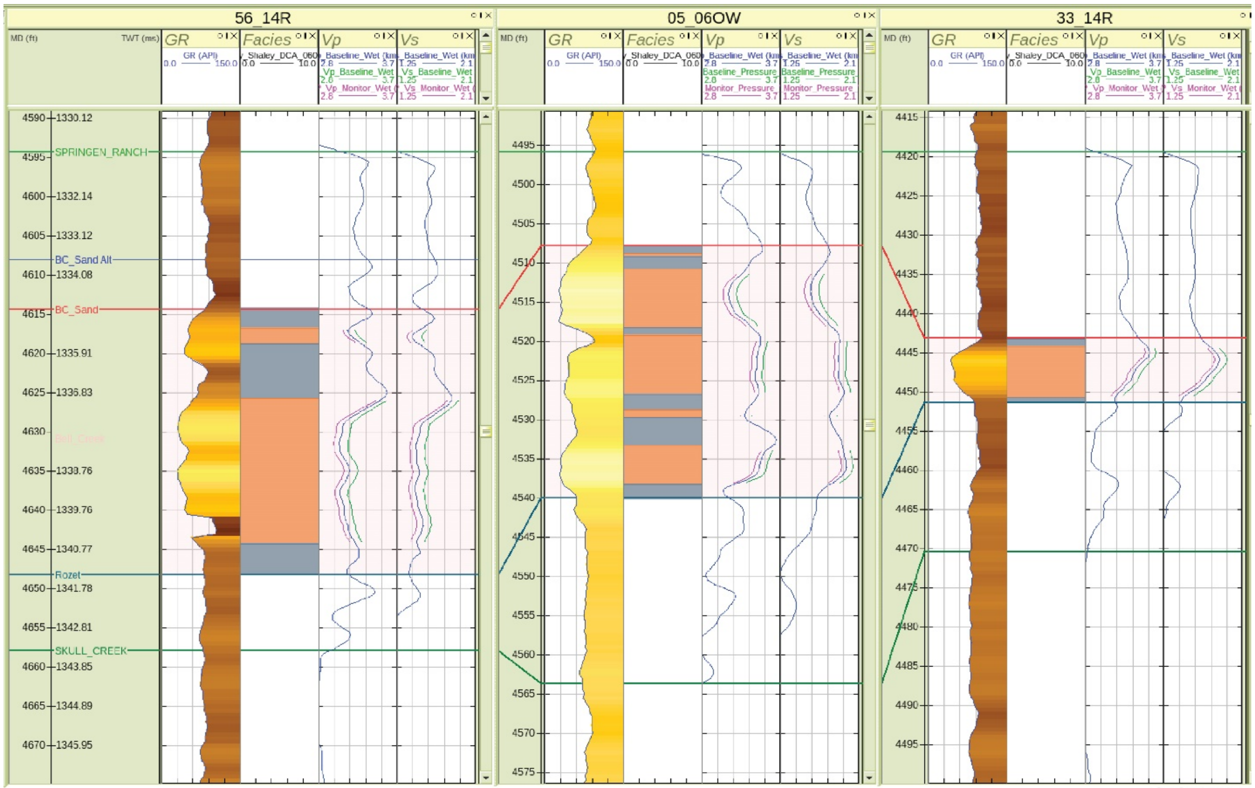

Figure 38. Results of pressure sensitivity modeling for 56-14R, 05-06 OW, and 33-14R wells. Left to right tracks at each well: GR, facies (orange: sandy, gray: shaley), Vp and Vs. Blue curves: original water-saturated Vp and Vs.; green curves: baseline survey; pink curves: monitor survey.

Schlumberger RST SpectroLith analysis. Grain bulk modulus was calculated using standard properties and Voigt–Reuss–Hill average (Mavko and others, 2009). Porosity is based on density porosity on a sandstone matrix.

Elastic Properties of Fluids and Their Mixtures

Modeling of elastic fluid properties is critical to the quantitative time-lapse analysis of the Bell Creek reservoir. The FLAG modeling algorithm in RokDoc® software was used to model the elastic properties of brine, dead oil, and CO_2. Models of CO_2 saturated oil and water were built from empirical relationships from the literature (Han and others, 2012; Han and Sun, 2013). All models are based on the fitting of laboratory measurements of Vp and density of defined fluid mixtures under controlled temperature and pressure conditions.

For this study, fluid properties and reservoir conditions are required on four dates corresponding to the baseline (September 2012) and monitor (October 2014) seismic surveys and the wireline logging of the 05-06 OW well (December 2012) and 33-14R and 56-14R wells (March 2013). The fluid and reservoir properties required for modeling are given in Table E-1 in Appendix E. The modeled fluid properties are given in Table E-2 in Appendix E. According to the modeling results, the variation in oil and water properties between September 2012, December 2012, and March 2013 is very small. The September 2012 properties were used to cover all three dates. October 2014 corresponds to the post-CO_2-injection conditions.

As RokDoc FLAG model is designed to work with hydrocarbons and water, and mixtures of CO_2 with oil or water act differently, alternative models were used to model CO_2-saturated brine and oil. Mixtures of oil saturated with CO_2 were modeled using Han and others (2012) equations. This model is an extension of the Batzle and Wang (1992) model to cover CO_2-saturated oil where temperature is 40°–100°C, pressure 20–100 MPa with oil API 23–40 and GOR of CO_2 28–310 l/l. The reservoir and fluid properties model for Bell Creek except for pressure fall within this range.

The water saturated with CO_2 was modeled using Han and Sun (2013) equations. This model is an extension of the Batzle and Wang (1992) model to cover CO_2-saturated water where temperature is 25°–150°C, pressure 21–103 MPa, and GOWR of CO_2 25–35 l/l. The Bell Creek reservoir and fluid properties apart from pressure fall within this range. The solubility of CO_2 in water at Bell Creek is 1.12 mol/kg. Applying the ideal gas law, this translates to a GWR 26.9 l/l CO_2.

Figure 39 shows the model results. Notice the following:

1. Water and water saturated with CO_2 (GWR = 26.9) have very similar properties at the October 2014 reservoir conditions.
2. Dead oil is the second highest Vp fluid. Saturation with CO_2 lowers its velocity significantly and slightly increases its density.
3. CO_2 at reservoir conditions has the lowest velocity and density.

Any fluid other than water is unlikely to exist in the reservoir at 100% saturation, instead they will exist in mixtures primarily with water. Using Wood's (1941) equation to describe uniform mixing of fluids in Figure 40, it is observed that as water saturation increases, the fluid properties converge toward water. Expected water saturations are between irreducible water saturation of 0.25 and approximately 0.5–0.6, which is the approximate saturation after waterflooding before CO_2 EOR. The saturation after CO_2 EOR is expected to be near 0.35.

Fluid Substitution and Ji-Fi Fluid Facies

The fluid properties were used to create end member fluid models for Ji-Fi inversion (Table 5). The real fluid mixtures are expected to form a continuum; however, Ji-Fi was limited to three fluid facies models. Two fluid mixtures were selected to describe baseline (August 2012) reservoir conditions and four fluid mixtures to describe monitor (October 2014) reservoir conditions. Water saturations of 1.0, 0.55, and 0.35 were selected for wet reservoir, oil reservoir after water flood, and reservoir after CO_2 EOR, respectively.

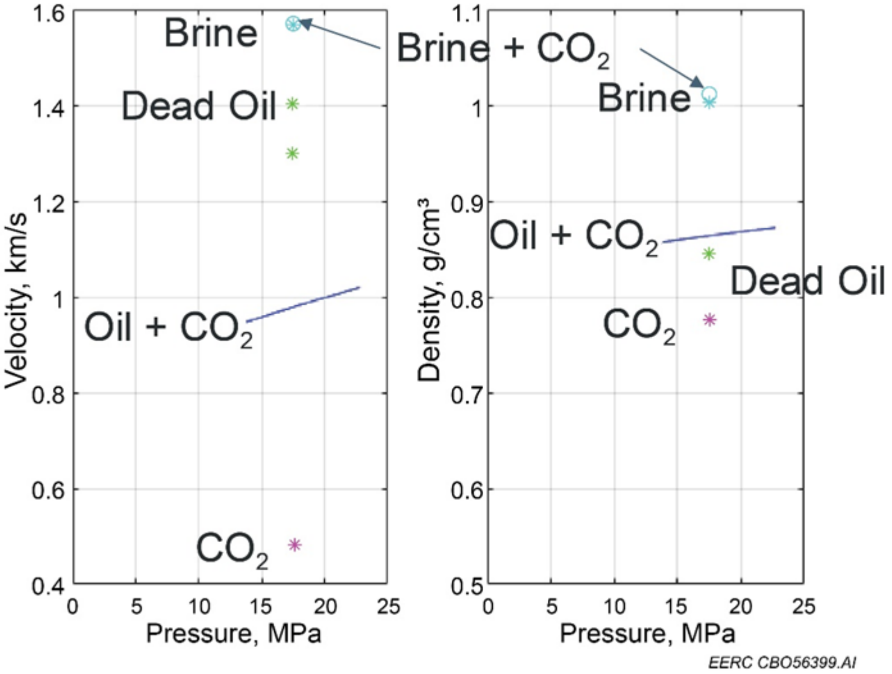

Figure 39. October 2014 fluid models. The plots show the velocities and densities of the various fluids. The modeled fluids are water, dead oil (no gas), CO_2, saturated mixture of oil and CO_2, and saturated mixture of water and CO_2.

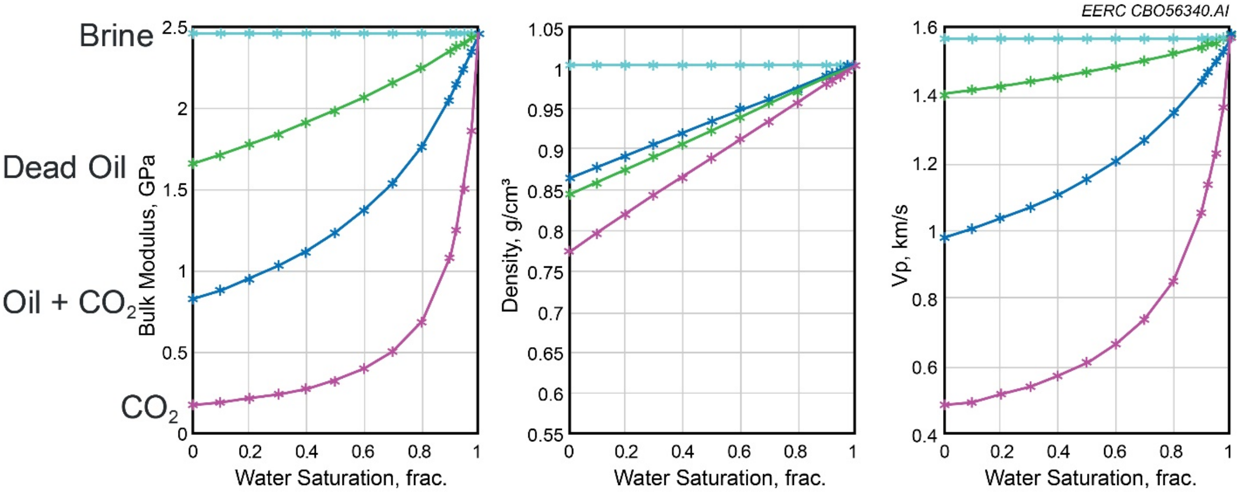

Figure 40. October 2014 fluids mixed with water using Woods equation. Initial water saturation before EOR is 0.5–0.6 and decreases to an average of 0.35 after EOR. Approximate irreducible water saturation for Bell Creek is Swirr = 0.25.

The fluid models represent:

1. All brine model – areas outside the field or below the oil water contact (OWC).
2. Dead oil and brine – reservoir after water flooding and before CO_2 effect.
3. (oil + CO_2) and brine – reservoir where EOR is active.
4. (brine + CO_2) and CO_2 – areas relatively close to the injectors.

Gassmann (1951)-based fluid substitution was conducted. It consisted of replacing the brine in the Bell Creek sandy facies of the pressure adjusted baseline and monitor models with fluid properties from the models in Table 5. Gassmann's equation was used with total porosity from density porosity and a rock model consisting of the volume fractions of quartz, carbonate, and clay. The baseline fluid model and the monitor model are September 2012 and October 2014, respectively. Fluid substitution is limited to the sandy facies which was also used in pressure substitution.

Table 5. Fluid Mixture Models for Fluid Substitution. The (&) symbol indicates fluid mixing with Woods equation while the (+) symbol indicates modeling with either the oil and CO_2 or water and CO_2 empirical fluid property models discussed above.

Baseline (September 2012)	Monitor (October 2014)
Brine	Brine
Dead Oil (So = 0.45) & Brine (Sw = 0.55)	Dead oil (So = 0.45) & brine (Sw = 0.55)
	Oil + CO_2 (S = 0.63) & brine (Sw = 0.35)
	Brine + CO_2 (S = 0.35) & CO_2 (S_{CO2} = 0.65)

Note: The symbol "&" indicates fluid mixing with Woods equation while the symbol "+" indicates modeling with either the oil and CO_2 or water and CO_2 empirical fluid property models mentioned in the main text.

Fluid substitution for the baseline case consisted of replacing the water in the water-saturated baseline pressure substituted model with a mixture of dead oil and water at four wells 05-06 OW, 56-14R, 33-14R, and 31-16R. The results for 05-06 OW are shown in Figure 41 (similar responses were estimated for the 33-14R and 56-14R wells (see Appendix E). A small reduction in Vp and density is relative to the brine saturated model observed for the mixture of dead oil and brine.

Fluid substitution for the monitor case consisted of replacing the water in the water-saturated monitor pressure-substituted model with mixtures of dead oil and water, oil – CO_2 and water, CO_2 and water at four wells 05-06 OW, 56-14R, 33-14R, and 31-16R. The results for 05-06 OW are shown in Figure 42. Vp and density decrease as brine is replaced with dead oil and brine, oil – CO_2 and water, and CO_2 and water, respectively.

Baseline and monitor models show a small separation between brine-saturated and dead oil + brine Vp curves. A larger separation is seen between CO_2 + brine, oil + CO_2, and dead oil + brine Vp curves, which suggests that the monitor CO_2 + brine, CO_2 + oil, and unchanged fluid may be easier to separate than the pre-CO_2 baseline fluids. The very small separation between the modeled density curves may be due to the unlikely contribution of very far angles in the AVO analysis to identify fluid saturations.

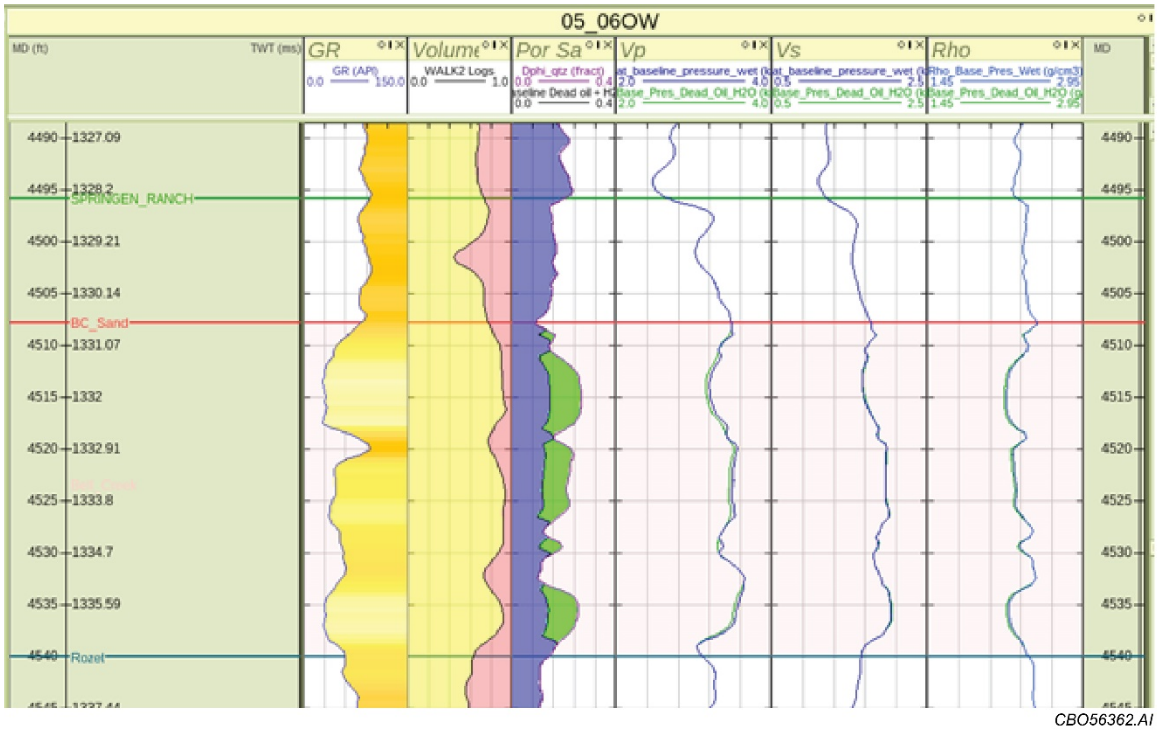

Figure 41. Baseline (September 2012) fluid substitution models into sandy facies for the 05-06 OW well. Left to right tracks: GR, lithology (volume), saturation with density porosity (Por Sa) (phid) (dark blue: brine, green: dead oil), P-wave velocity (Vp), S-wave velocity (Vs), density (rho). Blue curves: 1.0 brine saturation, green curves: dead oil + brine models.

Rock Response to Change in Pore Pressure and Saturation

The pressure and fluid substitution models can be summarized to show how changes in pressure and saturation affect rock properties (Figure 43). When pore pressure is increased from baseline to monitor models, Vp and Vs decrease (A: blue arrow). When the wet reservoir is replaced with either CO_2 + oil (B: green arrow) or CO_2 + water (C: orange arrow), Vp decreases significantly and Vs increases insignificantly because of the change in density of the fluid. Hence, saturation change affects Vp, but pore pressure change affects Vp and Vs. Inversion results for saturation can have a pore pressure overprint. The wide range of Vp and Vs for such a small porosity range is probably associated with the complexity of the reservoir.

Modeled Seismic Response

To determine the feasibility of inverting the time-lapse data for fluid saturation, the seismic response change due to saturation changes was modeled using the fluid substituted logs. Two types of modeling were used: 1) half-space models whose model reflection coefficients are given by the average rock properties and 2) convolutional models, which include interference effects from closely spaced reflection coefficients based on a supplied wavelet. The results of the modeling are shown in Appendix E.

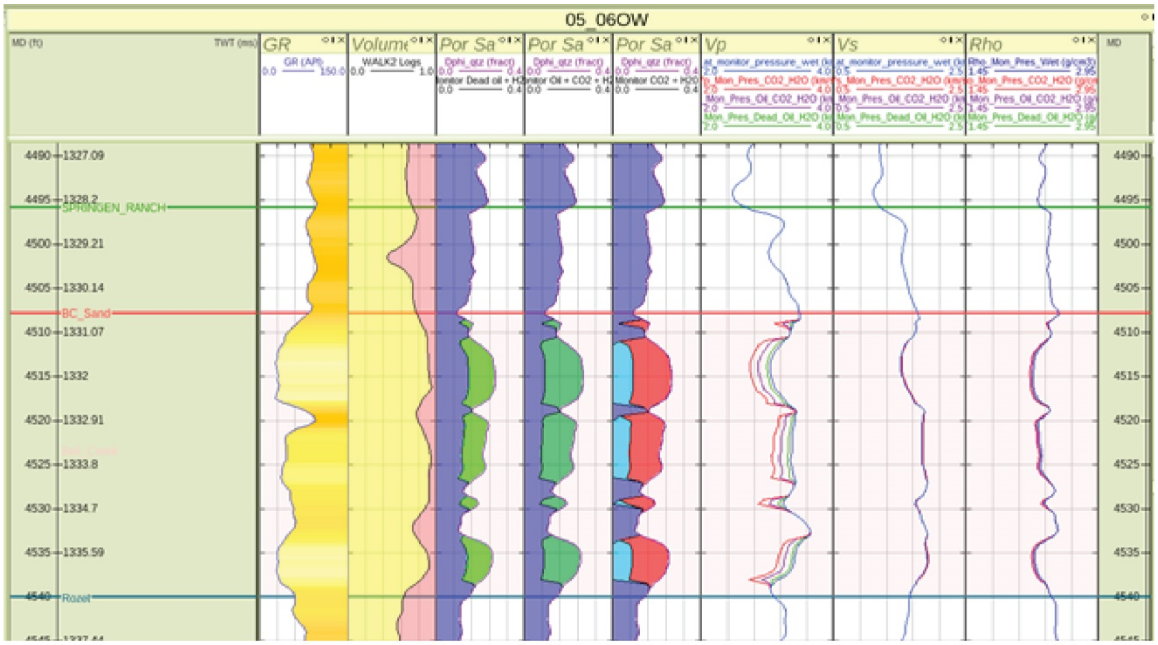

Figure 42. Monitor (October 2014) fluid substitution into sandy facies for 05-06 OW well. Left to right tracks: GR, lithology (volume), and three saturation with density porosity (Por Sa) (phid) scenarios: 1) brine (dark blue) and dead oil (green), 2) brine (blue) and CO_2-saturated oil (dark green), 3) brine (dark blue), CO_2-saturated brine (light blue) and supercritical CO_2 (red), P-wave velocity (Vp), S-wave velocity (Vs), and density (Rho). Blue curves: 1.0 brine saturation, green curves: brine + dead oil models, purple curve: brine and CO_2-saturated oil, red: CO_2-saturated brine and CO_2.

Facies from Well Logs and Rock Physics Modeling

Ji-Fi foregoes the traditional method of creating a low-frequency background model separate from a relative impedance inversion. Instead, it combines the two processes into an absolute inversion by constructing the background model iteratively from a set of defined elastic facies and related depth trends. Facies are used to classify rocks according to their appearance or composition. In the RokDoc® software, facies are used to make classifications of rocks based on properties such as their shale volume, porosity, and saturation (Ikon Science Manual). After creating facies logs from petrophysical logs, an automatic approach that consistently interprets the elastic logs (Vp, Vs, and density) for the facies classification was preferred to minimize the bias from the geologic interpretation. An unsupervised clustering approach was applied to the elastic logs of the 04-04, 05-01, 05-06 OW, 31-16R, 33-09R, 33-13, 33-14R, and 56-14R wells to estimate facies logs without fluids. In this approach, the only initial interpreter intervention is defining the number of expected facies. This “hard” constraint is used by the clustering algorithm in the multidimensional analysis of log data to estimate groups with maximum homogeneity between the elements of the groups and with the maximum of differences between groups. Several iterations were needed to estimate the dry facies according to geologic conditions of the study area (represented by the

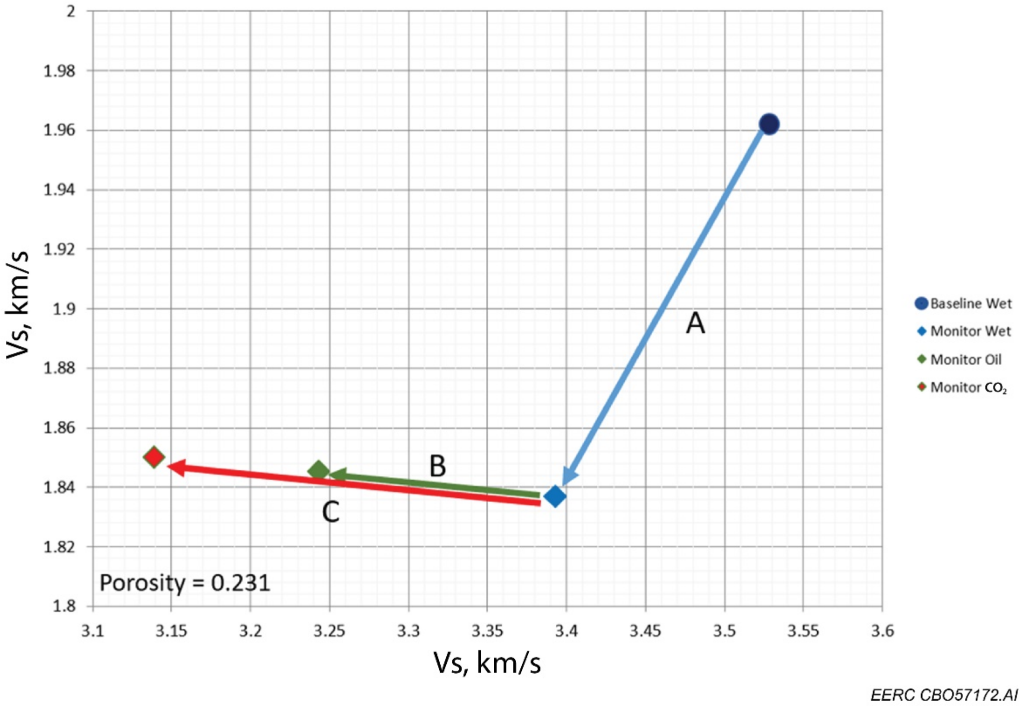

Figure 43. Response of average porosity (0.231) Bell Creek sand to changes in pore pressure and saturation. The blue arrow (A) indicates a change in velocity with increasing pore pressure between September 2012 and October 2014. The green arrow (B) indicates the change in velocity from dead oil + water to oil + CO_2 rock at monitor pressure. The red arrow (C) indicates the change in velocity from dead oil + water to CO_2 + water rock at monitor pressure. The color of the symbols indicates monitor fluid and pressure substitution models: blue = dead oil + water, green = oil + CO_2, and red = CO_2 + water.

petrophysical facies logs). In this process, the initial step consisted in analyzing the facies clusters obtained with no prior information on the geology and then relating them to geologic/petrophysical facies. The success of the clustering is reflected in the separation of the cluster in the seismic (elastic) domain and, therefore, in the Ji-Fi results.

Since only the reservoir interval corresponding to the Bell Creek sandstone was considered with fluid fill, the litho-fluid facies (facies reflecting not only rock type but also fluid fill) were created according to the fluid substitution modeling cases mentioned in Table 5 (monitor).

All the facies representing the geologic and fluid conditions in the period of the two seismic surveys (September 2012 – October 2014) at Bell Creek are shown in Table 6. These facies are integrated into the DTA already explained in a previous section.

Table 6. Facies Estimated at the 04-04, 05-01, 05-06 OW, 31-16R, 33-09R, 33-13, 33-14R, and 56-14R Wells

Color	Facies	Type	Comment
🟩	Shallow Marine 1	Siltstone	
🟧	Marine 1	Shale	
🟪	Marine 2	Shale	
🟨	Shell creek	Shale (lagoon, tidal flat)	
🟧	Barrier bar	Sandstone (bar)	
■	Shallow marine intrareservoir	Siltstone (transition)	
🟪	Extra shale	Shale	
🟦	Shallow Marine 2	Siltstone	
🟥	Marine 3	Shale (deep sea)	
🟩	Barrier bar – dead oil and water	Sandstone (bar)	Fluid substituting
🟩	Barrier bar – oil	Sandstone (bar)	Fluid substituting
🟥	Barrier bar – CO_2	Sandstone (bar)	Fluid substituting
🟦	Barrier bar – water	Sandstone (bar)	Fluid substituting

Note: The estimated geologic/petrophysical (dry) facies representing the Bell Creek reservoir at different wells are shallow marine intrareservoir, barrier bar, Shallow Marine 2, Marine 3, and Shell Creek. The fluid facies are assigned at the interval representing the Bell Creek sandstone (barrier bar facies). The prefix barrier bar is used in the name of the fluid facies to facilitate the identification of the reservoir interval.

The elastic facies are likely to be different from geologic facies. While geologic facies are distinctive rock units described in terms of a set of geologic characteristics such as sedimentary environment, elastic facies are rock units that have distinctive elastic properties described in terms of their elastic moduli and density or seismic velocity and density. In the Muddy Formation, as shown in Figure 44, geologic facies do not make perfect elastic facies.

In Ji-Fi, the ideal case is to derive elastic facies that separate reservoir from nonreservoir and for them be elastically distinctive so that they can be detected by the inversion. The Bell Creek is difficult to separate into reservoir and nonreservoir facies for several reasons, including complex sedimentary environment, high volume of silt in the shales, and the variable location of clay in the rock matrix. Critical clay volume from the Dvorkin–Gutierrez shaley sand model (Figure 37) can be used as a first-order separator for shaley sand and sandy shale facies. Assuming samples with dry clay volume < 0.26 are shaley sands and sands and samples with dry clay volume >0.26 are sandy shales and shales, a first-order separation can be obtained (Figure 45).

A refinement is to use polygons and a trend line to define rock physics friendly sandy vs. shaley facies in bulk modulus vs. porosity space with reference to various logs in depth space. The resulting facies are separated by a boundary line, as shown in Figure 45, with the following equation:

$$K_{eq} = -131.7841 * \text{Phid} + 38.81731 \qquad \text{[Eq. 1]}$$

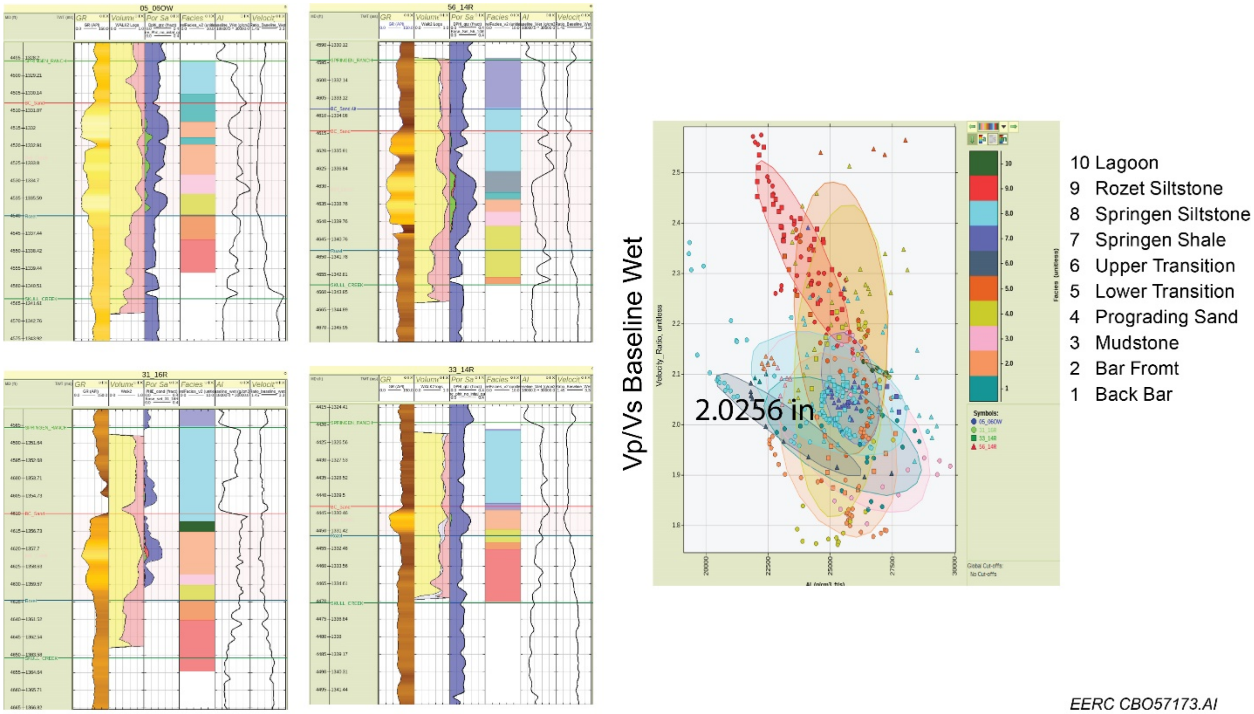

EERC CBO57173.AI

Figure 44. Geologic facies for the Muddy Formation from an interpreted model crossplotted in elastic space of velocity ratio (Vp/Vs) vs. AI. Logs from the four wells used in the facies plot are shown on the left. The wells clockwise from upper left are 56-14R, 05-06 OW, 33-14R, and 31-16R. The tracks for each plot from right to left are depth, GR, lithologic volume, porosity and saturation, geologic facies, acoustic impedance, and velocity ratio (Vp/Vs).

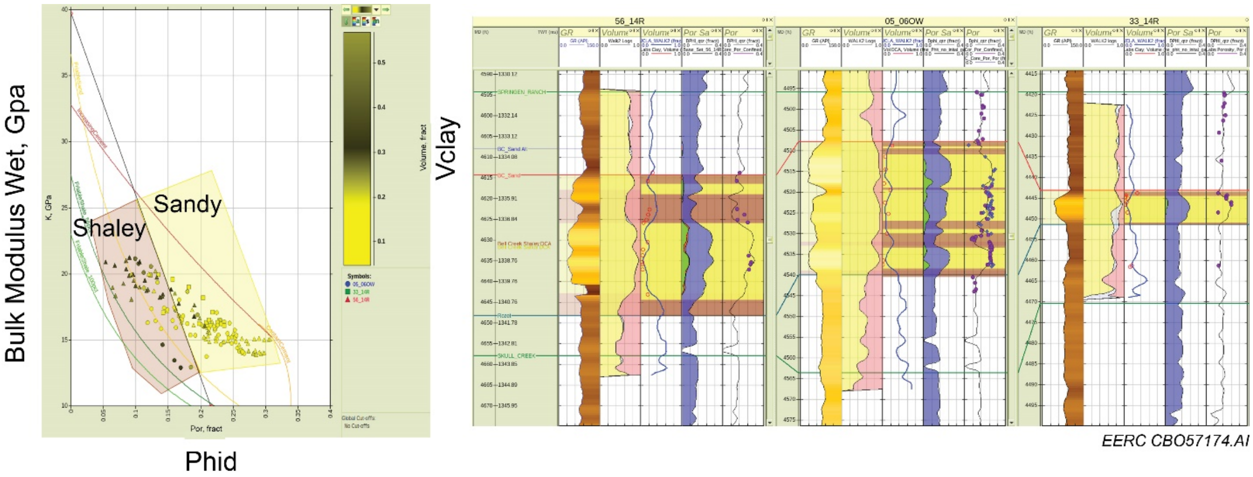

EERC CBO57174.AI

Figure 45. Sandy and shaley facies selected with polygons in bulk modulus vs. porosity space for the Bell Creek reservoir. Left panel: sandy and shaley polygons along with the line of separation. Right panel: alignment of the facies in the depth axis for the 56-14R, 05-06 OW, and 33-14R wells. Brown section: shaley facies, yellow section: sandy, circles: core data. Left to right log tracks: GR, volume (yellow: sand, pink: dry clay), dry weight fraction clay (Wcla) with volumes from XRD, density porosity (phid) with core porosity.

If the sample wet bulk modulus is greater than K_{eq}, then the facies is sandy otherwise it is shaley. The results at key wells are shown in Figure 46 and compared with geologic facies in Figure 47. The elastic reservoir facies are associated with the best geologic reservoir facies, and the remainder is associated with the nonreservoir facies. These facies were used for the Bell Creek rock physics modeling of pressure and fluid effects and in the Ji-Fi workflow.

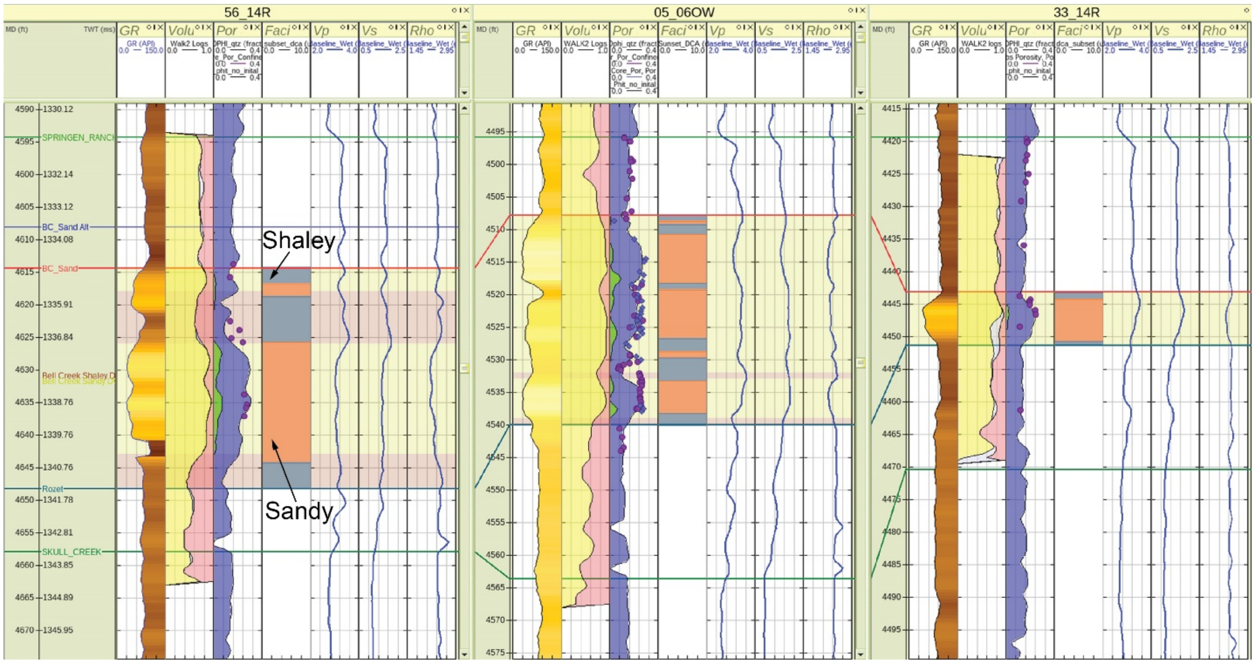

EERC CBO57175.AI

Figure 46. Sandy and shaley facies for the Bell Creek defined at 56-14R, 05-06 OW, and 33-14R wells. From left to right for each well the tracks are GR, dry lithology volumes with yellow and pink clay, facies where gray is shaley and orange is sandy, saturation relative to porosity, density porosity with discrete core porosity measurements, Vp wet (km/s), Vs wet (km/s), and density wet (g/cm^3).

Estimation of Seismic Wavelet: Well to Seismic Ties Using Full Stacks and Partial Stacks

Well to seismic data (full stacks and partial stacks) ties were performed to estimate the wavelets for the inversion. The 05-06 OW, 33-14R, 56-14R, 31-16R, and 33-09R wells were selected for this process as the original and predicted logs were adequate in the depths from Horizon 1 to the LBBC horizons, which were considered as the inversion model's limits. The effective wavelet length was between 80–128 ms, and the analysis window was approximately 400 ms. An initial bulk shift was made to maximize correlation over the analysis window with a statistical 180-degree phase rotation wavelet or with a group average Bayesian wavelet (simultaneous multiwell wavelet estimation method). Next, the Roy White method (White, 1997) was used on the selected wells and surrounding seismic data. After estimating the deterministic

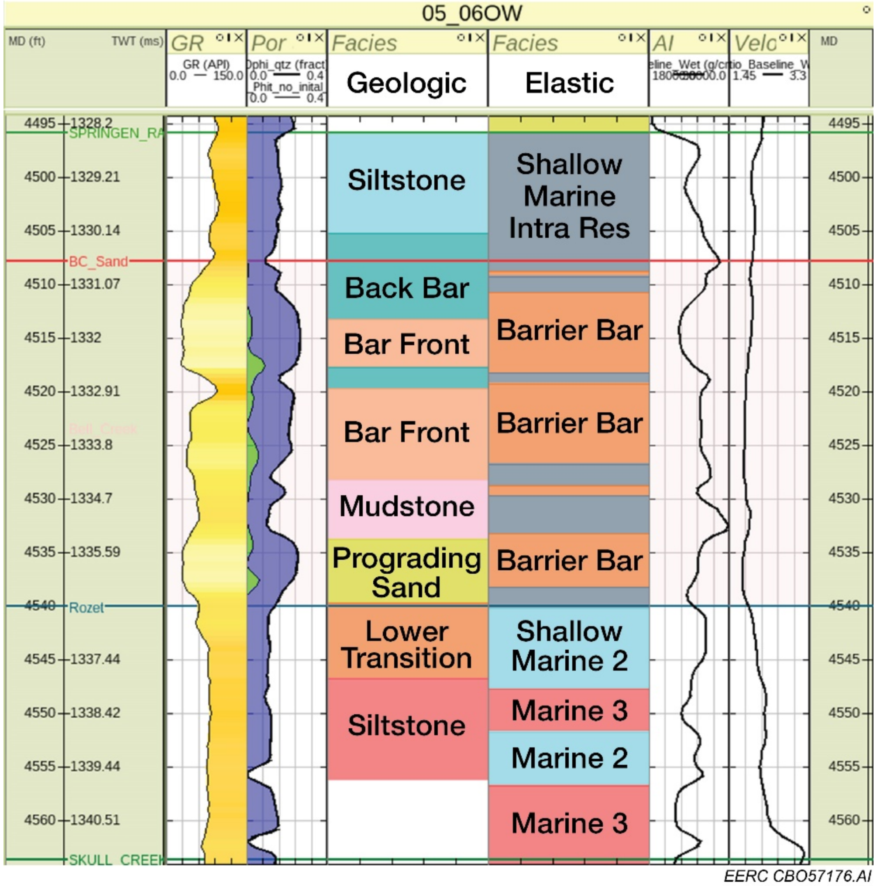

Figure 47. Comparison of geologic and elastic facies definitions in the 05-06 OW well. Tracks from left to right are GR, porosity and saturation, geologic facies, elastic facies, AI, and velocity ratio.

wavelets at each well, an average wavelet was created (see Figure 48) and used to make a final bulk shift at all the well locations. An example of the results obtained from the well to seismic tie at the 05-06 OW well using full-stack seismic data is shown in Figure 49. Notice the high cross-correlation and proportion of energy predicted (PEP) values and low phase error values on the seismic track (5–25 full stack). The other tracks in Figure 49 also demonstrate the quality of the tie at the reservoir level (Springen Ranch to Skull Creek markers). Similar results were obtained with the other seven wells (see Appendix F).

Comparable results to the well-to-full stack seismic data ties were obtained with partial stacks following the same methodology for full stacks mentioned above. However, in this case, one wavelet is estimated for each partial stack. While an averaged (Roy White) wavelet was estimated for the near angles, averaged Bayesian wavelets were estimated for the mid and far angles. The four wavelets are overlaid in Figure 50 to simplify the comparison. An example of the quality of the well to seismic tie obtained at the 05-06 OW well is shown in Figure 51. Notice the similarity between the synthetic and real seismic traces at the reservoir level. The high values of XCC (cross correlation), the PEP values, and low phase error confirm the high quality of the ties.

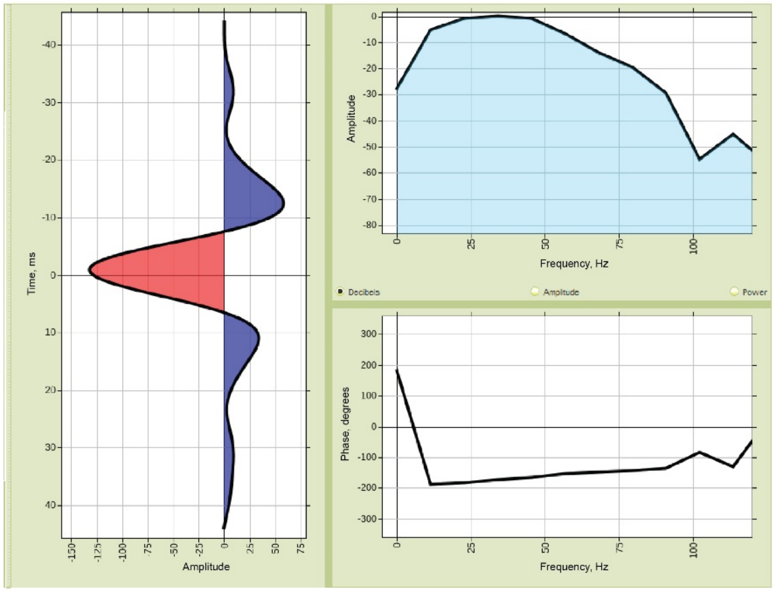

CBO56366.AI

Figure 48. Averaged Roy White wavelet and its amplitude and phase spectra for 05-06 OW, 33-14R, 56-14R, 31-16R, and 33-09R wells. Conditioning applied: tapered, smoothed, resampled to 1 ms for inversion, and trimmed to 89 samples.

Depth Trend Analysis for the Bell Creek Study Area

A DTA was performed to derive per facies relationships between Vp and depth and between Vp, Vs, and density (rho) using the facies derived from the eight wells considered in this project. The per facies background models and the rock physics relationships used in Ji-Fi are derived from the DTA relationships. An example of the DTAs used for the inversion of the Bell Creek data is shown in Figures 52 and 53. The colored circles represent the trends of each facies derived from well logs at an interval with the highest probabilities of finding specific facies. The colored crosses (the probability distribution or prior data) complement the rest of the background associated with a specific facies. Notice that in terms of input data for seismic inversion, one facies background model is the equivalent to a low-frequency model in standard model-based inversions.

Whereas Figure 52 shows the trends for the complete inversion interval using the Horizon 1 as a datum, Figure 53 shows only the facies associated to the reservoir and its lithological boundaries: Shell Creek, Shallow Marine intrareservoir, barrier bar with dead oil and water, barrier bar with oil, and barrier bar with CO_2. Ji-Fi inverts for the complete trend. However, the reservoir interval is the main inversion target.

The assessment of facies in the depth trends can be simplified when the facies are crossplotted. The trends in Figures 52 and 53 can be studied in crossplots of Vp vs. rho, Vp vs. Vs, AI vs. SI, and AI vs. Vp/Vs ratio with their respective probability distributions shown as ellipses for given standard deviations. Figure 54 depicts the AI vs. velocity ratio of the reservoir. The circles and the ellipses represent the distribution of the facies and their probability distribution

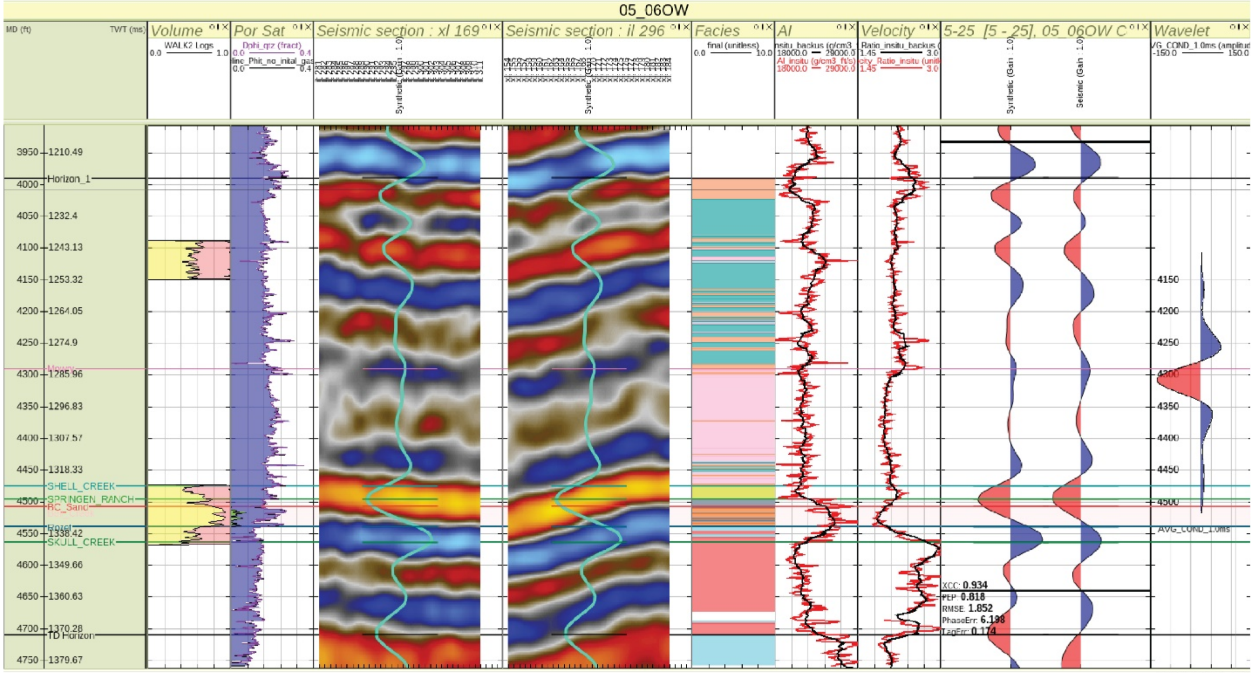

Figure 49. Example of 05-06 OW well to seismic tie. Volume: mineral log (mixing type: Voight–Reuss–Hill [weighting], quartz, kaolinite, and calcite); Por Sat: porosity–saturation (mineral: quartz; water = 1, oil = 0, gas = 0); seismic section: crossline (XL) 169; seismic section: inline (IL) 296; facies: estimated facies; AI: red line: well in situ AI; black line: seismic AI with Backus averaging; velocity: velocity ratio; red line: well velocity ratio; black line: seismic velocity ratio with Backus ratio; 5–25 (full stack from the 0–10, 10–20, and 20–30 partial angles): comparison of synthetic seismic trace (left) vs. real seismic trace (right). Wavelet: wavelet estimated from the well to seismic tie. Notice the parameters used to measure the quality of the tie on the Seismic Track 5–25: XCC, PEP, phase error, and tag error. The horizontal lines represent the markers associated with the main features of the logs: Horizon 1, Mowry, Shell Creek, Springen Ranch, Bell Creek Sand, Rozet, Skull Creek, and TD Horizon.

(one standard deviation), respectively. Note the separation in AI between the Shell Creek (yellow) and shallow marine intrareservoir facies (gray). The separation between the three litho-fluid facies, barrier bar with dead oil and water (dark green), barrier bar with oil (bright green) and barrier bar with CO_2 (red), is also evident from low AI and low velocity ratio to high AI and velocity ratio. This type of separation reflects not only the geological/petrophysical/fluid/seismic characteristics of the reservoir but also the quality of the initial facies estimation. In addition to high-quality input facies, a target zone and an estimation of the proportion of each facies in the target zone are fundamental for running Ji-Fi. The estimation of proportions can be derived from empirical observations generated from previous inversions or reservoir simulations.

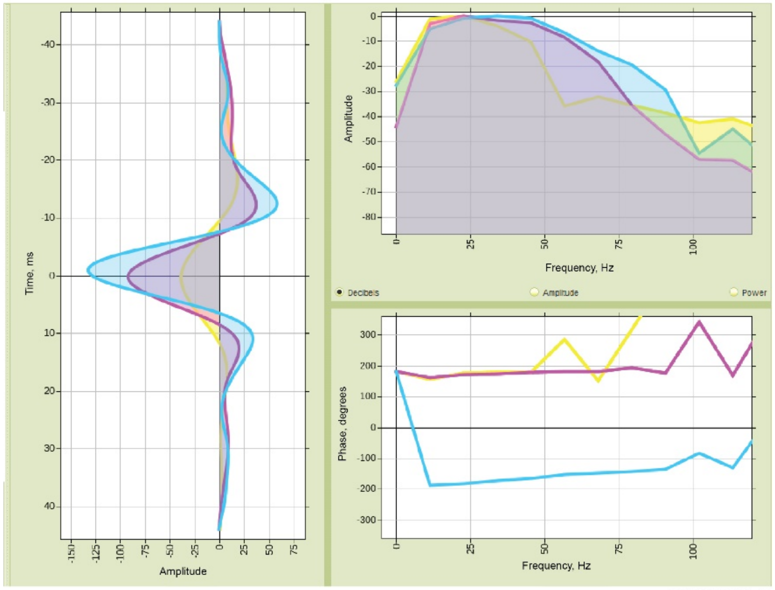

Figure 50. Wavelets estimated from the well to seismic tie using partial stacks; blue line: average conditioned wavelet for near partial stack (0–10 degrees), pink line: Bayesian wavelet for partial midstack (10–20 degrees), yellow line: Bayesian wavelet for partial far stack (20–30 degrees). Individual wavelets can be found in Appendix G.

Ji-Fi Application to Baseline and Monitor Seismic Surveys

When the Ji-Fi algorithm is applied to baseline and monitor seismic data sets, each survey is inverted separately. Therefore, the analysis of the time-lapse effect due to changes in fluid conditions in the reservoir is conducted with two sets of impedances and (most probable) facies. This analysis can be simplified when Ji-Fi is applied to arbitrary lines defined through specific areas of interest in the seismic cubes. Several arbitrary lines were defined as part of the work developed here. The arbitrary line presented here joins the 56-14R, 05-06 OW, 05-01, 04-04, and 33-09R wells (see Figure 28). Several time-lapse anomalies are observed along this line that were key to refining the Ji-Fi parameters and for the fast validation of results.

Figure 55 shows the most probable facies estimated by Ji-Fi for the arbitrary line of the baseline and monitor data sets and the in situ facies (no fluids) at the well locations. The inversion target zone includes the interval between the Horizon 1 (top of the target zone) and the LBBC horizon (bottom of target zone). Although the wells are not used as constraints in the Ji-Fi algorithm (as is the case with standard inversions), a good match is observed for the estimated Ji-Fi facies with the facies at wells outside of the reservoir. The comparison of in situ (no fluids) from the wells with the litho-fluid facies reflect the distribution the fluid facies in the in situ facies. The changes between the litho-fluid facies in the reservoir from baseline to monitor correctly predict the location of CO_2 and oil saturated with CO_2 in the profile. These changes are easily seen on the estimated litho-fluid facies derived from the 3-D Ji-Fi on a horizon at 6 ms from the top of the

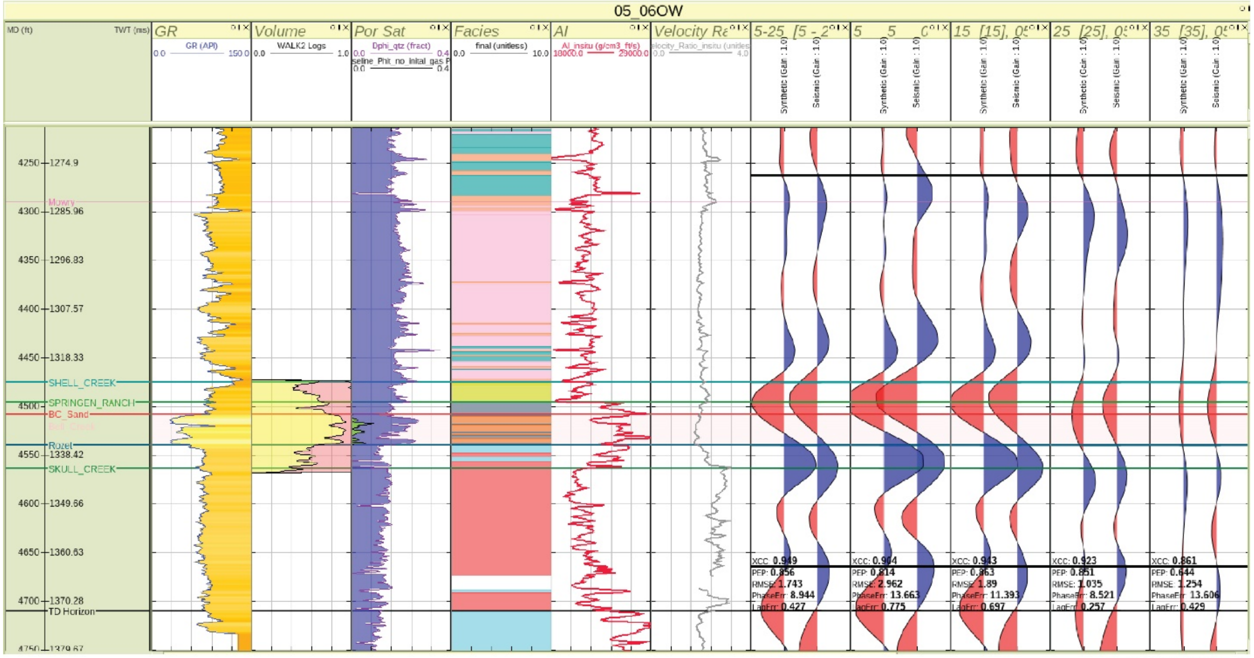

EERC CBO56375.AI

Figure 51. Well to seismic tie for 05-06 OW using full stack (0–30 degrees) and partial stacks (0–10, 10–20, 20–30 degrees). Left to right tracks: GR, volume: mineral log, Por Sat: porosity-saturation (mineral: quartz; water = 1, oil = 0, gas = 0), facies: estimated facies, AI: red line, velocity ratio, seismic: 5–25 (full-stack), 0–10 degrees, 10–20 degrees, and 20–30 degrees' partial angles), estimated wavelets are on top of each seismic track. Notice the parameters used to measure the quality of the tie on Seismic Track 5–25: XCC, the PEP, phase error, and tag error. The horizontal lines represent the markers associated with the main features of the logs: Horizon 1, Mowry, Shell Creek, Springen Ranch, Bell Creek Sand, Rozet, Skull Creek, and TD Horizon.

reservoir (Figure 56). The good performance of the Ji-Fi algorithm is also demonstrated in Figures 57 and 58. The estimated AI decrease is because of reservoir fluids changes in the monitor survey.

Several parameterizations of Ji-Fi were tested for the baseline and monitor (not shown here). Combinations of parameters generated some variations in the estimated facies and acoustic impedances. Eight Ji-Fi realizations were combined in a multirealization scheme to estimate the most probable facies and the probabilities of the barrier bar with different fluids. The most probable facies (without fluids) results from this methodology are shown in Figure 59. Notice the good match with the wells in the complete target zone that covers above, in the reservoir, and below the reservoir. Figures 60 to 63 show the results of the probabilities for the barrier bar without fluids, with fluids, for CO_2 and oil saturated with CO_2, oil saturated with CO_2, and free CO_2, respectively.

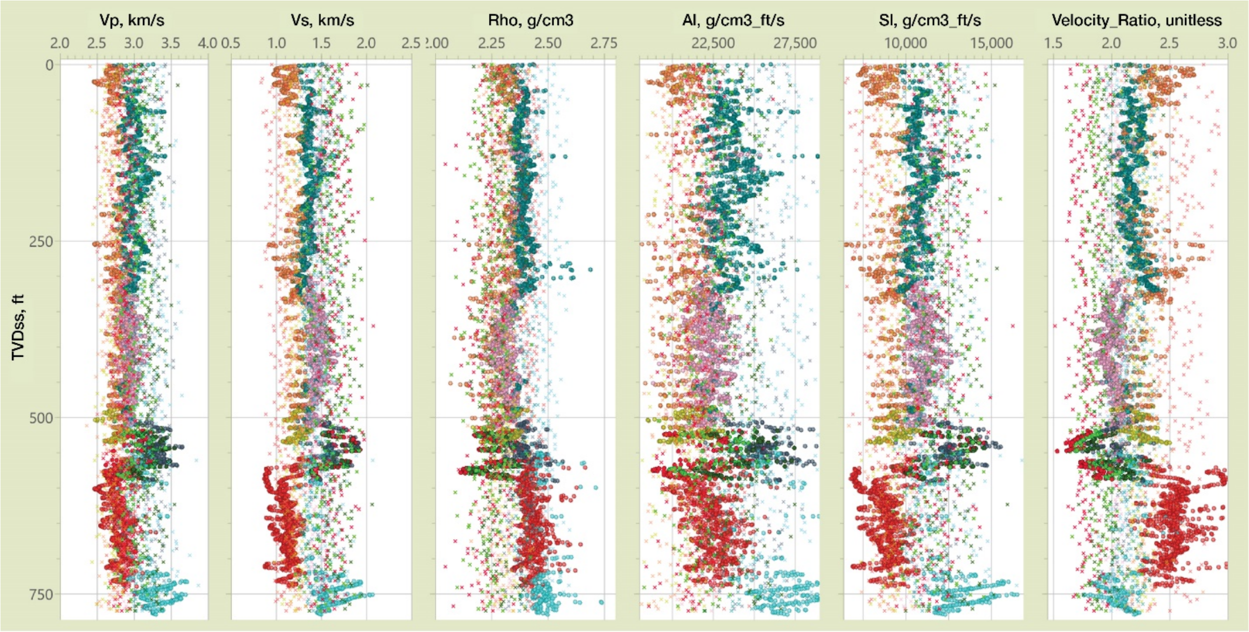

Figure 52. DTA, including fluid cases used in the Ji-Fi application to the Bell Creek seismic data. Horizon 1 is the reference datum (0 ft in the plot) of the trends. Left to right tracks: P-wave velocity (Vp), shear-wave velocity (Vs), density (rho), AI, SI, Vp/Vs ratio. Circles: the trend of specific facies at the highest probability interval; cross: prior data (probability distribution) of the specific trend covering the complete inversion interval. The colors of the symbols represent the facies (see Table 6).

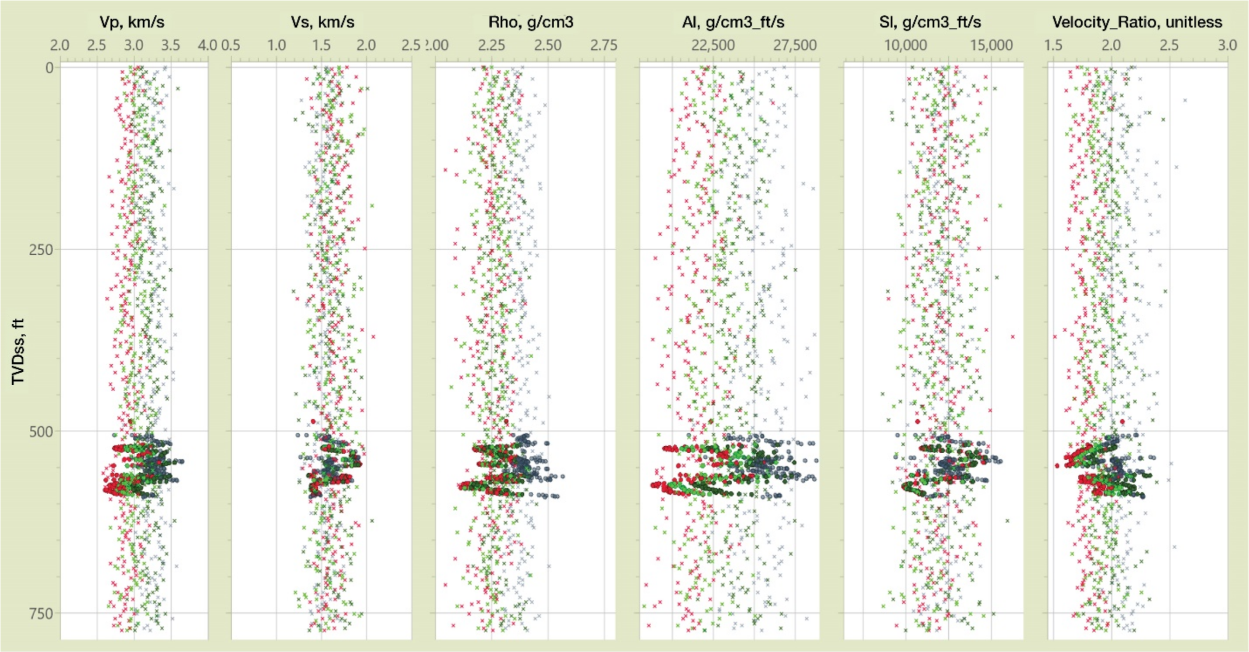

EERC CBO57179.AI

Figure 53. DTA, including only the facies associated with the reservoir: shallow marine intrareservoir (gray), barrier bar with dead oil and water (dark green), barrier bar with oil (bright green), and barrier bar with CO_2 (red). Horizon 1 is the reference datum (0 ft in the plot) of the trends. Left to right tracks: P-wave velocity (Vp), shear-wave velocity (Vs), density (rho), AI, SI, and Vp/Vs ratio. Circles: trend of specific facies at the highest probability interval; cross: prior data (probability distribution) of the specific trend covering the complete inversion interval. The color of the symbols represents the facies (see Table 6).

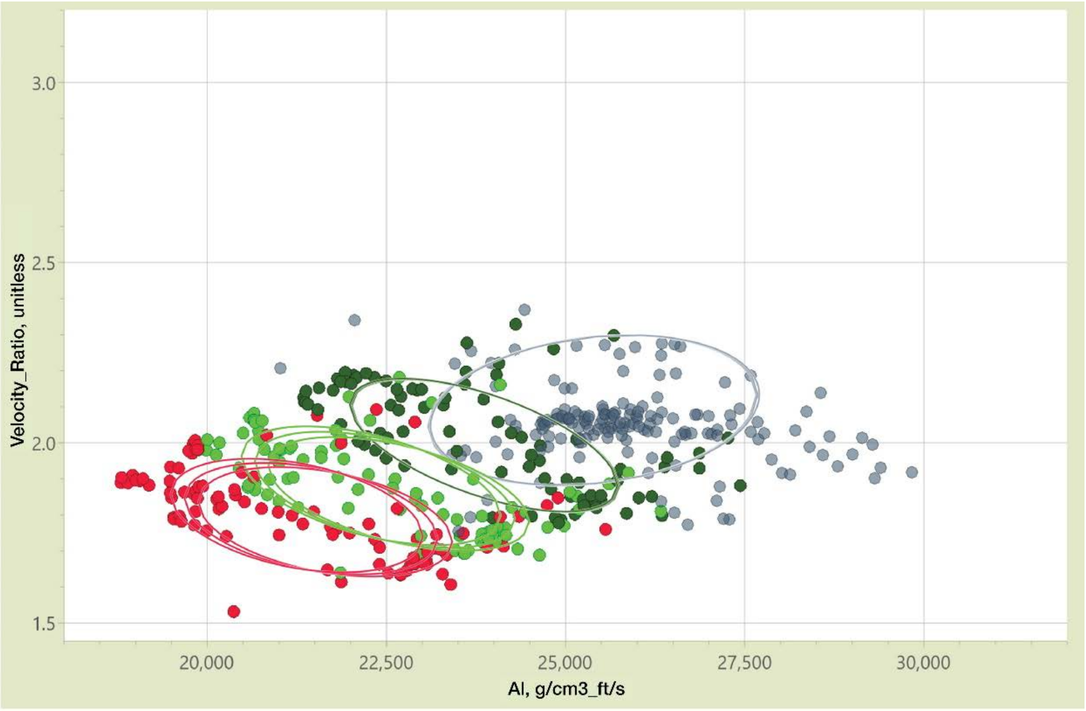

EERC CBO57180.AI

Figure 54. AI vs. velocity ratio crossplot of the DTA shown in Figure 19. Circles: individual facies; ellipses: one standard deviation of prior data (probability distribution). Facies: Shell Creek (yellow); shallow marine intrareservoir (gray), barrier bar with dead oil and water (dark green), barrier bar with oil (bright green), and barrier bar with CO_2 (red).

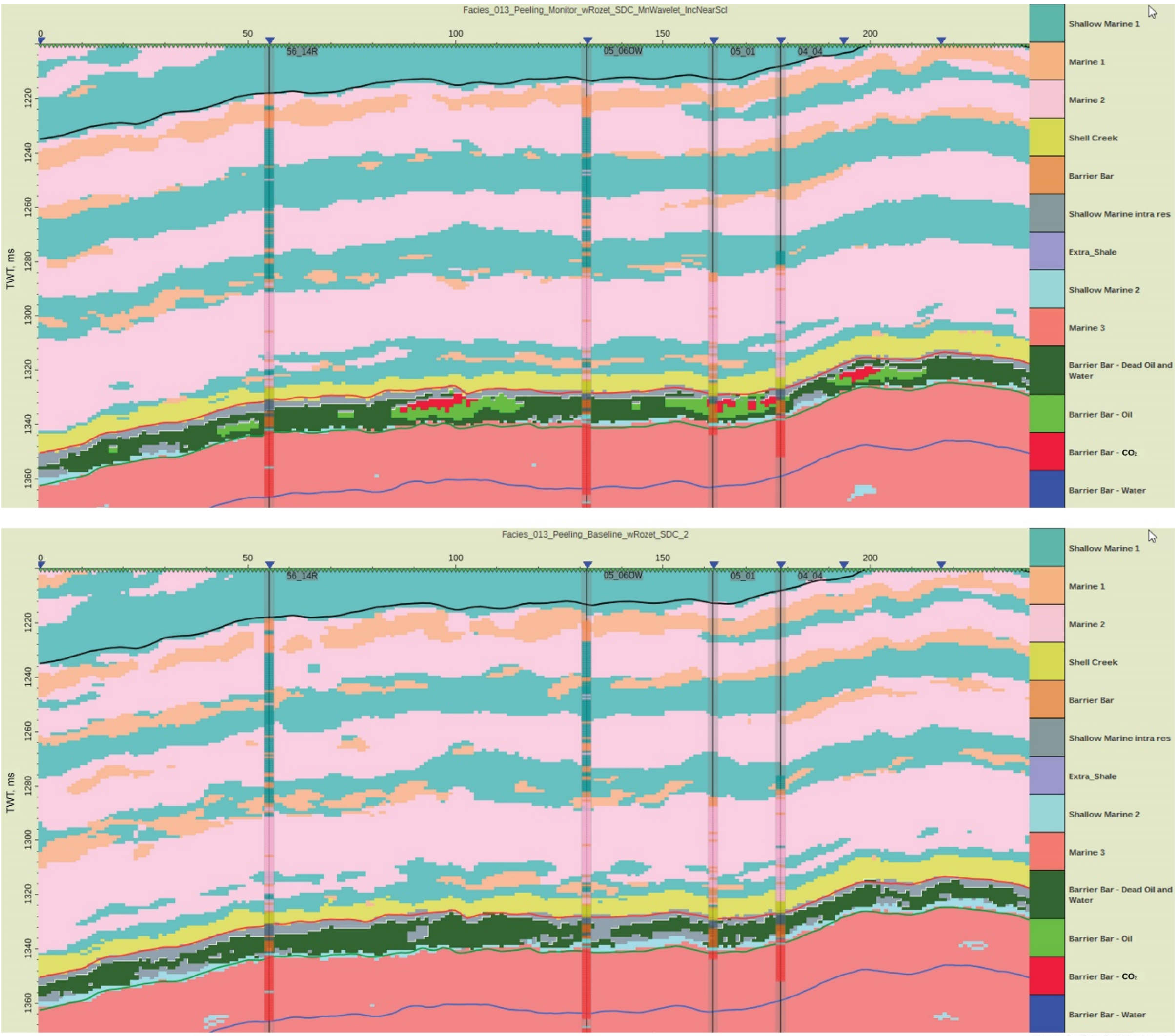

EERC CBO57181.AI

Figure 55. Most probable facies estimated by the Ji-Fi algorithm along the arbitrary line for the baseline (top) and monitor (bottom) seismic data sets. The 56-14R, 05-06 OW, 05-01, 04-04, and 33-09R wells (from left to right) show the estimated in situ facies (no fluids). The seismic inversion shows the results using litho-fluid facies at the reservoir as input.

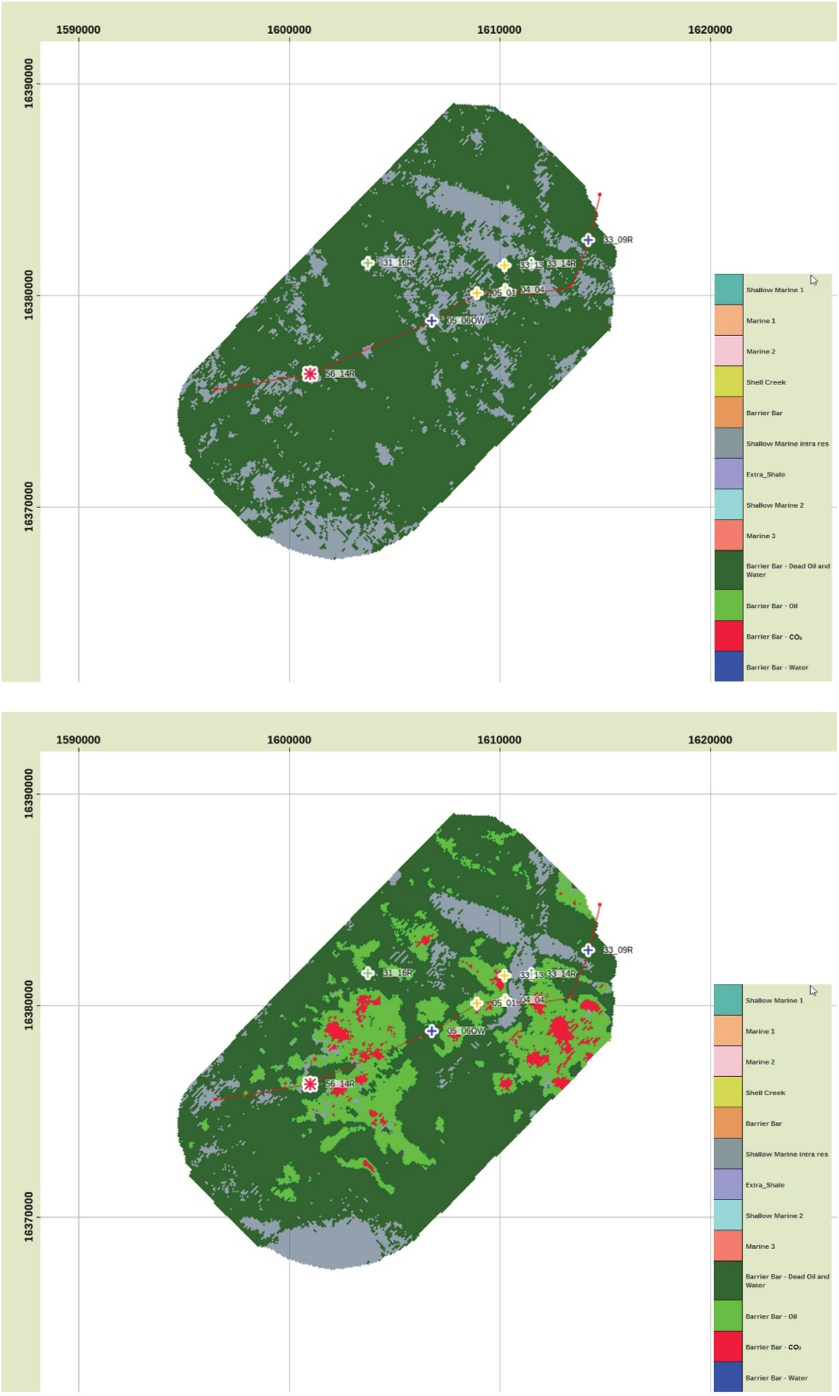

EERC CBO57182.AI

Figure 56. Horizon of the most probable facies estimated by the Ji-Fi algorithm at the reservoir level (6 ms down from the top of the reservoir) for the baseline (top) and monitor (bottom) seismic data sets. The red line joining the 56-14R, 05-06 OW, 05-01, 04-04, and 33-09R wells (from left to right) is the arbitrary line analyzed in this report.

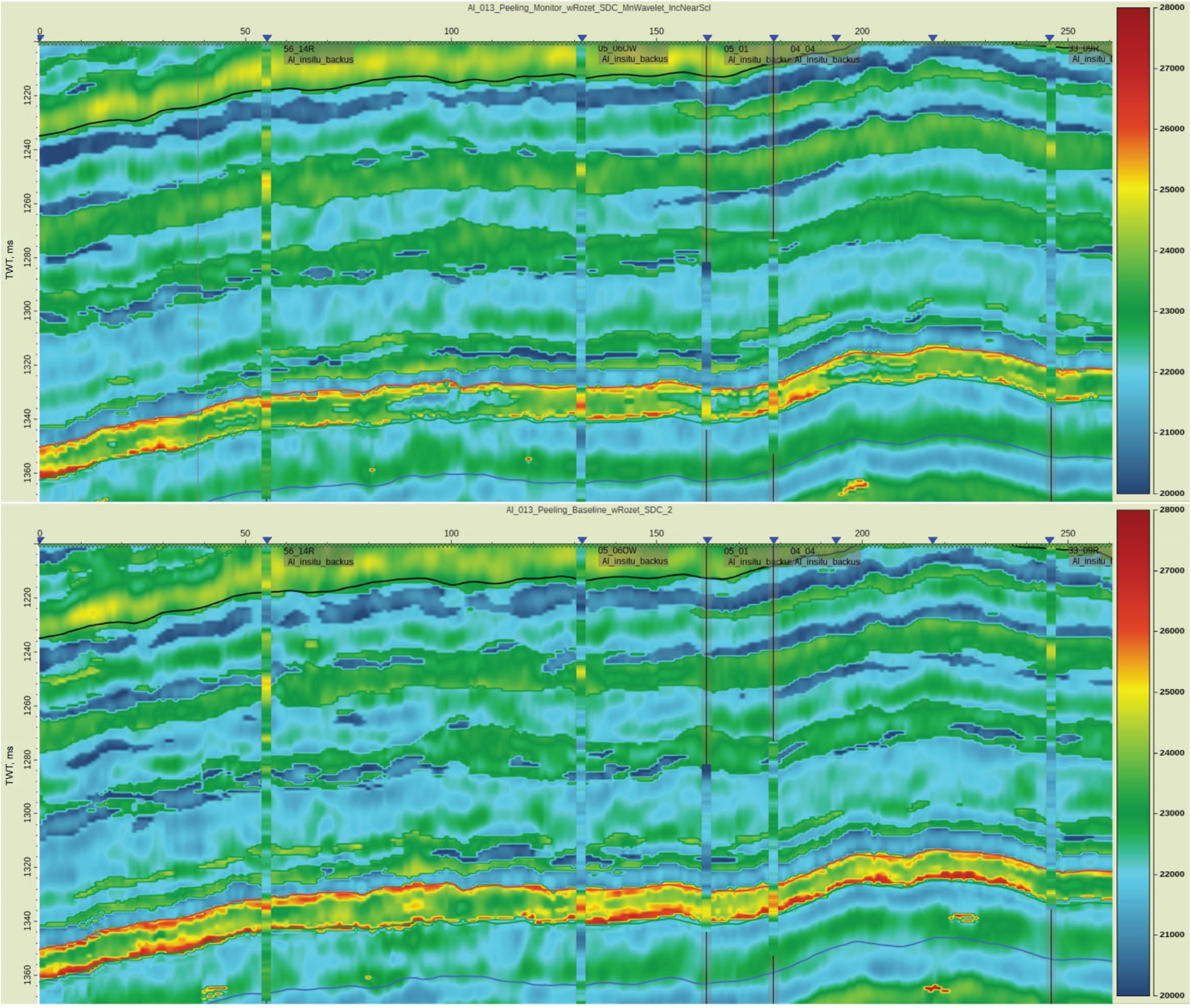

EERC CBO57183.AI

Figure 57. AIs estimated by the Ji-Fi algorithm along the arbitrary line for the baseline (top) and monitor (bottom) seismic data sets. The 56-14R, 05-06 OW, 05-01, 04-04, and 33-09R wells (from left to right) show the estimated in situ AIs (no fluids). The seismic inversion used litho-fluid facies at the reservoir as input.

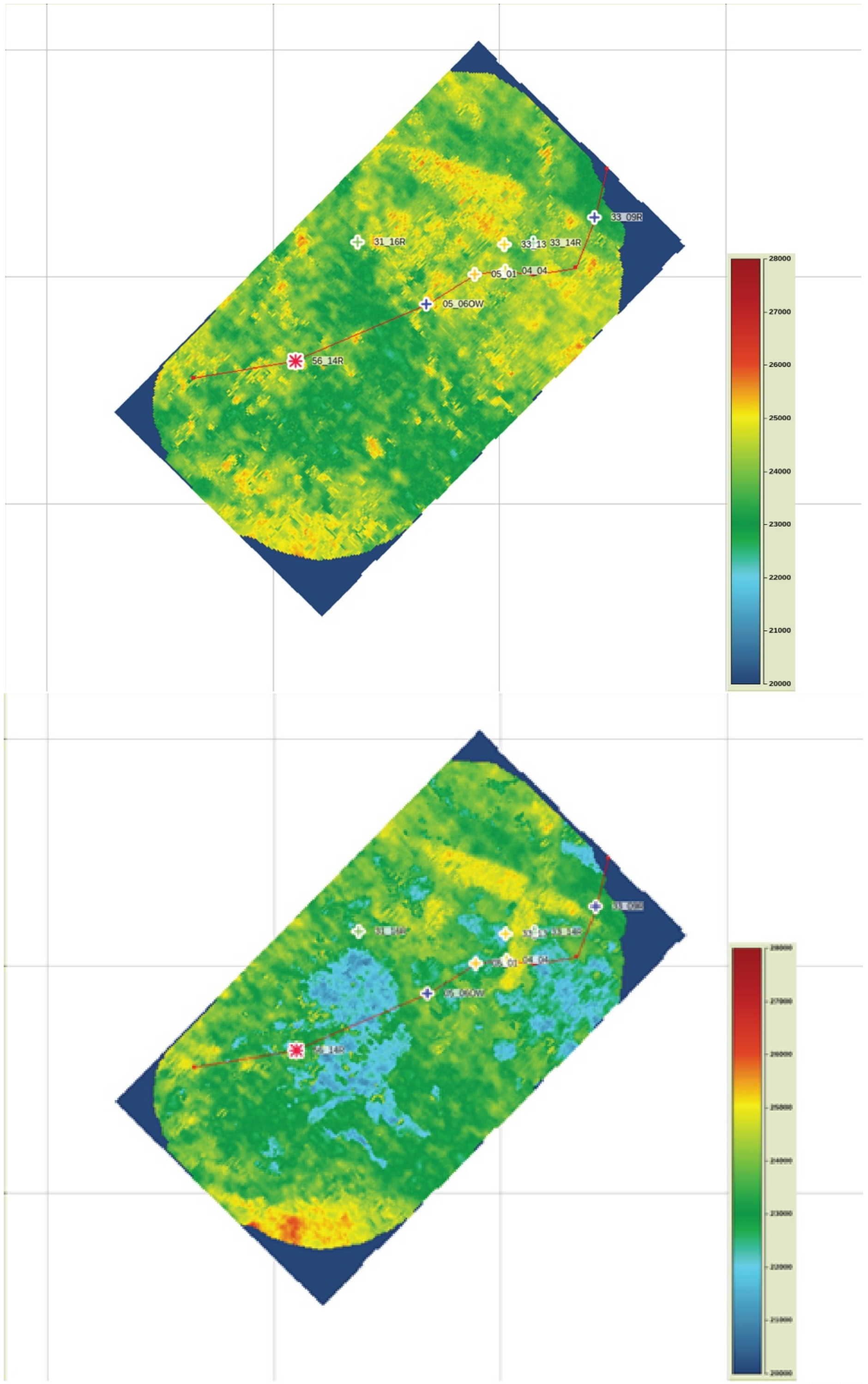

EERC CBO57183.AI

Figure 58. Horizon of the AI estimated by the Ji-Fi algorithm at the reservoir level (6 ms down from the reservoir) for the baseline (top) and monitor (bottom) seismic data sets. The red line joining the 56-14R, 05-06 OW, 05-01, 04-04, and 33-09R wells (from left to right) is the arbitrary line analyzed in this report.

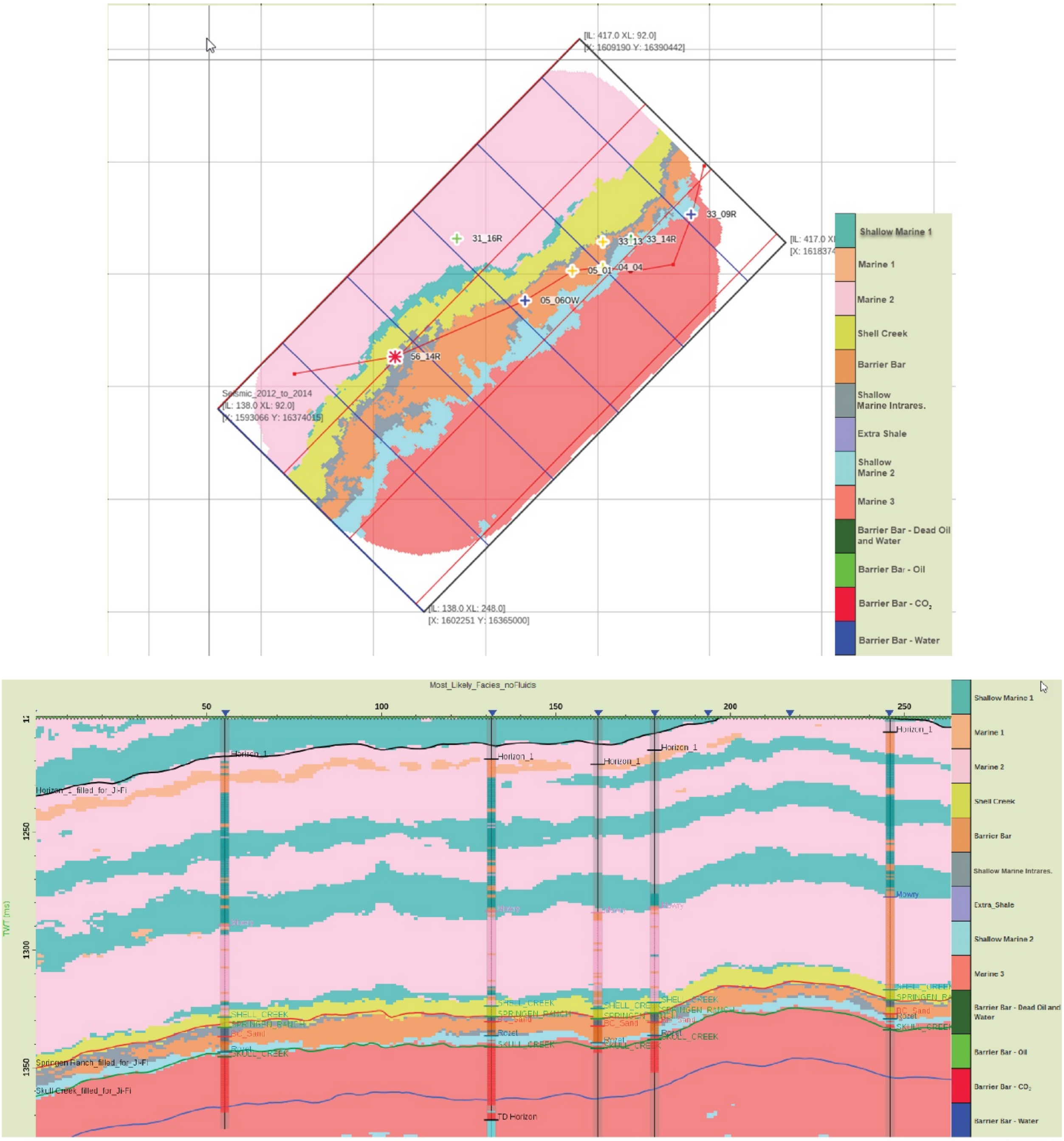

EERC CBO56384.AI

Figure 59. Time slice at 1332 ms (top) and profile (bottom) of most likely facies (no fluids) from a multirealization approach that combines eight Ji-Fi runs. The time slice is at the Bell Creek reservoir level. The red line on the map joining the 56-14R, 05-06 OW, 05-01, 04-04, and 33-09R wells (from left to right) is the arbitrary line shown in the bottom. The wells show the estimated in situ facies (no fluids).

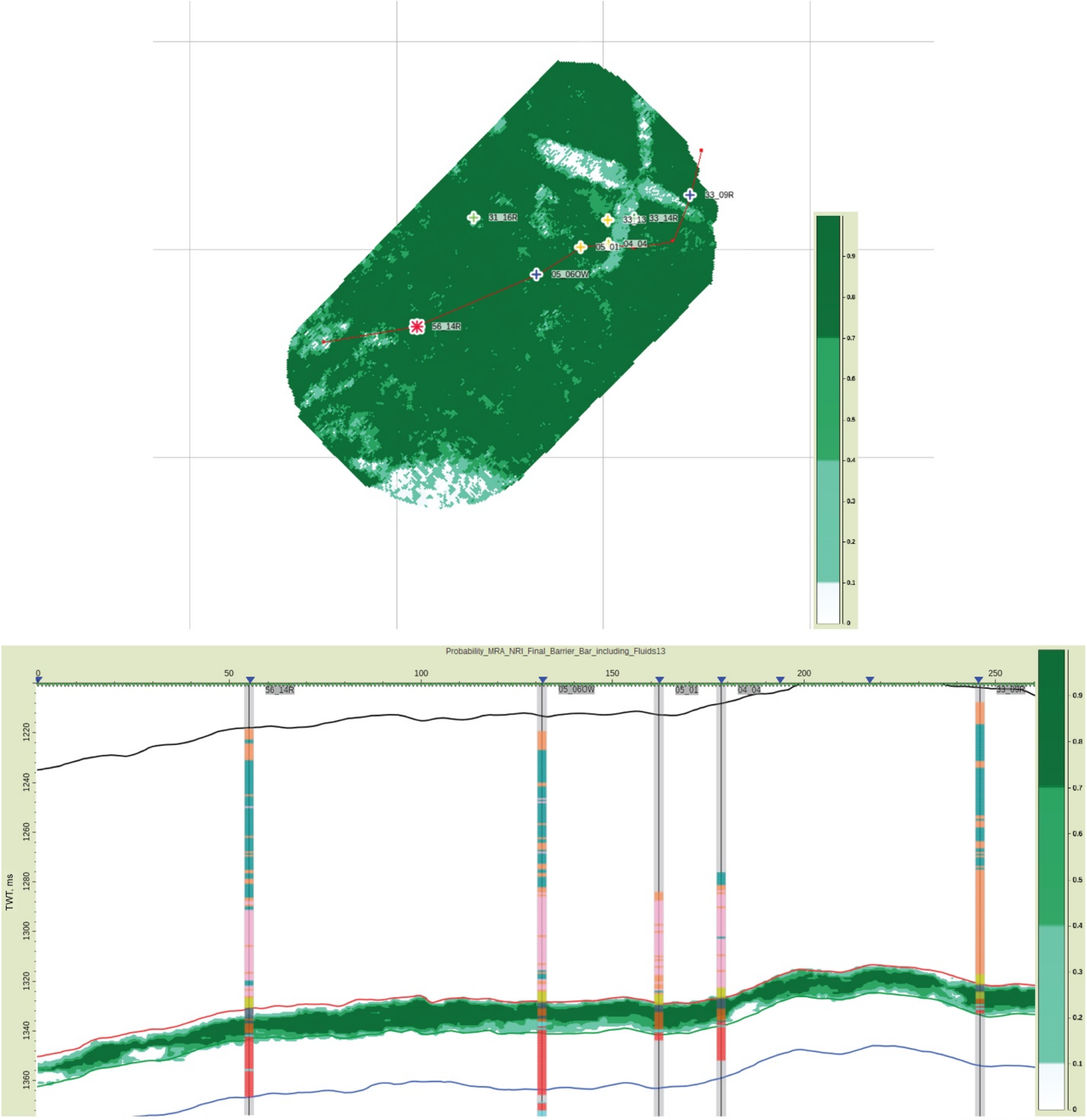

EERC CBO57184.AI

Figure 60. Horizon at 6 ms down from the top of the reservoir (top) and profile (bottom) of estimated probabilities for barrier bar with fluids using a multirealization approach that combines eight Ji-Fi runs. The 56-14R, 05-06 OW, 05-01, 04-04, and 33-09R wells (from left to right) show the estimated in situ facies (no fluids).

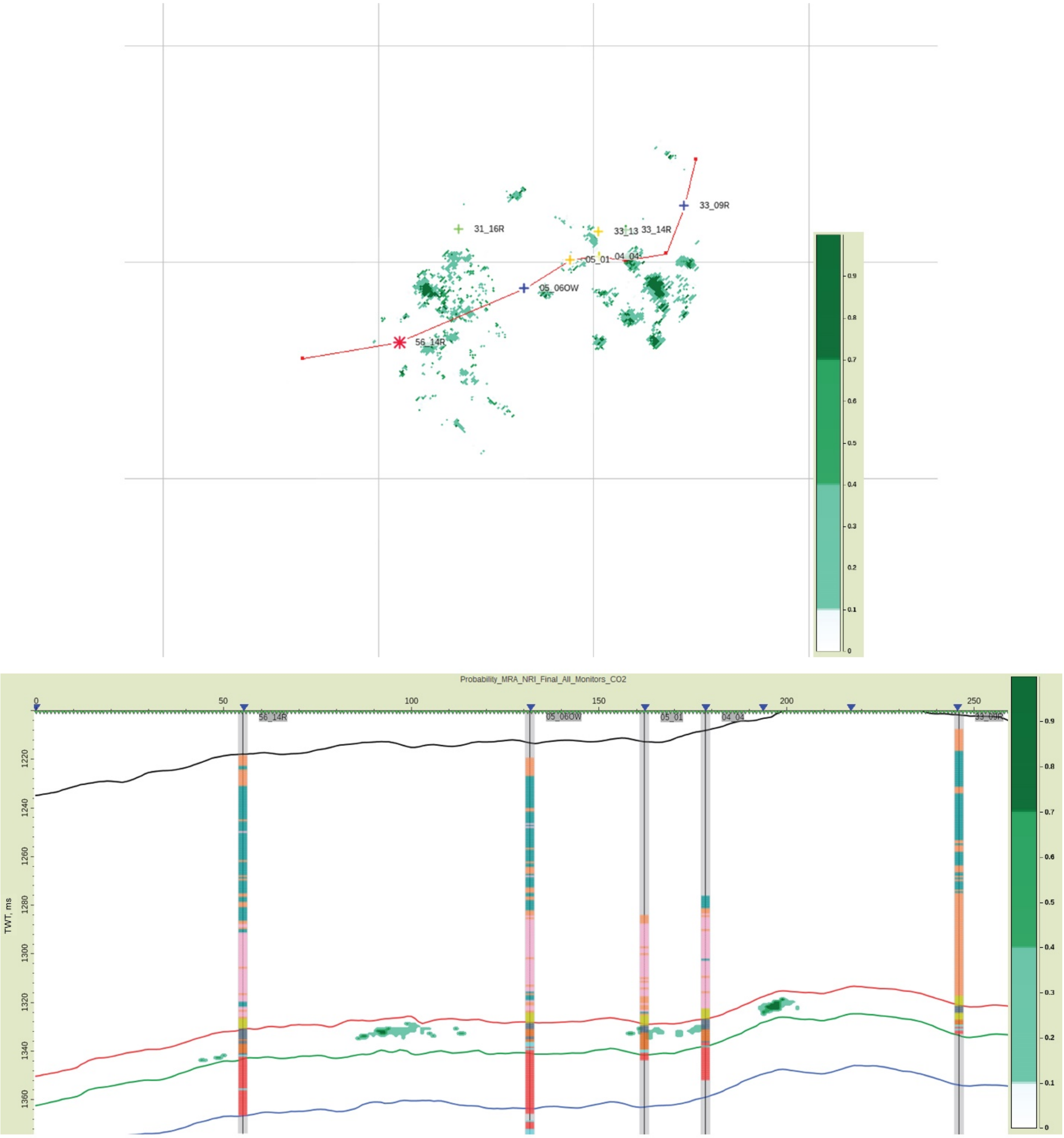

EERC CBO57185.AI

Figure 61. Horizon at 6 ms down from the top of the reservoir (top) and profile (bottom) of estimated probabilities for CO_2 using a multirealization approach that combines eight Ji-Fi runs. The 56-14R, 05-06 OW, 05-01, 04-04, and 33-09R wells (from left to right) show the estimated in situ facies (no fluids).

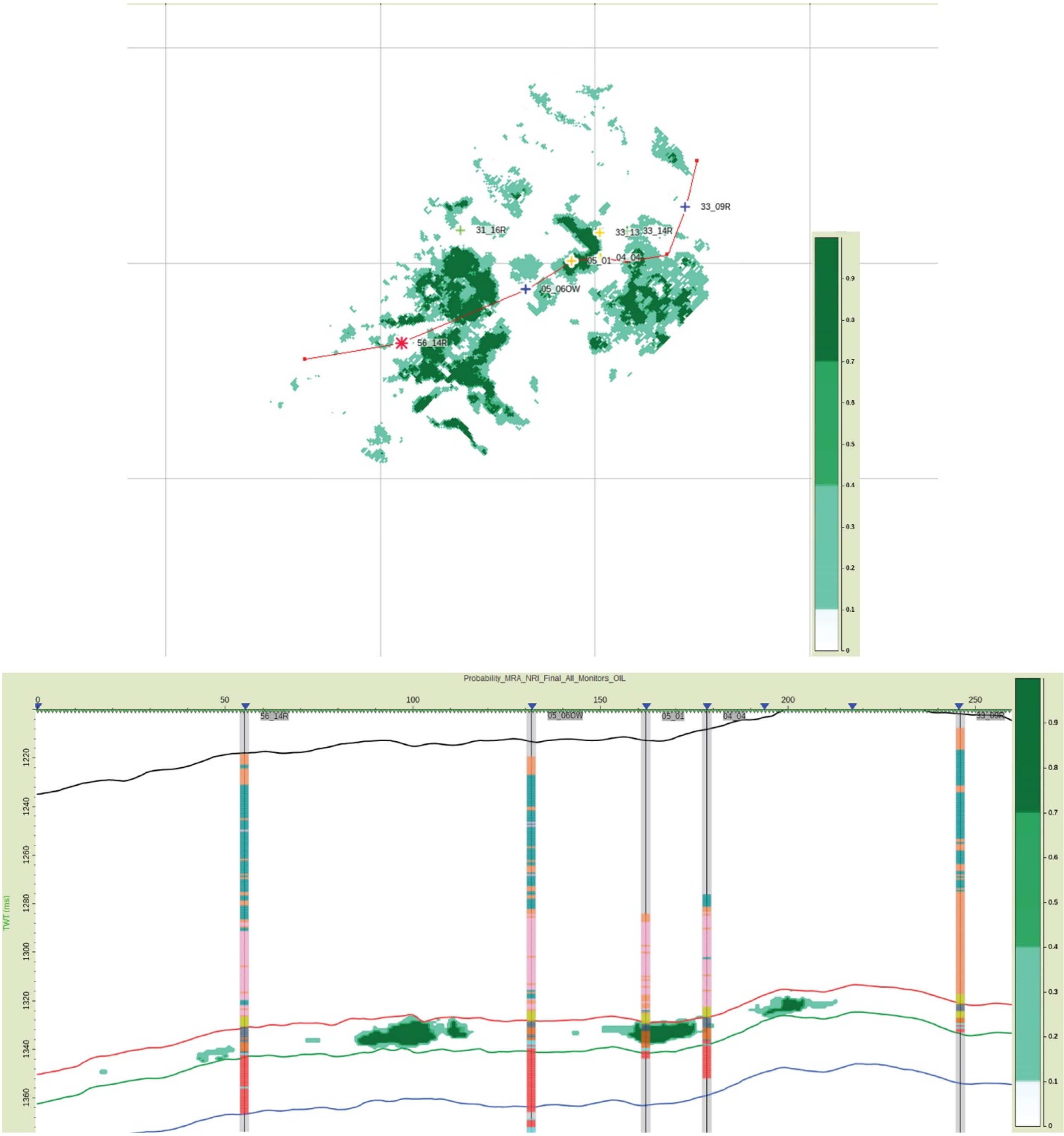

EERC CBO57186.AI

Figure 62. Horizon at 6 ms down from the top of the reservoir (top) and profile (bottom) of estimated probabilities for oil saturated with CO_2 using a multirealization approach that combines eight Ji-Fi runs. The 56-14R, 05-06 OW, 05-01, 04-04, and 33-09R wells (from left to right) show the estimated in situ facies (no fluids).

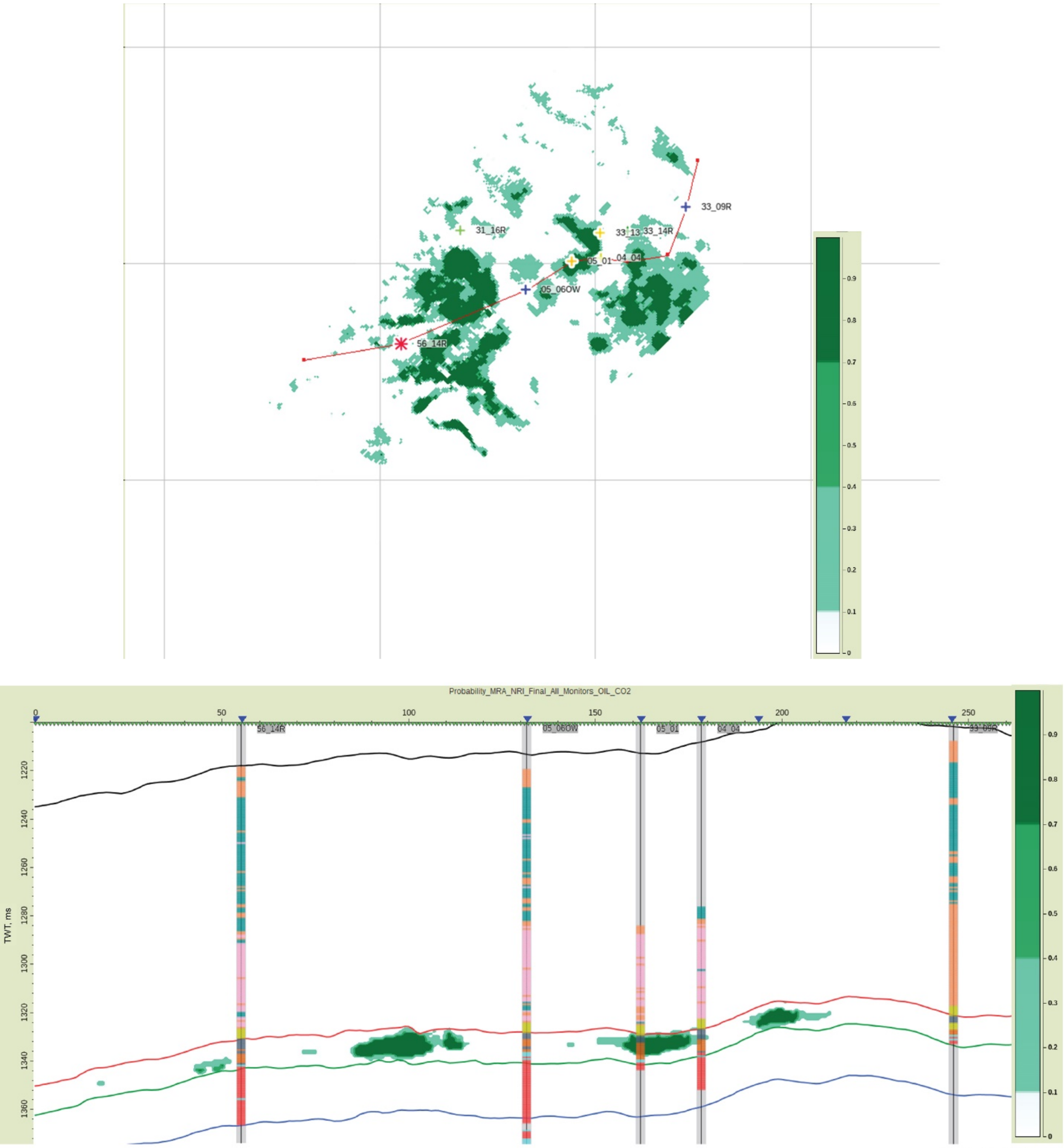

EERC CBO57187.AI

Figure 63. Horizon at 6 ms down from the top of the reservoir (top) and profile (bottom) of estimated probabilities for free CO_2 using a multirealization approach that combines eight Ji-Fi runs. The 56-14R, 05-06 OW, 05-01, 04-04, and 33-09R wells (from left to right) show the estimated in situ facies (no fluids).

INTEGRATION AND VALIDATION

4-D seismic data add spatial constraints to the simulation model in addition to the production and injection historical data. As a result, the simulation model has a better description of the reservoir and provides more reliable forecasts of the reservoir performance when the model is constrained with both spatially distributed seismic responses and dynamic flow response (Suman, 2009). The goal of this section is to integrate the inverted seismic parameters (obtained from the WEB-AVO and Ji-Fi methods) into the simulation model and then validate the parameters with field data as shown in Figure 64. The first part of this section is focused on seismic results integration, which describes the existing reservoir simulation model of the studied area and how to integrate the inverted seismic reservoir parameters into the model. The second part is seismic results validation, which provides an analysis of fluid flow mechanisms in the reservoir, simulation model update, and comparison of results with field data.

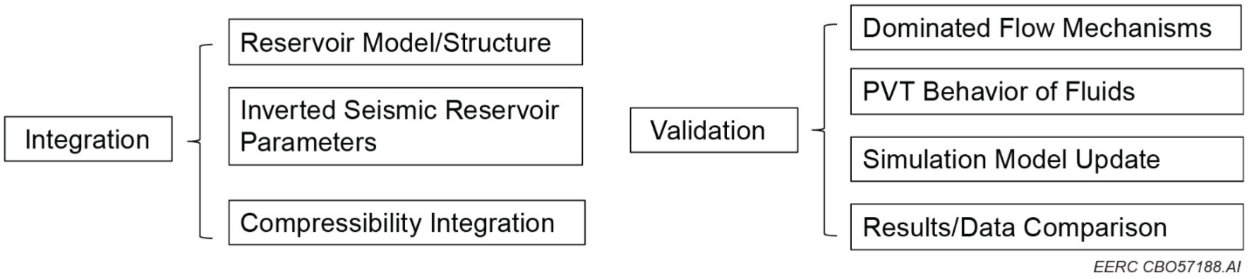

Figure 64. Structure of seismic data integration (left) and validation (right) using reservoir simulation and actual field data.

Seismic Data Integration

Because of the uncertainties in subsurface formations, geologic and reservoir simulation models can always be improved by a better reservoir characterization when more data become available in the reservoir development processes. The Bell Creek Field studied in this project is an excellent example of continuous reservoir characterization updating with data acquired from PNLs, additional well drilling, and fluid sampling and analysis, etc. The field has already been developed by pressure depletion and waterflooding operations. Currently, tertiary oil recovery with CO_2 flooding is ongoing in the field. Therefore, large amounts of data on fluid production and injection are available. A variety of seismic activities including 4-D seismic surveys have also been conducted in the field to better understand the reservoir dynamics and monitor the distribution of CO_2 and pressure plumes in the reservoir. The seismic data sets considered in this study correspond to the surveys acquired in September 2012 (baseline) and October 2014 (monitor) (see Figure 4).

Reservoir Model Description

The Muddy Formation is the main oil pay zone within the Bell Creek Field, where the formation is dominated by high-porosity, high-permeability sandstones with a stratigraphic trapping mechanism. The reservoir structure dips from east–southeast to west–northwest at about 100 feet/mile (~1°), with a complex of deltaic and nearshore-deposited sands which pinch-out into shale facies serving as a trap (Burt and others, 1975; Saini and others, 2012; Bosshart and others, 2015). The vertical heterogeneity of the reservoir sands is clearly illustrated in Figure 65; there are three sand layers in a 30-ft interval.

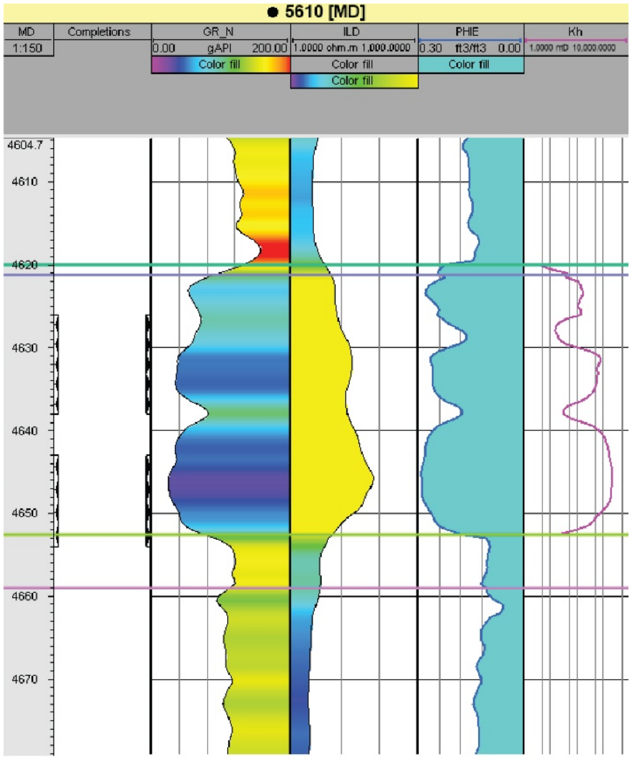

EERC CBO57189.AI

Figure 65. Well logs from a producer in the Phase 1 area, showing the vertical heterogeneity in the reservoir.

Several versions of static geologic models have been developed to characterize the reservoir structure. Based on the previous simulation efforts, the Version 2 (V2) geologic model covering a 200-square-mile area centered on Phase 1 serves as the base geologic model to develop the dynamic simulation model used in this study (Braunberger and others, 2013; Liu and others, 2014; Bosshart and others, 2015). Figure 66 shows a reservoir simulation model used in this study. The simulation model was cut from the V2 geologic model and covers Phases 1–2 and their surrounding areas with dimensions of 259 × 158 × 21 cells (859,362 cells in total). There are 102 wells in the model, including 53 producers and 59 injectors. As shown in the figure, an aquifer attaches to the west boundary of the Phase 1 area where the evidence of water encroachment from the aquifer to production wells is clear based on the water cut behavior of wells close to the aquifer–Phase 1 boundary (Bosshart and others, 2015). Important reservoir properties such as porosity and permeability are distributed in a wide range across the reservoir as demonstrated in Figure 67. The majority of the porosity and permeability values distribute in ranges of 0.1–0.3 and 1–2500 mD, respectively.

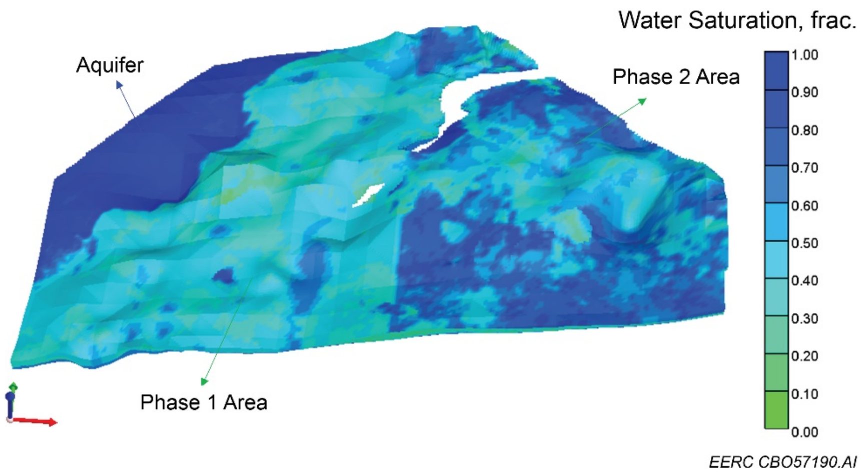

Figure 66. Water saturation distribution in Phases 1–2 and their surrounding areas.

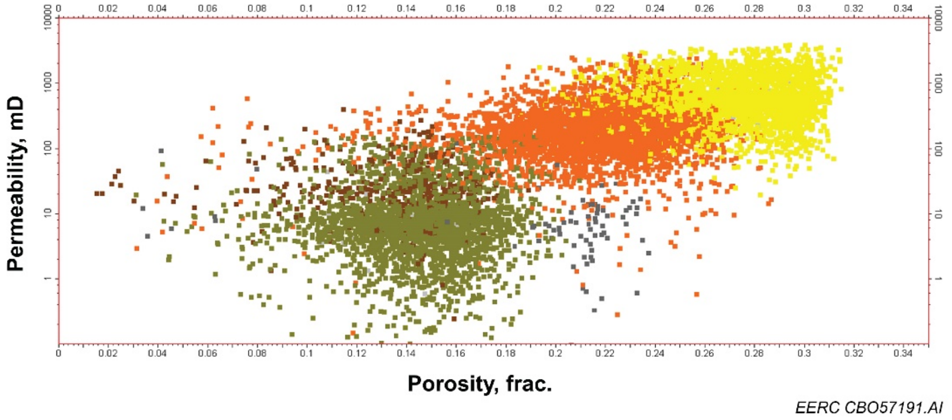

Figure 67. Distribution of porosity and permeability in the reservoir.

Inverted Seismic Reservoir Parameters

The change of seismic amplitudes associated with the CO_2 injection acting as a fluid tracer can capture the heterogeneity of the Bell Creek reservoir very well (Salako and others, 2017). The inversion of seismic amplitudes can provide more details of the interaction between CO_2 injection and the geology of the reservoir. Two seismic joint inversion methods were applied to the 2012 and 2014 time-lapse seismic datasets from the Bell Creek Field. The first method, the WEB-AVO, provides information about the reservoir in terms of compressibility (1/bulk modulus) and shear compliance (1/shear modulus) from the solution of the full elastic wave equation. These parameters can deliver a more detailed spatial description of the complex interaction between the reservoir's sedimentary conditions and the physical/chemical processes related to changes in water saturation, CO_2 saturation, and pressure. The second method, the Ji-Fi, estimates the probability of the presence of particular facies in the reservoir, which guides the estimation of rock and fluid property distributions. The Ji-Fi litho-fluid facies can also deliver detailed information about the saturation and pressure changes in the reservoir because of CO_2 injection. Furthermore, probabilities of the litho-fluid facies distribution estimated by Ji-Fi can reduce uncertainty in forecasting CO_2 saturation changes within the target reservoir.

One of the advantages of formulating the wave equation to solve the WEB-AVO inversion is to directly derive rock compressibility (κ), which is highly sensitive to the time-lapse saturation changes in the reservoir because of CO_2 injection (Figure 68). This parameter can be conditioned for integration into the reservoir simulation workflow.

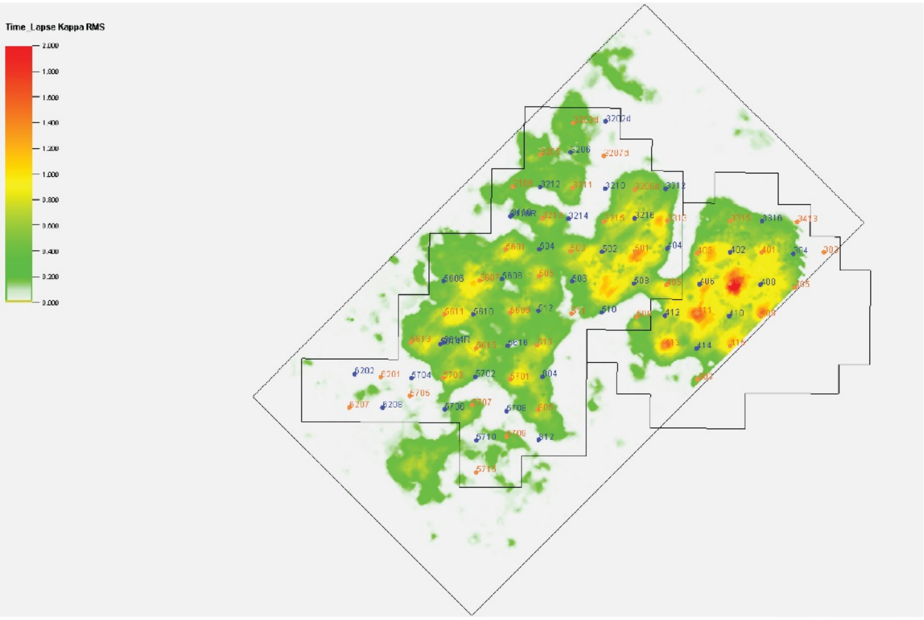

EERC CBO57192.AI

Figure 68. The time-lapse difference in compressibility (kappa). The RMS values of kappa are calculated from the Springen Ranch to Skull Creek horizons using a grid size of 82.5 × 82.5 ft.

Integration of Rock Compressibility

As an inherent property of a reservoir, pore compressibility is defined as a measure of the change in pore volume with a change in pressure at constant temperature as shown in the following equation (Baker and others, 2015):

$$C_p = \frac{1}{V_p}\frac{dV_p}{dp} \qquad \text{[Eq. 2]}$$

Where C_p is the pore compressibility, *1/psi*; V_p is the pore volume, ft^3; and p is the pressure, *psi*. Since the pore volume is a function of porosity and bulk rock volume as shown below:

$$V_p = \emptyset V_b \qquad \text{[Eq. 3]}$$

Where ϕ is the porosity, *fraction*; V_b is the bulk rock volume, ft^3. Therefore, Equation Eq. can be rearranged as follows:

$$C_p = \frac{1}{V_b}\frac{dV_b}{dp} + \frac{1}{\emptyset}\frac{d\emptyset}{dp} \qquad \text{[Eq. 4]}$$

The rock bulk volume includes rock matrix volume constituted with solid grains and pore volume filled with reservoir fluids. Compared to the change of pore volume change with pressure, the change of bulk volume with pressure is an order of magnitude smaller, so the pore compressibility is often estimated based on the porosity of a rock. Several correlations developed from experimental and field data sets are available to calculate the pore compressibility of sandstones (Hall, 1953; Horne, 1995):

$$C_p = (1.87\emptyset^{-0.415}) \times 10^{-6} \qquad \text{[Eq. 5]}$$

$$C_p = \exp\,(5.118 - 36.26\emptyset + 63.98\emptyset^2) \times 10^{-6} \qquad \text{[Eq. 6]}$$

Equation 5 is referred as Hall's correlation, which is one of the most frequently used correlations to calculate pore compressibility of sandstones using porosity. The correlation was developed by Hall based on laboratory measurements (Hall, 1953). Hall's correlation is considered reasonable for normally pressured sandstones. However, the correlation tends to underpredict pore compressibility under high-pressure conditions (Fekete, 2019). Equation 6 was also a frequently used correlation which was developed for consolidated sandstones (Horne, 1995). This correlation covers a wider range of pressure conditions compared to Hall's correlation. Figure 69 shows a comparison of the pore compressibility calculated by the two correlations.

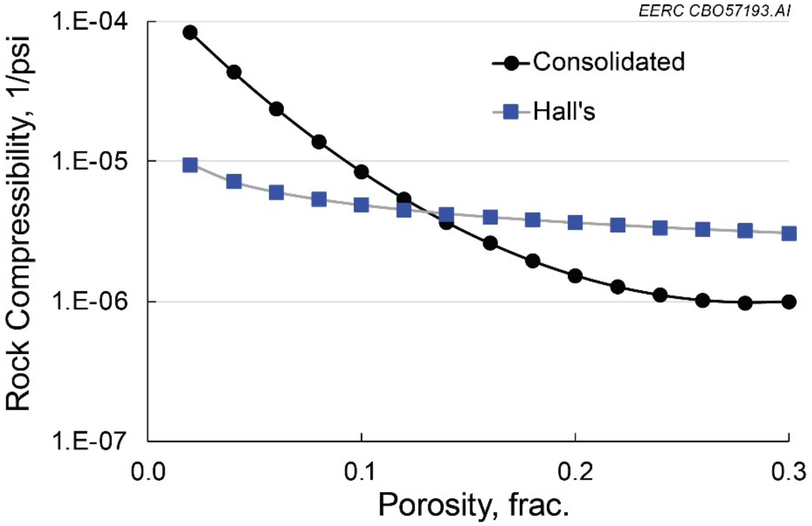

Figure 69. Comparison of pore compressibility calculated by different correlations.

Although pore compressibility is a required variable in reservoir simulation models, it is usually assumed to be a constant with respect to pore pressure in most reservoir engineering calculations except in geomechanical studies, because the change of pore volume with pressure is considered minimal. However, the inverted seismic data clearly indicate that the compressibility values (including compressibility of both rock and fluids in the reservoir) are not a constant in the Bell Creek reservoir during the CO_2 flooding process.

In order to consider the effects of pore compressibility on simulation results, two scenarios of pore compressibility distribution were generated based on Equations Eq. 3 and 4, the porosity distribution in the Bell Creek Phase 1–2 areas (Figure 70). Figures 71 and 72 clearly demonstrate the contrast of compressibility distribution when different correlations are used in the same study area.

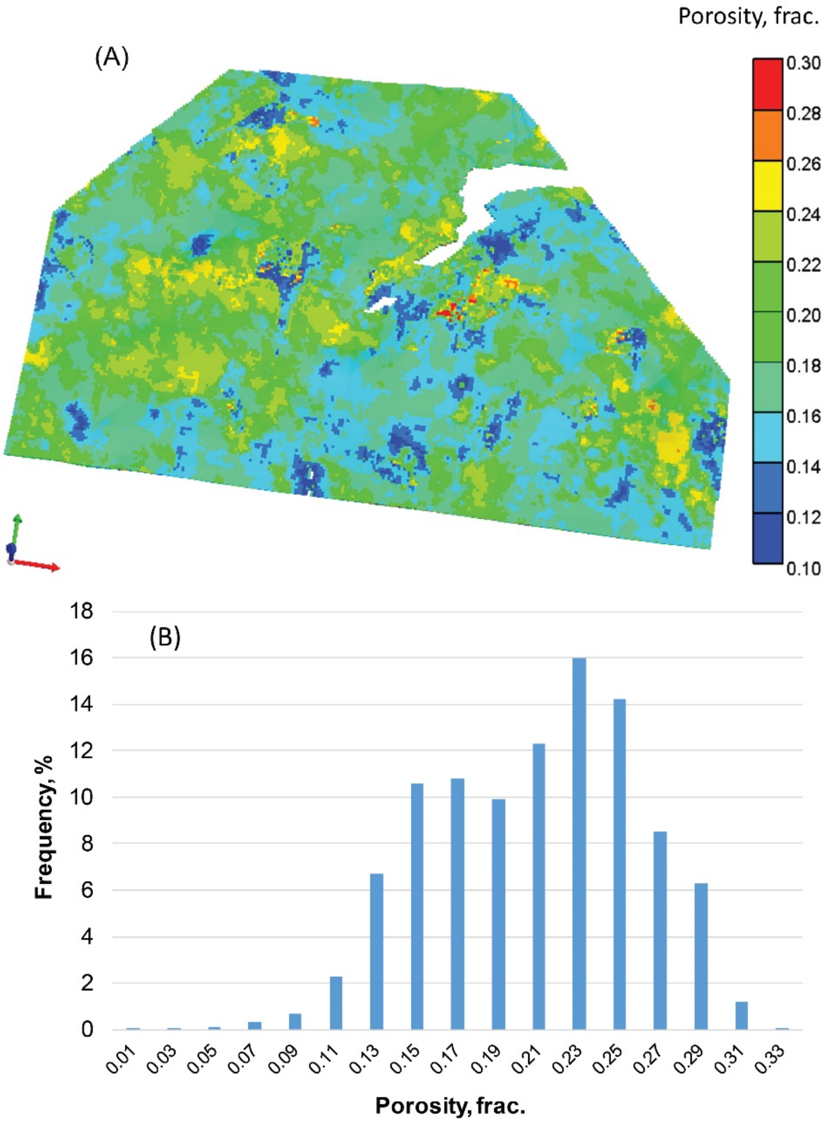

EERC CBO57194.AI

Figure 70. Porosity distribution (A – spatial and B – statistical) in the Bell Creek Phase 1–2 areas.

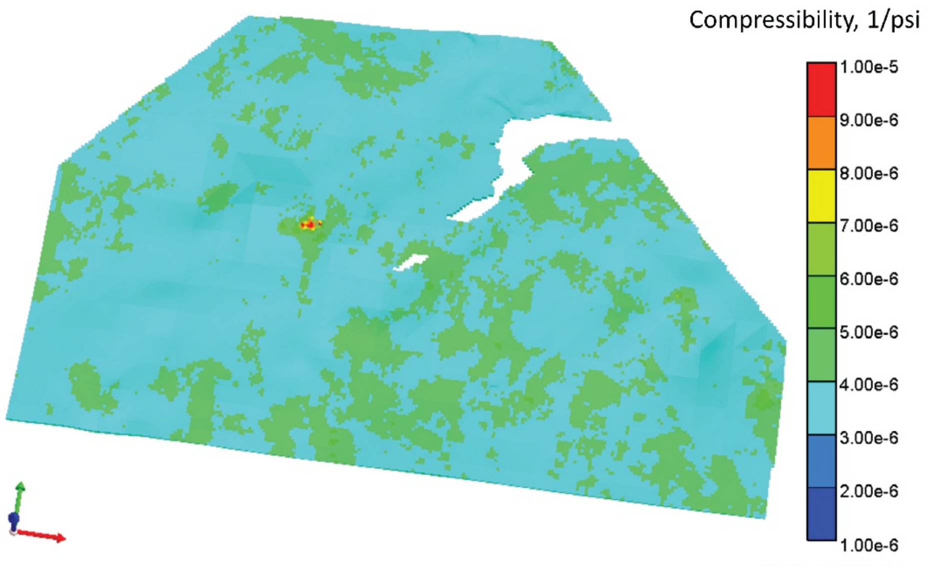

EERC CBO57195.AI

Figure 71. Pore compressibility distribution in the Bell Creek Phase 1–2 areas based on Hall's correlation for sandstones (Equation Eq. 3).

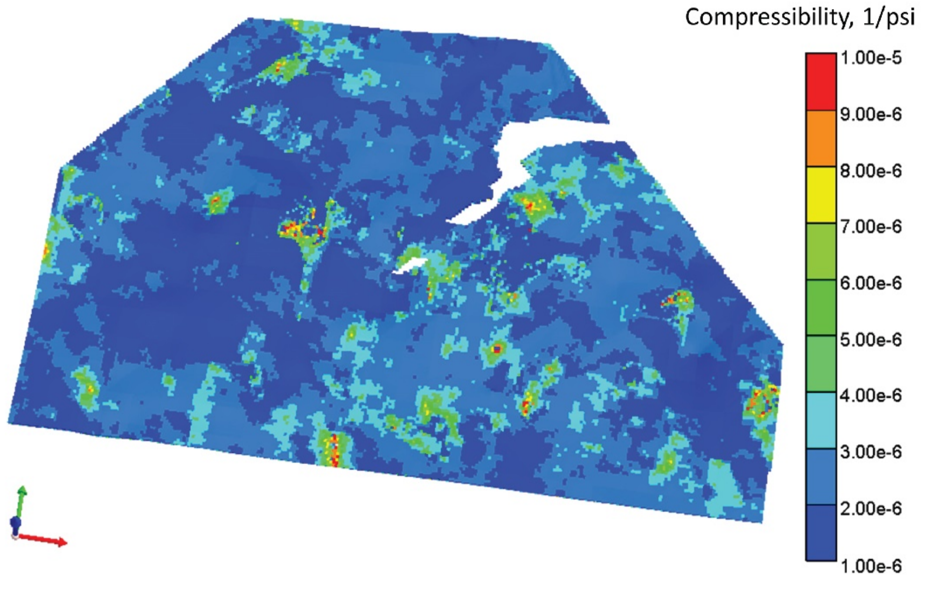

EERC CBO57196.AI

Figure 72. Pore compressibility distribution in the Bell Creek Phase 1–2 areas based on the correlation for consolidated sandstones (Equation Eq. 4).

Seismic Data Validation

Since the seismic surveys were conducted before and after CO_2 flooding started in the field, multiple factors may have effects on the compressibility values inverted from the seismic data. The main factors include reservoir pressure, oil compressibility, water compressibility, and CO_2 compressibility. Figure 73 shows a schematic of gas and pore compressibility distribution in a gas reservoir with different pressure conditions. Three regions can be divided based on the impact of formation energy (overall compressibility) on production behavior (Fekete, 2019):

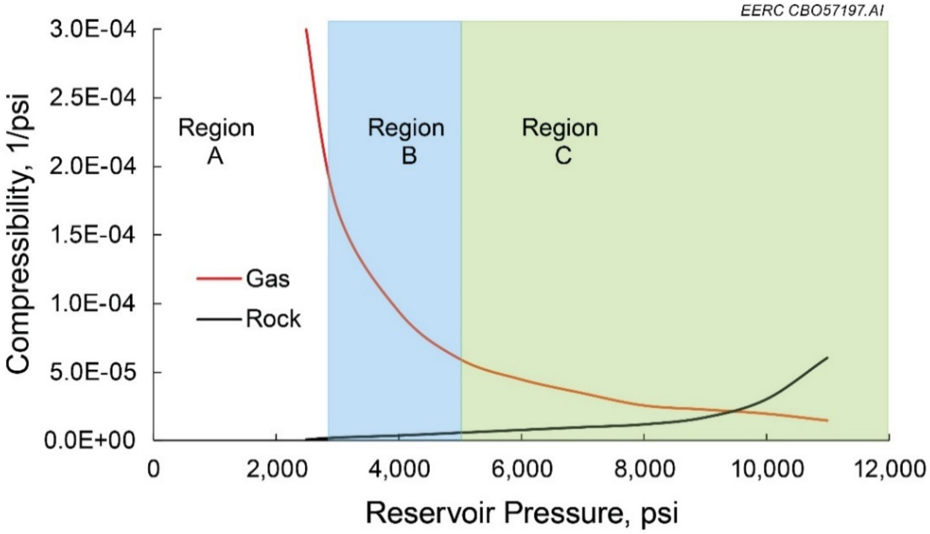

Figure 73. Schematic of influential regions of formation energy in a gas reservoir based on gas and pore compressibility distribution in the reservoir.

Region A: formation energy is negligible
Region B: formation energy becomes influential
Region C: formation energy is important

For an oil reservoir, the boundary of Region B may shift left considerably because the compressibility difference between oil and rock could be small. As the Bell Creek Field has oil, water, and gas in the reservoir and the reservoir is a little overpressured to ensure miscible flooding in the EOR process, it is necessary to consider dominated fluid flow mechanisms and pressure–volume–temperature (PVT) behavior of the fluids when validating the seismic data.

Fluid Flow in the Bell Creek Reservoir

Bell Creek is a typical conventional oil reservoir with good porosity and permeability as discussed above. Oil is displaced by water and gas from injectors to producers as the reservoir is developed by the water alternating gas (WAG) mode during the EOR process. Oil and water are slightly compressible while gas (mainly CO_2) is more compressible in the reservoir. The dominated flow mechanisms can be described by diffusivity equations as shown below (Lee and Wattenbarger, 1996; Baker and others, 2015):

For slightly compressible fluids:

$$\frac{1}{r}\frac{\partial r}{\partial}\left(r\frac{\partial p}{\partial r}\right) = \frac{\emptyset\mu_l C_{t\_l}}{0.0002637k}\frac{\partial p}{\partial t} \qquad \text{[Eq. 7]}$$

$$C_{t\_l} = C_p + C_l \qquad \text{[Eq. 8]}$$

Where, r is the radius from the well, *ft*; μ_l is the viscosity of liquid, *cp*; C_{t_l} is the total compressibility of liquid and rock, *1/psi*; k is the permeability, *mD*; t is the time, *day*; C_l is the compressibility of liquid (either oil or water), *1/psi*. Equation 7 is the diffusivity equation for flow of slightly compressible fluids in conventional reservoirs. The flow of oil and water in the Bell Creek reservoir follows this equation.

For compressible fluids:

$$\frac{1}{r}\frac{\partial r}{\partial r}\left(r\frac{p}{\mu_g z}\frac{\partial p}{\partial r}\right) = \frac{\emptyset\mu_g C_{t\_g}}{0.0002637k}\frac{p}{\mu_g z}\frac{\partial p}{\partial t} \qquad \text{[Eq. 9]}$$

$$C_{t\_g} = C_p + C_g \qquad \text{[Eq. 10]}$$

Where μ_g is the viscosity of gas, *cP*; C_{t_g} is the total compressibility of rock and gas, *1/psi*; z is the compressibility factor, *dimensionless*. The compressibility factor (z) is a measure of how much the thermodynamic properties of a real gas deviate from those expected of an ideal gas. This is an important thermodynamic property for modifying the ideal gas law to account for the phase behavior of real gases in reservoirs (Çengel and others, 2001; Baker and others, 2015). The flow of CO_2 in the Bell Creek reservoir follows Equation 9, which is the diffusivity equation for flow of compressible fluids in conventional reservoirs.

Since the seismic response includes both pressure and fluid saturation effects in the reservoir, while pressure correlates to the fluid properties as shown in Equations 7 to 10, therefore, the PVT behavior of fluids becomes important in order to understand and validate the seismic data.

PVT Behavior of Fluids in the Bell Creek Reservoir

A series of experimental activities and engineering calculations have been conducted to characterize the PVT behavior of the Bell Creek fluids at reservoir temperature (108°F). Constant composition expansion (CCE), differential liberation (DL) analysis, separator, swelling test, and fluid compositional analysis data were used in this study to describe the oil properties. Based on the experimental results, the physical properties of the reservoir fluids can be precisely characterized (Hawthorne and others, 2016). An equation of state (EOS) model with seven components (shown in Table 7) was developed based on the experimental data. The Peng–Robinson (PR) EOS method was applied to fine-tune the model and calculate the CO_2 and water properties using Computer Modelling Group's (CMG's) WINPROP® module (Jin and others, 2018).

Table 7. Composition of the Crude Oil in the Bell Creek Oil Field

Oil Composition	Mole Fraction
CO_2	0.0042
N_2 to C_2H	0.1961
C_3H to NC_4	0.0428
IC_5 to C07	0.1526
C08 to C13	0.2860
C14 to C24	0.1997
C25 to C36+	0.1184

Figure 74 shows that the EOS model can capture the oil behavior satisfactorily. The oil and water compressibility are shown in Figure 75, which clearly indicates that the compressibility of oil is greater than that of water in the Bell Creek reservoir. Using the tuned EOS model, the compressibility factor (z) of CO_2 can be determined as shown in Figure 76. The gas (CO_2) compressibility can then be calculated using the following equation (Lee and Wattenbarger, 1996):

$$C_g = \frac{1}{p} - \frac{1}{z}\frac{\partial z}{\partial p} \qquad \text{[Eq. 11]}$$

Simulation Model Update

Because reservoir properties and developing methods vary from field to field, a variety of workflows have been developed for updating reservoir simulation models with 4-D seismic data integration (Huang and others, 1997; Landa and Horne, 1997; Castro and others, 2006, 2009; Suman, 2009; Jin and others, 2011, 2012). Since considerable reservoir modeling and simulation efforts have been made to the field and many simulation results were available for analysis, a three-level simulation model updating approach was used in this study based on a workflow outlined by Jin and others (2012). The general workflow is illustrated in Figure 77. In the first level, 4-D seismic data were used to provide quality control (QC) for the simulation model by qualitatively comparing the CO_2 plume distribution with simulation results in the Phase 1–2 areas. In the second level, pore compressibility was calculated using available correlations and compared to the inverted seismic data. The range of possible compressibility values in the study area can be determined in this step. In the third level, the simulation model was iteratively updated with different compressibility distribution scenarios in a closed loop as shown in Figure 78. The reservoir pressure was outputted and compared with field observation to select the optimized simulation for the reservoir.

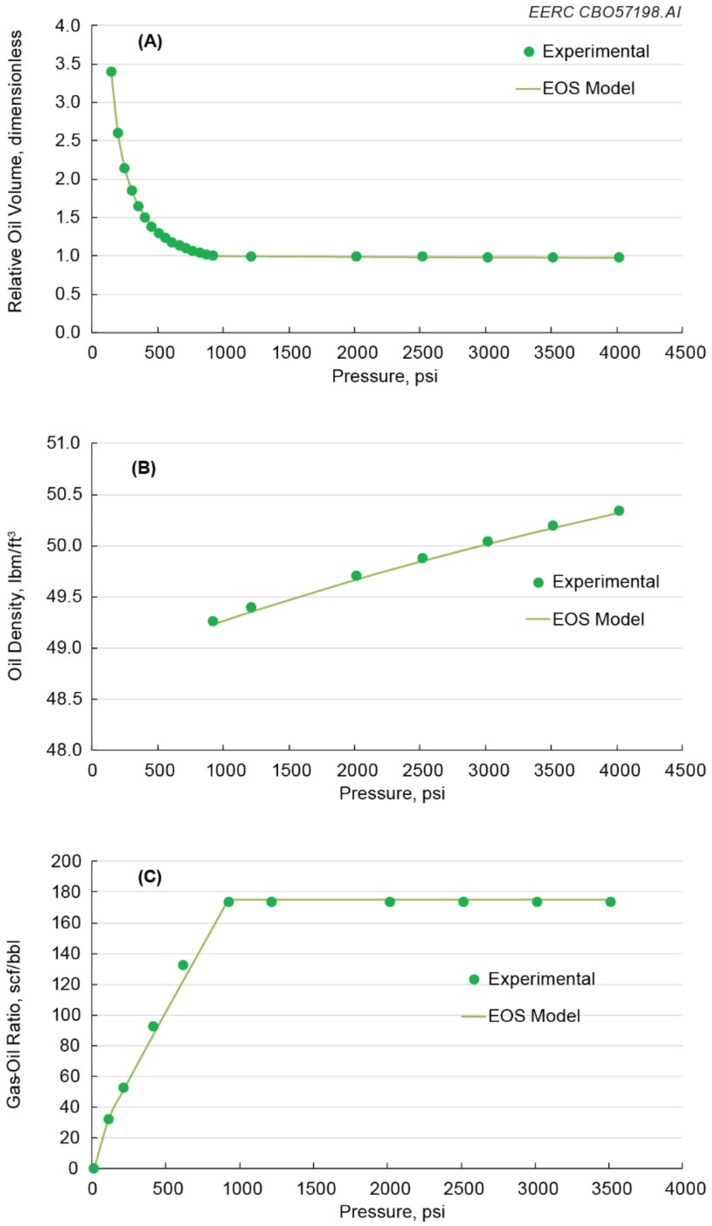

Figure 74. Comparison of experimental and simulation results for (A) relative oil volume, (B) oil density, and (C) GOR.

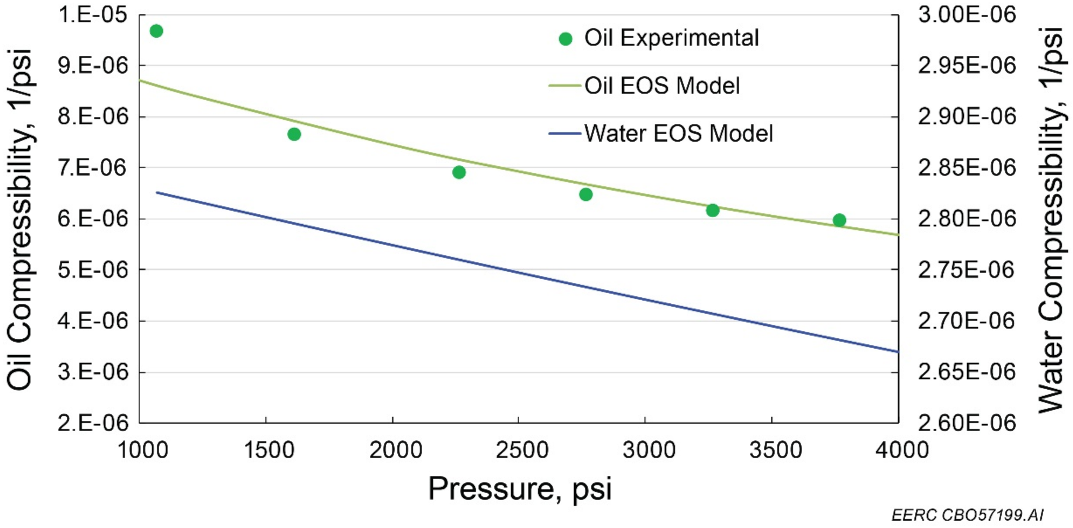

Figure 75. Oil and water compressibility in the Bell Creek reservoir.

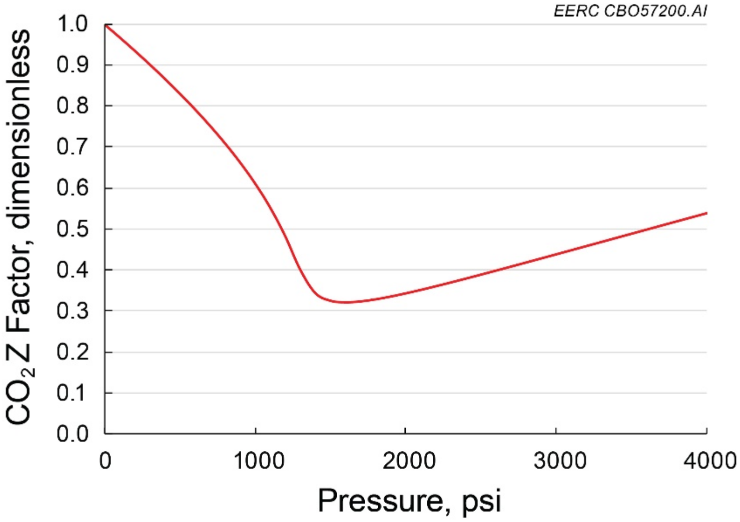

Figure 76. CO_2 compressibility factor (z) under Bell Creek reservoir conditions (108°F).

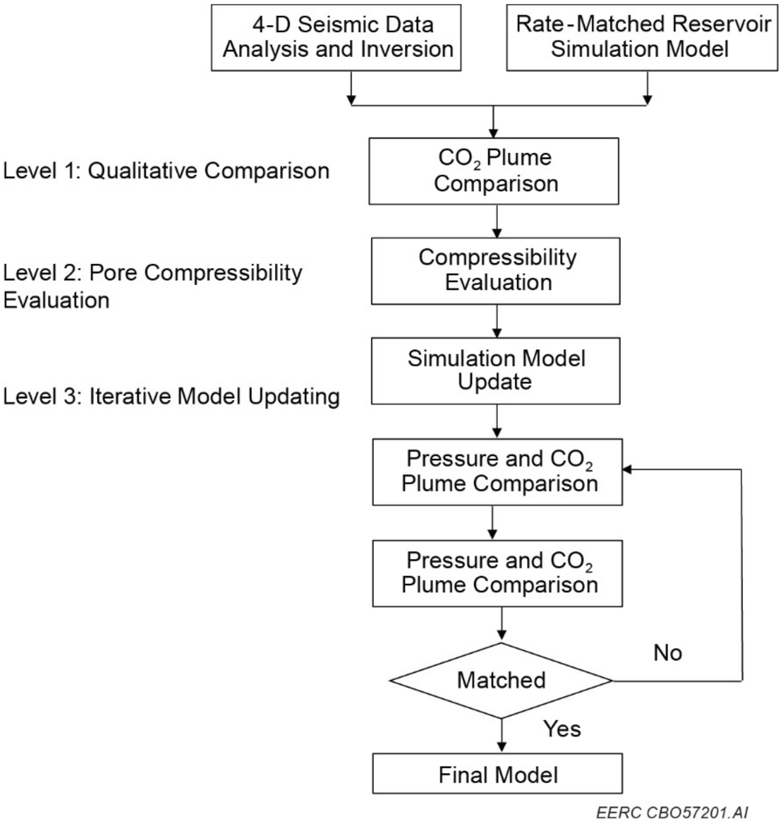

Figure 77. A workflow used for simulation model updating with 4-D seismic data in the Bell Creek Field.

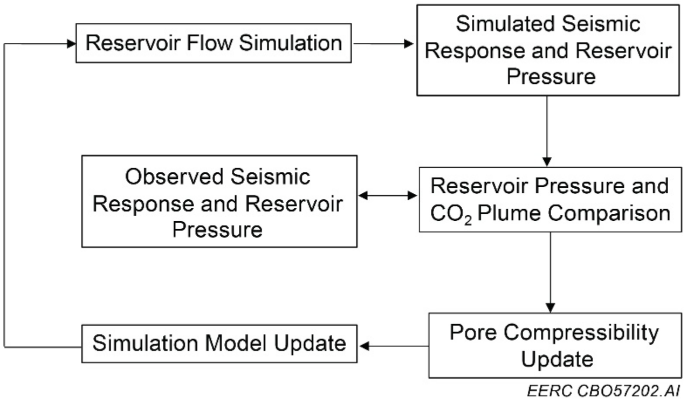

Figure 78. Level 3: a closed-loop iterative simulation model update approach.

Analysis of Results

A systematic flow simulation was conducted to match the production and injection historical data in the Phase 1–2 areas of the Bell Creek Field starting from the initial condition of the reservoir. Based on an inspectional analysis of the physical parameters involved in the actual production and injection processes, the variables were reduced from over 20 in dimensional space to 10 in dimensionless space. The reduction of variables greatly increases the simulation efficiency by removing the unimportant cases in the simulation designing matrix. Combined with a detailed analysis of production and injection data (oil production rate, water cut, and water injection rate, etc.) in the primary depletion and waterflooding stages, satisfactory history match results were achieved for oil, water, and gas rates in both production and injection processes as shown in Figures 79–81 (Bosshart and others, 2015). Figure 82 demonstrates that the simulated CO_2 plume matches the WEB-AVO compressibility in a reasonable level.

Although the fluid rates were well matched, there was still uncertainty in the pressure calculation as the pore compressibility was assumed to be one value for the entire reservoir ($6.9*10^{-6}$ 1/psi).

The time-lapse difference in compressibility (Figure 68) and the compressibility results calculated using porosity distribution Figure 67) indicate that the pressure prediction could be further improved by updating the rate-matched simulation model with the inverted seismic data. Although it is difficult to assign pore compressibility to each cell in the simulation model without

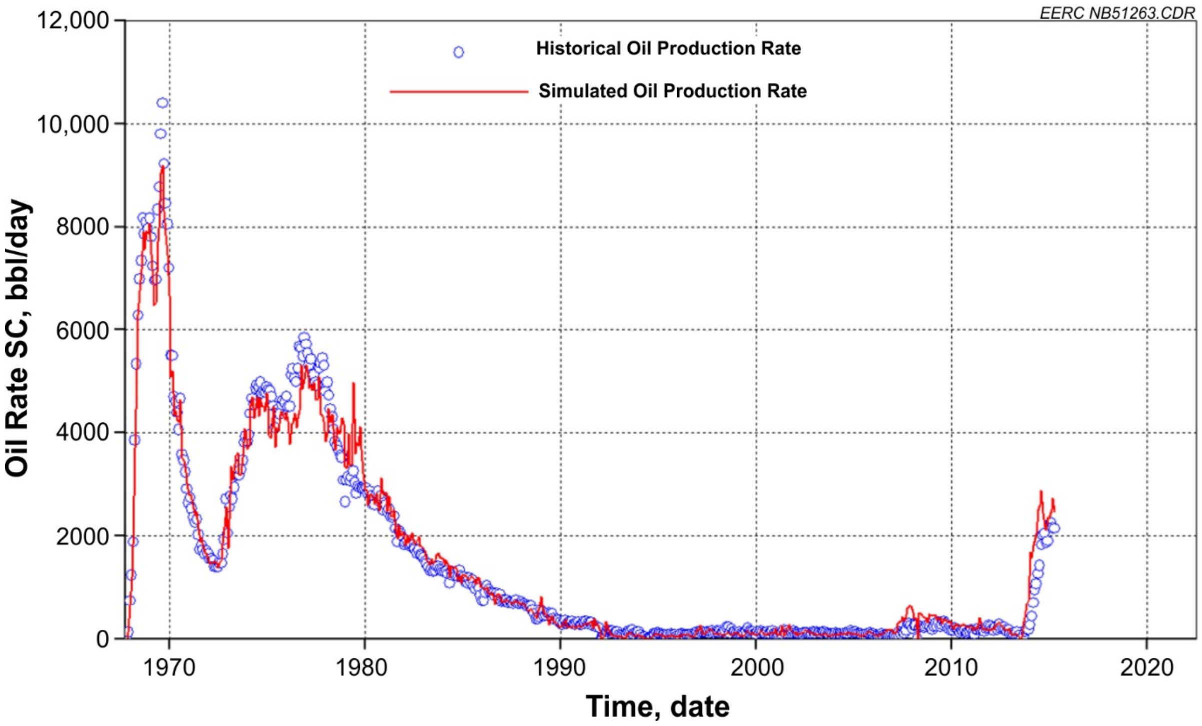

Figure 79. Oil production rate history match results.

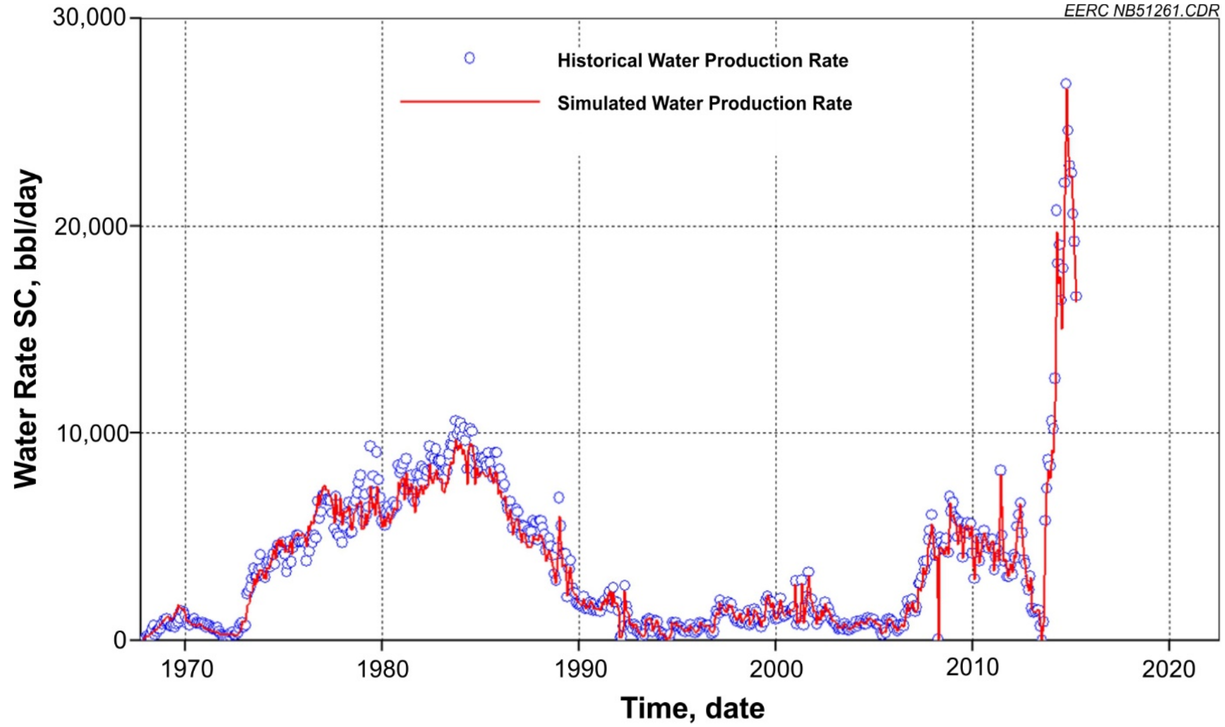

Figure 80. Water production rate history match results.

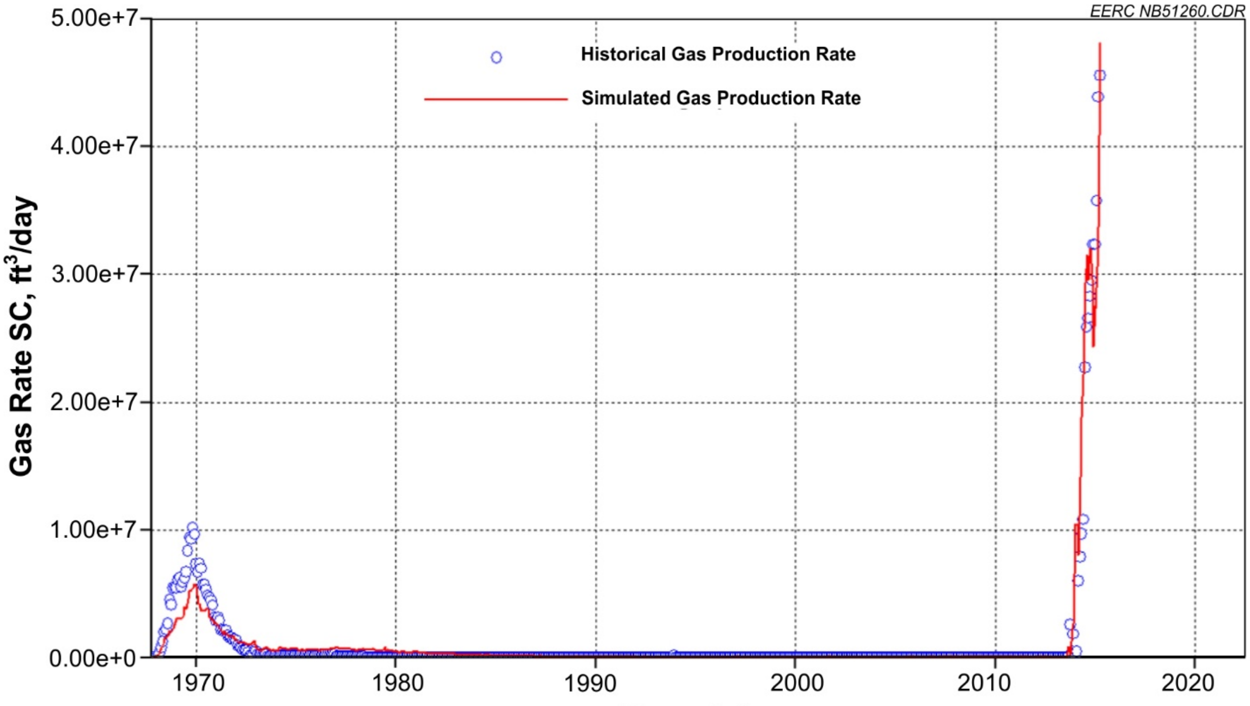

Figure 81. Gas production rate history match results.

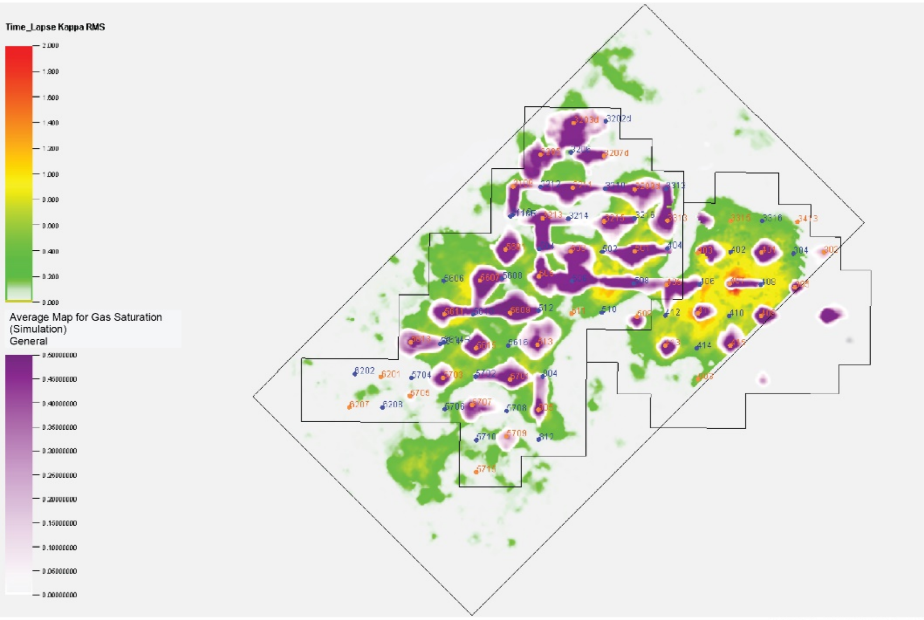

EERC CBO57203.AI

Figure 82. RMS WEB-AVO time-lapse compressibility (Kappa) vs. gas saturation from reservoir simulation.

considering geomechanics, it is possible to divide the model into different sections based on the spatial distribution of pore compressibility. Figure 83 shows an example of four-section division in the model. Since pore compressibility is also pressure dependent as shown in Equation 2, the pressure calculation may be further improved by dynamically updating the compressibility values in the reservoir model during the simulation process.

Figure 84 shows a comparison of pressure between field observation and simulation cases with different pore compressibility distribution scenarios. Although all four cases capture the pressure trend in the reservoir, there is 400 psi difference in the CO_2 flooding stage (after May 2013). A constant pore compressibility value ($6.9*10^{-6}$ 1/psi) was assigned in Case 1, and a random pore compressibility distribution was assigned in Case 4. Compressibility values calculated using Hall's correlation and consolidated sandstone correlation were assigned to Cases 2 and 3, respectively. The figure also clearly demonstrates that Cases 2 and 3 can reproduce the field response better than Cases 1 and 4. The comparison illustrates that the seismic response is valid to indicate the different pore compressibility distribution in the field and assigning pore compressibility based on widely accepted correlations can improve simulation accuracy in the Bell Creek Field. Figure 85 depicts the sensitivity of pressure to CO_2 injection in the Phase 1–2 areas from (A) 4-D seismic survey (the RMS WEB-AVO time-lapse shear compliance) and (B) simulation results, which show that pressure response in Phase 2 is more sensitive than in Phase 1 when CO_2 is injected into the reservoir. The possible explanation is that the reservoir thickness in Phase 2 is smaller than in Phase 1, and there is no aquifer attaching to Phase 2. The aquifer in the west boundary of Phase 1 could perform as a buffer zone and reduce the sensitivity of pressure there.

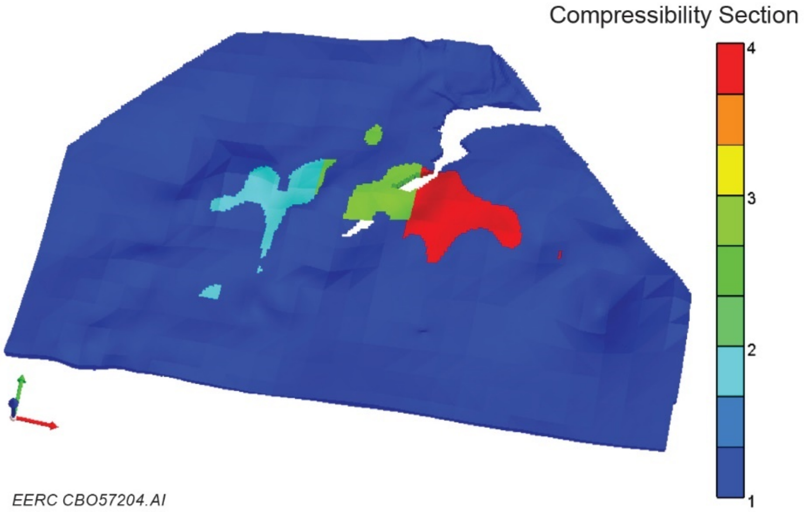

Figure 83. Example of section division in the model based on pore compressibility distribution.

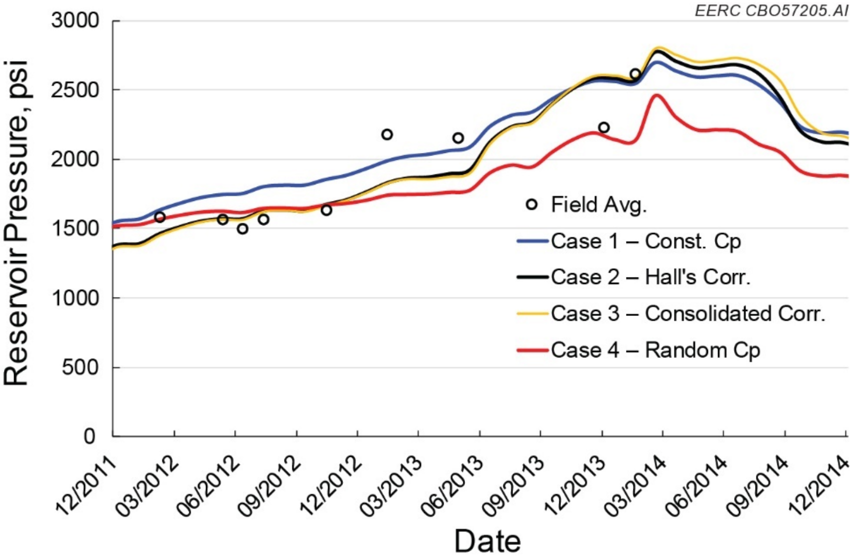

Figure 84. Comparison of pressure response using different pore compressibility distribution scenarios.

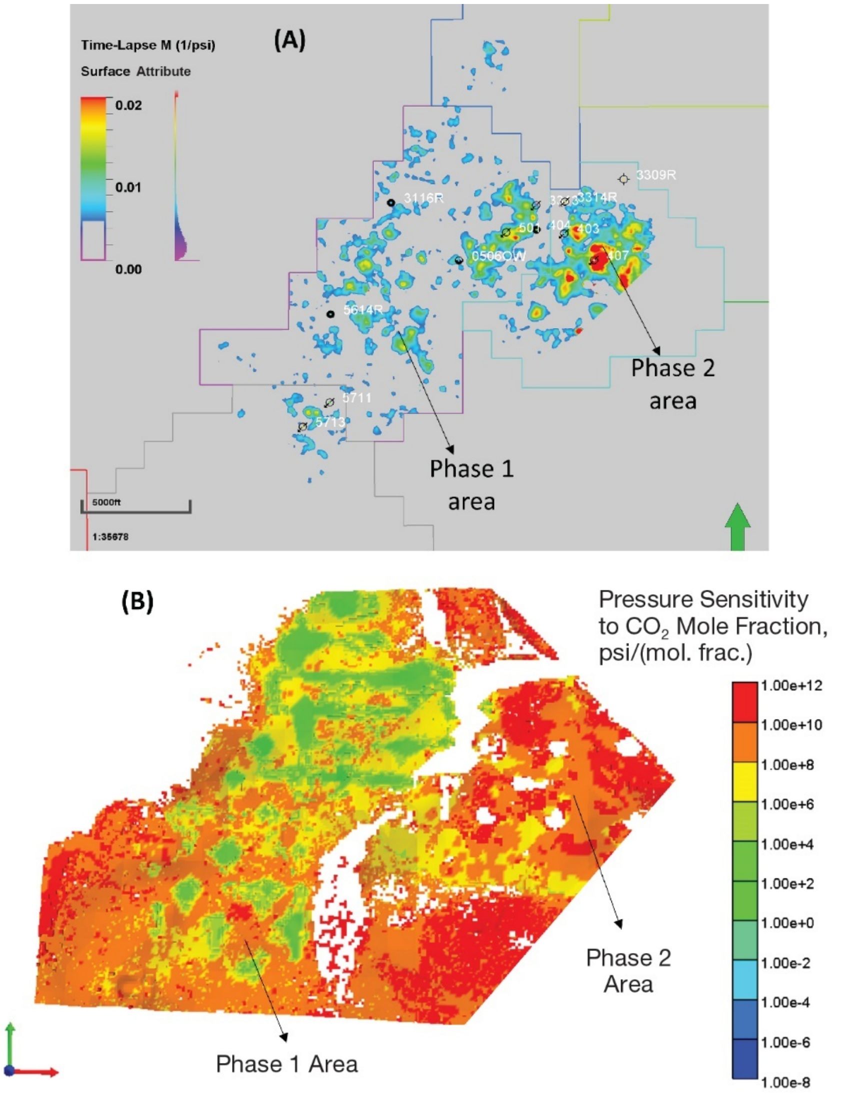

EERC CBO57206.AI

Figure 85. Sensitivity of pressure to CO_2 injection in the Phase 1–2 areas (A) RMS WEB-AVO time-lapse shear compliance and (B) simulation results.

Fluid Saturation from Ji-Fi vs. Saturation from Reservoir Simulation

The probabilities of facies fluid distribution in the Bell Creek Reservoir estimated by Ji-Fi are compared here with gas saturation distribution derived from reservoir simulations in Figures 86–88. The gas distribution from reservoir simulation corresponds to Layer 11 from October 2014, the same month when the seismic monitor survey was acquired. This layer was selected because of its location approximately at the middle of the reservoir interval. The Ji-Fi probability fluid distribution is represented by a horizon with the same geometry as the Springen

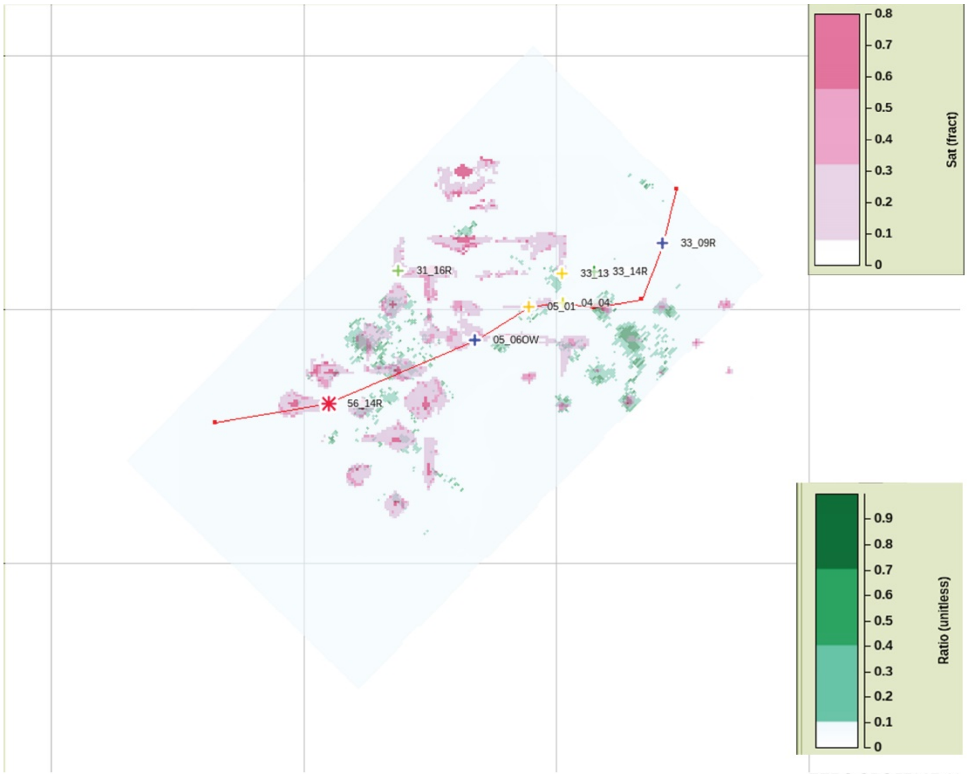

EERC CBO57207.AI

Figure 86. Comparison of gas saturation from reservoir simulation results at Layer K11 (October 2014) with estimated probabilities for free CO_2 using a Ji-Fi multirealization approach. The Ji-Fi results overlay the reservoir simulation results. Green color bar: Ji-Fi, pink color bar: reservoir simulation.

Ranch horizon which represents the top of the reservoir. The Ji-Fi horizon was placed 6 ms down from the top of the reservoir. Notice that although the geometry of Layer 11 and Ji-Fi horizon are not the same, it was expected that both surfaces cross similar features of the reservoir. Overlaying the Ji-Fi facies probabilities horizon on the gas distribution map for free CO_2, oil saturated with CO_2 and the combination of free CO_2 with oil saturated with CO_2 shows a good correlation with the spatial distribution of the gas saturation from reservoir simulation which confirms the ability of Ji-Fi to track CO_2 and other fluids in the reservoir.

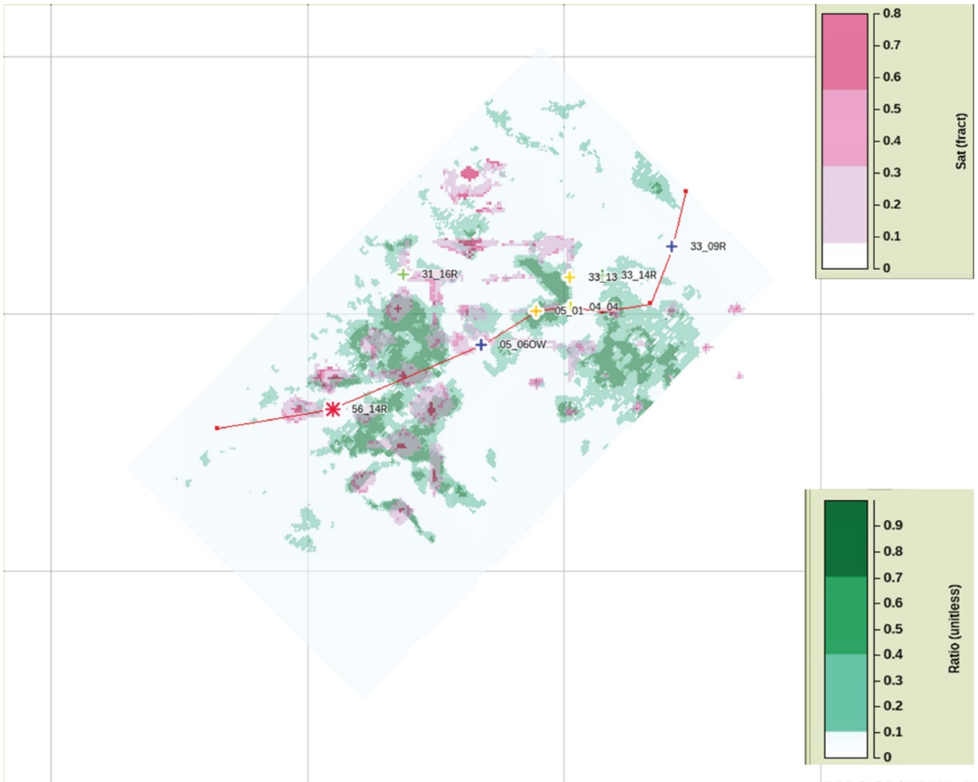

EERC CBO57208.AI

Figure 87. Comparison of gas saturation from reservoir simulation results at Layer K11 (October 2014) with estimated probabilities for oil saturated with CO_2 using a Ji-Fi multirealization approach. The Ji-Fi results overlay the reservoir simulation results. Green color bar: Ji-Fi, pink color bar: reservoir simulation.

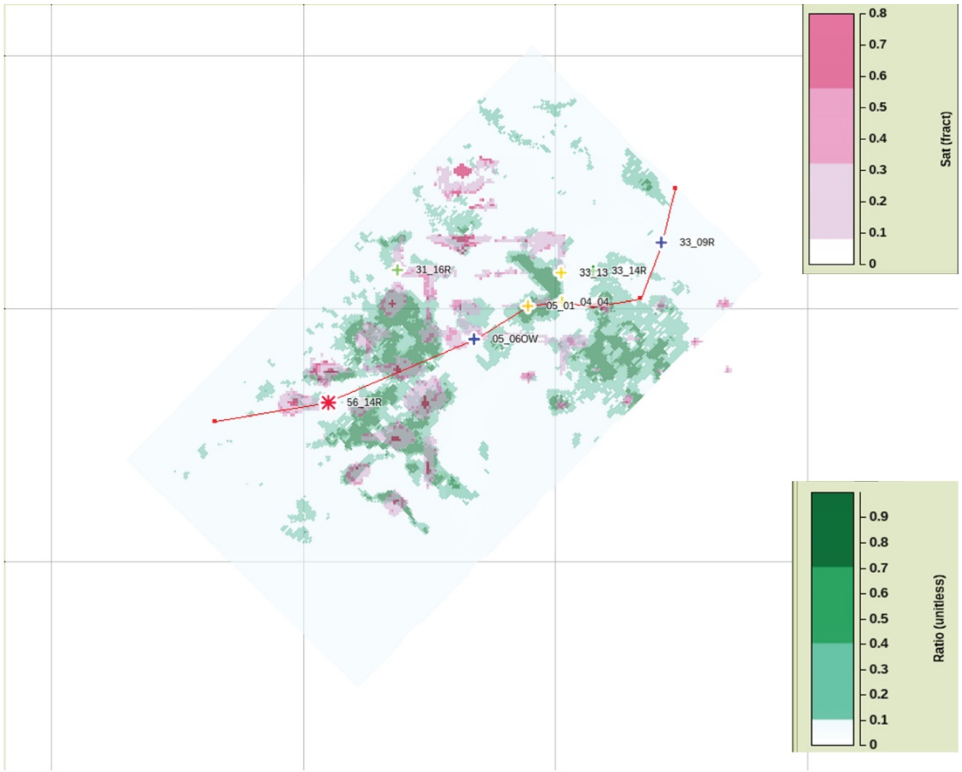

EERC CBO57209.AI

Figure 88. Comparison of gas saturation from reservoir simulation results at Layer K11 (October 2014) with estimated probabilities for free CO_2 and oil saturated with CO_2 using a Ji-Fi multirealization approach. The Ji-Fi results overlay the reservoir simulation results. Green color bar: Ji-Fi, pink color bar: reservoir simulation.

Even though the results of the comparison confirm the ability of Ji-Fi to track CO_2 and other fluids in the reservoir, similarly, as the comparison with WEB-AVO results, some discrepancies in the correlation are observed in the northwestern part of Phase 1. To assess this discrepancy, PNLs of some wells in the study area were used to review the geologic and fluid conditions in the reservoir at selected locations. Figure 89 shows the available PNLs of the wells 05-06 OW, 05-01, 33-13, and 32-03 wells and their location in the Ji-Fi reservoir simulation comparison map. Whereas the PNLs of the 05-01 and 33-13 show a well-defined saturation in the reservoir, and therefore a high-probability of reservoir fluids estimated by Ji-Fi, the 05-06 OW and 32-03 PNLs show a small saturation area. Unfortunately, only one PNL was available from the 32-03 well where the main discrepancy in the correlation of WEB-AVO and Ji-Fi versus reservoir simulation was observed. If the small saturation area observed in the PNL is considered as a reference for the thickness of the reservoir, it is expected that the such thickness is below the resolution of the seismic method.

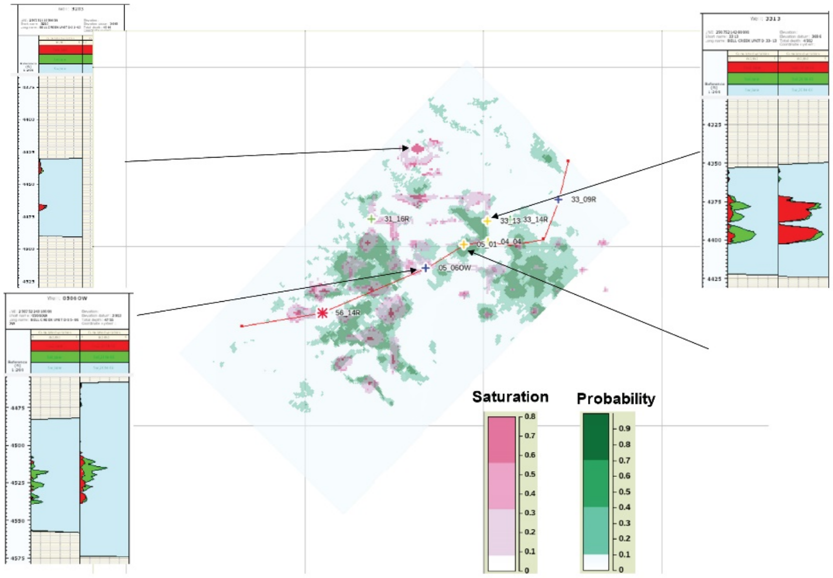

EERC CBO57210.AI

Figure 89. Comparison of gas saturation from reservoir simulation results at Layer K11 (October 2014) with estimated probabilities for free CO_2 and oil saturated with CO_2 using a Ji-Fi multirealization approach. Time-lapse PNL of 05-06OW, 05-01, 33-13 wells from the same time of acquisition as the seismic survey. The PNL from 32-03 well is only available after the CO_2 injection. Green color bar: Ji-Fi, pink color bar: reservoir simulation.

CONCLUSIONS

The effectiveness of time-lapse seismic monitoring for qualitatively determining the distribution of CO_2 in geologic formations has been demonstrated in the literature (e.g., Wang and Morozov, 2017; Van Dok and others, 2016). Burnison and others (2016) and Salako and others (2017) were able to improve the geologic interpretation of the Bell Creek reservoir (Muddy Formation) using the time-lapse change of seismic amplitudes associated with CO_2 injection. The Bell Creek reservoir contains significant heterogeneity such as sand with fluvial channels, back barrier, lagoonal deposits, permeability barriers, baffles, and communication pathways between various compartmentalized geobodies (e.g., Burnison and others, 2016).

The remarkable heterogeneity of the Bell Creek reservoir and its 6–9-m thickness at the limit of the seismic resolution represents a challenge for the successful application of inversion methods to derive reservoir parameters. Using a linear relationship in a dynamic well tie to invert for the pore-volume-scaled changes in saturation and pressure changes of the Bell Creek reservoir, Salako and others (2018) reported a good correlation of the seismic velocity and impedance with the pore volume changes.

Since the interaction of the seismic wavefield with the matrix and fluids characteristics of the reservoir creates nonlinear effects, the success of inverting seismic amplitudes for reservoir parameters depends upon considering these effects in the inversion scheme. The two joint inversion methods used in this project are formulated to solve nonlinear problems using different innovative approaches. On the one hand, the WEB-AVO algorithm considers the full seismic wavefield traveling through the reservoir in the estimation of seismic reservoir parameters. In this approach, it is assumed that all the wave phenomena associated with the complexity of the reservoir is captured, when the full elastic wave-equation is solved for the target reservoir. On the other hand, the Ji-Fi method has an integral representation of the geology in the inversion algorithm using elastic facies, which provides information about the spatial distribution of the geologic heterogeneities controlling the distribution of fluids in the reservoir.

In this project, the WEB-AVO algorithm was extended to invert the baseline and monitor data sets simultaneously. This type of inversion provides several benefits. Firstly, the simultaneous inversion solves for the baseline reservoir properties plus the associated time-lapse differences. As only very local time-lapse changes are expected, a sparseness constraint on the time-lapse property differences is used to stabilize the inversion procedure. This stabilization is due to having the same amount of seismic data with a significantly reduced number of unknown reservoir properties. Furthermore, the inversion becomes robust against the well-known challenge of repeatability of seismic surveys and associated noise. The simultaneous estimation of baseline compressibility and shear compliance and the associated time-lapse differences is a groundbreaking upgrade of the WEB-AVO technology that can facilitate the time-lapse monitoring of CO_2 distribution in the reservoir with less stringent data acquisition and processing requirements.

The performance of the time-lapse joint WEB-AVO inversion workflow was assessed on real data and synthetic data experiments driven by rock physics simulations. The extensive 1-D (wells), 2-D (arbitrary lines), and 3-D tests confirmed the stability and robustness of the new algorithm. This extension of the WEB-AVO algorithm is one of the objectives of this project to upgrade the technique from a TRL3 to TRL4.

The time-lapse compressibility and shear compliance changes estimated by the simultaneous time-lapse WEB-AVO provide a detailed spatial description of the complex interaction between the reservoir's sedimentary conditions and the physical/chemical processes related to changes in water saturation, CO_2 saturation, and pressure. While compressibility matches the time-lapse softening and hardening signature reported in the literature for this reservoir, results of the rock physics and seismic simulations showed that the shear compliance represents a good indicator of the pressure effect due to the CO_2 EOR activities in the Bell Creek reservoir.

Although the estimation of geologic facies is another critical aspect of reservoir characterization, conventional simultaneous seismic inversion cannot correctly handle the physics of the facies away from the geologic boundaries where facies change (Kemper and Gunning, 2014). The Ji-Fi technology has been proposed as a Bayesian joint impedance and facies algorithm that overcomes this issue using depth-dependent trends for each of the expected reservoir and nonreservoir facies, seismic data, seismic wavelets, and a set of prior facies proportions (Waters and others, 2016). A detailed workflow using well logs and some geological knowledge about the facies distribution in the study area is required to create the DTA for each facies (a set of facies-dependent depth trends).

In this report, a Ji-Fi workflow was introduced to derive the optimum input data for the application of Ji-Fi to the baseline and monitor surveys from the study area. Comprehensive rock physics analyses using core data and well logs were conducted to establish the background geologic information and estimate the litho-fluid facies of the Bell Creek reservoir. This information was used to create a DTA. The uncertainties in the facies models were assessed by using the facies-dependent probability density functions to perform Bayesian classification along with existing upscaled well elastic data. Good agreement was found between the upscaled petrophysical facies log and the Bayesian classification log with associated probabilities for each facies. The facies and their probability distributions corresponding to the highly heterogeneous target reservoir and its fluid conditions due to the CO_2 EOR activities were successfully separated in the seismic elastic space. This separation provided favorable conditions for the application of the Ji-Fi method.

Following a similar approach as with the other inversion method mentioned above, extensive Ji-Fi tests were conducted at wells, 2-D arbitrary lines, and 3-D data to define the optimum parameters for the inversion. Separate Ji-fi of the baseline and monitor surveys and the differencing analysis to capture changes due to CO_2 were performed. Single and multirealization inversion schemes were also run and analyzed. Reliable acoustic impedances and most probably litho-fluid facies of the target reservoir were obtained. Information about the probability of the presence of litho-fluid facies is paramount to reducing uncertainty in forecasting CO_2 saturation changes within the target reservoir.

Geologic and reservoir simulation models can always be improved by a better reservoir characterization when more data become available in the reservoir development processes. The simulation model has a better description of the reservoir by including spatial constraints derived from time-lapse seismic surveys and, therefore, provides more reliable forecasts of the reservoir performance.

WEB-AVO compressibility data were integrated into the reservoir simulation model by employing two widely accepted compressibility-porosity correlations for sandstones. Flow mechanism analysis and engineering calculations showed that pore and fluids compressibility could affect the pressure response in the reservoir. A closed-loop workflow was developed in this study to integrate the seismic inversion data into an existing reservoir simulation model and update the model with different pore compressibility distribution scenarios. The comparison of simulation results with field observations confirms the estimated time-lapse seismic response for compressibility and saturation distribution in the Bell Creek Field.

REFERENCES

Avseth, P., Mukerji, T., and Mavko, G., 2005, Quantitative seismic interpretation—applying rock physics tools to reduce interpretation risk, 1st ed.: Cambridge University Press.

Baker, R.O., Yarranton, H.W., and Jensen, J., 2015, Practical reservoir engineering and characterization: Gulf Professional Publishing.

Batzle, M., and Wang, Z., 1992, Seismic properties of pore fluids: Geophysics, v. 57, p. 1396–1408.

Bosshart, N.W., Jin, L., Dotzenrod, N.W., Burnison, S.A., Ge, J., He, J., Burton-Kelly, M.E., Ayash, S.C., Gorecki, C.D., Hamling, J.A., Steadman, E.N., and Harju, J.A., 2015, Bell Creek test site—simulation report: Plains CO_2 Reduction (PCOR) Partnership Phase III Task 9 Deliverable D66 (Update 4) for U.S. Department of Energy National Energy Technology Laboratory Cooperative Agreement No. DE-FC26-05NT42592, EERC Publication 2016-EERC-10-09, Energy & Environmental Research Center, Grand Forks, North Dakota, August.

Braunberger, J.R., Pu, H., Gorecki, C.D., Bailey, T.P., Bremer, J.M., Peck, W.D., Gao, P., Ayash, S.C., Liu, G., Hamling, J.A., Steadman, E.N., and Harju, J.A., 2013, Bell Creek test site – simulation report: Plains CO_2 Reduction (PCOR) Partnership Phase III Task 9 Deliverable D66 (Update 2) for U.S. Department of Energy National Energy Technology Laboratory Cooperative Agreement No. DE-FC26-05NT42592, August.

Burnison, S.A., Bosshart, N.W., Salako, O., Reed, S., Hamling, J.A., and Gorecki, C.D., 2016, 4-D seismic monitoring of injected CO_2 enhances geological interpretation, reservoir simulation, and production operations: Paper presented at the 13th International Conference on Greenhouse Gas Control Technologies (GHGT-13).

Burt, R.A., Haddenhorst, F.A., and Hartford, J.C., 1975, Review of Bell Creek waterflood performance – Powder River, Montana: Journal of Petroleum Technology, v. 27.

Castro, S., Caers, J., Otterlei, C., Høye, T., Andersen, T., and Gomel, P., 2006, A probabilistic integration of well log, geological information, 3D/4D seismic, and production data—application to the Oseberg Field: Paper SPE 103152 presented at the SPE Annual Technical Conference and Exhibition, San Antonio, Texas, September 24–27, 2006.

Castro, S., Otterlei, C., Meisinget, H., Høye, T., Gomel, P., Zachariassen, E., and Caers, J., 2009, Incorporating 4-D seismic data into reservoir models while honoring production and geologic data: The Leading Edge, v. 28, p. 1498–1505.

Çengel, Y.A., Turner, R.H., and Cimbala, J.M., 2001, Fundamentals of thermal-fluid sciences: New York, McGraw-Hill.

Doulgeris, P., Anestoudis, D., Haffinger, P., Droujinina, A., and Gisolf, D., 2018, Quantifying the effect of overburden multiples on Miocene reservoirs in the Levantine Basin: Paper presented at the 80th EAGE Annual Conference and Exhibition, June 11–14, 2018, Copenhagen, Denmark.

Dvorkin, J., and Gutierrez, M.A., 2002, Grain sorting, porosity, and elasticity: Petrophysics, v. 43, no. 3, p. 185–196.

Eylands, K.E., Kurz, B.A., Hamling, J.A., Heebnik, L.V., Smith, S.A., LaBonte, J.A., Mibeck, B.A.F., Kleven, P.L., Klapperich, R.J., Braunberger, J.R., and Gorecki, C.D., 2013, Bell Creek 05-06 OW sidewall core mineralogy assessment: 2013-EERC-04-02 Report.

Fekete. Geomechanical Reservoir Models. Technical manual of Fekete Harmony, 2019.

Gassmann, F., 1951, Elastic waves through a packing of spheres: Geophysics, v. 16, no. 4, p. 673–685.

Gisolf, A., Haffinger, P.R., and Doulgeris, P., 2017, Reservoir-oriented wave-equation-based seismic amplitude variation with offset inversion: Interpretation, August, p. 43–56.

Hall, H.N., 1953, Compressibility of reservoir rocks: Journal of Petroleum Technology, v. 5, no. 01, p. 17–9.

Han, D., and Sun, M., 2013, Velocity and density of water with dissolved CH_4 and CO_2: SEG Annual International Meeting, Expanded Abstracts.

Han, D., Sun, M., and Liu, J., 2012, Velocity and density of CO_2–oil miscible mixtures: SEG Annual International Meeting, Expanded Abstracts.

Hawthorne, S.B., Miller, D.J., Jin, L., and Gorecki, C.D., 2016, Rapid and simple capillary-rise/vanishing interfacial tension method to determine crude oil minimum miscibility pressure—pure and mixed CO_2, methane, and ethane: Energy Fuels, v. 30, no. 8, p. 6365–6372.

Horne, R.N., 1995, Modern well test analysis: Petroway Inc.

Huang, X., Meister, L., and Workman, R., 1997, Reservoir characterization by integration of time-lapse seismic and production data: SPE Annual Tech. Conf. and Exhibition.

Jin, L., Castineira, D., Fu, S., van den Hoek, P., Pirmez, C., Fehintola, T., Tendo, F., and Olaniyan, E., 2011, 4-D seismic history matching using flood front information: Paper presented at the 73rd EAGE Conference and Exhibition, Vienna, Austria, May 23–26.

Jin, L., Tiller, G., Weber, D., Fu, S., Ferrandis, J., van den Hoek, P., Pirmez, C., Fehintola, T., Tendo, F., and Olaniyan, E., 2012, Workflows for quantitative 4-D seismic data integration—a case study: IPTC 14458, Proceedings of International Petroleum Technology Conference.

Jin, L., Bosshart, N.W., Oster, B.S., Hawthorne, S.B., Peterson, K.J., Burton-Kelly, M.E., Feole, I.K., Jiang, T., Pekot, L.J., Peck, W.D., Ayash, S.C., and Gorecki, C.D., 2016, Bell Creek test site – simulation report: Plains CO_2 Reduction (PCOR) Partnership Phase III draft Task 9 Deliverable D66 (Update 6) executive summary for U.S. Department of Energy National Energy Technology Laboratory Cooperative Agreement No. DE-FC26-05NT42592, Grand Forks, North Dakota, Energy & Environmental Research Center, August.

Jin, L., Pekot, L.J., Hawthorne, S.B., Salako, O., Peterson, K.J., Bosshart, N.W., Jiang, T., Hamling, J.A., and Gorecki, C.D., 2018, Evaluation of recycle gas injection on CO_2 enhanced oil recovery and associated storage performance: International Journal of Greenhouse Gas Control, v. 75, p. 151–61.

Kemper, M., and Gunning, J., 2014, Joint impedance and facies inversion—seismic inversion redefined: First Break, v. 32, p. 89–95.

Kemper, M., Paiva, M., and Waters, K., 2017, Facies-based inversion through the asset lifecycle: Fifteenth International Congress of the Brazilian Geophysical Society, p. 1–4.

Kennett, B.L.N., 1984, An operator to forward modeling, data processing and migration: Geophysical Prospecting, v. 32, p. 1074–1090.

Landa, J.L., and Horne, R.N., 1997, A procedure to integrate well test data, reservoir performance history and 4-D seismic information into a reservoir description: Paper SPE 38653 presented at the SPE Annual Technical Conference and Exhibition, San Antonio, Texas, October 5–8.

Lee, W.J. and Wattenbarger, R.A., 1996, Gas reservoir engineering: SPE Textbook Series, v. 5, 349 p.

Liu, G., Braunberger, J.R., Pu, H., Gao, P., Gorecki, C.D., Ge, J., Klenner, R.C.L., Bailey, T.P., Dotzenrod, N.W., Bosshart, N.W., Ayash, S.C., Hamling, J.A., Steadman, E.N., and Harju, J.A., 2014, Bell Creek test site – simulation report: Plains CO_2 Reduction (PCOR) Partnership Phase III Task 9 Deliverable D66 Update 4 for U.S. Department of Energy National Energy Technology Laboratory Cooperative Agreement No. DE-FC26-05NT42592, August.

MacBeth, C., 2004, A classification for the pressure-sensitivity properties of a sandstone rock frame: Geophysics, v. 69, no. 2, p. 497–510.

Marion, D., Nur, A., Yin, H., and Han, D., 1992, Compressional velocity and porosity in sand-clay mixtures: Geophysics, v. 57, no. 4, p. 554–563.

Mavko, G., Mukerji, T., and Dvorkin, J., 2009, The rock physics handbook—tools for analyzing seismic properties: Cambridge University Press.

Molnar, P.S., and Porter, M.L., 1990, Geologic reservoir study of the Bell Creek Field, Carter and Powder River Counties, Montana: Exxon USA Reservoir Technology.

Pasternack, E., 2009, Bell Creek Petrophysics: Outsource Petrophysics Inc.

Reed, S., Ge, J., Burnison, S.A., Bossart, N.W., Hamling, J., and Gorecki, C.D., 2018, Viability of InSAR as a monitoring tool in challenging terrain: Bell Creek, Montana: 14th International Conference on Greenhouse Gas Control Technologies, GHGT-14.

Salako, O., Jin, L., Barajas-Olalde, C., Hamling, J.A., and Gorecki, C.D., 2018, Implementing adaptive scaling and dynamic well tie for quantitative 4-D seismic evaluation of a reservoir subjected to CO_2 enhanced oil recovery and associated storage: International Journal of Greenhouse Gas Control, v. 78, p. 306–326.

Salako, O., Jin, L., Burnison, S.A., Hamling, J.A., Gorecki, C.D., Reed, S., and Richards, T., 2017, The value of 4-D seismic monitoring at Bell Creek—a mature oil field undergoing CO_2 enhanced oil recovery: Paper presented at the 79th European Association of Geoscientists and Engineers Conference & Exhibition.

Saini, D., Braunberger, J.R., Pu, H., Bailey, T.P., Ge, J., Crotty, C.M., Liu, G., Hamling, J.A., Gorecki, C.D., Steadman, E.N., and Harju, J.A., 2012, Bell Creek test site – simulation report: Plains CO_2 Reduction (PCOR) Partnership Phase III Task 9 Deliverable D66 Update 1 for U.S. Department of Energy National Energy Technology Laboratory Cooperative Agreement No. DE-FC26-05NT42592, August.

Suman, A., 2009, Uncertainties in rock pore compressibility and effects on seismic history matching: M.S. Thesis, Stanford University.

Sutherland, R.B., 2011, Bell Creek Petrophysical Analysis Notes: Denbury internal report.

Van Dok, R., Fuller, B., Larry, W., Kramer, N., Anderson, P., and Richards, T., 2016, Permanent borehole sensors for CO_2 injection monitoring – Hasting Field, Texas: SEG Technical Program Expanded Abstracts, p. 5511–5515.

Wang, Y., and Morozov, I., 2017, Time-lapse acoustic impedance variations after CO_2 injection in Weyburn Field: SEG Technical Program Expanded Abstracts, p. 5890–5894.

Waters, K., Somoza, A., Byerley, G., and Rose, P., 2016, Detecting by-passed pay from 3D seismic data using a facies based Bayesian seismic inversion, Forties Field, UKCS: SEG International Exposition and 86th Annual Meeting, Expanded Abstracts, p. 2871–2875.

White, R.E., 1997, The accuracy of well ties—practical procedures and examples: SEG Annual International Meeting, Expanded Abstracts, v. 2, p. 2126.

Wood, A.B., 1941, A textbook of sound: MacMillan.

APPENDIX A

COMPLEMENT OF WELL-TO-SEISMIC TIE FOR WEB-AVO

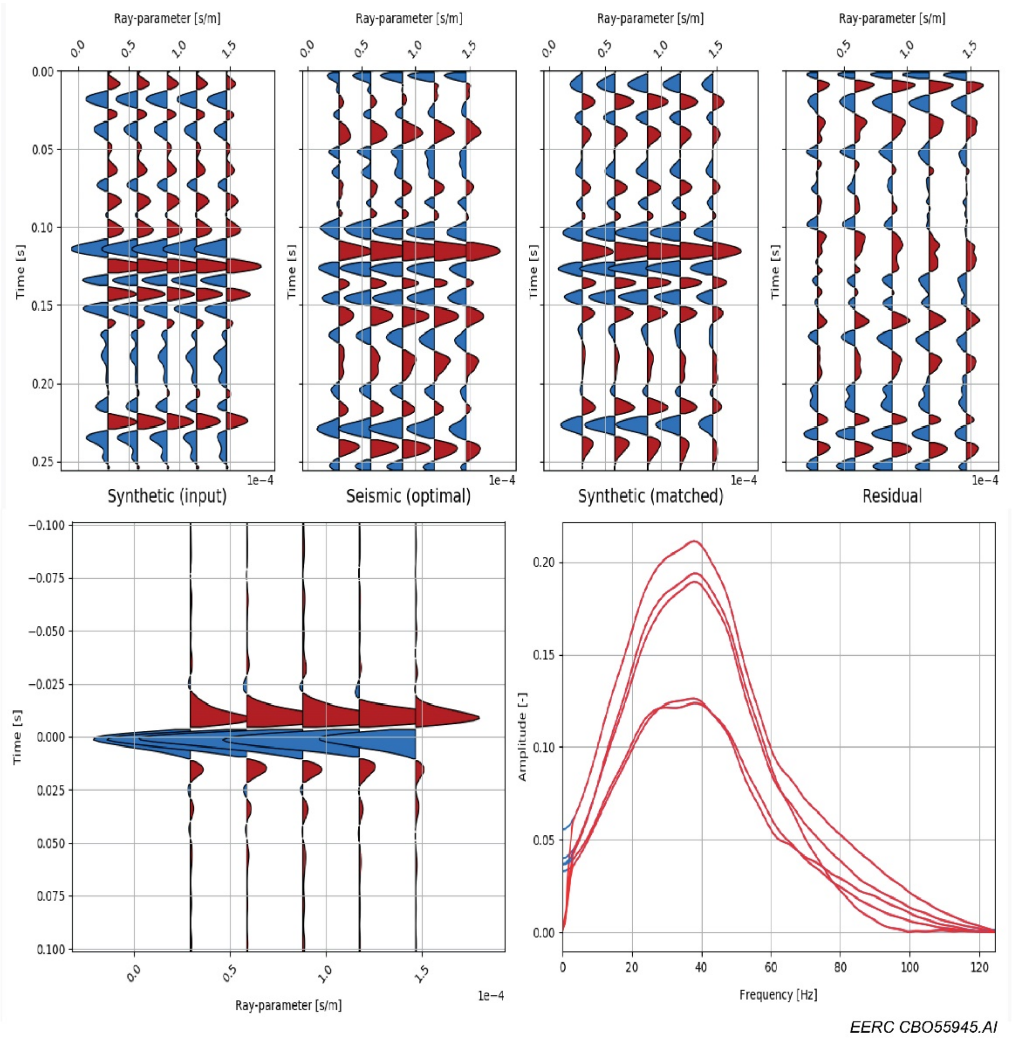

Figure A-1. Example of seismic-to-well tie at Well 56-14R using the Kennett modeling method to generate synthetic data. Top (left to right): initial synthetic data, seismic data, matched synthetic data, and residuals. Bottom (left to right): estimated wavelets in the time and frequency domains.

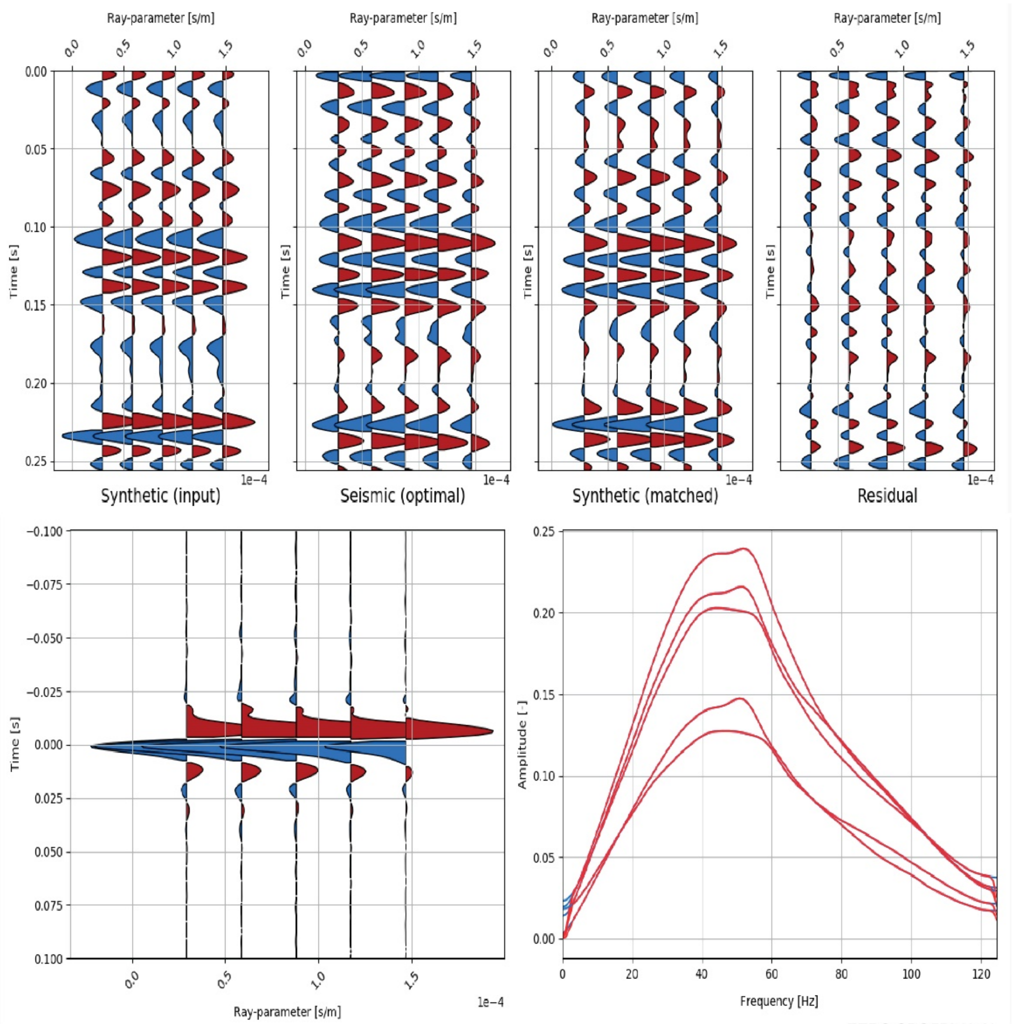

EERC CBO55946.AI

Figure A-2. Example of seismic-to-well tie at Well 33-14R using the Kennett modeling method to generate synthetic data. Top (left to right): initial synthetic data, seismic data, matched synthetic data, and residuals. Bottom (left to right): estimated wavelets in the time and frequency domains.

APPENDIX B

COMPLEMENT OF SIMULTANEOUS WEB-AVO INVERSION OF THE BASELINE AND MONITOR SURVEYS

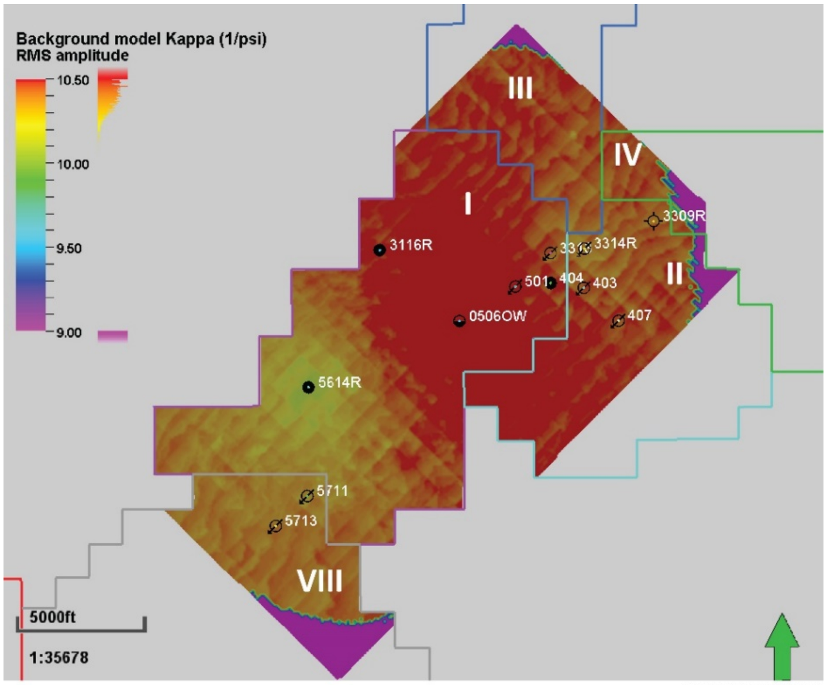

EERC CBO55947.AI

Figure B-1. Background map of compressibility (kappa). The root mean square (RMS) values of kappa are calculated from the Springen Ranch to Skull Creek horizons using a grid size of 82.5 × 82.5 ft.

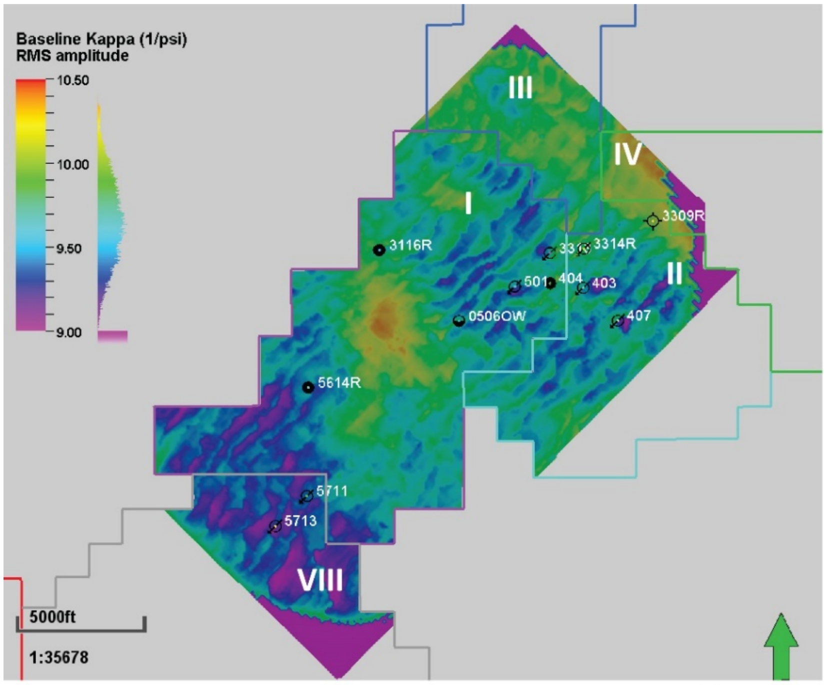

EERC CBO55948.AI

Figure B-2. Baseline map of compressibility (kappa). The RMS values of kappa are calculated from the Springen Ranch to Skull Creek horizons using a grid size of 82.5 × 82.5 ft.

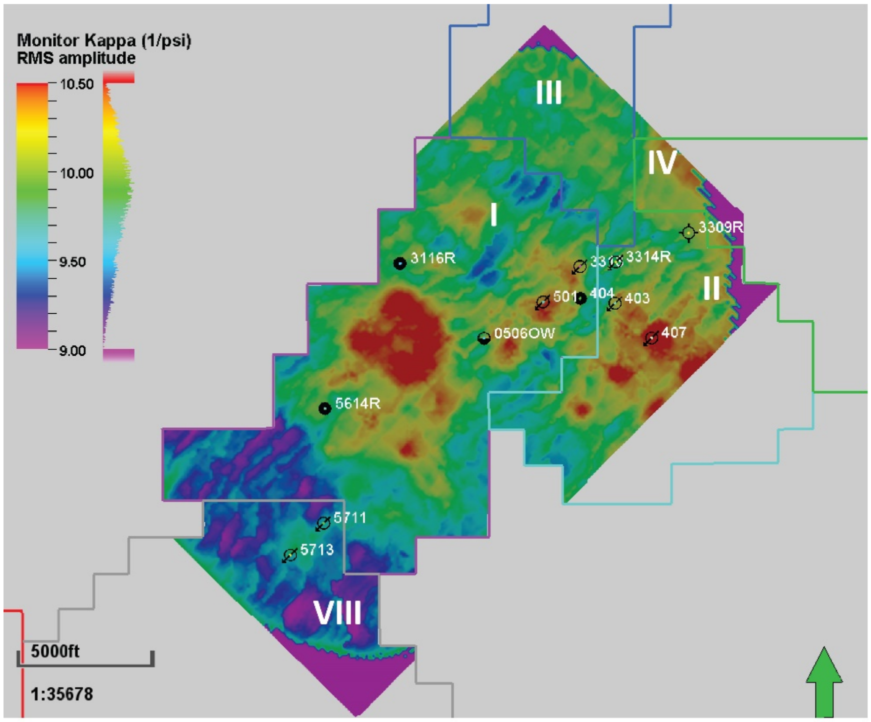

EERC CBO55949.AI

Figure B-3. Monitor map of compressibility (kappa). The RMS values of kappa are calculated from the Springen Ranch to Skull Creek horizons using a grid size of 82.5 × 82.5 ft.

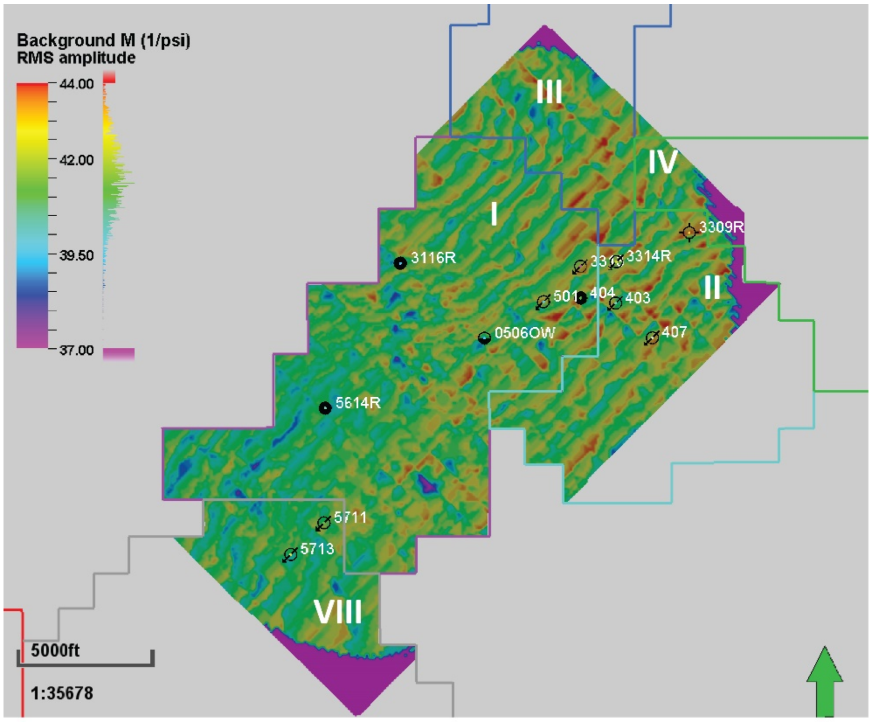

EERC CBO55950.AI

Figure B-4. Background map of shear compliance (M). The RMS values of M are calculated from the Springen Ranch to Skull Creek horizons using a grid size of 82.5 × 82.5 ft.

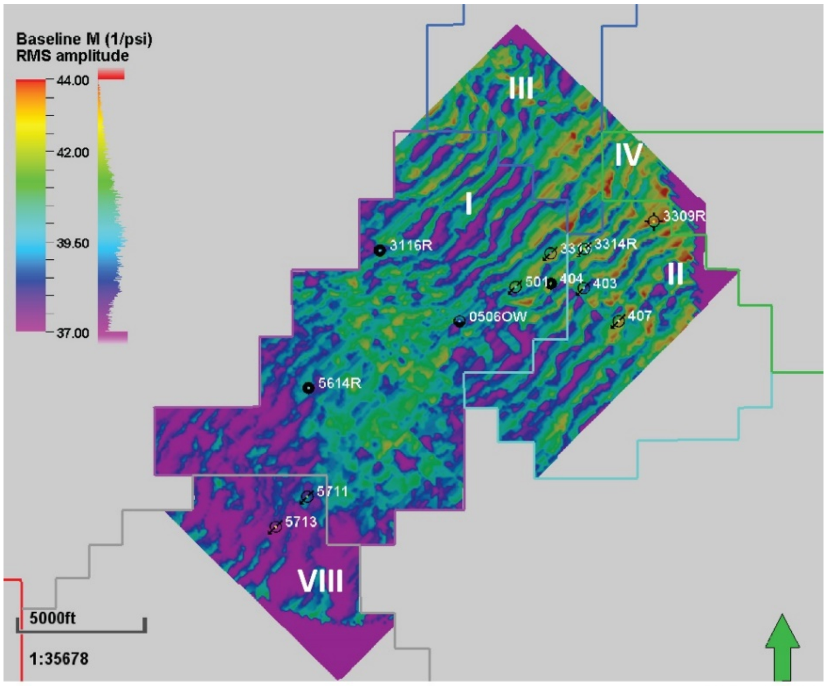

EERC CBO55951.AI

Figure B-5. Baseline map of shear compliance (M). The RMS values of M are calculated from the Springen Ranch to Skull Creek horizons using a grid size of 82.5 × 82.5 ft.

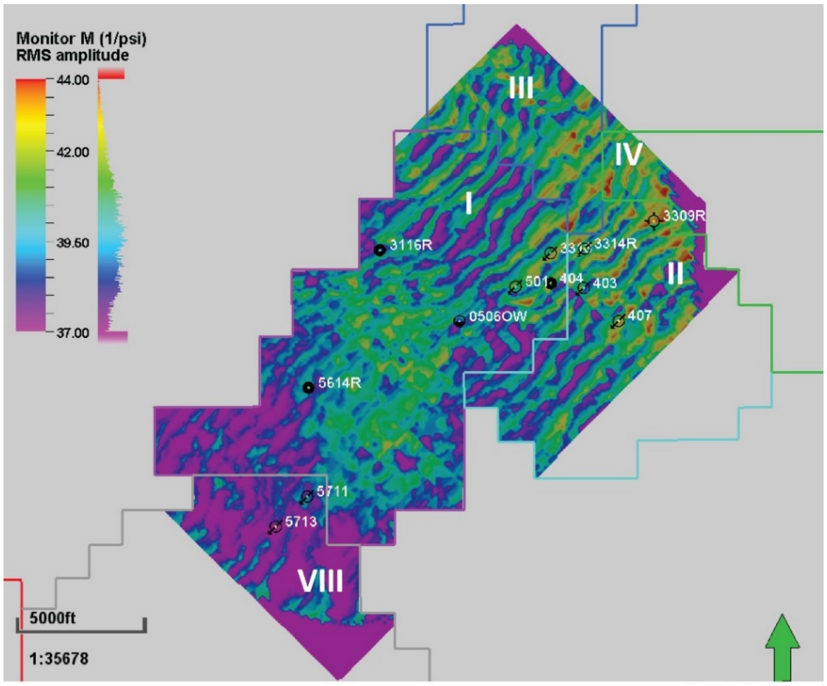

EERC CBO55952.AI

Figure B-6. Monitor map of shear compliance (M). RMS values of M values calculated from the Springen Ranch to Skull Creek horizons using a grid size of 82.5 × 82.5 ft.

APPENDIX C

COMPLEMENT OF WEB-AVO TO RESERVOIR PROPERTIES

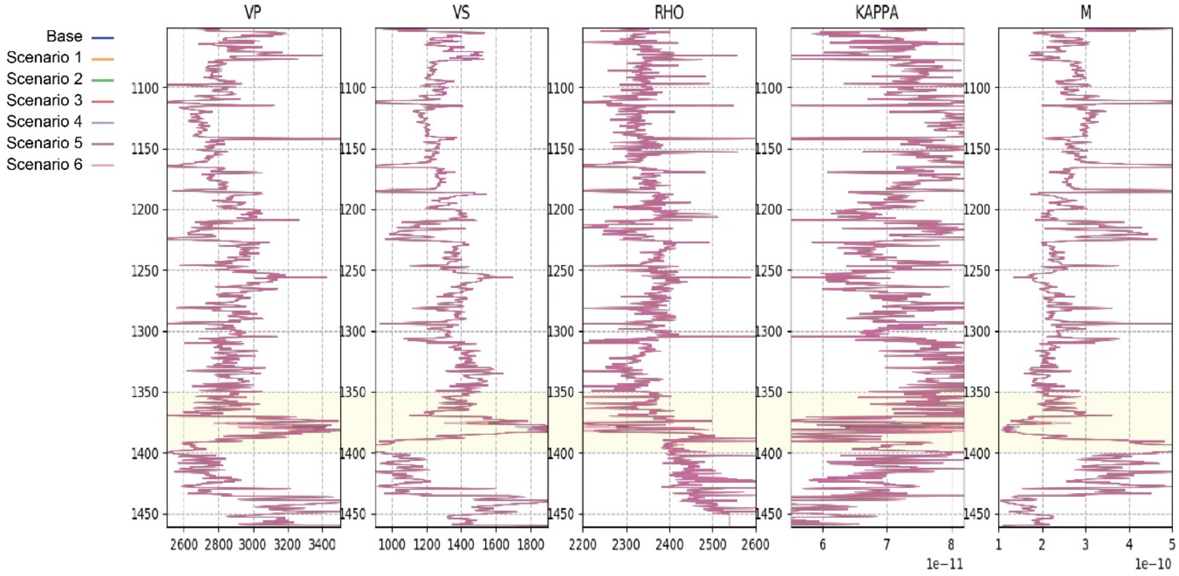

EERC CBO55954.AI

Figure C-1. Simulated logs for different rock physics scenarios. Elastic properties of different scenarios based on Well 05-06 OW: Vp, Vs, density (rho), compressibility (kappa), and shear compliance (M).

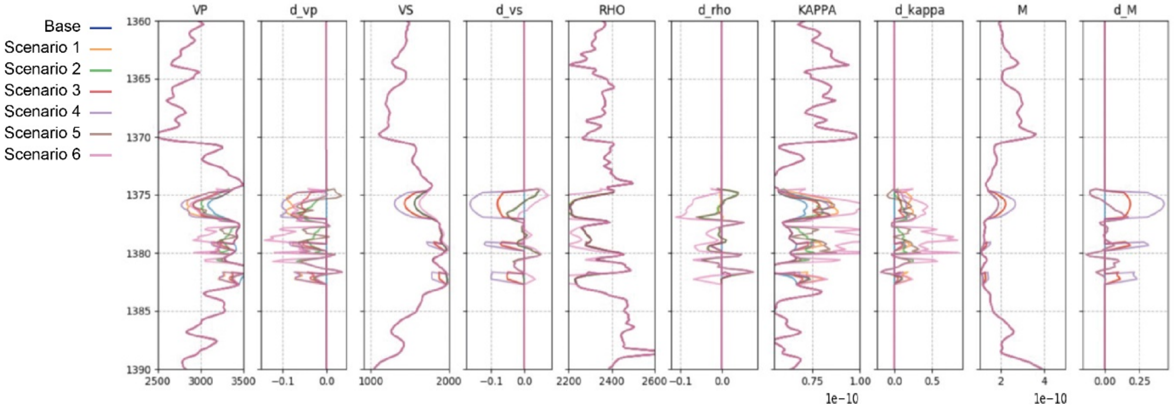

EERC CBO55955.AI

Figure C-2. Simulated logs for different rock physics scenarios. Zoom in to the interval of 1360–1390 m of the originally estimated logs. Vp, Delta_Vp (changes of Vp), Vs, Delta_Vs (changes of Vs), density (rho), Delta_Rho (changes of density), compressibility (kappa), Delta_Kappa (changes of compressibility), shear compliance (M), and Delta_M (changes of shear compliance).

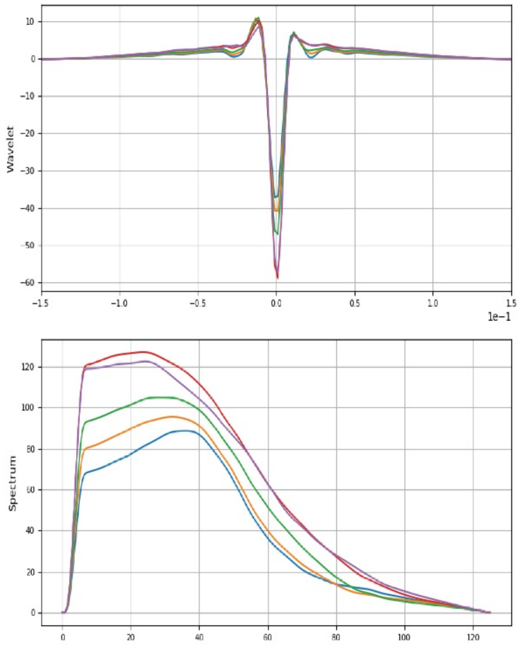

EERC CBO55956.AI

Figure C-3. Input to simulated synthetic seismic data using the Kennett modeling method. Estimated wavelets based on the baseline logs.

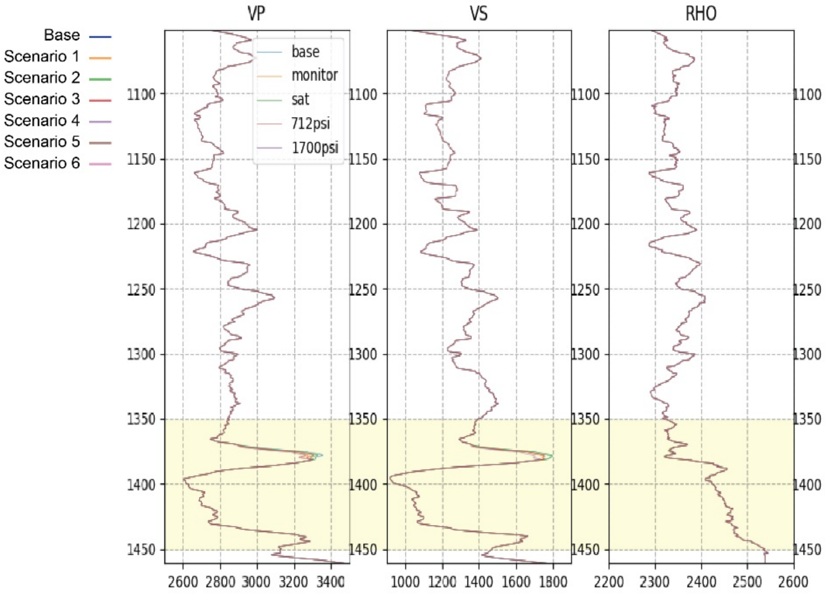

EERC CBO55957.AI

Figure C-4. Log properties of different scenarios for the simulated synthetic data.

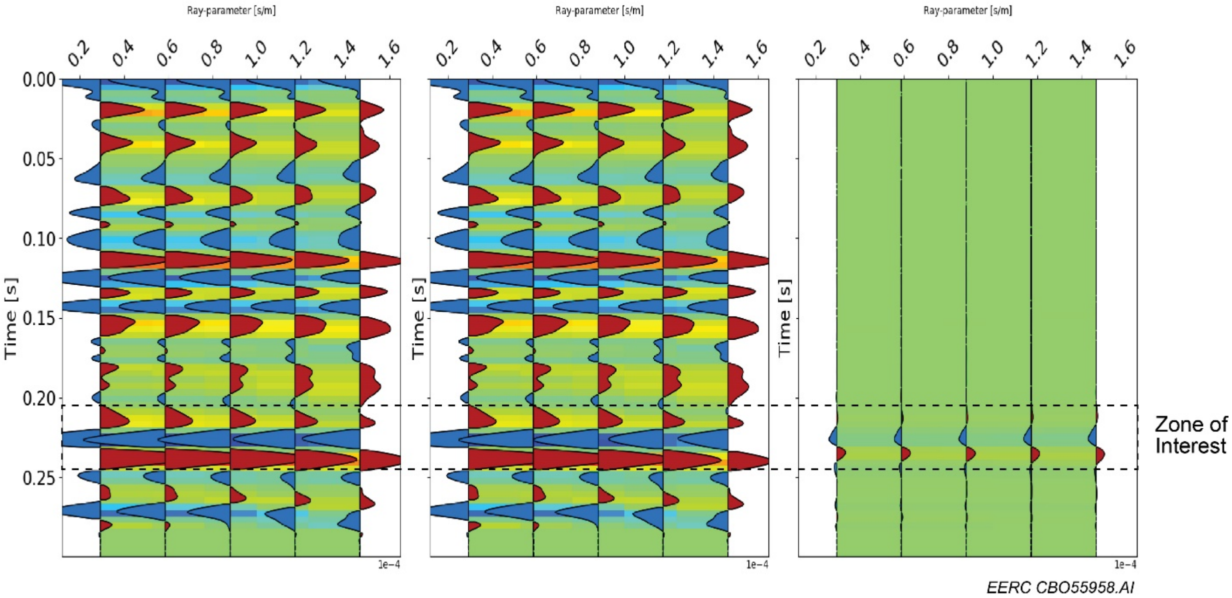

Figure C-5. Simulated synthetic seismic data at Well 05-06 OW. Scenario 5: time-lapse changes due only to the substitution of all the oil by CO_2 (assuming constant pressure). Left to right panels: baseline, monitor, difference. A very small time-lapse signal due to replacing oil with CO_2 and a small AVO effect is observed.

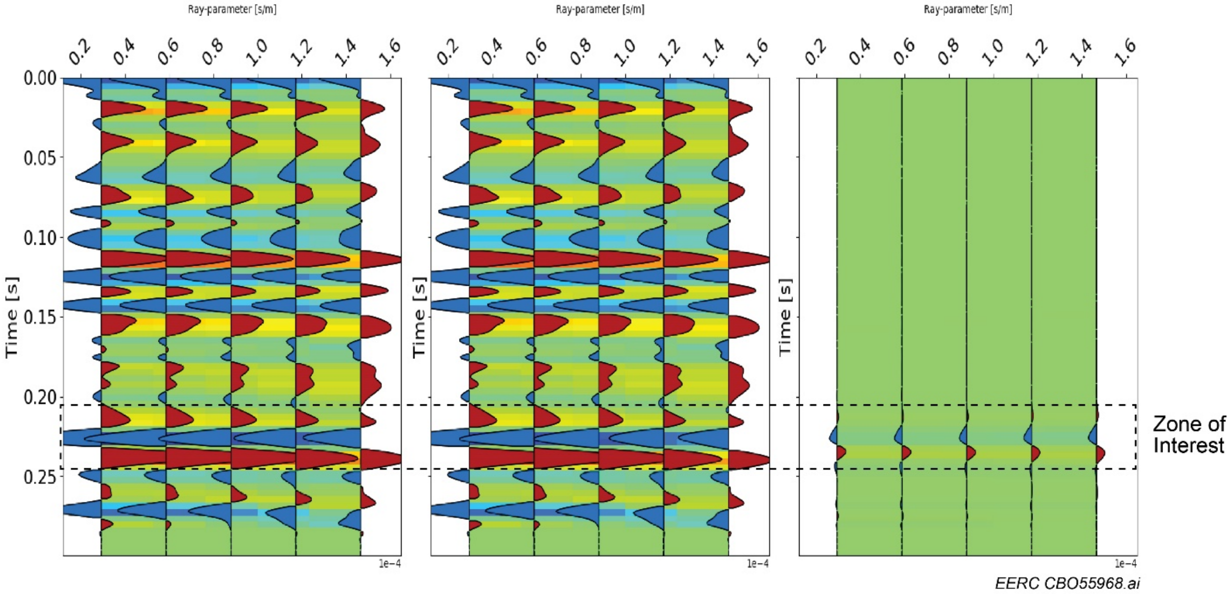

Figure C-6. Simulated synthetic seismic data at Well 05-06 OW. Scenario 6: time-lapse changes due only to the substitution of all the water by CO_2 (assuming constant pressure). Left to right panels: baseline, monitor, difference. A strong time-lapse signal due to replacing water with CO_2 and a small AVO effect is observed.

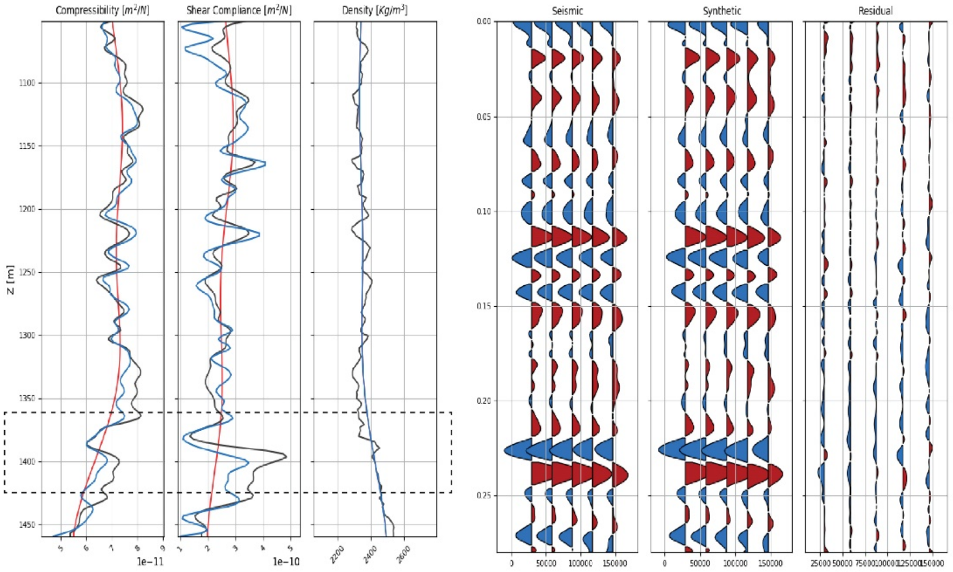

EERC CBO55959.AI

Figure C-7. WEB-AVO inversion of synthetic scenarios. Baseline: saturation and in situ pressure of baseline data are considered. First three panels from the left: red line: background, black line: true properties, blue line: inverted results.

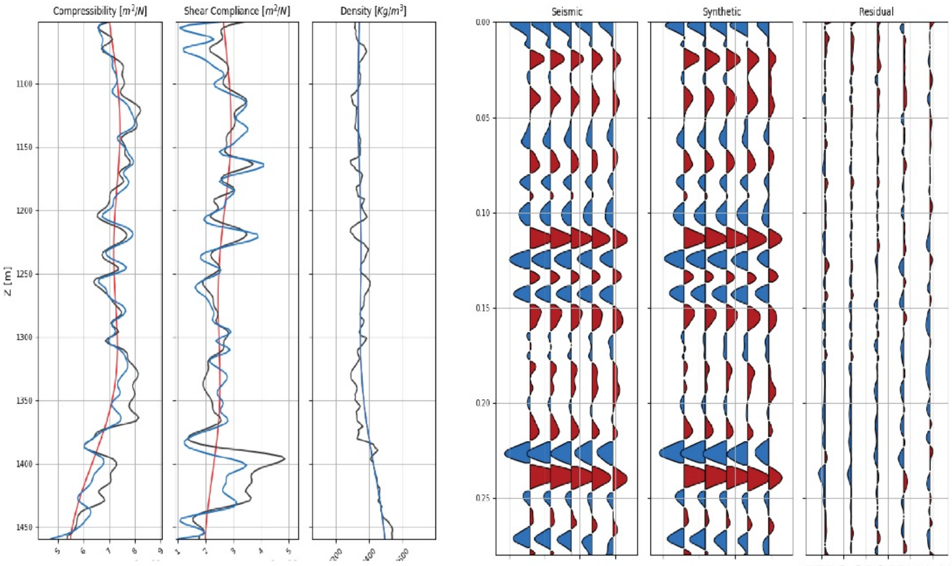

EERC CBO55960.AI

Figure C-8. WEB-AVO inversion of synthetic scenarios. Scenario 1: saturation and pressure change (712 psi) of monitor data are considered. First three panels from the left: red line: background, black line: true properties, blue line: inverted results.

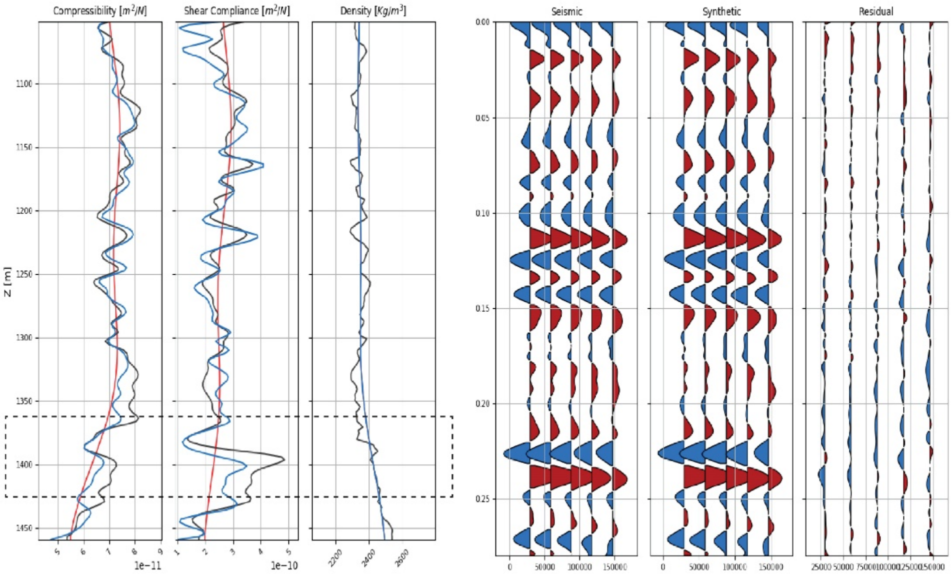

EERC CBO55961.AI

Figure C-9. WEB-AVO inversion of synthetic scenarios. Scenario 2 (only saturation changes): saturation of monitor and in situ pressure. First three panels from the left: red line: background, black line: true properties, blue line: inverted results.

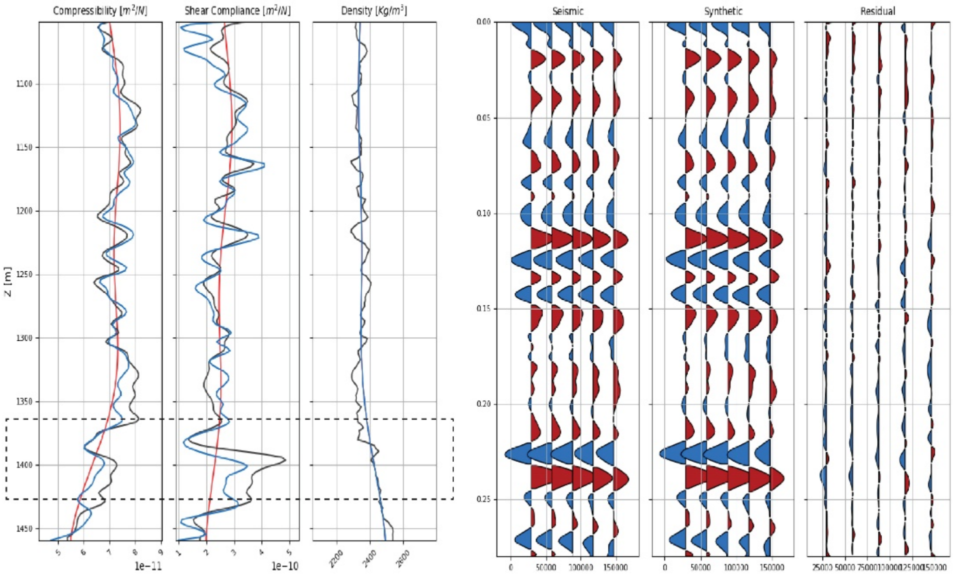

EERC CBO55962.AI

Figure C-10. WEB-AVO inversion of synthetic scenarios. Scenario 3 (only pressure changes): baseline saturation and monitor pressure changes (712 psi). First three panels from the left: red line: background, black line: true properties, blue line: inverted results.

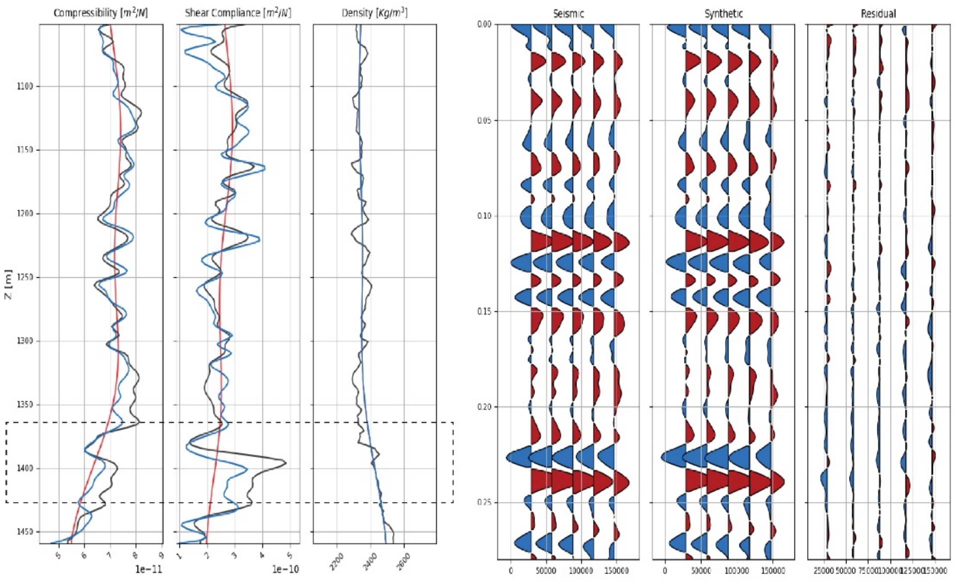

EERC CBO55963.AI

Figure C-11. WEB-AVO inversion of synthetic scenarios. Scenario 4 (only pressure changes): baseline saturation and exaggerated pressure changes (1700 psi). First three panels from the left: red line: background, black line: true properties, blue line: inverted results.

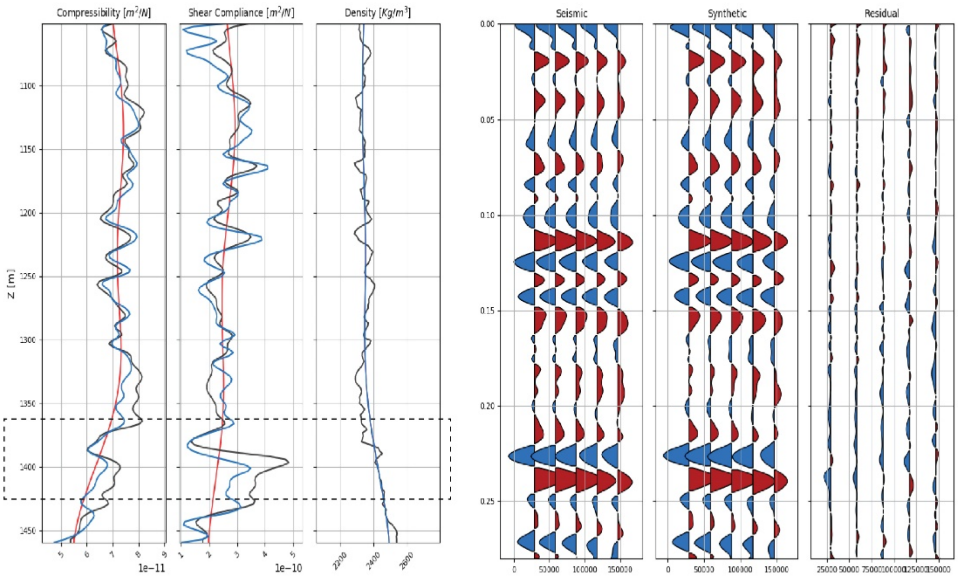

EERC CBO55964.AI

Figure C-12. WEB-AVO inversion of synthetic scenarios. Scenario 5 (oil by O_2): oil replaced with CO_2 and in situ pressure. First three panels from the left: red line: background, black line: true properties, blue line: inverted results.

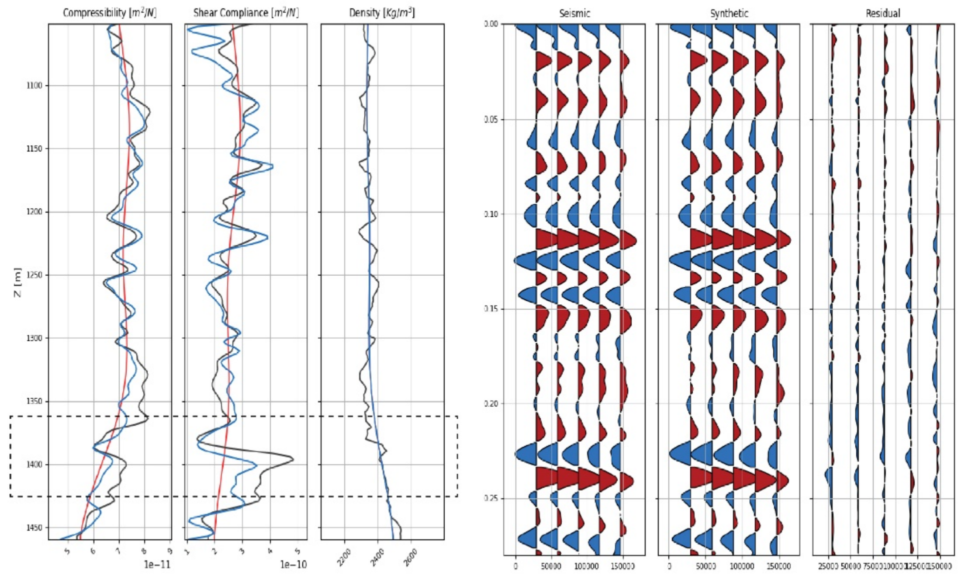

EERC CBO55965.AI

Figure C-13. WEB-AVO inversion of synthetic scenarios. Scenario 6 (water by CO_2): water replaced with CO_2 and in situ pressure. First three panels from the left: red line: background, black line: true properties, blue line: inverted results.

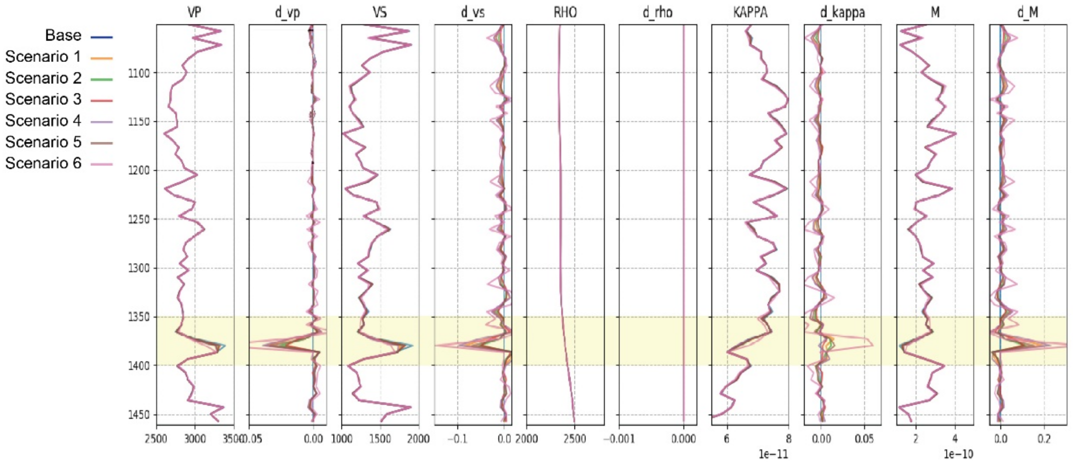

EERC CBO55966.AI

Figure C-14. WEB-AVO inversion of synthetic scenarios. Summary of inversion results for well logs in the interval 1051–1461 m.

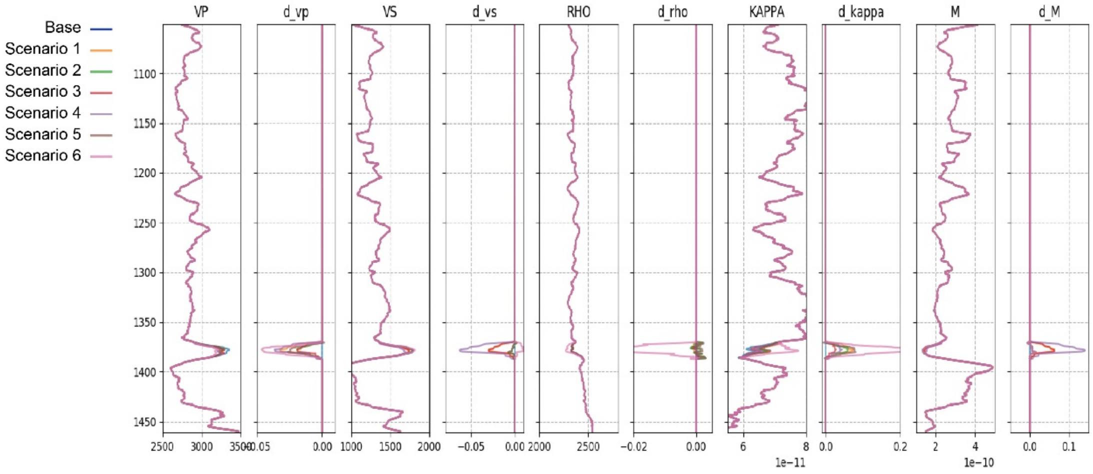

EERC CBO55967.AI

Figure C-15. WEB-AVO inversion of synthetic scenarios. Summary of inversion results for well logs in the interval 1051–1461 m. A 10-m Backus averaging was used to upscale the logs to effective properties on the seismic scale.

APPENDIX D

LOG PREDICTION

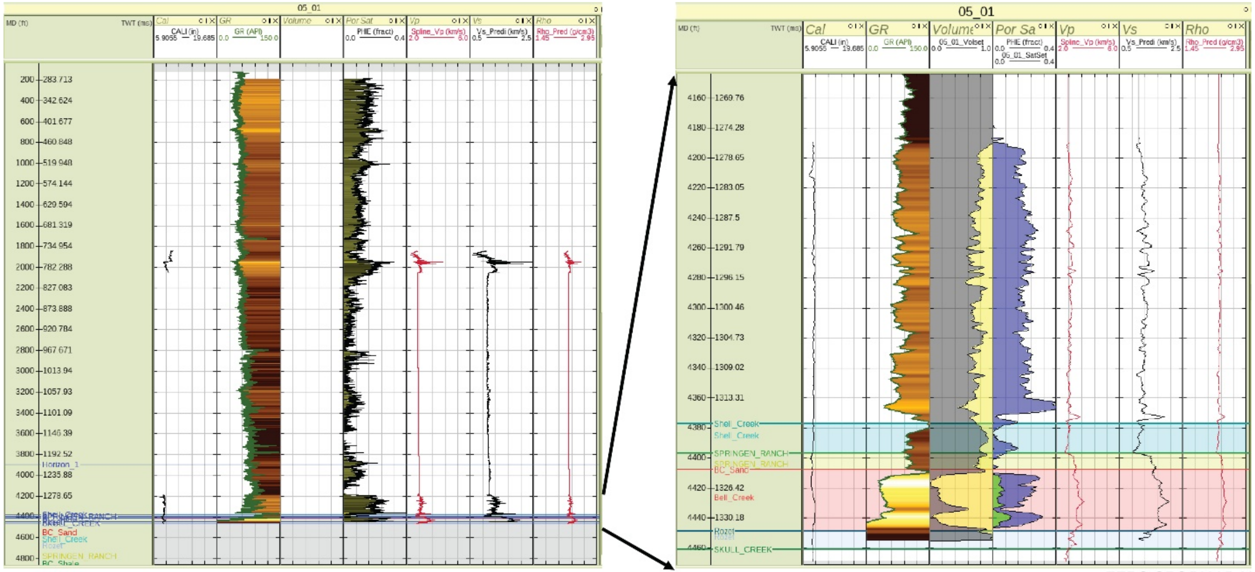

EERC CBO56395.AI

Figure D-1. Example of shear-wave velocity (Vs) and density (rho) prediction for 05-01 well according to the procedure described in the main text. Left to right log tracks: caliper (Cal), gamma ray (GR), volume (Volset), effective porosity and saturation (PHIE and SatSet), P-wave velocity (Vp), shear-wave velocity (Vs), and density (rho).

APPENDIX E

PRESSURE SENSITIVITY AND FLUID SUBSTITUTION

Table E-1. Reservoir and Fluid Properties Compiled from Petrophysics, Geology, and Reservoir Simulations May 20, 2019, Version. Gas-oil ratio (GOR) for September 2012 to March 2013 is for hydrocarbon gas. Since the hydrocarbon gas in GOR is so low, the GOR for October 2014 is primarily for CO_2.

Belle Creek Reservoir	Sep-12	Dec-12	Mar-13	Oct-14
Temperature (degC)	108 deg F	108 deg F	108 deg F	108 deg F
Ave Reservoir Pore Pressure (psi)	1718 psia @ 05-06OW	2262 psia @ 05-06OW	2269 psia @ 05-06OW	2539 psia @ 05-06OW
Water				
Salinity (ppm)	6013	6013	6013	6013
Composition Na, K, Ca (%)	0.98, 0.01, 0.01	0.98, 0.01, 0.01	0.98, 0.01, 0.01	0.98, 0.01, 0.01
Na+, mg/L	44-1350	44-1350	44-1350	44-1350
K+, mg/L	8.4-9.3	8.4-9.3	8.4-9.3	8.4-9.3
Ca2+, mg/L	12.7-207	12.7-207	12.7-207	12.7-207
Maximum GWR for CO2				26.9 l/l or 1.12 mol/kg
Oil				
GOR Hydrocarbon (liter/liter)	0-1.78	0-1.78	0-1.78	173
API oil	37.8	37.8	37.6	33.1
Gas Gravity (air)	0.83	0.84	0.84	2.18

Table E-2. Fluid Properties Modeled with FLAG Algorithm in RokDoc

Sept 2012	Rho (g/cc)	Vp (km/s)	K (Gpa)
Water	1001	1.557	2.428
Dead Oil	0.817	1.342	1.472
Gas	0.157	0.389	0.024

Mar 2013	Rho (g/cc)	Vp (km/s)	K (Gpa)
Water	1.002	1.564	2.450
Dead Oil	0.820	1.363	1.521
Gas	0.220	0.453	0.045

Dec 2012	Rho (g/cc)	Vp (km/s)	K (Gpa)
Water	1.002	1.564	2.450
Dead Oil	0.820	1.362	1.521
Gas	0.219	0.453	0.045

Oct 2014	Rho (g/cc)	Vp (km/s)	K (Gpa)
Water	1.003	1.567	2.462
Dead Oil	0.844	1.403	1.662
Pure CO2	0.774	0.481	0.179

Note: In FLAG oil gas saturation and gas gravity is intended hydrocarbon gas. Use with CO_2 produces an approximation of questionable quality.

Table E-3. Properties Used in the FLAG Model to Estimate Brine, Dead Oil, and CO_2 Fluid Model in Figure 40. All fluids were at 2540 psi and 108°F.

Oct 2014	Rho (g/cc)	Vp (km/s)	K (Gpa)
Water	1.003	1.567	2.462
Dead Oil	0.844	1.403	1.662
Pure CO2	0.774	0.481	0.179

Table E-4. Properties Used in the Han and Others Model (2012) to Estimate Oil + CO_2 Fluid Model in Figure 40. All fluids were at 2540 psi and 108°F.

Oct 2014	Rho (g/cc)	Vp (km/s)	K (Gpa)
Oil+CO2	0.864	0.978	0.826

Table E-5. Properties Used in the Han and Sun Model (2013) to Estimate Brine + CO_2 Fluid Model. In Figure 40. All fluids were at 2540 psi and 108°F.

Oct 2014	Rho (g/cc)	Vp (km/s)	K (Gpa)
H2O+CO2	1.012	1.570	2.494

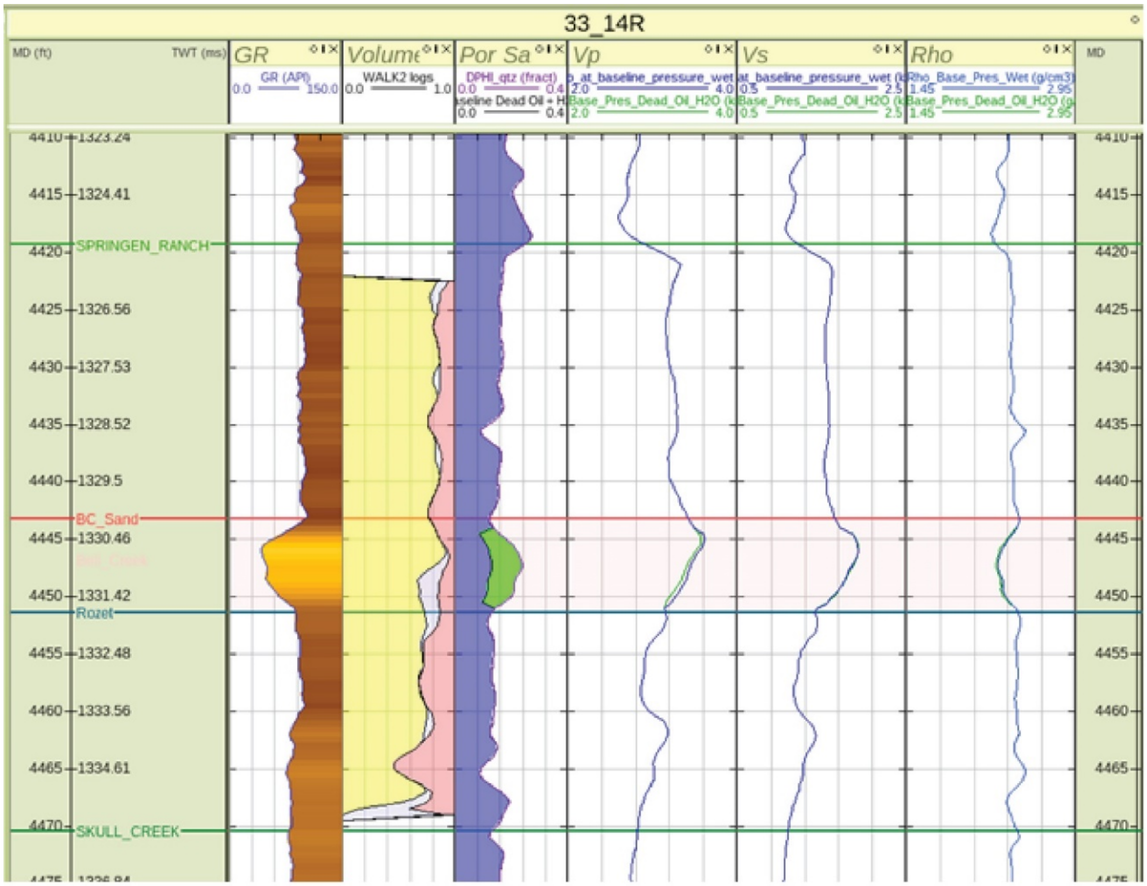

EERC CBO56341.AI

Figure E-1. Baseline (September 2012) fluid substitution models into sandy facies for 33-14R well. Left to right tracks: gamma ray (GR), lithology (volume), saturation with density porosity (Por Sa) (phid) (dark blue: brine; green: dead oil), P-wave velocity (Vp), S-wave velocity (Vs), density (Rho). Blue curves: 1.0 brine saturation, green curves: dead oil + brine models.

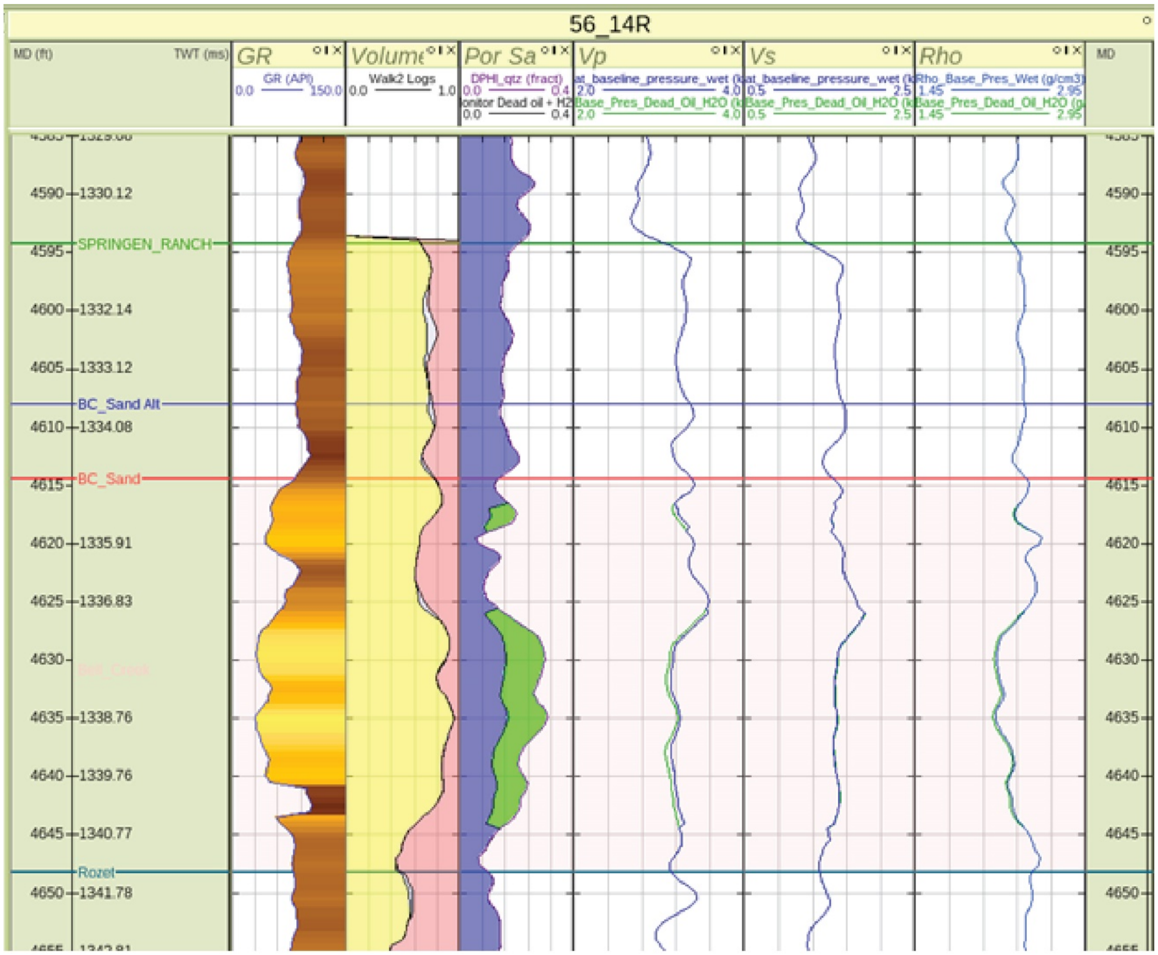

EERC CBO56342.AI

Figure E-2. Baseline (September 2012) fluid substitution models into sandy facies for 56-14R well. Left to right tracks: gamma ray (GR), lithology (volume), saturation with density porosity (Por Sa) (phid) (dark blue: brine; green: dead oil), P-wave velocity (Vp), S-wave velocity (Vs), density (Rho). Blue curves: 1.0 brine saturation, green curves: dead oil + brine models.

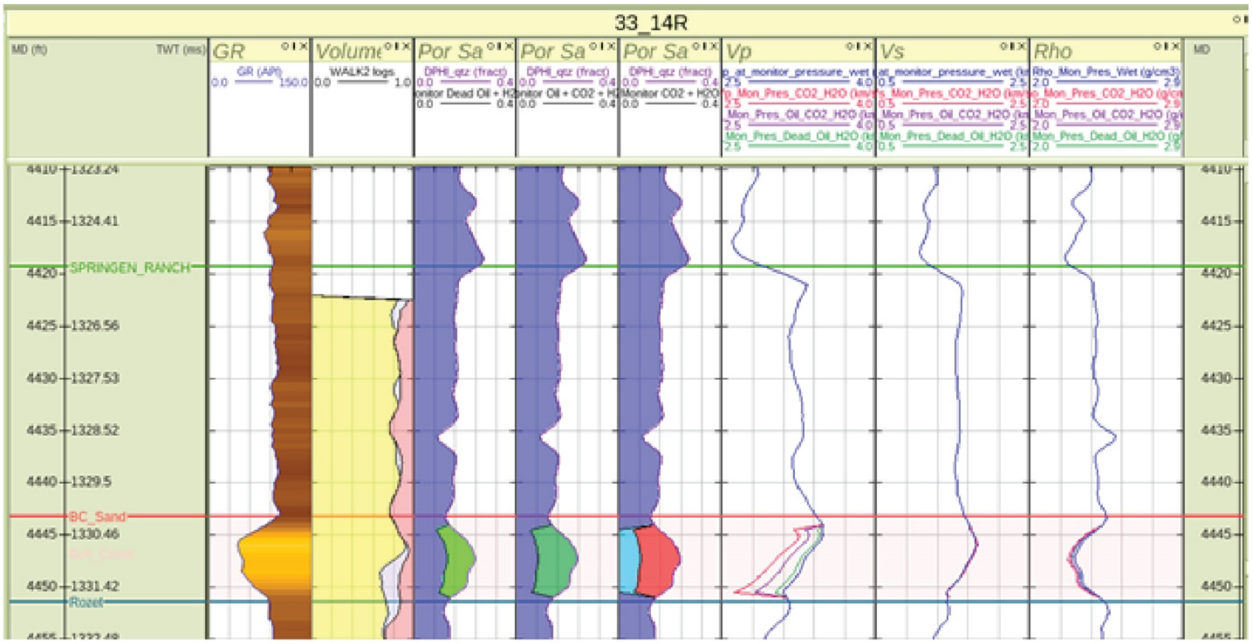

EERC CBO56343.AI

Figure E-3. Monitor (October 2014) fluid substitution into sandy facies for 33-14R well. Left to right tracks: gamma ray (GR), lithology (volume), and three saturation with density porosity (Por Sa) (phid) scenarios: 1) brine (dark blue) and dead oil (green), 2) brine (blue) and CO_2 saturated oil (dark green), 3) brine (dark blue), CO_2 saturated brine (light blue) and supercritical CO_2 (red), P-wave velocity (Vp), S-wave velocity (Vs), density (rho). Blue curves: 1.0 brine saturation, green curves: brine + dead oil models, purple curve: brine and CO_2 saturated oil, red: CO_2 saturated brine and CO_2.

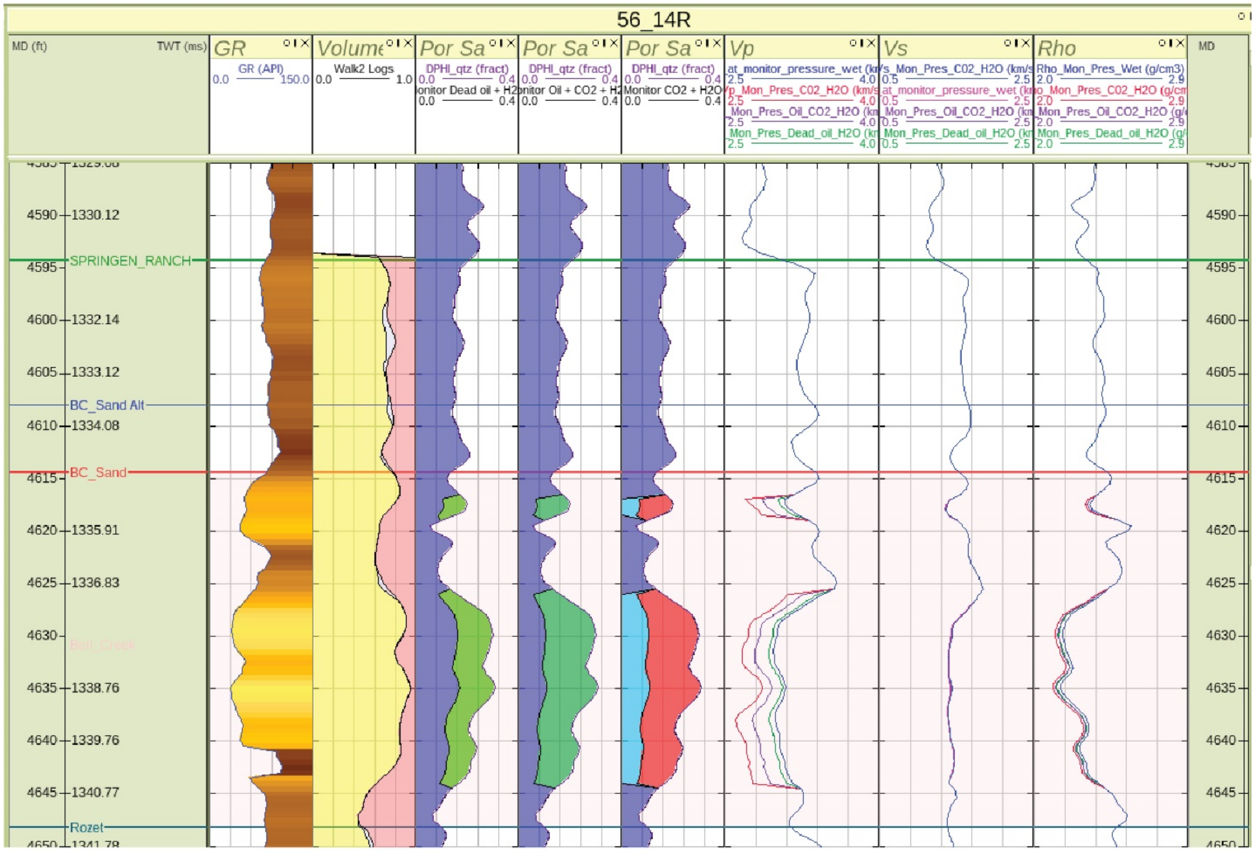

EERC CBO56344.AI

Figure E-4. Monitor (October 2014) fluid substitution into sandy facies for 56-14R well. Left to right tracks: gamma ray (GR), lithology (volume), and three saturation with density porosity (Por Sa) (phid) scenarios: 1) brine (dark blue) and dead oil (green), 2) brine (blue) and CO_2-saturated oil (dark green), 3) brine (dark blue), CO_2-saturated brine (light blue) and supercritical CO_2 (red), P-wave velocity (Vp), S-wave velocity (Vs), density (rho). Blue curves: 1.0 brine saturation, green curves: brine + dead oil models, purple curve: brine and CO_2-saturated oil, red: CO_2-saturated brine and CO_2.

Layer over Half-Space Models

The layer over half-space models representing the simplest form of AVO modeling was considered. The model properties are averages of the intervals of interest, normally consisting of the reservoir and surrounding shales. The Bell Creek reservoir has a thickness that is close to one-third of seismic tuning which is too thin to be representative of the properties affecting the seismic data. The full Muddy Formation is close to seismic tuning thickness. The average properties of the Muddy Formation were used with appropriate fluid substitutions in Bell Creek. The seal intervals are the Mowry and the Skull Creek above and below the Muddy.

Layer over half-space models were generated for the monitor fluid substitution models. The baseline cases are expected to be like the brine-filled and dead oil + brine cases of the monitor models. The baseline pore and effective pressures are different. However, since the baseline fluids are gas-free, this should have little effect on the AVO response. The reflection coefficients are calculated using two-term Aki and Richards (1980) approximation over angles of incidence from 0° to 50°.

The predicted AVO response in Figure E-5 is Class 1 or 2 except when the Muddy is missing, then it is Class 4. Replacement of brine in the Bell Creek sand with fluids with lower density and bulk modulus causes dimming. The greatest amplitude reduction is associated with the replacement of brine with a mixture of CO_2 saturated brine + CO_2. The models suggest that the 33-14R is the least sensitive to fluids which is consistent with its thinner, lower-porosity Bell Creek reservoir.

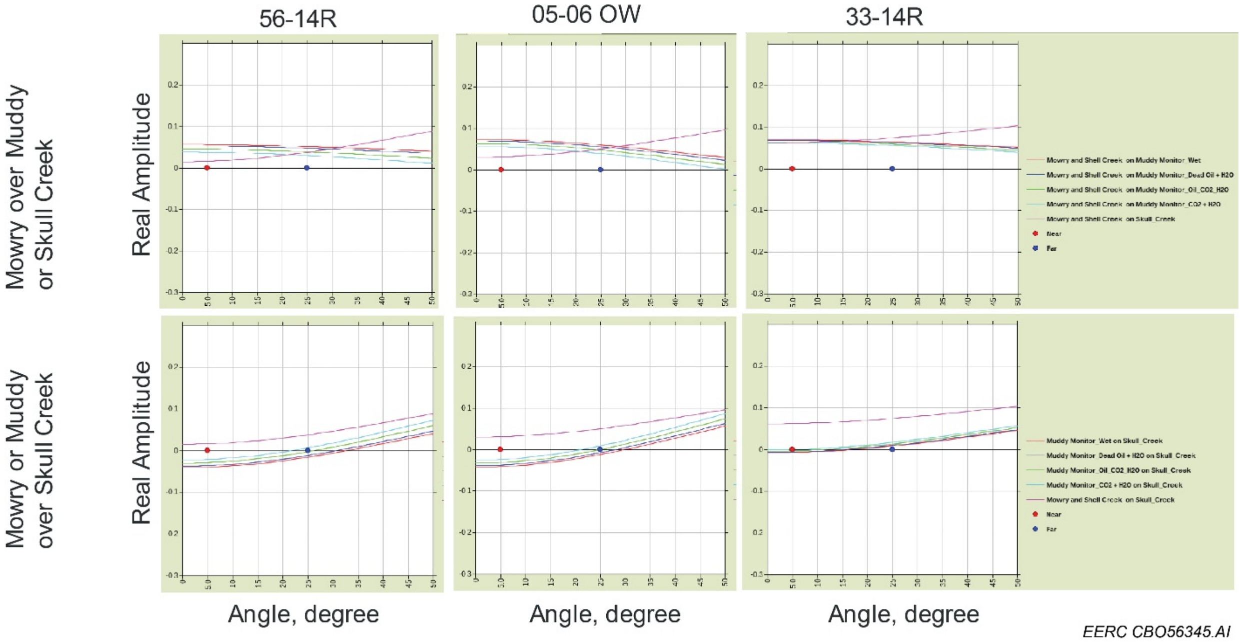

EERC CBO56345.AI

Figure E-5. Amplitude variation with offset (AVO) modeling using a layer over half-space models. Top row: Mowry over Muddy with various fluid substitutions in the Bell Creek sand. Bottom row: Muddy with various fluid substitutions in Bell Creek sand over Skull Creek. Left to right: 56-14R, 05-06 OW, and 33-14R wells. The pink model is the case where the Muddy is absent. The mixture models are brine-saturated with CO_2 + CO_2 (cyan), oil saturated with CO_2 + brine (green), mixture of dead oil and brine (blue), brine (red). The models exhibit Class 2 AVO response.

Synthetic Seismic Gathers

Synthetic seismic gathers were generated for the monitor models. The baseline cases are expected to be like the brine-filled and dead oil + brine of the monitor models. Based on the fluid substitution in the sandy facies cases, we generated 1-D synthetics for the 56-14R (Figure E-6), 33-14R (Figure E-7), and 05-06 OW (Figure E-8) wells. The fluid-substituted logs discussed above were Backus-averaged with a 15-ft smoothing window. The window length passes tests described by Liner and Fei (2007) for a 30 Hz dominant frequency and Folstad and Schoenberg (1992) for a 70-Hz maximum frequency. The reflection coefficient sequence was calculated from the Backus-averaged logs using three-term Aki and Richards (1980) approximation over angles of incidence from 0° to 30° and convolved with an average wavelet (Figure E-9) derived from wavelet extractions in RokDoc at five wells.

The Bell Creek is well below tuning in all three wells. The top and base reflections appear to be related to the approximate top and base of the Muddy which includes the Springen Ranch, Bell Creek, and Rozet intervals. The results are consistent with the simple layer over half-space models. Over the three wells and 12 models, the zero offset amplitude is observed to increase with the bulk modulus and density of the fluids. Wet sand has the highest amplitude and CO_2- and water-saturated sand the lowest. The gradients are similar between each well's models. The brine-filled 05-06 OW sands produce the highest intercept amplitude while the 56-14R produces the lowest intercept amplitude. This appears related to sand quality and reservoir thickness.

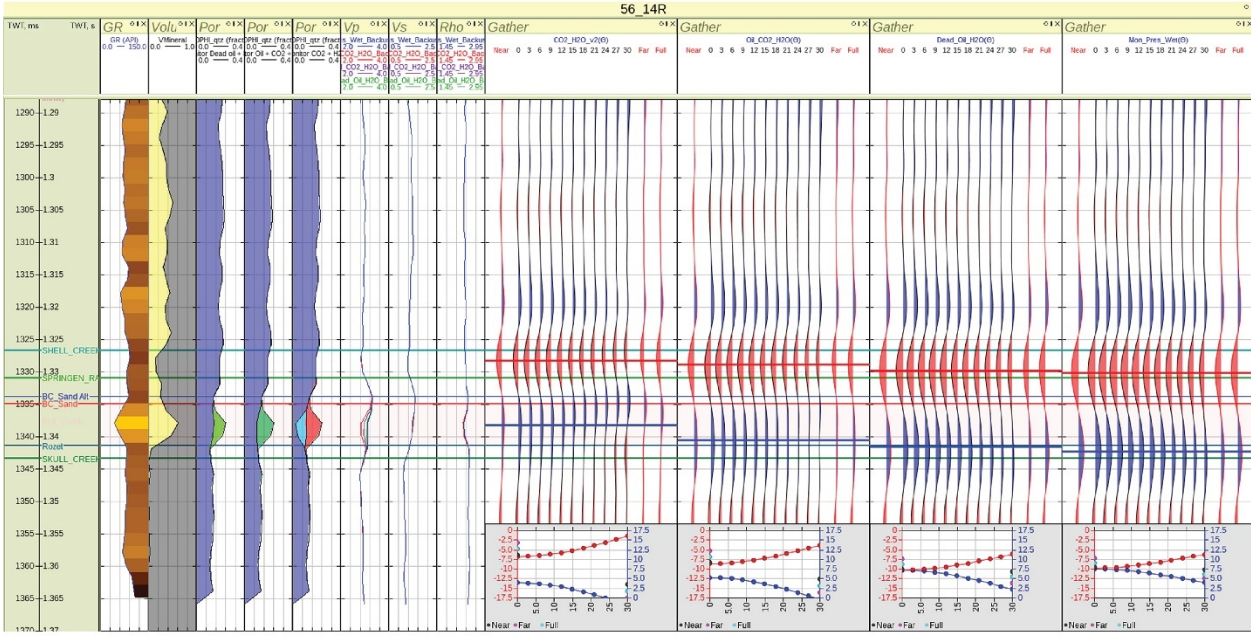

EERC CBO57213.AI

Figure E-6. Synthetic seismograms for the 56-14R well. The mixture models from left to right are brine saturated with CO_2 + CO_2, oil saturated with CO_2 + brine, a mixture of dead oil and brine, and brine. The models exhibit Class 2 AVO response. Intercept amplitude increases from left to right, and gradient is approximately constant.

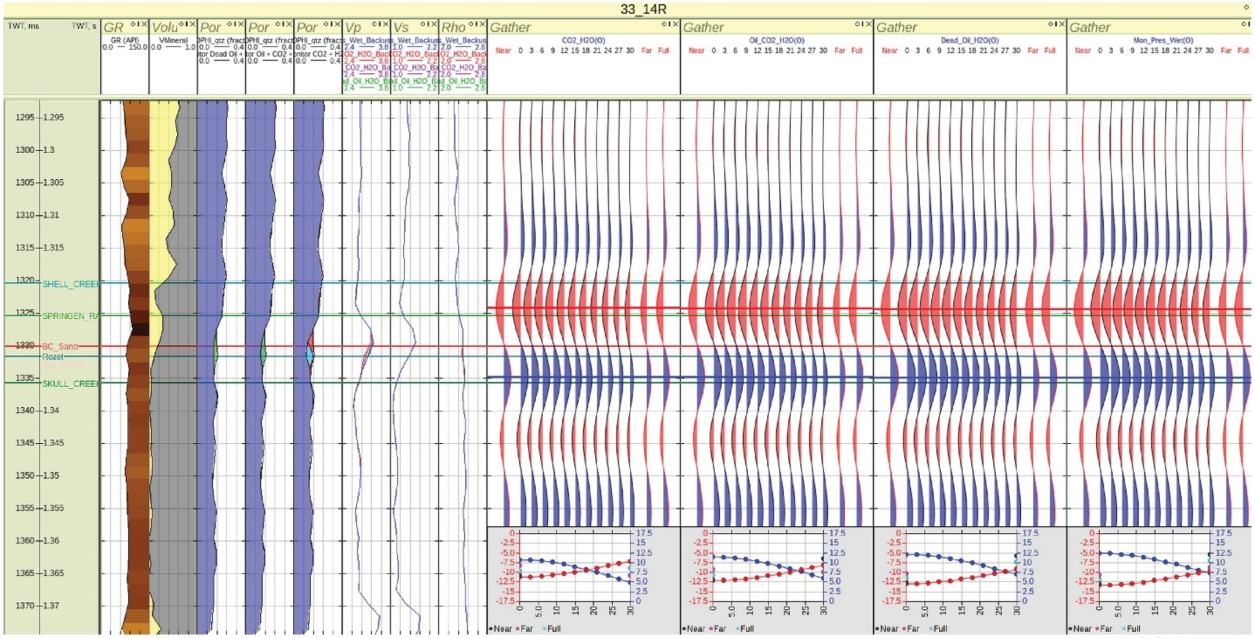

EERC CBO57214.AI

Figure E-7. Synthetic seismograms for the 33-14R well. The mixture models from left to right are brine saturated with CO_2 + CO_2, oil saturated with CO_2 + brine, a mixture of dead oil and brine, and brine. The models exhibit Class 2 AVO response. Intercept amplitude increases from left to right, and gradient is approximately constant.

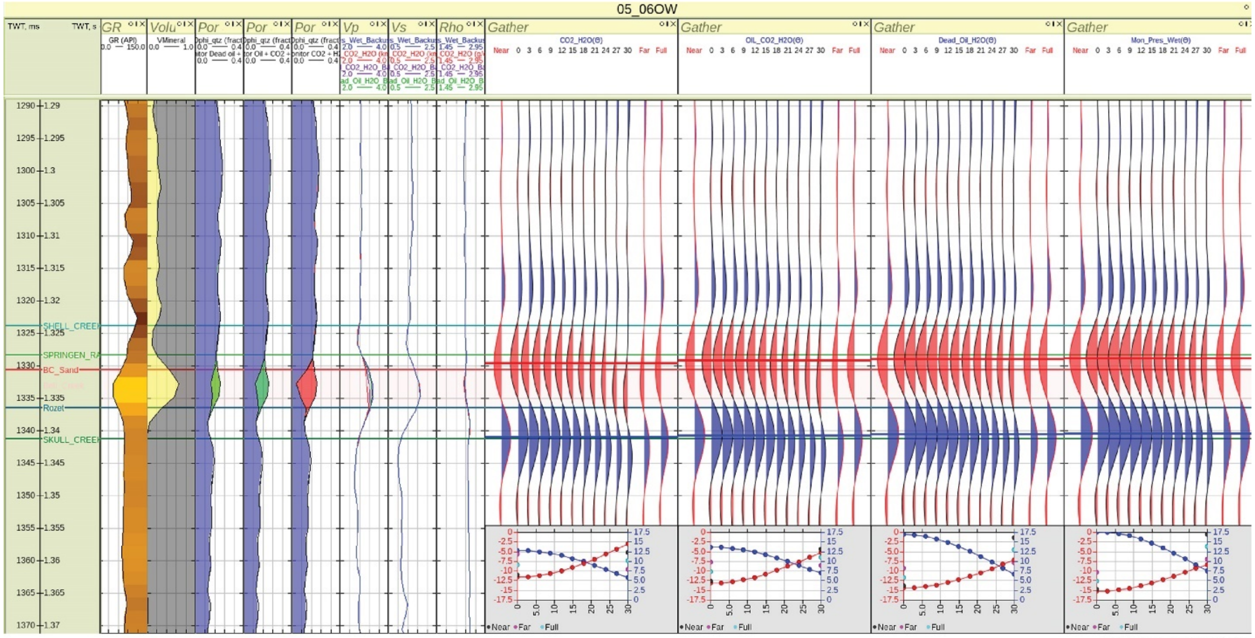

EERC CBO57215.AI

Figure E-8. Synthetic seismograms for the 05-06 OW well. The mixture models from left to right are brine saturated with CO_2 + CO_2, oil saturated with CO_2 + brine, a mixture of dead oil and brine, and brine. The models exhibit Class 2 AVO response. Intercept amplitude increases from left to right, and gradient is approximately constant.

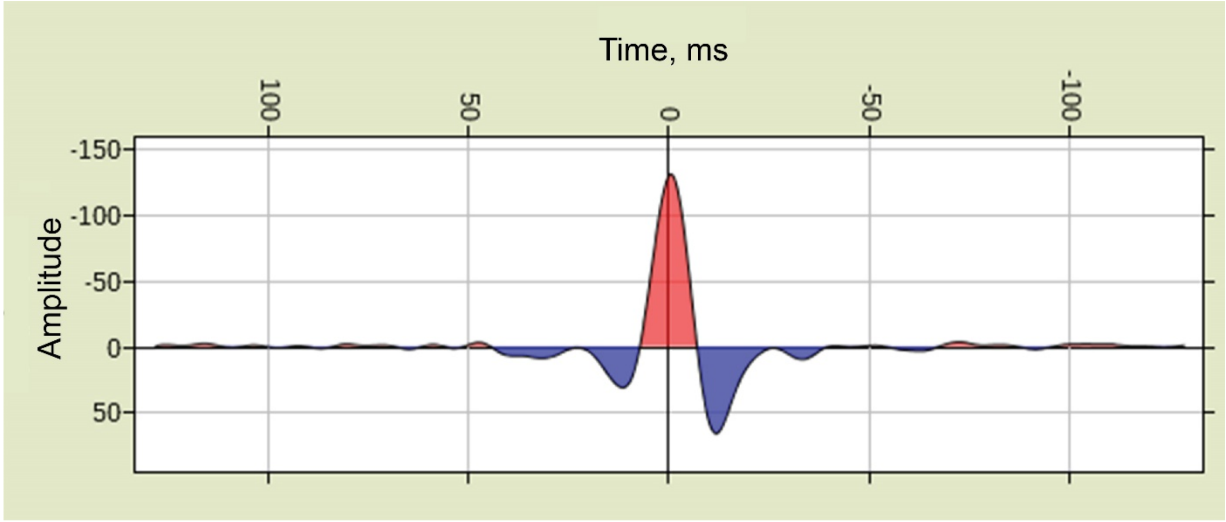

EERC CBO57216.AI

Figure E-9. Wavelet used for modeling. A poststack wavelet derived by averaging the wavelets extracted at 33-09R, 05-06 OW, 33-14R, 56-14R, and 31-16R wells.

REFERENCES

Aki, K., and Richards, P.G., 1980, Quantitative seismology—theory and methods: v. 1, W.H. Freeman and Company.

Folstad, P.G., and Schoenberg, M., 1992, Low-frequency propagation through fine layering: SEG Expanded Abstract, p. 1297–1281.

Liner, C., and Fei, T., 2007, The Backus number—the leading edge: no. 4, p. 420–426.

APPENDIX F

QUALITY CONTROL OF WELL TO FULL SEISMIC STACK TIES FOR JI-FI

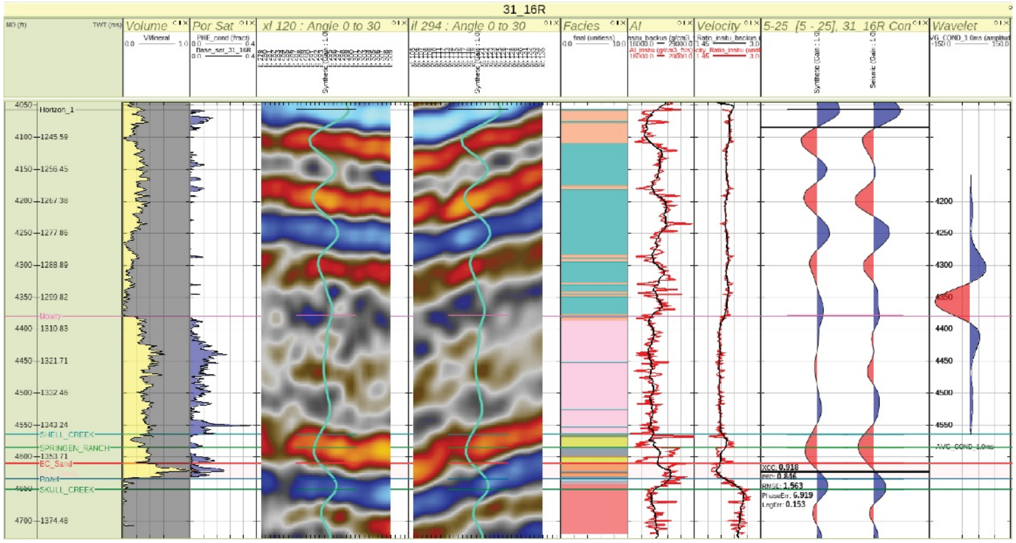

EERC CBO56400.AI

Figure F-1. Example of 31-16R well to seismic tie. Volume: mineral log (mixing type: Voight-Reuss-Hill (weighting), quartz, kaolinite, and calcite); Por Sat: porosity-saturation (mineral: quartz; water = 1, oil = 0, gas = 0); seismic section: crossline (XL) 120; seismic section: inline (IL) 294; facies: estimated facies; AI (acoustic impedance): red line: well in situ AI; black line: seismic AI with Backus averaging; velocity: velocity ratio; red line: well velocity ratio; black line: seismic velocity ratio with Backus ratio; 5–25 (full stack from the 0–10, 10–20, and 20–30 partial angles): Comparison of synthetic seismic trace (left) vs. real seismic trace (right). Wavelet: wavelet estimated from the well to seismic tie. Notice the parameters used to measure the quality of the tie on Seismic Track 5–25: cross correlation (XCC), proportion of energy predicted (PEP), phase error, and tag error. The horizontal lines represent the markers associated with the main features of the logs: Horizon 1, Mowry, Shell Creek, Springen Ranch, Bell Creek (BC) Sand, Rozet, Skull Creek, and TD Horizon.

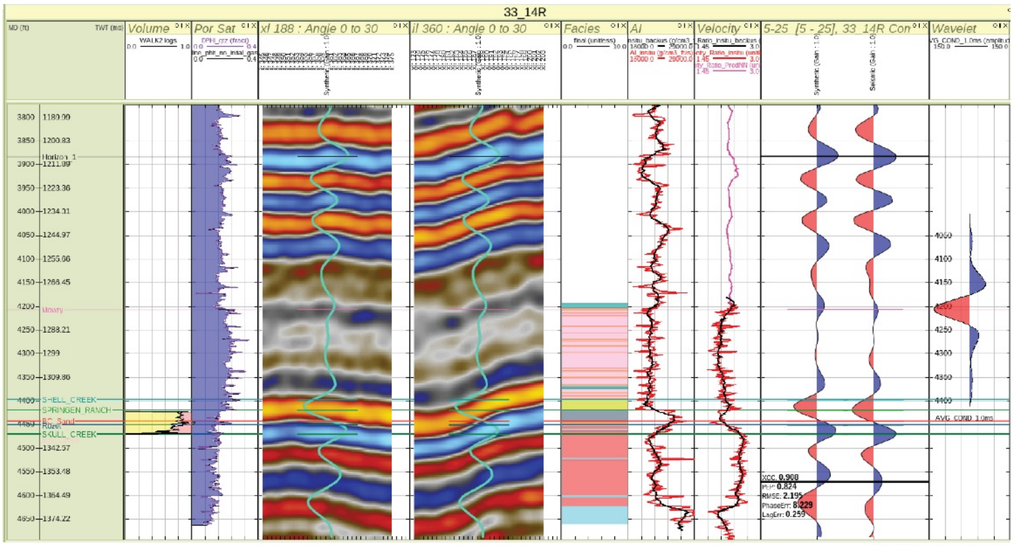

EERC CBO56401.AI

Figure F-2. Example of 33-14R well to seismic tie. Volume: mineral log (mixing type: Voight-Reuss-Hill (weighting), quartz, kaolinite, and calcite); Por Sat: porosity-saturation (mineral: quartz; water = 1, oil = 0, gas = 0); seismic section: crossline (XL) 188; seismic section: inline (IL) 360; facies: estimated facies; AI: red line: well in situ AI; black line: seismic AI with Backus averaging; velocity: velocity ratio; red line: well velocity ratio; black line: seismic velocity ratio with Backus ratio; 5–25 (full stack from the 0–10, 10–20, and 20–30 partial angles): Comparison of synthetic seismic trace (left) vs. real seismic trace (right). Wavelet: wavelet estimated from the well to seismic tie. Notice the parameters used to measure the quality of the tie on Seismic Track 5–25: cross correlation (XCC), proportion of energy predicted (PEP), phase error, and tag error. The horizontal lines represent the markers associated to the main features of the logs: Horizon 1, Mowry, Shell Creek, Springen Ranch, BC Sand, Rozet, Skull Creek, and TD Horizon.

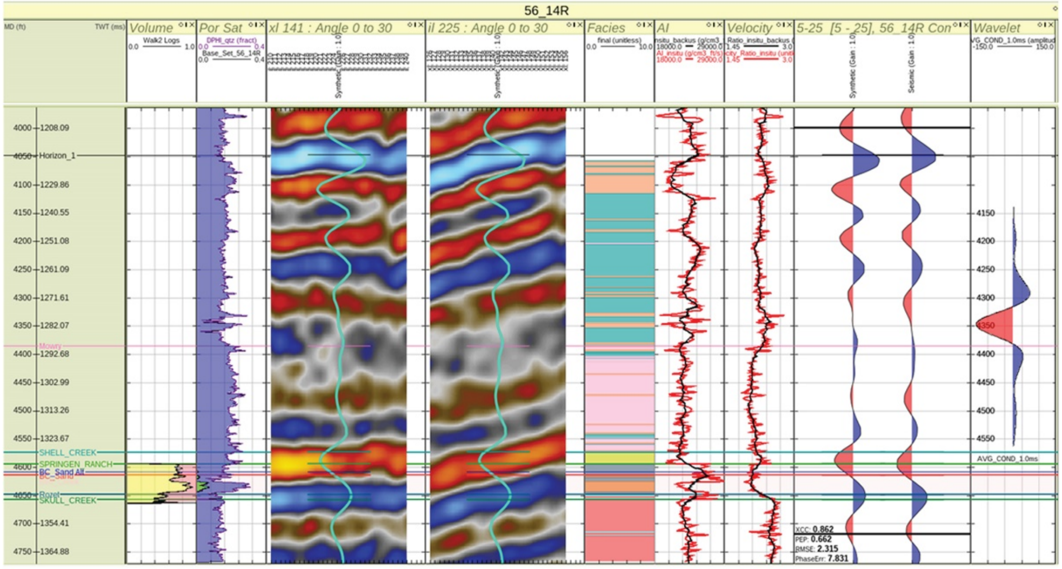

EERC CBO56445.AI

Figure F-3. Example of 56-14R well to seismic tie. Volume: mineral log (mixing type: Voight-Reuss-Hill (weighting), quartz, kaolinite, and calcite); Por Sat: porosity-saturation (mineral: quartz; water = 1, oil = 0, gas=0); seismic section: crossline (XL) 141; seismic section: inline (IL) 225; facies: estimated facies; AI: red line: well in situ AI; black line: seismic AI with Backus averaging; velocity: velocity ratio; red line: well velocity ratio; black line: seismic velocity ratio with Backus ratio; 5–25 (full stack from the 0–10, 10–20, and 20–30 partial angles): Comparison of synthetic seismic trace (left) vs. real seismic trace (right). Wavelet: wavelet estimated from the well to seismic tie. Notice the parameters used to measure the quality of the tie on Seismic Track 5–25: cross correlation (XCC), proportion of energy predicted (PEP), phase error, and tag error. The horizontal lines represent the markers associated to the main features of the logs: Horizon 1, Mowry, Shell Creek, Springen Ranch, BC Sand, Rozet, Skull Creek, and TD Horizon.

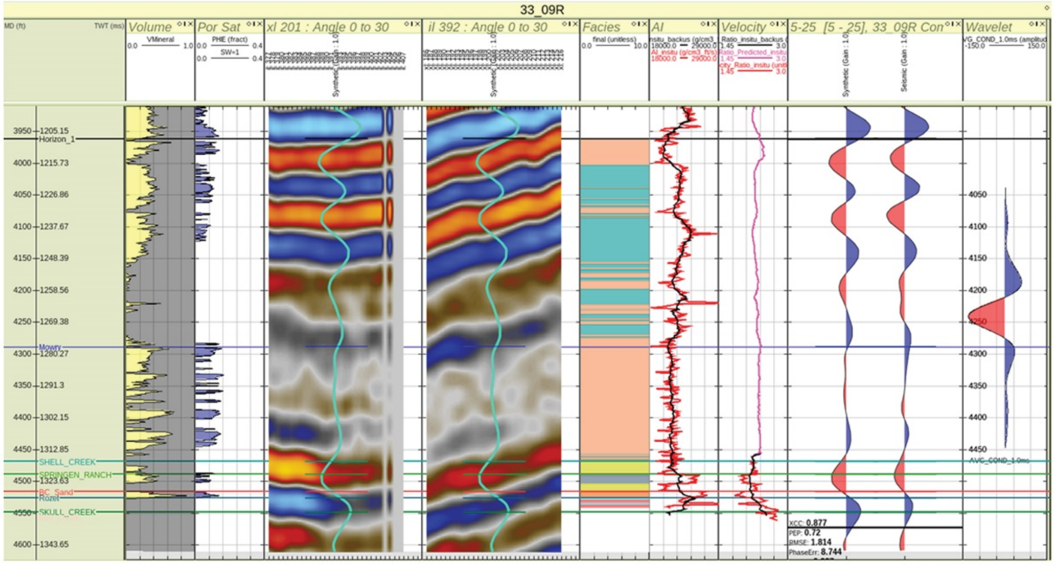

EERC CBO56446.AI

Figure F-4. Example of 33-09R well to seismic tie. Volume: mineral log (mixing type: Voight-Reuss-Hill (weighting), quartz, kaolinite, and calcite); Por Sat: porosity-saturation (mineral: quartz; water = 1, oil = 0, gas = 0); seismic section: crossline (XL) 201; seismic section: inline (IL) 392; facies: estimated facies; AI: red line: Well in situ AI; black line: seismic AI with Backus averaging; velocity: velocity ratio; red line: well velocity ratio; black line: seismic velocity ratio with Backus ratio; 5–25 (full stack from the 0–10, 10–20, and 20–30 partial angles): Comparison of synthetic seismic trace (left) vs. real seismic trace (right). Wavelet: wavelet estimated from the well to seismic tie. Notice the parameters used to measure the quality of the tie on Seismic Track 5–25: cross correlation (XCC), proportion of energy predicted (PEP), phase error, and tag error. The horizontal lines represent the markers associated to the main features of the logs: Horizon 1, Mowry, Shell Creek, Springen Ranch, BC Sand, Rozet, Skull Creek, and TD Horizon.

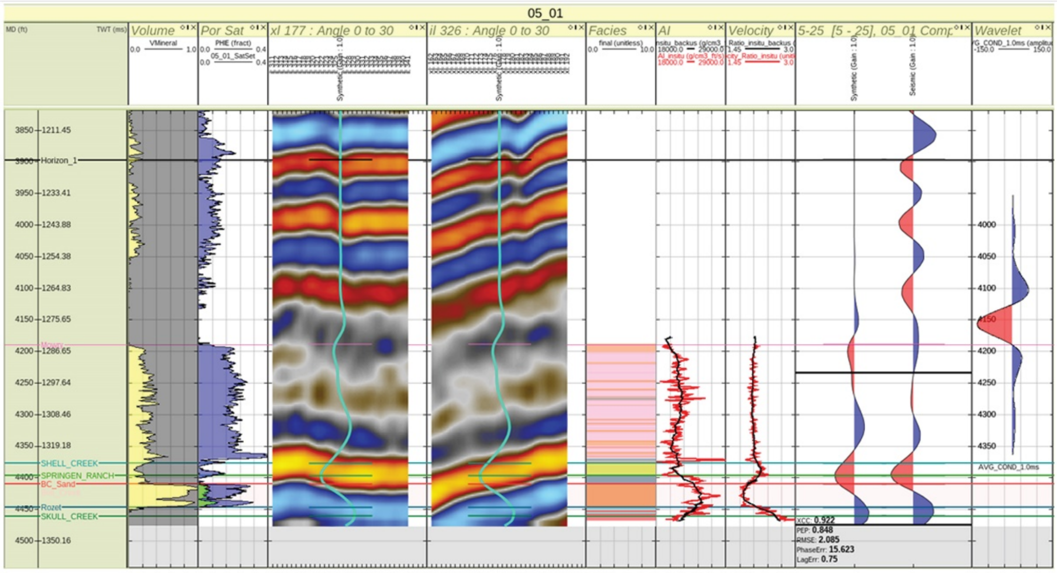

EERC CBO56447.AI

Figure F-5. Example of 05-01 well to seismic tie. Volume: mineral log (mixing type: Voight-Reuss-Hill (weighting), quartz, kaolinite, and calcite); Por Sat: porosity-saturation (mineral: quartz; water = 1, oil = 0, gas = 0); seismic section: crossline (XL) 177; seismic section: inline (IL) 326; facies: estimated facies; AI: red line: well in situ AI; black line: seismic AI with Backus averaging; velocity: velocity ratio; red line: well velocity ratio; black line: seismic velocity ratio with Backus ratio; 5–25 (full stack from the 0–10, 10–20, and 20–30 partial angles): Comparison of synthetic seismic trace (left) vs. real seismic trace (right). Wavelet: wavelet estimated from the well to seismic tie. Notice the parameters used to measure the quality of the tie on Seismic Track 5–25: cross correlation (XCC), proportion of energy predicted (PEP), phase error, and tag error. The horizontal lines represent the markers associated to the main features of the logs: Horizon 1, Mowry, Shell Creek, Springen Ranch, BC Sand, Rozet, Skull Creek, and TD Horizon.

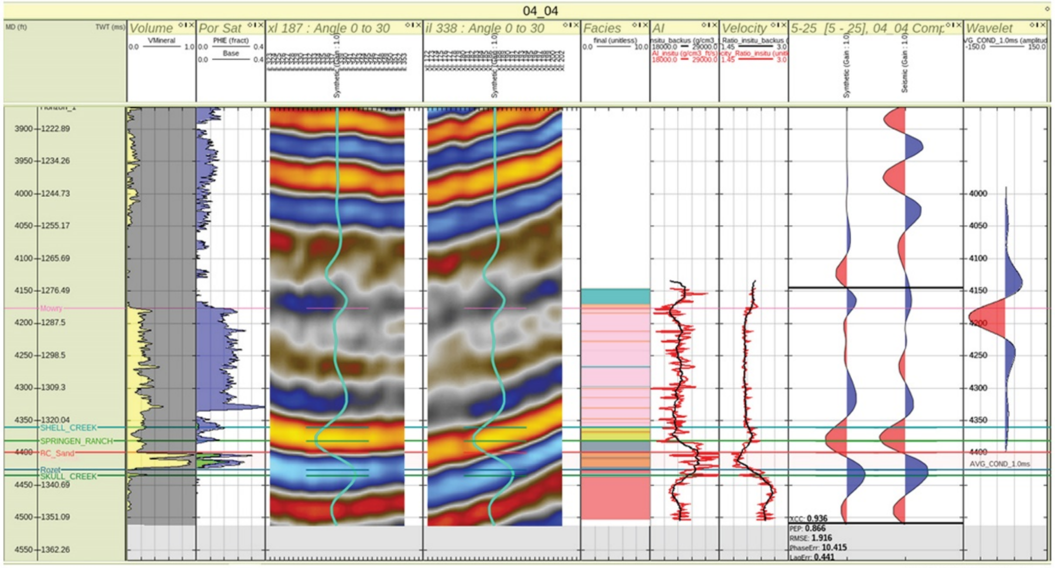

EERC CBO56448.AI

Figure F-6. Example of 04-04 well to seismic tie. Volume: mineral log (mixing type: Voight-Reuss-Hill (weighting), quartz, kaolinite, and calcite); Por Sat: porosity-saturation (mineral: quartz; water = 1, oil = 0, gas = 0); seismic section: crossline (XL) 187; seismic section: inline (IL) 338; facies: estimated facies; AI: red line: well in situ AI; black line: seismic AI with Backus averaging; velocity: velocity ratio; red line: well velocity ratio; black line: seismic velocity ratio with Backus ratio; 5–25 (full stack from the 0–10, 10–20, and 20–30 partial angles): Comparison of synthetic seismic trace (left) vs. real seismic trace (right). Wavelet: wavelet estimated from the well to seismic tie. Notice the parameters used to measure the quality of the tie on Seismic Track 5–25: cross correlation (XCC), proportion of energy predicted (PEP), phase error, and tag error. The horizontal lines represent the markers associated to the main features of the logs: Horizon 1, Mowry, Shell Creek, Springen Ranch, BC Sand, Rozet, Skull Creek, and TD Horizon.

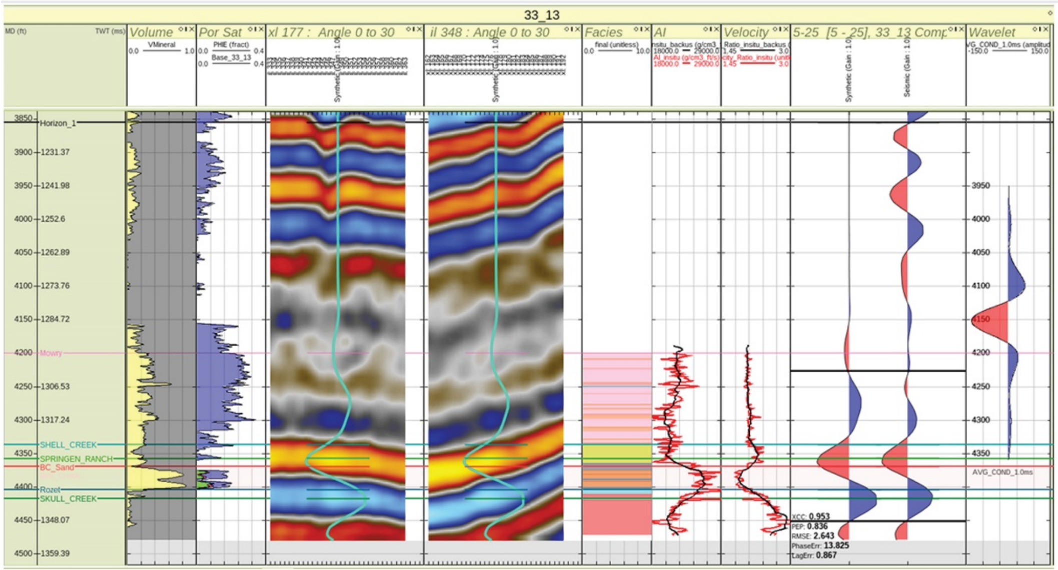

EERC CBO56449.AI

Figure F-7. Example of 33-13 well to seismic tie. Volume: mineral log (mixing type: Voight-Reuss-Hill (weighting), quartz, kaolinite, and calcite); Por Sat: porosity-saturation (mineral: quartz; water = 1, oil = 0, gas = 0); seismic section: crossline (XL) 177; seismic section: inline (IL) 348; facies: estimated facies; AI: red line: well in situ AI; black line: seismic AI with Backus averaging; velocity: velocity ratio; red line: well velocity ratio; black line: seismic velocity ratio with Backus ratio; 5–25 (full stack from the 0–10, 10–20, and 20–30 partial angles): Comparison of synthetic seismic trace (left) vs. real seismic trace (right). Wavelet: wavelet estimated from the well to seismic tie. Notice the parameters used to measure the quality of the tie on Seismic Track 5–25: cross correlation (XCC), proportion of energy predicted (PEP), phase error, and tag error. The horizontal lines represent the markers associated to the main features of the logs: Horizon 1, Mowry, Shell Creek, Springen Ranch, BC Sand, Rozet, Skull Creek, and TD Horizon.

Table F-1. Summary of the Well to Seismic Full Stack Tie Results

Well	XCC	PEP	Phase Error
05-06 OW	0.934	0.818	6.198
31-16R	0.918	0.846	6.919
33-14R	0.908	0.824	8.229
56-14R	0.862	0.662	7.831
33-09R	0.877	0.72	8.744
05-01	0.922	0.848	15.623
04-04	0.936	0.866	10.415

REFERENCES

Aki, K., and Richards, P.G., 1980, Quantitative seismology—theory and methods: v. 1, W.H. Freeman and Company.

Folstad, P.G., and Schoenberg, M., 1992, Low-frequency propagation through fine layering: SEG Expanded Abstract, p. 1297–1281.

Liner, C., and Fei, T., 2007, The Backus number—the leading edge: no. 4, p. 420–426.

APPENDIX G

QUALITY CONTROL OF WELL TO PARTIAL SEISMIC STACK TIES FOR JI-FI

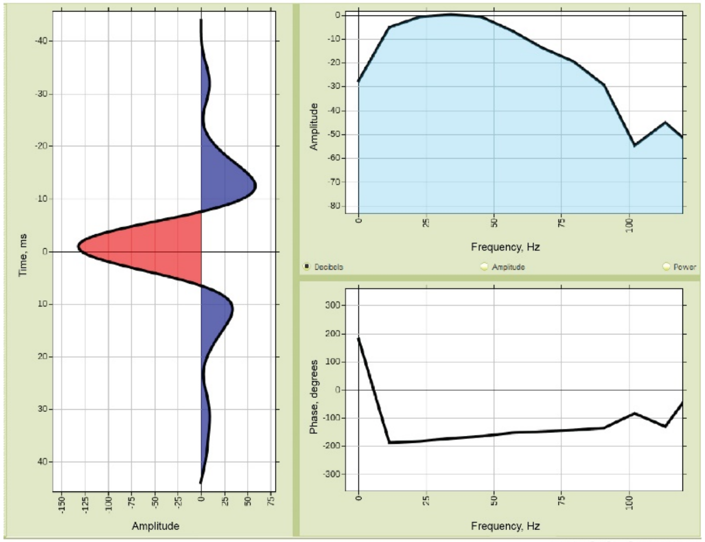

EERC CBO56404.AI

Figure G-1. Average wavelet estimated from the well to seismic tie using 0–10-degree partial stacks. Left wavelet; top right: amplitude spectrum. Bottom right: phase spectrum.

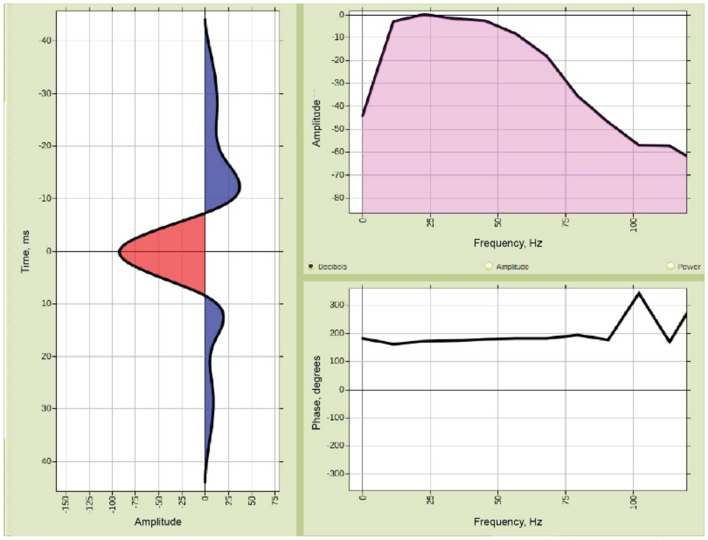

EERC CBO56405.AI

Figure G-2. Estimated Bayesian wavelet from the well to seismic tie using 10–20-degree partial stacks. Left wavelet; top right: amplitude spectrum. Bottom right: phase spectrum.

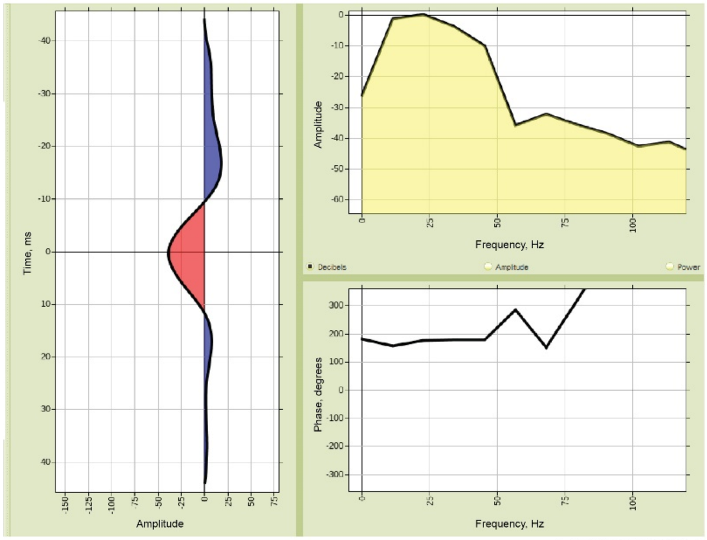

EERC CBO56406.AI

Figure G-3. Estimated Bayesian wavelet from the well to seismic tie using 20–30-degree partial stacks. Left wavelet; top right: amplitude spectrum. Bottom right: phase spectrum.

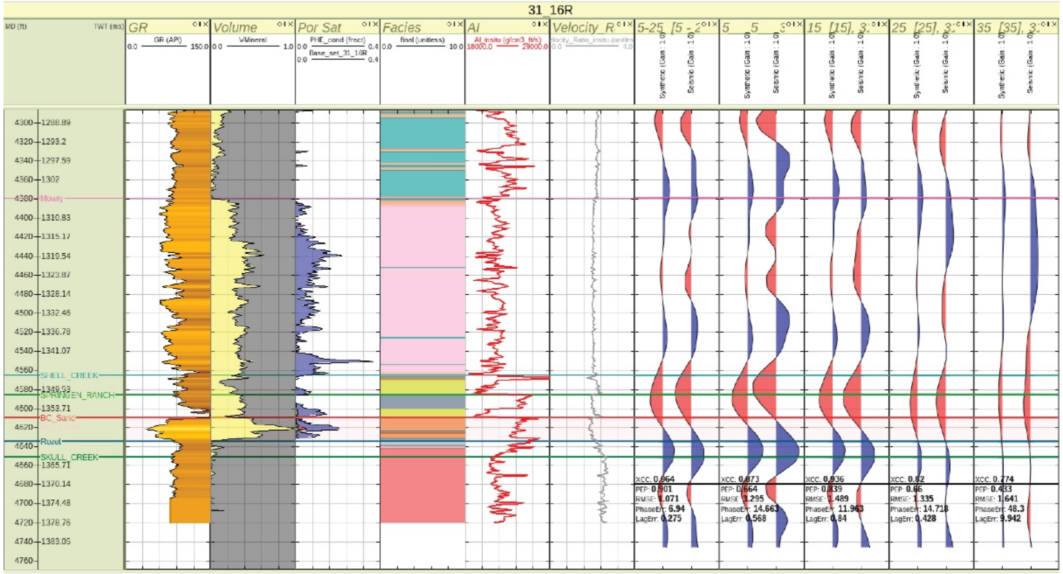

EERC CBO56407.AI

Figure G-4. Well tie for 31-16R using partial stacks, 0–30, 0–10, 10–20, 20–30, and 30–40 degrees. Left to right tracks: gamma ray (GR); volume: mineral log; Por Sat: porosity-saturation (mineral: quartz; water = 1, oil = 0, gas = 0); facies: estimated facies; AI (acoustic impedance): red line; velocity ratio; seismic: 5–25 (full stack); 0–10, 10–20, and 20–30-degree partial angles), estimated wavelets are on top of each seismic track. Notice the parameters used to measure the quality of the tie on Seismic Track 5–25: cross-correlation (XCC), the proportion of energy predicted (PEP), phase error, and tag error. The horizontal lines represent the markers associated with the main features of the logs: Horizon 1, Mowry, Shell Creek, Springen Ranch, Bell Creek (BC) Sand, Rozet, Skull Creek, and TD Horizon.

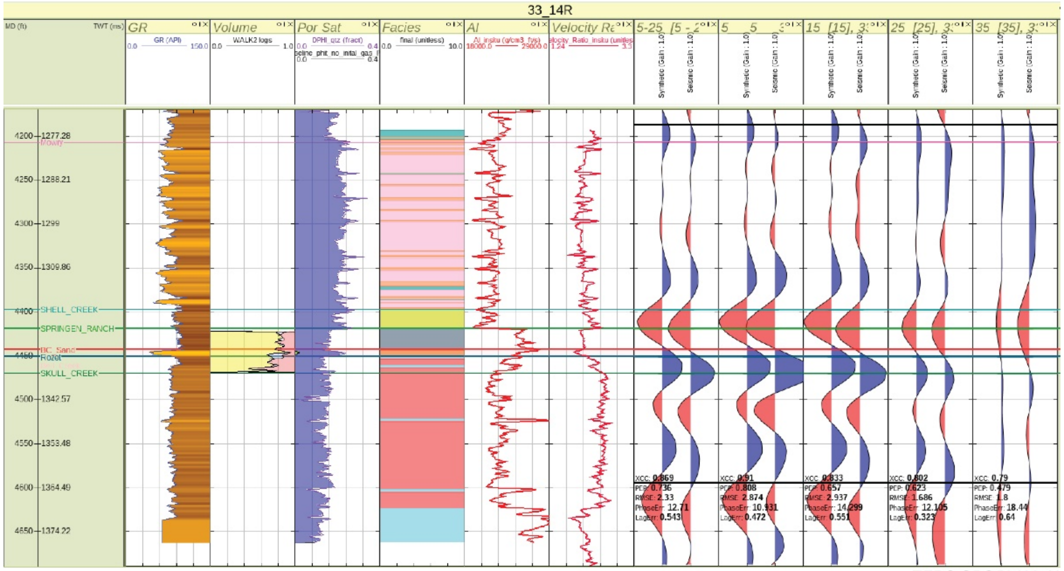

EERC CBO56408.AI

Figure G-5. Well tie for 33-14R using partial stacks, 0–30, 0–10, 10–20, 20–30, and 30–40 degrees. Left to right tracks: gamma ray (GR); volume: mineral log; Por Sat: porosity-saturation (mineral: quartz; water = 1, oil = 0, gas = 0); facies: estimated facies; AI: red line; velocity ratio; seismic: 5–25 (full stack); 0–10, 10–20, and 20–30-degree partial angles), estimated wavelets are on top of each seismic track. Notice the parameters used to measure the quality of the tie on Seismic Track 5–25: cross-correlation (XCC), the proportion of energy predicted (PEP), phase error, and tag error. The horizontal lines represent the markers associated with the main features of the logs: Horizon 1, Mowry, Shell Creek, Springen Ranch, BC Sand, Rozet, Skull Creek, and TD Horizon.

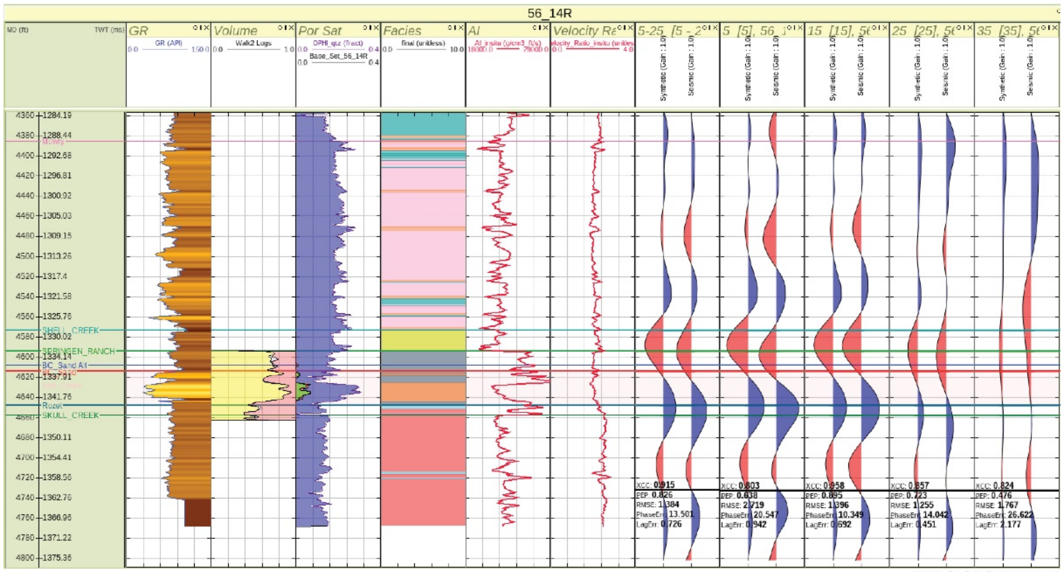

EERC CBO56409.AI

Figure G-6. Well tie for 56-14R using partial stacks, 0–30, 0–10, 10–20, 20–30, and 30–40 degrees. Left to right tracks: gamma ray (GR); volume: mineral log; Por Sat: porosity-saturation (mineral: quartz; water = 1, oil = 0, gas = 0); facies: estimated facies; AI: red line; velocity ratio; seismic: 5–25 (full stack); 0–10, 10–20, and 20–30-degree partial angles), estimated wavelets are on top of each seismic track. Notice the parameters used to measure the quality of the tie on Seismic Track 5–25: cross-correlation (XCC), the proportion of energy predicted (PEP), phase error, and tag error. The horizontal lines represent the markers associated with the main features of the logs: Horizon 1, Mowry, Shell Creek, Springen Ranch, BC Sand, Rozet, Skull Creek, and TD Horizon.

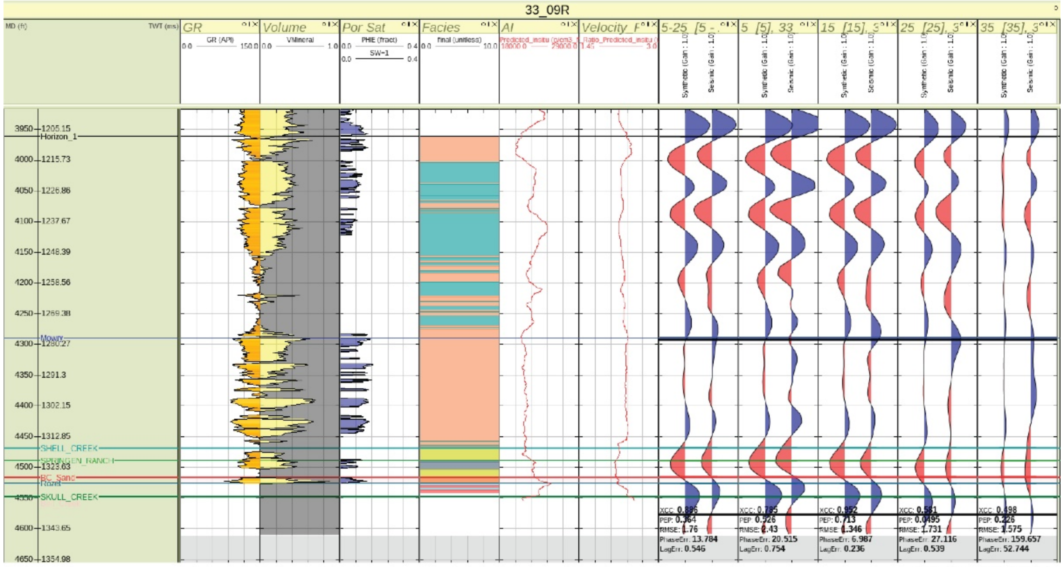

EERC CBO56410.AI

Figure G-7. Well tie for 33-09R using partial stacks, 0–30, 0–10, 10–20, 20–30, and 30–40 degrees. Left to right tracks: gamma ray (GR); volume: mineral log; Por Sat: porosity-saturation (mineral: quartz; water = 1, oil = 0, gas = 0); facies: estimated facies; AI: red line; velocity ratio; seismic: 5–25 (full stack); 0–10, 10–20, and 20–30-degree partial angles), estimated wavelets are on top of each seismic track. Notice the parameters used to measure the quality of the tie on Seismic Track 5–25: cross-correlation (XCC), the proportion of energy predicted (PEP), phase error, and tag error. The horizontal lines represent the markers associated with the main features of the logs: Horizon 1, Mowry, Shell Creek, Springen Ranch, BC Sand, Rozet, Skull Creek, and TD Horizon.

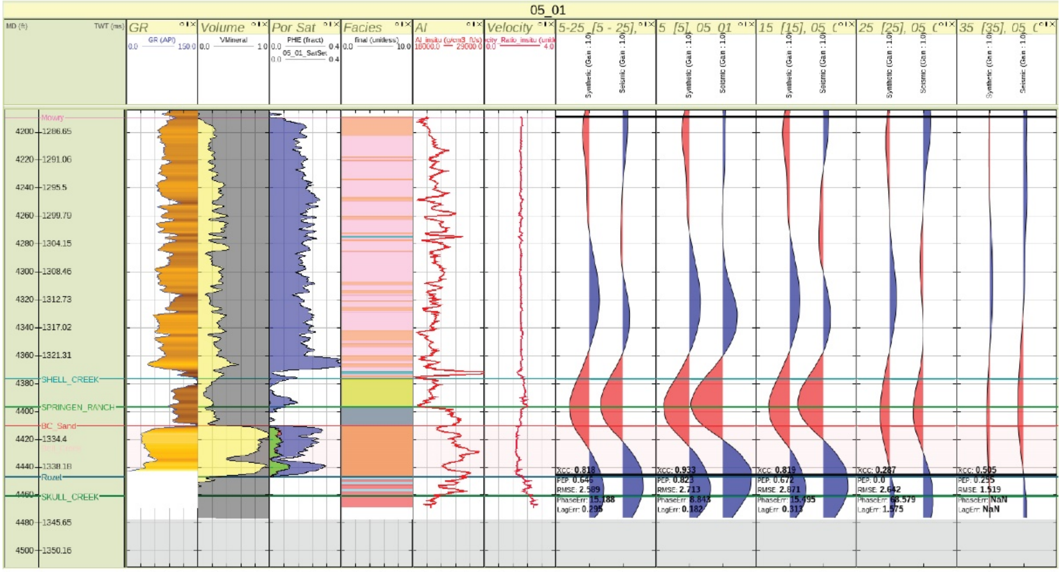

EERC CBO56411.AI

Figure G-8. Well tie for 05-01 using partial stacks, 0–30, 0–10, 10–20, 20–30, and 30–40 degrees. Left to right tracks: gamma ray (GR); volume: mineral log; Por Sat: porosity-saturation (mineral: quartz; water = 1, oil = 0, gas = 0); facies: estimated facies; AI: red line; velocity ratio; seismic: 5–25 (full stack); 0–10, 10–20, and 20–30-degree partial angles), estimated wavelets are on top of each seismic track. Notice the parameters used to measure the quality of the tie on Seismic Track 5–25: cross-correlation (XCC), the proportion of energy predicted (PEP), phase error, and tag error. The horizontal lines represent the markers associated with the main features of the logs: Horizon 1, Mowry, Shell Creek, Springen Ranch, BC Sand, Rozet, Skull Creek, and TD Horizon.

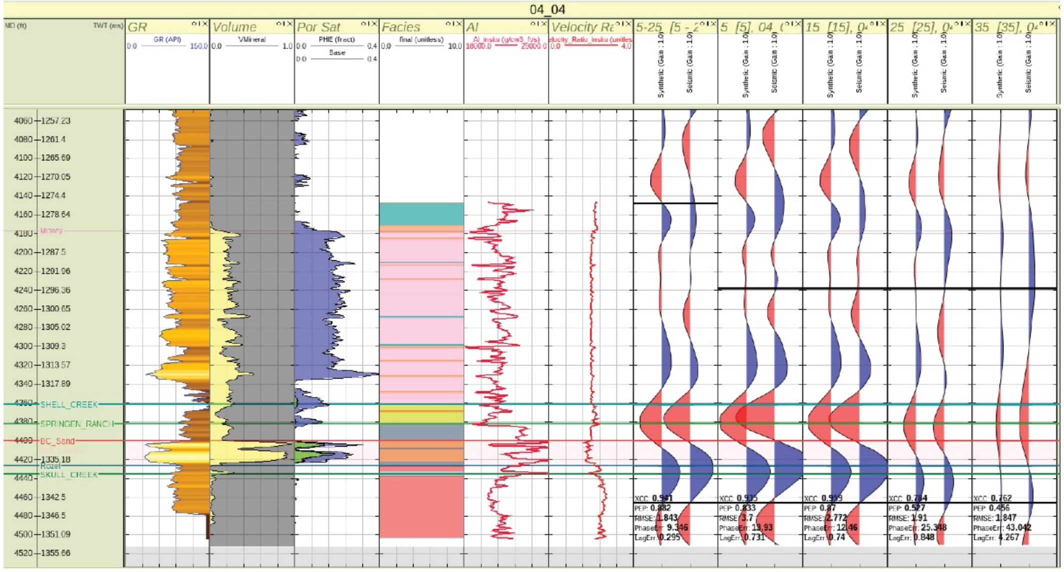

EERC CBO56412.AI

Figure G-9. Well tie for 04-04 using partial stacks, 0–30, 0–10, 10–20, 20–30, and 30–40 degrees. Left to right tracks: gamma ray (GR); volume: mineral log; Por Sat: porosity-saturation (mineral: quartz; water = 1, oil = 0, gas = 0); facies: estimated facies; AI: red line; velocity ratio; seismic: 5–25 (full stack); 0–10, 10–20, and 20–30-degree partial angles), estimated wavelets are on top of each seismic track. Notice the parameters used to measure the quality of the tie on Seismic Track 5–25: cross-correlation (XCC), the proportion of energy predicted (PEP), phase error, and tag error. The horizontal lines represent the markers associated with the main features of the logs: Horizon 1, Mowry, Shell Creek, Springen Ranch, BC Sand, Rozet, Skull Creek, and TD Horizon.

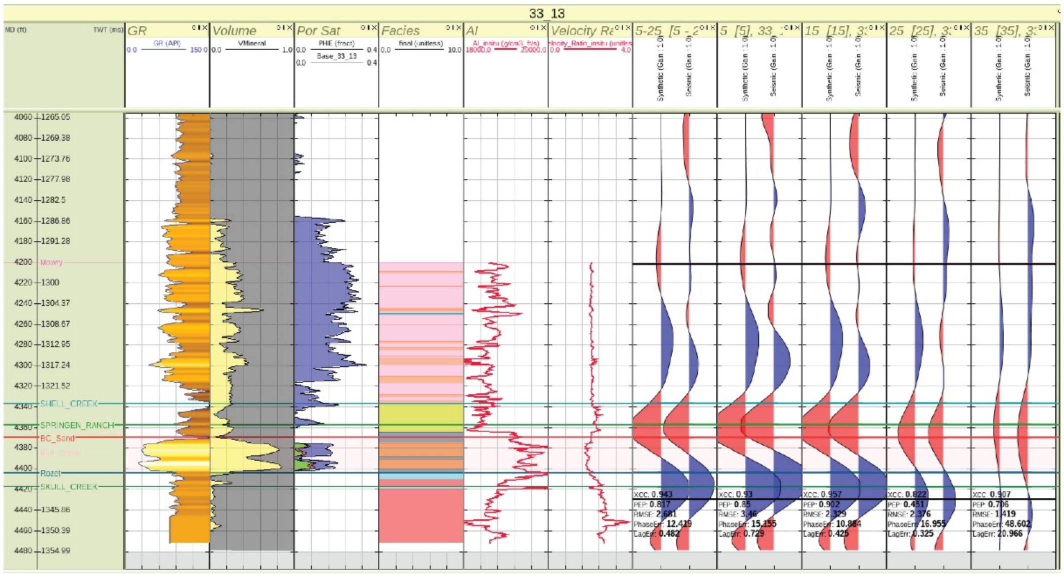

EERC CBO56413.AI

Figure G-10. Well tie for 33-13 using partial stacks, 0–30, 0–10, 10–20, 20–30, and 30–40 degrees. Left to right tracks: gamma ray (GR); volume: mineral log; Por Sat: porosity-saturation (mineral: quartz; water = 1, oil = 0, gas = 0); facies: estimated facies; AI: red line; velocity ratio; seismic: 5–25 (full stack); 0–10, 10–20, and 20–30-degree partial angles), estimated wavelets are on top of each seismic track. Notice the parameters used to measure the quality of the tie on Seismic Track 5–25: cross-correlation (XCC), the proportion of energy predicted (PEP), phase error, and tag error. The horizontal lines represent the markers associated with the main features of the logs: Horizon 1, Mowry, Shell Creek, Springen Ranch, BC Sand, Rozet, Skull Creek, and TD Horizon.

Table G-1. Summary of the Well to Seismic Partial Stacks Tie Results

Well	**0–30**			**0–10**			**10–20**			**20–30**			**30–40**		
	XCC	**PEP**	**PE***	**XCC**	**PEP**	**PE**	**XCC**	**PEP**	**PE**	**XCC**	**PEP**	**PE**	**XCC**	**PEP**	**PE**
O5-06 OW	0.949	0.856	8.94	0.904	0.814	13.66	0.943	0.863	11.39	0.923	0.851	8.52	0.861	0.644	13.60
31-16R	0.964	0.901	6.94	0.873	0.664	14.66	0.936	0.839	11.96	0.82	0.66	14.71	0.774	0.433	9.94
33-14R	0.869	0.736	12.71	0.91	0.808	10.93	0.833	0.657	14.29	0.802	0.623	12.10	0.79	0.479	18.44
56-14R	0.915	0.826	13.50	0.803	0.638	20.54	0.958	0.895	10.34	0.857	0.723	14.04	0.824	0.476	26.62
33-09R	0.886	0.364	13.78	0.785	0.526	20.51	0.952	0.713	6.98	0.581	0.495	27.11	0.498	0.226	159.6
05-01	0.818	0.646	15.18	0.933	0.823	8.84	0.819	0.672	15.49	0.287	0.0	68.57	0.505	0.255	
04-04	0.941	0.882	9.34	0.935	0.833	13.93	0.959	0.87	12.46	0.784	0.527	25.34	0.762	0.456	43.04
33-13	0.943	0.817	12.41	0.93	0.85	15.15	0.957	0.902	10.88	0.822	0.451	16.95	0.907	0.706	48.60

* Phase error.